An improved model for self-sensing heteropolar active magnetic bearings

Thesis submitted for the degree Doctor of Philosophy

at the Potchefstroom Campus of the

North-West University

Eugén O. Ranft

Promoter: G. van Schoor

December 2007

PREFACE

I would firstly like to thank my wife Desré for her love and support without which I could not have persevered. To my family, thank you for your loving support and encouragement.

Special thanks to my promoter, Prof. George van Schoor, for his guidance and support. I would also like to thank M-Tech Industrial and THRIP for the funding without which the research would not have been possible. Finally I would like to thank the McTronX team, especially André, Pieter, Kenny and Robert for their help and support.

"The Lord God is my Strength, and he will give me the speed of a deer
and bring me safely over the mountains." - Habakkuk 3:19

ABSTRACT

Active magnetic bearings (AMBs) use position feedback to actively control the forces generated by electromagnetic transducers, in order to realise stable suspension of a levitated object. The AMB concept is not new and since its introduction to industry, its application has grown extensively. Although they pose a number of novel qualities rendering them invaluable machine components in modern day industry, the technology has not yet reached its full potential. In the ongoing drive for even wider acceptance and application of AMB technology in industry, efforts with regards to system optimisation as a whole and component integration, are underway to make AMBs more reliable and economical.

Component integration impacts both cost and reliability and one area of research addressing this issue is self-sensing. Self-sensing is the concept where the actuation and sensing functions are realised with a single electromagnetic transducer. In the magnetic bearing the coil current and voltage waveforms are monitored and used to extract the rotor position information. Self-sensing poses a number of advantages over dedicated sensors and has the potential to realise major cost savings. Although self-sensing is not a new concept and the topic has been researched in the past, it remains a challenge. Self-sensing performance is degraded due to problems such as magnetic cross-coupling, eddy currents, saturation and high losses, to name but a few.

The focus of this thesis is on the development of an improved model for self-sensing heteropolar AMBs. The model must also be incorporated into an appropriate self-sensing scheme to demonstrate its ability to address the issues of saturation and magnetic cross-coupling.

In the thesis the amplitude modulation approach using the switching amplifier ripple as high frequency source is adopted. A coupled reluctance network model (RNM) is developed which models the coil impedance at the switching frequency. The model is refined and incorporated into a multiple input multiple output (MIMO) parameter estimation scheme to demonstrate its ability to overcome the aforementioned problems.

An analytical MATLAB®-based RNM is established from literature and refined with the help of finite element method (FEM) models and experimental measurements. Results obtained from the 40 node RNM were shown to closely correlate with results generated by a FEM model with 80,000 nodes. The fact that RNMs are much faster to solve than their FEM counterparts and their ability to precisely map the magnetic behaviour of magnetic bearings, render them the preferred option for online implementation in a self-sensing scheme.

The proposed self-sensing scheme is evaluated in a simulation environment which utilises a transient simulation model (TSM), incorporating important aspects that influence self-sensing performance, i.e. eddy currents, magnetic cross-coupling and hysteresis. Results show that it is possible to address saturation and magnetic cross-coupling with the RNM incorporated into a MIMO parameter estimation scheme. System sensitivity levels achieved, are satisfactory for long term operation. This demonstrates the viability of the proposed self-sensing scheme.

CONTENTS

LIST OF FIGURES

LIST OF TABLES

LIST OF SYMBOLS

Latin symbols

$\mathbf{A}$	Magnetic vector potential	[T m]
A	Magnetic vector potential scalar	[T m]
a	Cross-sectional area of the flux path	[m^2]
a_g	Air gap area	[m^2]
a_v	Coil window area	[m^2]
$\mathbf{B}$	Magnetic flux density	[T]
B	Magnetic flux density scalar	[T]
$B_1, \ldots, B_{40}$	Magnetic flux density of flux paths 1 to 40	[T]
b	Anhysteresis model shape parameter	[A/m]
$\mathbf{D}$	Electric flux density	[C/m^2]
D	Closed disc in complex plain for time varying gain	
d	Lamination thickness	[m]
$\mathbf{E}$	Electric field intensity	[V/m]
$E(s)$	Error between the estimated and true current differences	[A]
e_x	Error between estimated and true x-axis coil currents	[A]
e_y	Error between estimated and true y-axis coil currents	[A]
$F(s)$	Demodulation process transfer function	
F_d	Disturbance force	[N]
F_x	Resulting x-axis force on the rotor	[N]
F_y	Resulting y-axis force on the rotor	[N]
f_c	System critical frequency	[Hz]
f_s	Power amplifier switching frequency	[Hz]
$G(s)$	Estimator controller transfer function	
$G_c(s)$	AMB system closed loop transfer function	
$G_{ho}(s)$	Sampler and zero-order hold transfer function	
$G_o(s)$	AMB system open loop transfer function	
$G_s(s)$	AMB system sensitivity transfer function	
g_0	Nominal air gap length	[m]
$\mathbf{H}$	Magnetic field intensity	[A t/m]
H_e	Anhysteresis model effective field	[A t/m]
I_e	Eddy current	[A]
I_k	k^{th} average coil current	[A]
$\underline{I}_1, \ldots, \underline{I}_4$	Demodulated coil currents 1 to 4	[A]

$\hat{\underline{I}}_1, \ldots, \hat{\underline{I}}_4$	Estimates of demodulated coil currents 1 to 4	[A]
i	Coil current in the time domain	[A]
$\hat{i}$	Estimated coil current	[m]
$i_{avg1}, \ldots, i_{avg1}$	Average coil currents 1 to 4	[A]
$i_1, \ldots, i_4$	Coil currents 1 to 4 in time domain	[A]
$\mathbf{J}$	Current density vector	[A/m^2]
$\mathbf{J}^e$	Externally generated current density	[A/m^2]
J_k	kth coil current density scalar	[A/m^2]
j	$\sqrt{-1}$	
K	Time varying gain associated with duty cycle variation	
K_i	Integral constant of the PI controller	
K_p	Proportional constant of the PI controller	
k_{eq}	Equivalent stiffness parameter	[N/m]
$\mathbf{L}$	Bearing inductance matrix	[H]
L	Incremental / apparent inductance	[H]
L_{ek}	kth equivalent eddy current inductance	[H]
L_{jk}	Mutual inductance between the jth and kth coils	[H]
l	Magnetic path length	[m]
l_{ax}	Axial bearing length	[m]
l_c	Coil window length	[m]
l_g	Air gap length	[m]
l_p	Pole effective material path length	[m]
l_r	Rotor segment effective material path length	[m]
l_s	Stator segment effective material path length	[m]
$\mathbf{M}$	Material magnetisation vector	[A/m]
M_s	Anhysteresis model saturation magnetisation	[A/m]
N	Number of coil turns	
N_p	Number of primary coil turns	
N_s	Number of secondary coil turns	
P	Number of poles	
$P_1, \ldots, P_8$	Pole 1 to 8	
P_g	Total air gap permeance	[H]
P_{gf}	Fringing path air gap permeance	[H]
P_{gm}	Main air gap permeance	[H]
$PP_1, \ldots, PP_4$	Pole pair 1 to 4	
R	Winding resistance	[Ω]
R_{ek}	kth equivalent eddy current resistance	[Ω]
R_l	Parameter used in analytical fringing correction	[m]
r_c	Stator back iron inner radius	[m]
r_j	Journal outer radius	[m]
r_p	Stator pole radius	[m]
r_r	Journal inner radius	[m]
r_s	Stator outer radius	[m]
s	Laplace variable	
T_s	Sampling time	[s]
T_1	FFT window period	[s]
T_2	FFT execution interval	[s]
t_c	Coil window width	[m]
V_p	Power amplifier supply voltage	[V]
$\mathbf{v}$	Speed	[m/s]

v	Coil voltage in the time domain	[V]
$v_1, \ldots, v_4$	Coil voltages 1 to 4 in time domain	[V]
$\underline{V}_1, \ldots, \underline{V}_4$	Demodulated coil voltages 1 to 4	[V]
w	Pole width	[m]
$X(s)$	True x-axis rotor position	[m]
$\hat{X}(s)$	Estimated x-axis rotor position	[m]
$X_e(s)$	Stability analysis excitation signal [m]	
$X_s(s)$	Position sensor feedback signal [m]	
x	Rotor position in the x-axis	[m]
$\hat{x}$	Estimated x-axis position	[m]
x_{ref}	Rotor reference position in the x-axis	[m]
y	Rotor position in the y-axis	[m]
$\hat{y}$	Estimated y-axis position	[m]
y_{ref}	Rotor reference position in the y-axis	[m]
$\mathbf{Z}$	Coil complex impedance matrix	[Ω]

Greek symbols

α	Amplifier duty cycle	
$\alpha_1, \ldots, \alpha_4$	Duty cycle of coil 1 to 4	
β	Anhysteresis model mean field parameter	
λ	Flux linkage	[Wb t]
μ	Material permeability	[H/m]
μ_{fd}	Complex material permeability	[H/m]
μ_r	Relative material permeability	
$\mu_{r\Delta}$	Incremental relative material permeability	
μ_0	Permeability of free space	[H/m]
ω	Excitation frequency	[rad/s]
ω_s	Power amplifier switching frequency	[rad/s]
ϕ	Magnetic flux	[Wb]
ϕ_{gk}	Flux in bearing k$^{\text{th}}$ air gap	[Wb]
ϕ_{lk}	Flux in bearing k$^{\text{th}}$ leakage path	[Wb]
ϕ_{pk}	Flux in bearing k$^{\text{th}}$ pole	[Wb]
ϕ_{rk}	Flux in bearing k$^{\text{th}}$ rotor segment	[Wb]
ϕ_{sk}	Flux in bearing k$^{\text{th}}$ stator segment	[Wb]
$\phi_1, \ldots, \phi_{40}$	Magnetic flux through paths 1 to 40 of the reluctance network	[Wb]
$\Re$	Magnetic reluctance	[H^{-1}]
$\Re_{gk}$	k$^{\text{th}}$ air gap reluctance	[H^{-1}]
$\Re_{lk}$	k$^{\text{th}}$ leakage reluctance	[H^{-1}]
$\Re_{lm}$	Mutual leakage reluctance	[H^{-1}]
$\Re_{ls}$	Self-leakage reluctance	[H^{-1}]
$\Re_{pk}$	k$^{\text{th}}$ pole reluctance	[H^{-1}]
$\Re_{rk}$	k$^{\text{th}}$ rotor segment reluctance	[H^{-1}]
$\Re_{sk}$	k$^{\text{th}}$ stator segment reluctance	[H^{-1}]
ρ	Resistivity	[Ω m]
σ	Electrical conductivity of lamination material	[S/m]
θ	Pole pitch	[rad]

CHAPTER 1

Introduction

1.1 Motivation

Active magnetic bearings (AMBs) is not a new concept and since their introduction to industry, their application has grown extensively. AMBs pose a number of novel qualities rendering them invaluable machine components in the modern day industry. According to [1] AMB commercial applications can historically be divided into two types of machinery, i.e. equipment under the category of turbomachinery (e.g. centrifugal compressors, turbo-expanders, turbines etc.) and turbomolecular pumps (e.g. pumps used in the semiconductor industry to create ultra high vacuum environments).

New applications include blowers for new generation nuclear reactors, air conditioning, fuel cells, energy co-generation, nuclear reactor main shaft [2], biomedical applications [3] and aircraft jet engines to name but a few. The most successful application of the AMB technology to date is the turbomolecular pump used in the semiconductor industry with more than 60,000 units in operation.

Despite the successes, AMB technology has not jet reached its full potential. To achieve high volume production of AMB systems they must be economical and reliable. There are a number of research efforts under way to increase system reliability and to reduce cost which may facilitate wide industrial application of AMB technology. Cost reduction and increased reliability can be achieved by optimisation of the system as a whole or by combining component functions.

Component integration impacts both cost and reliability and one area of research addressing this issue is self-sensing. This technique combines the actuation and sensing functions into a single electromagnetic transducer. The application of the self-sensing concept eliminates the position sensors by estimating the position of the levitated body from the bearing coil current and voltage waveforms. Elimination of the position sensor can potentially increase system reliability due to the elimination of a possible point of failure. Cost reduction is also realised due to the elimination of the sensor and reduced wiring between the electronics and the electromagnetic transducer. Both of these advantages rely on the fact that the additional components necessary for self-sensing realisation are reliable and inexpensive.

Although self-sensing is not a new concept and the topic has been researched in the past, it remains a challenge [4]. The reason for this is that most self-sensing techniques are difficult to realise and lack robustness, which results in inferior sensing performance [5]. The proposed self-sensing methods are not easily realised and for this reason self-sensing has only recently (December 2005) found its first industrial application when it was integrated into a turbomolecular pump developed by S2M [6].

This type of position sensing has a number of advantages over dedicated sensors such as: cost reduction, increased reliability of the AMB, reduced maintenance, the AMB becomes more compact, fewer wires running between the electromagnetics and electronics, elimination of non-collocation effects and redundancy if the dedicated position sensors are not discarded [4].

1.2 Areas where contributions can be made

A recent survey on the topic of self-sensing [7] listed the following three aspects as problems which warrant further research: current ripple amplitude, eddy currents and saturation. Another problem that was identified in [8] is that of cross-coupling due to magnetic coupling which has the potential to destabilise the self-sensing system.

In [9] a multiple input multiple output (MIMO) parameter estimator structure is proposed as possible solution to the saturation problem. In [8] it is recommended that a coupled reluctance network model (RNM) is used in the self-sensing scheme to overcome the cross-coupling problem.

Throughout the self-sensing literature it is clear that the accuracy of the self-sensing technique depends strongly on the accuracy of the model it employs. More accurate modelling of the magnetic circuit is therefore also an area where a contribution can be made.

Another area where contributions can be made is the development of tools with which the robustness of self-sensing techniques may be analysed. This will facilitate the development of new self-sensing techniques with higher robustness.

1.3 Problem statement

Self-sensing systems suffer from modelling inaccuracies which include saturation and magnetic cross-coupling effects amongst others. The focus of this thesis is on the development of an improved model for self-sensing heteropolar magnetic bearings. The model must also be incorporated into an appropriate self-sensing scheme to demonstrate its ability to address the issues of saturation and magnetic cross-coupling. It should be noted that the optimisation of the self-sensing scheme does not form part of this thesis.

1.4 Research aims and objectives

The following research aims and objectives are identified:

- Identify self-sensing approach with the purpose of identifying the modelling requirements
- Identify mechanisms that degrade self-sensing performance
- Model refinement

  Develop comprehensive model

  Identify mechanisms contributing to modelling uncertainty

  Refine model

  Verify model

  Quantify the effect of each of these mechanisms
- Realise a self-sensing scheme with the refined model
- Evaluate the model's ability to address self-sensing problems

1.5 Research methodology

The methodology used to address the research aims and objectives as discussed in the previous section is as follows:

Self-sensing approach identification: A comprehensive literature study is undertaken to identify the most promising self-sensing approach and its modelling requirements. The qualifying parameters include bandwidth, accuracy and robustness.

Mechanisms that degrade performance: The mechanisms that degrade the performance of the identified self-sensing technique must be identified from literature with the purpose of inclusion in the self-sensing model.

Model refinement: As soon as a suitable self-sensing approach is chosen and the associated modelling requirements and shortcomings are identified, a process of model refinement commences. A comprehensive MATLAB®-based analytical model is derived for an existing 8-pole heteropolar AMB system. The model derivation process is facilitated through extensive finite element method (FEM) analyses.

Develop comprehensive model: A comprehensive MATLAB®-based analytical model is developed, using existing and new methods, incorporating all the important aspects as identified from literature. After the model is established an iterative process commences which comprises the following four aspects:

Identify mechanisms contributing to modelling uncertainty: Discrepancies between the MATLAB® model, FEM and measured results are analysed to identify the responsible mechanisms.

Refine model: When a mechanism is identified, the MATLAB® model is refined accordingly to alleviate or entirely eliminate the discrepancy.

Verify model: The MATLAB® model is iteratively verified with FEM and experimental measurements.

Quantify the effect of each of these mechanisms: The error induced by each mechanism is quantified by comparing results obtained from MATLAB® models, that respectively exclude each of these effects, to FEM and experimental results.

Self-sensing scheme realisation: Once a refined MATLAB® model is established, it must be incorporated into a self-sensing scheme. An appropriate self-sensing scheme is identified from literature and implemented as a first approach. The system is linearised and a stability analysis is performed on the position estimation scheme.

Evaluate model in self-sensing scheme: For the purpose of evaluating the self-sensing scheme, a MATLAB® transient simulation model (TSM) of an 8-pole heteropolar AMB system is realised. The TSM incorporates important aspects that degrade self-sensing performance, i.e. eddy currents, magnetic cross-coupling and hysteresis. The TSM is then used to evaluate the self-sensing scheme's ability to address issues such as saturation and magnetic cross-coupling. Implementation in the practical system poses unique challenges that were excluded from this study.

1.6 Contribution of research

The contribution of the thesis lies in combining existing methods and previous work to achieve a new method. The MIMO parameter estimator which was proposed by Noh [9] to solve the saturation problem, is realised with the use of a coupled RNM. Skricka [8] proposed the use of a

coupled RNM in a self-sensing scheme to eliminate the problem of magnetic coupling. This approach therefore addresses both saturation and cross-coupling aspects. Furthermore a frequency shifted model is used as proposed by Schammass [10] to reduce the computational intensity of the self-sensing scheme.

A novel first approach to split the estimation of the two axes while using a single coupled RNM is also presented. The RNM is developed using information gathered from [8], [11] and refined by implementing lookup tables for air gap reluctance and complex material permeability.

1.7 Overview

The thesis presents the development and refinement of a frequency shifted RNM for use in a novel MIMO parameter estimator approach to the self-sensing problem. A first approach to the MIMO parameter estimator is also presented and the self-sensing scheme is verified through simulation.

Chapter 2 presents a detailed literature study on the field of self-sensing which substantiates the contribution and the originality of the present work. It starts off with an introduction to AMBs followed by a section on sensors which highlights the relevance of self-sensing research. Next an introduction to the basic self-sensing concept is presented, followed by a dissection of the self-sensing research field. The current problems associated with self-sensing are highlighted to substantiate the relevance and originality of the research problem presented in the thesis. Chapter 2 is concluded with a section on two basic concepts, inductance and eddy currents, which serves as background for the next chapter.

Chapter 3 discusses the development and refinement as well as the verification of the improved model for self-sensing heteropolar AMBs. The chapter starts off with specifications for the improved model as well as a section on the bearing parameters and referencing convention used throughout the thesis. A model refinement process is also presented which is used to obtain the best possible improved model. The process compares modelled results to results generated by FEM models and experimental measurements to identify mechanisms that cause modelling error. These modelling discrepancies are addressed where possible to realise a model that will alleviate problems such as saturation and cross-coupling in a self-sensing scheme.

Chapter 4 is focussed on the position estimation scheme. As a first approach the position estimation of the x and y axes are done separately with two parameter estimators which use the same coupled RNM. The RNM is simplified and linearised and linear transfer functions are derived for the demodulation process and other components in the MIMO parameter estimation scheme. These transfer functions are used in a simplified stability analysis of the estimator. Chapter 4 also presents the TSM which serves as evaluation platform for the self-sensing technique. The chapter is concluded with self-sensing results that demonstrate the basic functionality of the nonlinear parameter estimation scheme.

Chapter 5 presents a detailed performance evaluation of the improved model in the first approach parameter estimator scheme utilising the TSM as evaluation platform. The performance evaluation is divided into two parts, i.e. a static evaluation and a dynamic evaluation. The static evaluation is conducted by forcing the rotor position in the simulation environment and applying dc or slow varying changes. Sensor linearity, duty cycle variation, saturation and cross-coupling effects are investigated in this manner. This is followed by the dynamic evaluation section where the position control loop is closed with the estimated positions and the system is subjected to dynamic tests. In this section cross-coupling, self-sensing bandwidth and system sensitivity are analysed. The chapter is concluded with a section on modelling uncertainty which analyses the effect of the modelling discrepancies, as identified in chapter 4, on the position estimate. Chapter 5 demonstrates that the proposed self-sensing scheme is realisable in simulation and results in sensitivity levels suitable for commercial application.

Chapter 6 starts with a short summary of the work presented which is followed by a section that highlights the contributions of the present work. Future work is also suggested and the thesis is concluded with a closure paragraph.

CHAPTER 2

Background

Chapter 2 contains an overview of relevant literature to give some background on self-sensing magnetic bearings. It starts with an active magnetic bearing (AMB) section discussing the history, typical applications, basic operating principles and sensors for AMBs. This is followed by an introduction to the basic concept of self-sensing with some advantages of this approach. Next the field of self-sensing is dissected and the different approaches are discussed. The limitations associated with self-sensing are highlighted to justify the need for further research. Finally two basic concepts, inductance and eddy currents are discussed as background for the following chapter.

2.1 Active magnetic bearing systems

2.1.1 Introduction

The AMB concept is not new and the first major advances in AMB technology were recorded in the 1930s. Researchers began exploring AMB technology for application in ultracentrifuges used for purifying isotopes of elements [1]. The application required high-speed operation in a vacuum which rendered AMB technology the preferred option.

Although early researchers laid a basis for practical AMB systems it was not until the introduction of high-speed electronics that AMBs became a viable option for high-speed rotating equipment. Even then it was not until the invention of reliable dry gas seals which eliminated the need for lubrication altogether that AMBs truly became a technically and economically viable option. In 1985 the first commercial field application of a centrifugal compressor suspended by AMBs was ordered by NOVA Gas Transmission Ltd. [12].

Since the introduction of AMBs to industry their application has grown extensively. With advances in the semiconductor industry, digital controller industry and magnetic materials, AMBs are now more compact, less expensive and even more reliable. Typical applications include [13]:

- turbomolecular pumps for ultra high vacuum in the semiconductor industry
- turbomachinery including centrifugal compressors, turbo-expanders and turbines
- machine tool spindles for the manufacturing industry (aluminium cutting)
- high speed flywheel energy storage systems and
- magnetically levitated vehicles (MAGLEV).

AMBs have a number of novel qualities rendering them invaluable machine components in the modern day industry. Their ability to suspend a rotor without mechanical contact results in

a no wear and no lubrication configuration. This renders the AMB an environmentally friendly technology that results in the reduction of machine maintenance and waste associated with the replacement of lubrication and bearings [1].

Magnetic bearings can be organised into two main groups, i.e. reluctance force bearings and Lorentz force bearings [13]. Of these two groups, magnetic bearings based on reluctance forces have found the widest range of practical application [14].

2.1.2 Operating principle

An AMB is a typical product of mechatronics which is an interdisciplinary area of engineering science based on the classical fields of mechanical and electrical engineering as well as computer science. This is clearly illustrated by the functional diagram of an AMB system in figure 2.1. The system comprises a position sensor, controller, power amplifier (PA) and electromagnetic actuator. The position sensor monitors the rotor's displacement from its reference position. The position information is supplied to the controller which generates an appropriate control signal. A PA converts the control signal into a control current which generates the magnetic force in the electromagnet. The controller manipulates the force in such a way as to correct the rotor displacement.

The controller is not only responsible for the stability of the system shown in figure 2.1 but also controls the stiffness and damping of the system. This is one of the advantages of an AMB system since the stiffness and damping parameters can be varied within physical limits to meet technical requirements [13].

Opposing electromagnets are driven in so-called differential mode to generate both positive and negative forces for one degree of freedom. A typical radial bearing will employ two of these configurations to stabilise the rotor in two degrees of freedom. For a fully suspended rotor two radial bearings and one axial bearing are used to stabilise the rotor in five degrees of freedom.

2.2 Sensors for active magnetic bearings

The accuracy and stability of the displacement sensor used in an AMB plays an important part in the performance of the AMB. Contact free sensors must monitor the rotating surface which implies that the surface quality and the homogeneity of the material will influence the measuring result. The bandwidth of the sensor must also exceed the PA bandwidth. Commercial application requires low cost sensors that are durable and stable. The sensors should also display low noise susceptibility [13]. A range of sensors can be used to obtain rotor position information which includes:

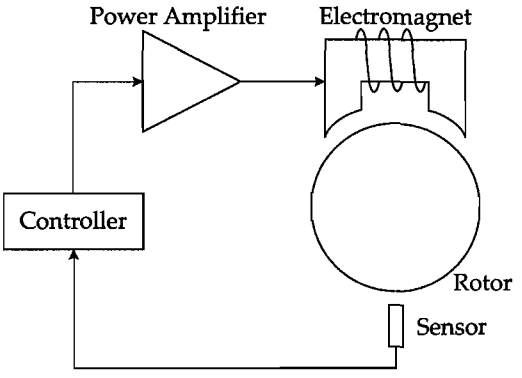

Figure 2.1: AMB functional diagram [13]

- Eddy-current sensors
- Inductive sensors
- Capacitive sensors
- Magnetic sensors
- Optical sensors

A sensor often used in AMB systems is the eddy-current sensor due to its high resolution, excellent temperature stability, small phase shift, high dc-stability and high bandwidth [15]. A coil encapsulated in the probe tip, radiates a high frequency magnetic field into the observed target. As a conductive surface approaches, eddy currents are induced which weaken the magnetic field. With appropriate signal conditioning a voltage proportional to the clearance is produced. The modulation frequency is usually in the range of 0.5 - 2 MHz with a measuring frequency range of 0 - 20 kHz [13]. Eddy-current sensors must be shielded for applications where they are located near high frequency magnetic fields.

Another popular sensor is the inductive displacement sensor. This sensor incorporates a ferrite inductor as part of an oscillating circuit. As a ferrous object approaches the ferrite inductor, its inductance changes and a signal proportional to the distance between the inductor and the object to be measured is produced. Two opposing sensors are frequently implemented differentially in a bridge circuit at a constant frequency. This configuration produces a nearly linear signal. The modulation frequency ranges from 5 kHz up to 100 kHz and the cut-off frequency of the output signal ranges between one tenth and one fifth of the modulation frequency. Inductive sensors are normally not very sensitive to the magnetic fields near the bearing magnets since they are shielded by the ferrite core. They may however display massive disturbances when a switching PA is used with a switching frequency close to that of the modulation frequency.

Capacitive displacement sensors display very high resolution (e.g. 0.02 μm at a measuring range of 0.5 mm), but are very expensive. The sensor is sensitive to dirt in the air gap which changes the dielectric constant, as well as electrostatic charging of the contact-less rotor.

Magnetic displacement sensors measure the air gap in a magnetic loop by applying a constant current and measuring the flux density B. The flux density is measured with Hall sensors or with field plates. These sensors are sensitive to interferences caused by external magnetic fields.

Optical displacement sensors are very sensitive to dirt and the resolution is limited due to diffraction effects which render them inappropriate for some applications.

Eddy-current and inductive sensors are expensive due to the complexity of the manufacturing process. Wiring to and from the sensors and the need for feedthrough terminals also increase cost. Research efforts are under way to develop low cost sensors. One such sensor is the printed circuit board (PCB) capacitive sensor. A plate type capacitive sensor is constructed with PCB-technology and collocated with the magnetic bearing. This sensor does however exhibit problems in the form of noise induced by the pulse width modulated (PWM) amplifiers used to drive the magnetic bearing and the tolerances on the PCB manufacturing technology and alignment process [16].

In [17] a patented [18] PCB eddy-current sensor is discussed. The manufacturing cost of this sensor is extremely low and the sensor displays good sensing characteristics. This concept can also be adapted for high temperature sensors using thick-film technology with silver tracks on a ceramic substrate [19]. Good results were obtained during tests where the sensor was subjected to temperatures ranging from room temperature up to 600 °C. The reduction in production cost, the increase in reliability and the measuring capability of this sensor topology renders it a competitive alternative to the self-sensing approach [19]. This sensor solution however does not eliminate the non-collocation problem and wires are still running to and from the sensor, posing a cost implication.

2.3 Self-sensing general concept

Transducers convert one form of energy into another and are usually classified by their function, namely sensors and actuators. Self-sensing describes a system that uses one transducer to both sense and actuate concurrently. Systems that have explored the self-sensing principle include brushless dc and variable reluctance motors, loudspeakers, micro-miniature devices, piezoelectric actuators, electrostatic bearings and magnetic bearings. A prerequisite for self-sensing is that the actuator can be modelled. The advantages for all these systems are the same: reduction in cost, reduction in complexity and an increase in reliability [20].

In an AMB system the rotor position information is most richly imbedded in the inductance of the electromagnetic transducer. The varying inductance can be estimated by monitoring the current and voltage waveforms of the magnetic actuator. Figure 2.2 displays a simplified bearing inductor model.

Making use of Faraday's and Ohm's laws the voltage v and the magnetic flux ϕ are related by:

$$v = N\frac{d\phi}{dt} + iR \tag{2.1}$$

with N the number of coil turns, i the coil current and R the coil resistance. Assuming a uniform distribution of flux throughout the magnetic material and the air gap and neglecting leakage, fringing and eddy-current effects, the magnetic flux can be expressed as:

$$\phi = \mu_0 a \frac{Ni}{2(g_0 - x) + \frac{l}{\mu_r}} \tag{2.2}$$

with μ_0 the permeability of free space, a the air gap area, l the effective magnetic material path length, μ_r the magnetic material relative permeability, g_0 the nominal air gap length and x the position of the suspended body. Taking the derivative of (2.2) and substituting it into (2.1) results in the following relation:

$$v = \mu_0 N^2 a \left[\frac{1}{2(g_0 - x) + \frac{l}{\mu_r}} \frac{di}{dt} + 2\frac{i}{\left(2(g_0 - x) + \frac{l}{\mu_r}\right)^2} \frac{dx}{dt} \right] + iR. \tag{2.3}$$

From (2.3) it is clear that the coil current is not only dependent on the applied coil voltage but also strongly dependent on the air gap length and its rate of change. With perfect knowledge of the coil voltage and current it should theoretically be possible to reconstruct the air gap and therefore determine the rotor position. There are a number of reasons why one would want to construct a self-sensing magnetic bearing:

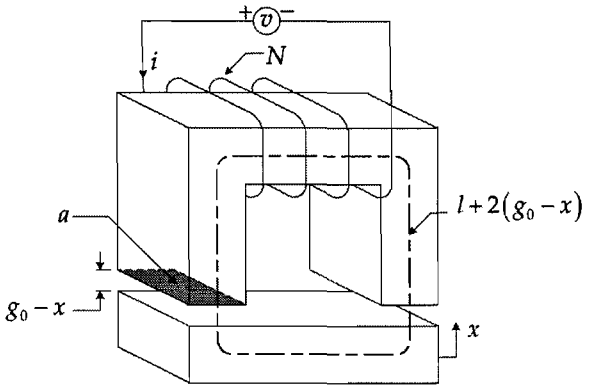

Figure 2.2: Simplified bearing inductor model

- **Reliability:** The cabling, physical sensing device, drive electronics, and signal processing hardware associated with each discrete position sensor can be eliminated. It is replaced by signal processing hardware and software to interpret the current and voltage signals. This reduces the amount of hardware in the potentially harsh machine environment and the amount of cabling between the machine and control cabinet. It is clear that a potentially large increase in reliability can be achieved provided that the system dynamics are not compromised [7].
- **Compactness:** With the elimination of a dedicated position sensor the rotor length can be reduced. This is advantageous from a rotordynamics point of view since the eigenfrequencies increase [4].
- **Collocation:** When the first bending mode of the rotor is within or near the small signal bandwidth of the AMB sensor/actuator non-collocation can cause stability problems. Modal phase reversal occurs when a node of a flexible mode is situated between the actuator and associated sensor. The controller can be designed to overcome this problem but the sensitivity of the node location to system parameter changes results in poor system robustness. Sensor/actuator non-collocation must therefore be avoided [7], [21]. AMBs utilising self-sensing avoid this problem by concurrently sensing and actuating with a single transducer.
- **Redundancy:** In systems that require fault tolerance the self-sensing technique can be used to obtain additional position information in the case of sensor failure.

Although self-sensing is not a new concept and the topic has been researched in the past, it remains a challenge [4]. The proposed self-sensing methods are not easily realised and for this reason it has only recently (December 2005) found its first industrial application when it was integrated into a turbomolecular pump developed by S2M [6]. The reason for this is that most self-sensing techniques are difficult to realise and lack robustness, which results in inferior sensing performance [5].

It is clear from the preceding discussion that self-sensing magnetic bearings pose potentially large benefits to the rotating equipment market. Further research is therefore warranted on the topics of increased self-sensing performance and robustness.

2.4 Self-sensing approaches

Self-sensing can be divided into two main approaches, namely state estimation and modulation [4]. In the state estimation approach the magnetic bearing and supported object is modelled as a complete system and the position is considered a state of the system. In the modulation approach the position is seen as a parameter of the system rather than a state. The self-sensing approaches can be categorised as displayed in figure 2.3 [4].

2.4.1 State estimation

Approach

Although (2.3) gives a framework to interpret the voltage and current signals and reconstruct the air gap, a mathematically simpler method was developed in [22] which was also the first formal description of a self-sensing AMB. A one mechanical degree of freedom AMB with two opposing electromagnets as shown in figure 2.4 was analysed. The system was driven in differential configuration which implies that the currents in the two opposing magnets are perturbed symmetrically about some bias point.

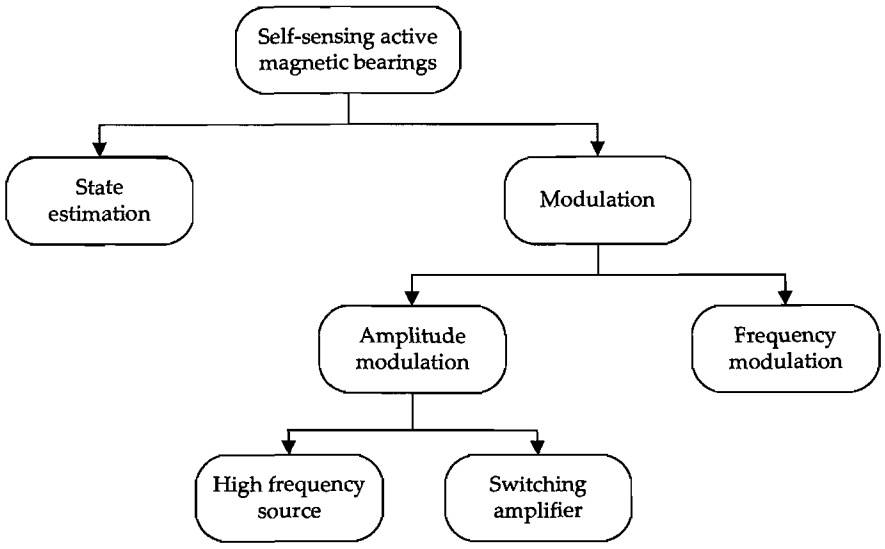

Figure 2.3: Self-sensing approaches [4]

Treating the magnetic bearing as a two port system with electrical inputs voltage and current and mechanical outputs force and velocity, it is shown that the resulting model of the bearing and suspended object is linear with time invariant coefficients. This linear time invariant (LTI) system may be studied using the vast machinery of linear control theory. In [22], [23] it is established that the system is both observable and controllable indicating that a controller can be constructed to stabilise the system leading to a potentially useful AMB.

Problems

Although the state estimation approach has been demonstrated successfully with experimental models [22], [24], [25], it poses serious drawbacks. The main reason for this is the presence of a right half plane pole and non-minimum phase (NMP) zero in the transfer function of the system from input voltage to output current which makes the stabilisation problem very difficult. It is possible to levitate these systems and obtain useful performance but they are sensitive to parameter changes.

In [26] full and reduced order observer-based controllers were analysed and it was shown that reduced-order controllers are always unstable while most of the full-order observer-based controllers are stable but may be destabilized by eddy-current effects. It is shown in [24] that the system is poorly observable for high frequencies which limits the robustness. The lack of robustness is evident in practical systems from the difficulty to tune controller parameters to achieve

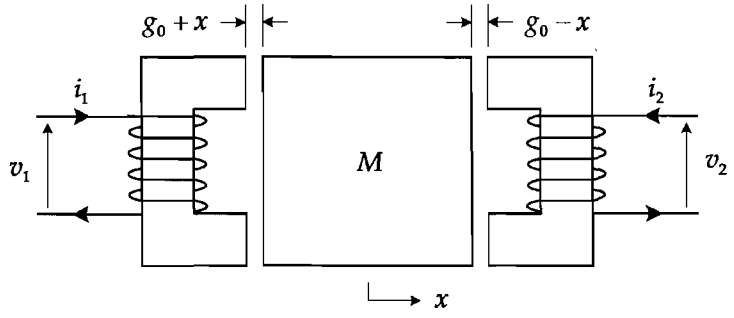

Figure 2.4: One dimensional magnetic bearing

stable suspension.

The fundamental limits on achievable robustness which LTI controllers cannot surpass were established in [27]. It was shown that when comparing the robustness limits of a self-sensing AMB and sensor configuration, the self-sensing system is significantly less robust. This is caused by the close proximity of the right half plane pole and NMP zero which is influenced by bearing dimensions and other physical bearing properties. For this reason the choice of bearing dimensions and other physical properties is critical to the achievable robustness and performance of a self-sensing system. In [27] the best achievable sensitivity value for physical reasonable parameters is about 10 [28]. According to the ISO standard 14839-3 [29] for AMB systems the sensitivity must be below 3.0 for acceptance of commercial systems. It was concluded therefore due to the high sensitivity that the state estimation self-sensing approach is not suitable for industrial applications.

In [30] it was established that a trade-off exists between robustness and performance, i.e. high stiffness results in low robustness. It is therefore critical to design the self-sensing magnetic bearing with the desired robustness and performance in mind since these may vary greatly with small variations in bearing parameter values.

Another drawback of the state estimation self-sensing approach is that it cannot reject dc force disturbances [31]. This is due to the dynamics of the suspended object being coupled to the bearing through back electro-motive-force (EMF). The inherent coupling of sensing and control signals is also a serious drawback [4], [32].

Practical applications

In [33] a practical application of the state estimation approach is presented where for the first time a rotor was suspended in four radial degrees of freedom without position sensors. The industrial turbo-molecular pump was spun up to 14,400 r/min. More recently the first commercial application of the state estimation approach was presented in [34] for elevator guideways. For this system the problems in robustness are managed by re-estimation of the parameters most responsible for the problems in sensitivity.

2.4.2 Modulation

Despite the discouraging results in section 2.4.1 many researchers have continued studies ([10], [35], [36], [37], [38], [39], [40], [41], [42]) making use of ad-hoc approaches in contrast to the system approach of section 2.4.1. They exploit the sensitivity of the electromagnet's inductance to the air gap and use a high frequency interrogation signal typically between 10 and 20 kHz. At this time scale the rotor position may be assumed constant and the bearing air gap can be treated as a time-varying parameter of the electromagnetic actuator system. The operating principle of this approach is similar to that of a variable reluctance sensor [43] with the sensor and actuator functions realised by one transducer. As shown in figure 2.3, this approach can make use of either amplitude or frequency modulation.

Amplitude modulation

Amplitude modulation is not a new idea and as early as 1952 an active suspension without position sensors was developed [44]. Self-sensing with the amplitude modulation approach can be accomplished by either injecting a high-frequency signal [36],[45] or using the PWM switching amplifier as a high-frequency source [8], [35], [37], [46], [47].

As the name suggests the high frequency injection method injects a high frequency signal to determine the inductance of the electromagnetic actuator. This is accomplished by demodulation of the resulting ripple current. Both linear [36] and PWM [45] PAs may be used to establish the

high frequency interrogation signal. A potential drawback to this approach is that sensing performance can be degraded by saturation effects [36]. Interestingly this is the method employed by S2M in their turbomelecular pump of which completely satisfactory performance is reported [6].

Another self-sensing approach is based on the differential transformer principle. In [40] this principle is applied to a self-bearing motor and in [41] it is used to assist superconducting magnetic bearings in liquid nitrogen. Self-sensing can also be realised with the LC resonant circuit approach and in [48] an amplitude modulation/demodulation approach with a positive feedback controller is used to realise stable suspension.

Many approaches exploit the fact that most practical AMB systems use switching amplifiers to drive the coils. As a result of the switching there is substantial ripple in the current waveform at high frequency (10-25 kHz). The rotor position may then be assumed essentially constant at the switching time scale. Okada [35] used the PWM switching amplifier as a high frequency source. In this topology the demodulation output is a function of the PA duty cycle. One solution to this problem is to compensate for duty cycle variations by dividing the demodulated current with the measured voltage ripple [8], [10], [46]. Another solution is to compensate for duty-cycle variation with a nonlinear observer considering the bearing coil model [9], [32], [37], [49]. Montie [50] applied this self-sensing technique to both axes of a single bearing and was able to spin the experimental rotor up to 60,000 r/min.

In [38] a self-sensing scheme for a homopolar bearing for a flywheel application is discussed. Bias flux is established by permanent magnets and two opposing coils are connected in series to form the actuating coil. The position is derived by measuring the centre point voltage of the two coils which are also driven by a PWM PA.

Another interesting approach is presented in [42] where two opposing electromagnets are used to suspend a one degree of freedom system by measuring the current change rate alone. The two electromagnets' coil currents are passed through opposing coils of a transformer with a third coil producing a signal proportional to the difference in current change rate between the two electromagnets. The difference in current change rate and the instantaneous coil voltage are used to determine the gap length. A drawback of this approach is that additional hardware is required [42].

Frequency modulation

Mizuno et al. [51] investigated the frequency modulation technique with hysteresis switching amplifiers. Since the switching frequency is dependent on the load impedance, the air gap information is frequency modulated with the switching signal. Demodulation is accomplished with a phase-locked loop circuit. Unfortunately this approach poses the same problem as the one in [35], i.e. the demodulation output is not only a function of the air gap but also of the PA duty cycle.

Improved robustness and sensitivity

Recent experiments, [4] and [52], relying on switching ripple achieved sensitivity levels below the best achievable levels predicted by [27]. In response to this, researchers have been working [52], [53], [54], [55] on a theoretical basis to explain this phenomenon. According to [53] the high levels of sensitivity predicted by [27] is due to an over simplification of the model. By modelling the bearing as a linear periodic system and introducing a high frequency flux component, predicted sensitivity levels are lowered to below acceptable industry levels [28], [53]. The linear periodic work in [28], [53], [55] establishes that the use of switching ripple for self-sensing leads to increased robustness. Unfortunately this approach has not yet yielded a commercially viable method and is therefore still only of theoretical value. In [28] it is demonstrated that a formal Lyapunov based approach may be used to synthesise a position estimator which is of practical value. Future work

will include the effects of eddy currents and a physical FPGA based implementation.

2.5 Self-sensing limitations

The self-sensing mechanism is fundamentally the same as a variable reluctance magnetic sensor [43]. A major drawback of self-sensing is that the actuator design objectives are in contrast with that of a sensor. Thermal and capacity considerations may lead to actuator designs where the magnetic path reluctances substantially exceed that of the air gaps at high frequency (20 kHz or more) [49]. In contrast, variable reluctance sensors achieve sensitivity and rejection of magnetic nonlinearity by ensuring that the magnetic path reluctance is much smaller than the air gap reluctance. The overall sensing performance of a self-sensing magnetic bearing may therefore be expected to be inferior to that of a variable reluctance sensor in terms of sensitivity, bandwidth and linearity. In the subsequent sections more drawbacks associated with self-sensing systems are discussed.

2.5.1 Cross-coupling

Cross-coupling in the self-sensing context refers to the phenomenon where a change in position or force in one axis induces an error in the estimated position of the perpendicular axis. Cross-coupling and the effect it has on the magnetic bearing radial force was analysed in [56], [57]. The effects of cross-coupling on self-sensing were investigated in [8], [32], [46]. Cross-coupling in the self-sensing context may be divided into two mechanisms [32]:

Geometric cross-coupling

Due to the pole face curvature in the circular bearing geometry, movement in one direction may cause air gap changes in the perpendicular direction. In [8] the effects of geometric cross-coupling are analysed and quantified for both homopolar and heteropolar magnetic bearings. The effects can be included in the self-sensing model by accurately modelling the air gap as a function of both axes of the radial bearing [8].

Magnetic coupling

In standard heteropolar radial magnetic bearings the different poles are coupled by stator back iron. Mutual inductances therefore exist between poles. A reluctance network model was constructed in [32] to quantify the effect of magnetic coupling. It was found that the mutual inductance terms were negligible when compared to the self-inductance terms. Skricka [8] however demonstrated that excluding the effect of magnetic coupling from the self-sensing model may lead to failure of the self-sensing scheme under certain conditions. Magnetic coupling is often avoided in self-sensing systems by separation of the individual magnets with air gaps in the stator [4]. Unfortunately this simple solution results in higher manufacturing cost of the bearing. Another approach to the problem as suggested in [8] is to make use of a coupled reluctance network model in the self-sensing scheme.

2.5.2 Ripple amplitude

Important results obtained from [53] and [55] indicated that, regardless of the signal processing approach, the robustness of the self-sensing AMB is determined by the ripple amplitude. In the case where the ripple amplitude goes to zero the robustness does not go to zero but is substantially diminished. The performance of self-sensing approaches will therefore tend to improve with the presence of high levels of high frequency current ripple.

This is a significant observation since high levels of high frequency current ripple result in high eddy current losses and acoustic emissions. This is in contrast with the recent trend to move from two state ($+V_p$, $-V_p$) PAs to three state ($+V_p$, 0, $-V_p$) PAs in order to improve efficiency. According to Maslen [7] this limitation seems fundamental and implies that robust self-sensing systems will be less efficient in terms of electrical power consumption.

2.5.3 Eddy currents

The primary problem is that eddy currents reduce the magnetic material permeability [11]. The sensitivity of the magnetic bearing as a sensor therefore reduces as the excitation frequency increases [4]. A frequency dependent model of a magnetic bearing was developed to investigate this phenomenon. A unique contribution of the model is the inclusion of the winding parasitic capacitance. The model is documented in appendix A and also shows a decrease in sensitivity with an increase in excitation frequency. Furthermore eddy currents introduce abrupt changes in the current waveform of a magnetic bearing driven by a two state PA. For unlaminated thrust actuators such abrupt changes can be as large as 30 % of the bias current level [7]. Unfortunately the eddy current effect is not influenced by a change in air gap and therefore greatly reduces the sensitivity of the waveform to air gap.

One solution to this problem is to lower the switching frequency and voltage of the excitation signal. Another is to use an interrogation signal of which the frequency is selected just below the bandwidth of the actuator. This approach presented in [58] attempts to preserve the sensitivity to gap by minimising production of eddy currents by the interrogation signal.

2.5.4 Saturation

Fundamentally all self-sensing schemes rely on the sensitivity of the electromagnetic coil impedance to a change in air gap. Saturation reduces this sensitivity in the same way as eddy currents since the magnetic material permeability reduces at high flux densities. According to Maslen [7] saturation is the most vexing problem faced by self-sensing researchers. Numerous studies ([32], [46], [52] amongst others) have shown that the sensitivity of the switching ripple to air gap may actually reverse due to saturation leading to ambiguous position estimates. Saturation must therefore be included in the model used for self-sensing [8], [10], [32].

A solution to the ambiguous position estimate problem is proposed in [8] and [59] where the position is estimated by making use of both opposing actuators in the magnetic bearing to obtain a single position estimate. This approach relies on the fact that only one of the two actuators can be saturated at any given time. In [9] a multiple input multiple output (MIMO) parameter estimation scheme is suggested which results in stability under saturation conditions for short periods of time.

2.6 Inductance

Inductance is a constant of proportionality relating current to flux and is measured in henrys[1](H). It is an intrinsically positive quantity and plays much the same role in electrical circuits that mass plays in mechanical systems [60]. In this section the different forms of inductance are discussed as background for the nonlinear model verification section of the thesis. Using Faraday's law the voltage applied to a lossless coil in figure 2.2 is obtained by (2.4).

$$v = N\frac{d\phi}{dt} = \frac{d\lambda}{dt} = \frac{\partial\lambda}{\partial i}\frac{di}{dt} \tag{2.4}$$

[1] a henry is a volt-second per ampere

The right-hand expression in (2.4) is obtained by implementing the chain rule from calculus. The relation $\partial\lambda/\partial i = d\lambda/di$ holds for the case where λ is a function of i alone. For the case at hand however λ is influenced by the multiple excitation coils and the rotor position. The partial derivative is therefore retained and the definition for inductance is given by:

$$L = \frac{v}{di/dt} = \frac{\partial\lambda}{\partial i}|_o = N\frac{\partial\phi}{\partial i}|_o \tag{2.5}$$

with o the point of operation as indicated in figure 2.5. The quantity obtained from (2.5) is known as the *incremental inductance* and is merely the slope of the magnetisation curve as shown in figure 2.5. L is a function of the point of operation and decreases as the operating point moves deeper into the saturation region. If the ferromagnetic material exhibits linear behaviour, the $\lambda - i$ plot will result in a straight line. L is then no longer a function of the point of operation and can be obtained from:

$$L = \frac{\lambda}{i} = \frac{N\phi}{i}. \tag{2.6}$$

The inductance obtained by (2.6) is known as *apparent inductance* [61]. Apparent inductance is widely used in magnetic circuit analysis for circuits that operate outside of the saturation region.

2.7 Eddy currents

A one-dimensional eddy current model for laminated material has been available since [62]. In this work it is shown that eddy currents cause a change in the winding impedance. Firstly eddy currents set up ohmic losses which must be drawn from the supply and secondly eddy currents reduce the flux carrying capacity of the core. For an outside observer with only access to the terminals of the winding this appears as an apparent increase in resistance and decrease in inductance of the equivalent series *R-L* circuit. This effect can be modelled in different ways. One approach is to use a rate dependent material permeability term as presented in [11], [62]:

$$\mu_{fd}(s) = \mu\left[\frac{\tanh\left(\sqrt{s\sigma\mu}\frac{d}{2}\right)}{\sqrt{s\sigma\mu}\frac{d}{2}}\right] \tag{2.7}$$

where d is the lamination thickness, σ is the electrical conductivity, $\mu = \mu_0\mu_r$ is the material permeability and s is the complex frequency.

In [11] it is shown that the eddy currents may also be modelled by a single turn coil around each laminated section driving a chain of resistors and inductors as pictured in figure 2.6. The

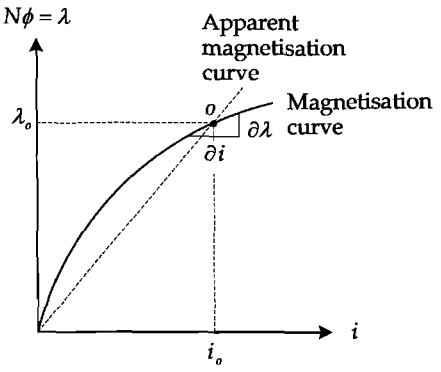

Figure 2.5: Magnetisation of ferromagnetic material [61]

relationship between the eddy current I_e and magnetic flux ϕ is given by (2.8).

$$\frac{I_e(s)}{\phi(s)} = \frac{-s}{R_{e1} + \frac{1}{\frac{1}{sL_{e1}} + \frac{1}{R_{e2} + \frac{1}{\frac{1}{sL_{e2}} + \ldots}}}} \tag{2.8}$$

The equivalent inductance and resistance values can be obtained from:

$$L_{ek} = \frac{\mu a}{(4k+1)l} \tag{2.9}$$

$$R_{ek} = \frac{4(4k-1)a}{\sigma l d} \tag{2.10}$$

with a and l the cross sectional area and length of the lamination section respectively.

At the heart of the frequency dependent magnetic bearing model presented in appendix A lies the $\mu_{fd}(j\omega)$ term. This form of the eddy current model may be used to obtain the harmonic response at any particular ω. On the other hand, the Laplace domain model given by (2.8) is suitable for system analysis with the broad range of control theory tools that are available. This model also allows for transient time domain modelling.

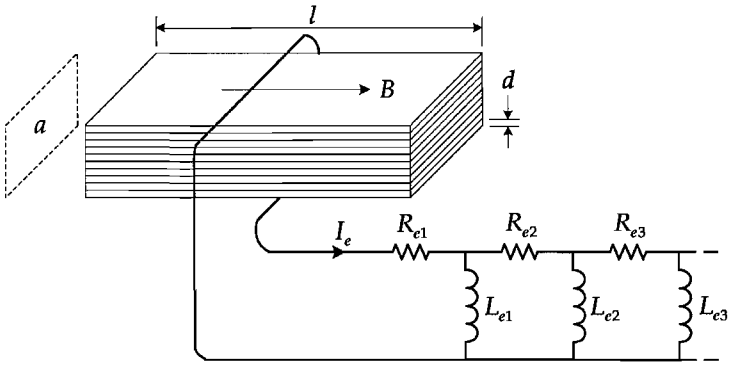

Figure 2.6: Equivalent circuit model for eddy currents [11]

A prerequisite for self-sensing is that the actuator can be modelled and, as shown in the above sections, the performance of a self-sensing system is closely related to the accuracy and comprehensiveness of the magnetic bearing inductor model. Furthermore it is shown that the use of high frequency ripple increases robustness of self-sensing systems and is a relevant direction to pursue.

The present work focusses on the high frequency ripple and makes use of an amplitude modulation approach. The switching amplifiers are used to establish the high frequency ripple since they are readily available in AMB systems and this approach requires less additional hardware. The power amplifiers are configured in two state switching mode ($+V_p$, $-V_p$) in order to ensure high ripple amplitude to further increase the achievable robustness.

The self-sensing technique is implemented on a typical heteropolar magnetic bearing and the model must therefore cater for the following effects: cross-coupling, eddy currents, saturation, leakage and fringing. A MIMO parameter estimation scheme is investigated making use of a coupled reluctance network model of the heteropolar magnetic bearing. In the following chapter the coupled reluctance network model is developed and verified.

CHAPTER 3

Modelling

Chapter 3 discusses the development of a reluctance network model (RNM) for an eight-pole heteropolar active magnetic bearing (AMB). The chapter starts off by specifying the model requirements from a self-sensing point of view. This is followed by an introduction to the experimental model with model parameters and the referencing convention utilised throughout the document. A model refinement process is presented next which facilitates the process of establishing a high fidelity model, suitable for self-sensing implementation. In the refinement process the mechanisms contributing to modelling error and uncertainty are identified and addressed where possible. The finite element method (FEM) model which is one of the tools utilised in the verification process is also discussed. The air gap reluctance is identified first as a mechanism that degrades model accuracy. Another mechanism responsible for modelling error is the choice of leakage path in the RNM. The RNM is also verified with RLC-meter measurements for dc conditions. An eddy current correction term is then included in the RNM and its impedance response compared to experimental results at the power amplifier switching frequency. The eddy current correction term is also identified as a source of modelling error. To overcome this problem a novel approach of experimentally determining the complex permeability and incorporating it into the model using a lookup table is presented. It is shown that this approach reduces the modelling error.

3.1 Self-sensing model specification

Basically, magnetic bearings can be divided into two structural shapes as shown in figure 3.1, i.e. heteropolar and homopolar. The flux in a homopolar magnetic bearing (figure 3.1 (b)) flows parallel to the axis of the rotor. This keeps rotational hysteresis losses smaller since the rotor iron passes below poles with similar polarity. This bearing type is mostly used when it is not possible to laminate the rotor [13].

Heteropolar magnetic bearings (figure 3.1 (a)) produce flux perpendicular to the rotor axis making this configuration similar to electromotors and relatively simple to manufacture. Hysteresis and eddy current losses are kept low by laminating the magnetic structure. Furthermore, if an eight-pole structure is used, two adjacent poles may be paired and geometrically opposing pole pairs driven differentially to form an actuator. Two actuators are realised with this configuration which can be assigned to Cartesian coordinates x and y respectively. The simulation of the mechanical system, controller design and rotor motion measurement are usually based on these coordinates which simplify bearing control [13].

Present work focuses on an eight-pole heteropolar magnetic bearing configuration. The choice was influenced by the following factors:

- The heteropolar configuration is a popular choice for industrial applications due to the sim-

ple manufacturing process.

- Eight is the minimum amount of poles needed to realise four relatively independent actuators by configuring adjacent poles in reverse series; realising the classical NSSNNSSN arrangement. The actuators may then be configured in the so-called differential mode where two actuators operate symmetrically around a bias point which greatly simplifies the control requirements.

In chapter 2 it was established from literature that high frequency ripple increases robustness of self-sensing systems. This statement was supported by both theoretical analysis ([52], [53], [55]) and experiments ([4], [52]) and appears to be the appropriate direction to pursue.

This work therefore focuses on the high frequency ripple and makes use of an amplitude modulation approach. The high frequency switching ripple of the power amplifiers (PAs) is used since it is inherently available in AMB systems; eliminating the need for additional hardware. The PAs are configured in two state switching mode ($+V_p$, $-V_p$) in order to ensure high ripple amplitude; increasing the achievable robustness [7].

The different pole pairs in the experimental eight-pole heteropolar magnetic bearing are magnetically connected by stator back-iron. This may give rise to cross-coupling[1] which cannot be ignored for certain conditions [8]. As proposed in [8] a coupled RNM is used to realise self-sensing. Other effects that will also be included are: eddy currents, saturation, leakage and fringing.

Once a comprehensive model of the magnetic bearing is established, position estimation can be accomplished by one of two possible methods. The first is using an inverse of the model which will be very difficult to implement for the coupled RNM when material nonlinearities are included. The second approach, illustrated in figure 3.2, utilises a nonlinear estimator based on the model. The model is supplied with the necessary inputs to produce a current output. The current produced by the model is compared to the actual current and the error is fed to a proportional integral (PI) controller which yields a position estimate. This approach was proposed by Noh [32] and Montie [52] and made use of a complete inductor model for low and high frequencies. The disadvantage of this approach is that the signal processing bandwidth must be higher than the switching frequency.

Schammass [4] suggested that a frequency shifted model must be used together with the demodulated current and voltage signals. This approach would then have the advantage of requiring much lower signal processing bandwidth. The present work will therefore focus on a model that accurately models the terminal impedance of the coils at the switching frequency. The fundamental (switching frequency) components of the current and voltage waveforms may then be used in conjunction with the model to realise a nonlinear estimator based self-sensing system.

Self-sensing relies on the assumption that the actuator can be modelled. The performance of a self-sensing system is directly related to the accuracy and comprehensiveness of the model. The

[1] movement in one direction results in a change in parameters in the perpendicular direction

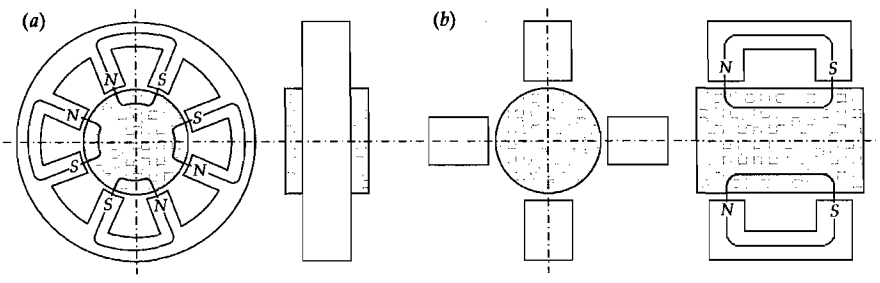

Figure 3.1: Structural shapes of (a) heteropolar and (b) homopolar magnetic bearings

remainder of this chapter focuses on the development and verification of a coupled RNM which accurately models the high frequency coil terminal impedance.

3.2 Bearing parameters and referencing convention

The referencing convention used throughout the thesis is illustrated in figure 3.3. Adjacent poles are paired by connecting their respective coils in complementing polarity. Pole 1 (P_1) and pole 2 (P_2) constitute pole pair 1 (PP_1) with electrical terminal descriptors v_1 and i_1. The remaining three pole pairs are paired in a like manner.

The model is verified with results obtained from an experimental eight-pole heteropolar AMB system with geometry as shown in figure 3.4. Important parameters of the experimental system are summarised in table 3.1.

One of the uncertainties in the air gap reluctance is the actual air gap length, more specifically the pole radius (r_p). The stator material was laser cut to size and upon inspection it was found that the final dimensions may vary as much as 200 μm. Furthermore there is also a tolerance on the interface between the laminations and the stator housing. Figure 3.5 depicts the stator laminations with a pole-to-pole diameter of d_a and a tolerance of (0 + 200 μm). The lamination-stator interface uncertainty is depicted by δ and the final dimension that can be measured is given by d_b. The pole-to-pole diameters of all four opposing pole pairs of the stator lamination pack were measured and the results are: 71.21 mm, 71.16 mm, 71.22 mm and 71.15 mm.

As a first order approximation the smallest measurement (71.15 mm) is taken as the lower end of a Gaussian distribution and the upper end as 71.15 mm + 200 μm. A random generator which generates a data set with Gaussian distribution is used to assign a diameter to each of the laminations in the stator pack. Since the objective is to determine an accurate value for the air gap reluctance it is not sufficient to take the mean of the diameters. A pole radius r_p is obtained by

$$r_p = \frac{n_{lam}}{2\sum_{i=1}^{n_{lam}} \frac{1}{d_{ai}}} \tag{3.1}$$

with $d_{ai} = 71.15 \times 10^{-3} + (1 + \varepsilon_i)100 \times 10^{-6}$ where ε_i is a random variable sampled from the standard normal distribution (i.e. $\varepsilon_i \sim N(0,1)$). n_{lam} is the number of laminations in the stack. (3.1) yields $r_p = 35.626$ mm which is only 0.07 % larger than the previous value but results in a 4 % increase in air gap length.

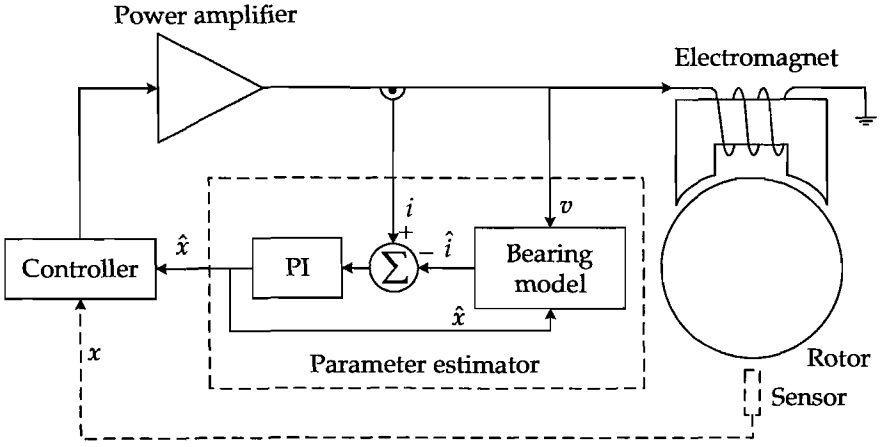

Figure 3.2: Parameter estimation self-sensing scheme functional diagram

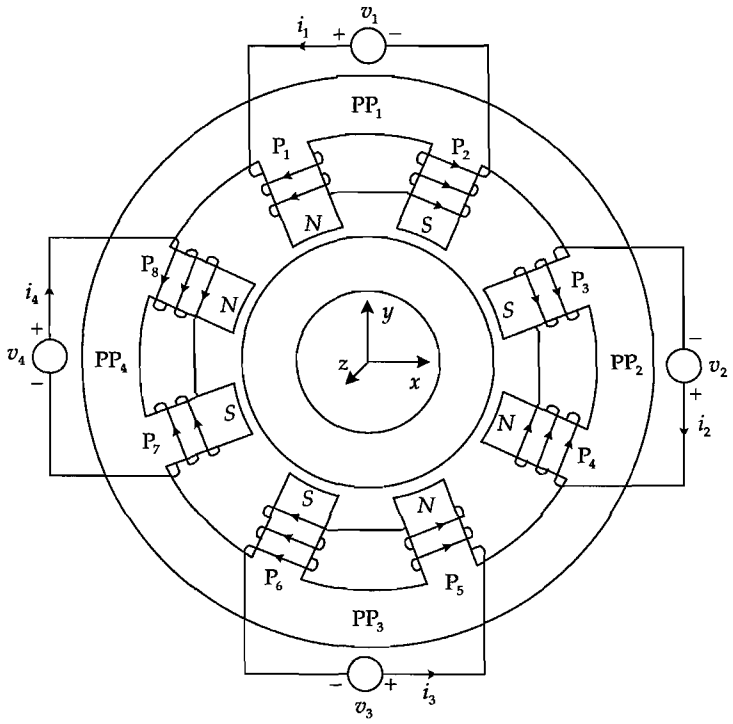

Figure 3.3: Referencing convention illustration

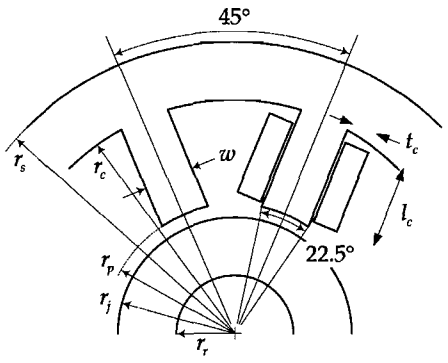

Figure 3.4: Magnetic bearing dimensions

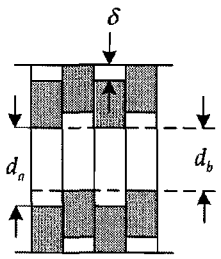

Figure 3.5: Stator lamination dimensions and corresponding tolerances

Table 3.1: Magnetic bearing parameters

Parameter	Value	Unit	Description
l_{ax}	44.358e-3	m	Axial bearing length
r_r	15.875e-3	m	Journal inner radius
r_j	34.95e-3	m	Journal outer radius
r_p	35.626e-3	m	Stator pole radius
r_c	60e-3	m	Stator back iron inner radius
r_s	75e-3	m	Stator outer radius
w	13.89e-3	m	Pole width
g_0	0.676e-3	m	Nominal air gap
a_g	$w \cdot l_{ax}$	m^2	Air gap area
t_c	6e-3	m	Coil window width
l_c	22e-3	m	Coil window height
a_v	$t_c \cdot l_c$	m^2	Coil window area
μ_0	$4\pi \times 10^{-7}$	H/m	Permeability of free space
μ_r	4000		Relative permeability
N	50		Coil turns

3.3 Model refinement process

The process followed to realise a refined model of the experimental system is outlined in figure 3.6. This refinement process commences by obtaining bearing parameters which are used to construct a preliminary RNM. A FEM model of the experimental system is also constructed and the results are used to verify the RNM. In the case of poor correlation the contributing mechanism is identified and the effect is quantified. The RNM is refined and the process is repeated until satisfactory correlation is obtained. The RNM results are then compared to experimental results obtained by an RLC-meter. If discrepancies between the results exist, the bearing parameters are refined and the process repeated until good correlation is obtained. At this point a RNM is established that accurately models the steady state (dc) conditions of the experimental system.

The next step is to include switching frequency effects in the model of which the eddy current phenomenon is the most prominent. As shown in section 2.7 the eddy current effect may be modelled by either a rate dependent permeability term or a single turn winding driving a chain of resistors and inductors. The present work utilises the rate dependent permeability term to include the effects of eddy currents. Results obtained from the RNM are then compared to experimental results. Again sources of discrepancies are identified and quantified and the model refined until satisfactory correlation is obtained. The outcome of this process is a high fidelity fundamental frequency model that may be utilised in the parameter estimation self-sensing scheme.

3.4 Finite element method model

FEM models have been used in studies to analyse magnetic nonlinearities and cross-coupling effects on both the bearing radial force [57] and self-sensing position estimates [8]. In this section the FEM model used in the verification of the RNM is discussed to provide background on the process followed in obtaining the FEM results. The use of apparent inductance as verification parameter for the nonlinear models is also motivated.

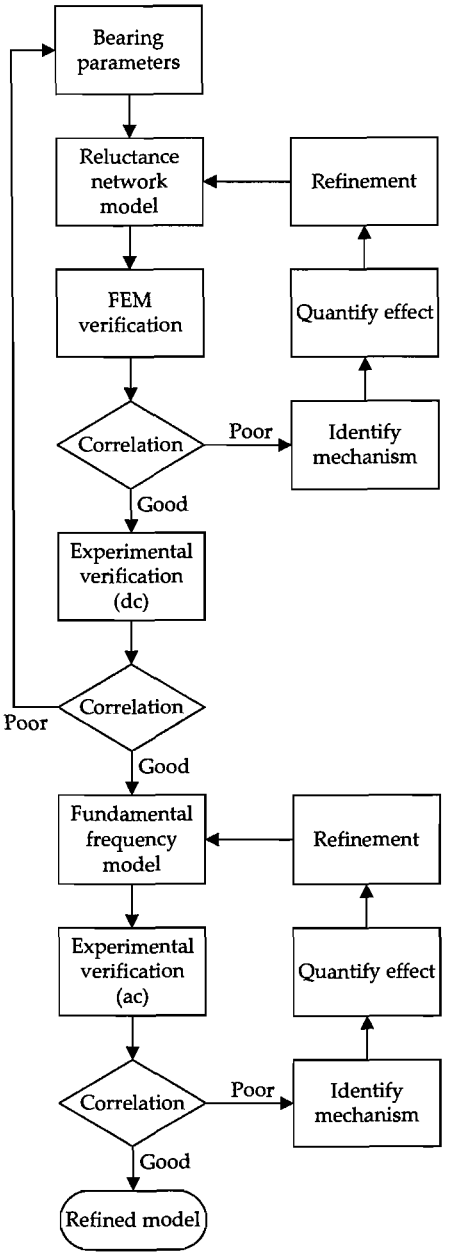

Figure 3.6: Model refinement process

3.4.1 Governing equations

A magnetostatic FEM analysis is undertaken to obtain results in terms of flux distribution and both self- and mutual inductances. COMSOL Multiphysics™ AC/DC Module 3.3 is utilised for this purpose. A parametric study of the flux distribution and inductances is conducted by using COMSOL's MATLAB® interface and a script file. Results are generated for a range of rotor positions and excitation coil currents. The perpendicular induction currents, vector potential application mode is used. The governing equations for this application mode are obtained from [63]. For the quasi-static case it is assumed that $\partial \mathbf{D}/\partial t = 0$ and Maxwell's equations reduce to:

$$\nabla \times \mathbf{H} = \sigma(\mathbf{E} + \mathbf{v} \times \mathbf{B}) + \mathbf{J}^e \tag{3.2}$$

$$\nabla \times \mathbf{E} = \frac{-\partial \mathbf{B}}{\partial t} \tag{3.3}$$

$$\nabla \cdot \mathbf{B} = 0 \tag{3.4}$$

$$\nabla \cdot \mathbf{D} = \rho \tag{3.5}$$

$$\nabla \cdot \mathbf{J} = 0 \tag{3.6}$$

By making use of the definitions of the magnetic and electric potentials

$$\mathbf{B} = \nabla \times \mathbf{A} \tag{3.7}$$

$$\mathbf{E} = -\nabla V - \frac{\partial \mathbf{A}}{\partial t} \tag{3.8}$$

and the constitutive relation $\mathbf{B} = \mu_0(\mathbf{H} + \mathbf{M})$, Ampère's law, (3.2), can be written as:

$$\sigma\frac{\partial \mathbf{A}}{\partial t} + \nabla \times (\mu_0^{-1}\nabla \times \mathbf{A} - \mathbf{M}) - \sigma\mathbf{v} \times (\nabla \times \mathbf{A}) + \sigma\nabla V = \mathbf{J}^e. \tag{3.9}$$

For the perpendicular induction current application mode it is assumed that there is no variation in the z direction and the electric field is parallel to the z axis. ∇V can be written as $-\Delta V/l$ with ΔV the potential difference over the distance l. For the magnetostatic case the first term of (3.9) is dropped. Making use of this information (3.9) can be simplified to:

$$-\nabla \cdot \left(\mu_0^{-1}\nabla A_z - \begin{bmatrix} -M_y \\ M_x \end{bmatrix}\right) + \sigma\mathbf{v} \cdot \nabla A_z = \sigma\frac{\Delta V}{l} + J_z^e. \tag{3.10}$$

This is the basis on which the COMSOL Multiphysics™ AC/DC Module 3.3 conducts the magnetostatic analysis. Other details regarding the FEM process (details regarding the solvers for example) are omitted from this section and can be found in [63].

3.4.2 Inductance calculation

Figure 3.7 displays the FEM geometry used during the parametric study. Once a solution is obtained the information needed to verify the RNM can be extracted. The self- and mutual inductances are obtained by (3.11).

$$L_{jk} = l_{ax}\frac{\int A_j J_k \, da_k}{I_j I_k} \tag{3.11}$$

A_j is the component of A established by the j^{th} coil, J_k the current density in the k^{th} coil and I_j and I_k the currents in the j^{th} and k^{th} coils respectively. da_k indicates that the integral is taken over the area of the k^{th} coil [11]. Self-inductances can be calculated directly using (3.11) whereas for mutual inductance calculations it can be simplified by using the relation $N_k I_k = J_k a_k$. Substituting for J_k in (3.11) results in:

$$L_{jk} = l_{ax}\frac{N_k}{a_k I_j}\left(\int_{J_{k+}} A_j \, da_k - \int_{J_{k-}} A_j \, da_k\right) \tag{3.12}$$

A is calculated with only coil j energised and two separate integrals are then evaluated. The first and second integrals in the brackets are evaluated over the region of the coil windings pointing in the positive and negative A directions respectively [64].

The techniques outlined in (3.11) and (3.12) for determining the self- and mutual inductances of the magnetic bearing hold for the linear case. In order to make use of the same tools this technique will also be used to verify the RNM with the FEM model under nonlinear conditions. This implies that the apparent inductance values for both models will be used. In the RNM the inductance is obtained by:

$$L = \frac{N^2}{\Re} \tag{3.13}$$

with the reluctance $\Re = l/(\mu a)$ where l and a are the effective magnetic material path length and cross sectional area respectively and μ is defined by the relation:

$$\mu = \frac{B}{H} \tag{3.14}$$

which implies apparent inductance. In the case of the FEM model the flux can be determined by:

$$\phi = \int_s \mathbf{B} \cdot d\mathbf{a} = \int_s \nabla \times \mathbf{A} \cdot d\mathbf{a} = \oint_p \mathbf{A} \cdot d\mathbf{l} \tag{3.15}$$

where p is the perimeter bounding the surface s [60]. Using (3.15) the apparent inductance (2.6) can be expressed as:

$$L = NI\frac{\oint_p \mathbf{A} \cdot d\mathbf{l}}{I^2}. \tag{3.16}$$

The vector sign may then go on the current resulting in:

$$L = N\frac{\oint_p \mathbf{A} \cdot \mathbf{I}\, dl}{I^2}. \tag{3.17}$$

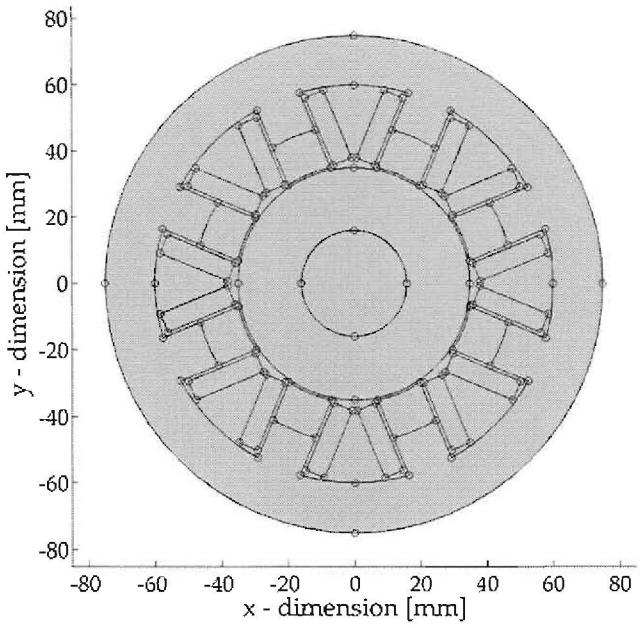

Figure 3.7: FEM model geometry

(3.17) can be further generalised to volume currents by making use of the relation $J = NI/a$:

$$L = \frac{\int_v \mathbf{A} \cdot \mathbf{J}\, d\tau}{I^2}. \tag{3.18}$$

For the case at hand it is assumed that there is no variation in the z axis and the apparent inductance is given by (3.19) which is the same as (3.11).

$$L = l_{ax} \frac{\int_s \mathbf{A} \cdot \mathbf{J}\, da}{I^2} \tag{3.19}$$

It is clear that by comparing the inductances obtained from (3.13) and (3.19) the apparent inductances of the two models are compared. This quantity will be used to verify the RNM with the FEM model.

3.4.3 FEM model limitations

Two-dimensional FEM models are used to verify the RNM and to compare with experimental results. For the verification of the RNM the results are expected to correlate closely since both models ignore axial effects. Discrepancies are however expected between the experimental and FEM results since a two-dimensional FEM solution is applied to a three-dimensional problem. This introduces errors that are not related to the accuracy of the FEM analysis. For more accurate modelling and better correlation between the FEM and experimental results, a three-dimensional FEM analysis must be considered.

The node density of the FEM model shown in figure 3.7 was determined by initially increasing the node density to the maximum amount that could be modelled in a reasonable period of time. This rendered a model with over 300,000 nodes. The number of nodes were decreased and the results were compared to the 300,000 nodes model. Finally a model with 80,000 nodes was selected of which the results closely correlated with that of the 300,000 nodes model. Care was taken in the FEM model to ensure that the node density in the vicinity of sharp corners and fringing fields was adequate to ensure high levels of accuracy.

3.5 Air gap reluctance

During the course of the refinement process the air gap reluctance model was identified as one of the mechanisms contributing to modelling error. The amplitude modulation approach which utilises the switching ripple estimates the rotor position by monitoring the coil impedance at the switching frequency. This is possible due to the fact that the coil impedance is mainly dominated by the air gap reluctance which is dependent on the air gap length. It is therefore fundamental to accurately model the air gap reluctance in order to obtain highly accurate self-sensing results.

A parametric study is undertaken that consists of two parts: (a) an analytical model of the air gap reluctance ignoring fringing and (b) a finite element method (FEM) model. The rotor position will be varied in both the x- and y-axis and the air gap reluctance will be monitored. The results of the two models may then be compared to determine the percentage error introduced by ignoring fringing effects.

3.5.1 Pole face curvature

The air gap reluctance in a radial magnetic bearing is not only dependent on the displacement normal to the pole surface but also dependent on transverse displacement. This is due to the curved surface of the pole faces and rotor. Figure 3.8 shows the rotor and stator geometry as well

as the effect of transverse displacement. As shown in [8] the air gap length l_g is now a function of φ and can be obtained from (3.20).

$$l_g = r_p - \left(x_1 \cos(\varphi) + y_1 \sin(\varphi) + \sqrt{r_j^2 - (x_1 \sin(\varphi) - y_1 \cos(\varphi))^2} \right) \tag{3.20}$$

The air gap magnetic permeance $P_g(x, y)$ can now be determined through numerical integration as a function of rotor position:

$$P_g(x, y) = \int_{\varphi_1}^{\varphi_2} dP_g = \int_{\varphi_1}^{\varphi_2} \frac{\mu_0 \, l_{ax}}{l_g(\varphi, x_1, y_1)} \, r_p \, d\varphi \, . \tag{3.21}$$

The air gap reluctance is then determined by simply inverting the magnetic permeance as determined by (3.21).

3.5.2 Analytical air gap fringing models

Fringing refers to the spreading of the flux at the air gap, enlarging the effective area which in turn reduces the air gap reluctance. In self-sensing the rotor position information is extracted from the air gap reluctance and it is therefore necessary to investigate and quantify the effect fringing has on this parameter for different working points.

It is common to model fringing in the air gap by introducing an additional flux path constituting a semi-circle [65]. Figure 3.9 displays an air gap with the main flux travelling straight across the air gap. The fringing flux leaves the high permeability material and travels with a quarter-circle path whereafter it travels straight for a length l_g and returns to the high permeability material with a quarter-circle path. The total air gap permeance is therefore given by the sum of the main permeance P_{gm} and two times the fringing permeance P_{gf} as shown in (3.22).

$$P_g = P_{gm} + 2P_{gf} \tag{3.22}$$

The main permeance is given by:

$$P_{gm} = \frac{\mu_0 \, a_g}{l_g} \tag{3.23}$$

where $a_g = w \, l_{ax}$ with l_{ax} the axial length of the stack. The fringing permeance is obtained through integration as shown in (3.24)

$$P_{gf} = \int_0^{R_i} \frac{\mu_0}{l} \, da = \int_0^{R_i} \frac{\mu_0 \, l_{ax}}{l_g + \pi r_l} \, dr_l \tag{3.24}$$

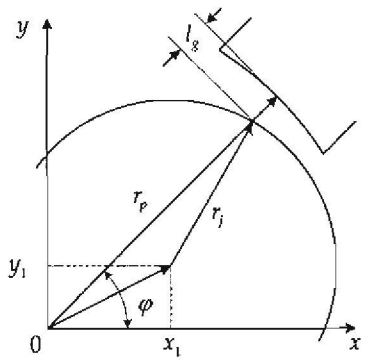

Figure 3.8: Radial magnetic bearing pole and rotor geometry

with $da = l_{ax} dr_l$ and $l = l_g + \pi r_l$. An explicit solution for this integral is given by (3.25).

$$P_{gf} = \frac{\mu_0 l_{ax}}{\pi} \ln(l_g + \pi r_l) \Big|_0^{R_l} = \frac{\mu_0 l_{ax}}{\pi} \ln\left(1 + \frac{\pi R_l}{l_g}\right) \tag{3.25}$$

The only unknown parameter in (3.25) is the length that the fringing permeance extends up the sides of the pole, denoted by R_l. R_l is normally chosen to be a multiple of the air gap length l_g and the exact value is not that critical since the contribution of the differential permeance decreases as one moves further away from the air gap. R_l must therefore be chosen large enough to ensure that the change in total air gap permeance becomes negligible when R_l is further increased.

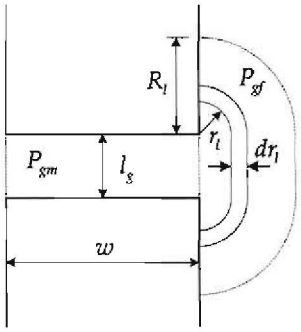

Figure 3.9: Air gap fringing

Figure 3.10 displays the fringing path for a radial AMB consisting of one circle-like path followed by a straight line. The arc is greater than $\pi r_l/2$ as was the case in the previous section and is a function of r_p, r_j, w, R_l and the rotor position. Determining the exact air gap reluctance, including fringing, for varying rotor positions proves to be difficult. The complexity of the analytical expression may render it impractical for air gap reluctance modelling.

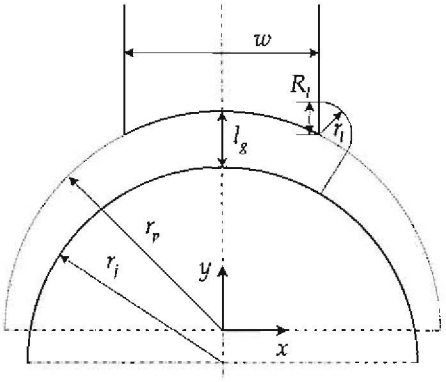

Figure 3.10: Air gap fringing in radial magnetic bearing

More accurate analytical models for the air gap reluctance, which includes fringing, may be derived, making use of conformal mapping techniques. Conformal mapping or transformation is a standard method for solving boundary value problems in (two-dimensional) potential theory [66]. According to [67] it is the most powerful method for analytical solution of Laplacian fields. Compared to other analytical methods, conformal transformation is capable of analysing boundaries with more complicated shapes.

Conformal mapping is used to map a complicated domain onto a domain of which the solution is known or can easily be determined. The solution is then mapped back to the original

domain [66]. When deriving field solutions this consists of determining suitable functions relating a given field to one of which the solution is known or can easily be determined [67]. The solutions often take simple forms which yield expressions for flux density and permeance in magnetic fields and allow direct calculation of magnetic field maps [67].

In [68] a conformal transformation is used to determine the magnetic field distribution in the air gap and the slot of a permanent magnet machine with a slotted stator. The transformation is based on an idealised single slot model. The problem of fringing fields in the vicinity of the AMB poles may also be analysed and conformal mapping may yield analytical expressions for the air gap reluctance. In the present work this approach was however not adopted. In the following section this problem is approached with a FEM model.

3.5.3 FEM parametric study

The air gap reluctance $\Re_g$ is studied with a magnetostatic FEM analysis to determine the effect of fringing. In order to simplify the parametric study only one pole of the AMB is analysed and the magnetic material is assumed to be infinitely permeable. Figure 3.11 displays the simplified geometry of the FEM model where the solution is taken only in the air between the rotor and the stator. Once again COMSOL and the governing equations discussed in section 3.4.1 are used to solve for the magnetic vector potential in the solution area. In the FEM analysis the infinitely permeable material is modelled by implementing the boundary condition

$$\nabla A \cdot \mathbf{n} = 0 \tag{3.26}$$

at the air-iron interface with $\mathbf{n}$ a vector normal to the interface. In the COMSOL environment the boundary condition is realised by using the *Electric insulation* setting which is implemented by (3.27).

$$\mathbf{n} \times \mathbf{H} = 0 \tag{3.27}$$

Once the solution of A is determined with the single excitation coil as shown in figure 3.11, the air gap reluctance can be obtained. One way to obtain the air gap reluctance is by deriving it from the total inductance of the single pole. The current analysis is linear and therefore the inductance can be obtained from (3.19). The integration is taken over the entire solution area with the only nonzero contribution in the area of the coil.

The analysis determines the total inductance for a single pole which includes self-inductance and leakage inductance. Due to the fact that there are no additional poles in close proximity of the excitation pole it is assumed that the only leakage path present is the self-leakage path around the coil. Since the material is infinitely permeable the leakage reluctance is in parallel with the air gap reluctance. An equivalent circuit model for the self- and leakage reluctances is shown in

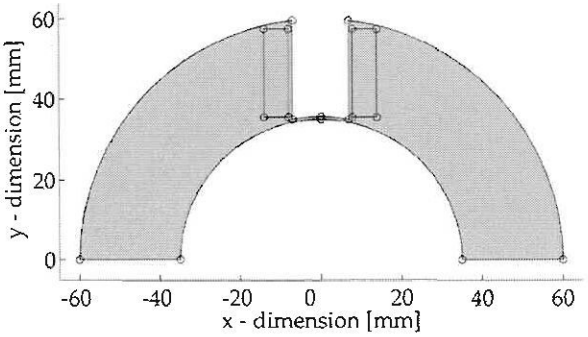

Figure 3.11: Parametric study FEM model geometry

figure 3.12. The self-leakage reluctance must now be specified in order to obtain values for the air gap reluctances. Isolation of the self- and leakage inductances from the total inductance may however prove to be a challenge.

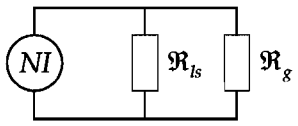

Figure 3.12: Fringing equivalent circuit model

3.5.4 Results

For the case at hand the leakage inductance is obtained making use of a genetic algorithm optimisation approach which is discussed in section 3.6.2. The resulting self-leakage reluctance value is: $\Re_{ls} = 3.5119 \times 10^8\ \mathrm{H}^{-1}$. Next the equivalent reluctance of the circuit in figure 3.12 is simply obtained from:

$$\Re_t = \frac{N^2}{L} \tag{3.28}$$

and the air gap reluctance is then determined from (3.29).

$$\Re_g = \frac{\Re_t \Re_{ls}}{\Re_{ls} - \Re_t} \tag{3.29}$$

Figure 3.13 displays the air gap reluctance as determined by the inverse of (3.21) and the FEM approach for a variation in the y-axis (x position = 0). The absolute percentage error between the FEM and analytical results is obtained for y-axis position ($y(k)$) within the backup bearing range using:

$$e_{\Re_g}(y(k)) = \left| \frac{\Re_{g\,Analyt}(y(k)) - \Re_{g\,FEM}(y(k))}{\Re_{g\,FEM}(0)} \right| 100. \tag{3.30}$$

$\Re_{g\,FEM}(0)$ represents the air gap reluctance as determined by the FEM analysis for the center position ($x = 0,\ y = 0$). It is clear from figure 3.13 that the air gap fringing may not be neglected with a maximum percentage error of 34 % between the FEM and analytical results. Deriving an analytical expression for the effect of fringing may however prove to be impractical as discussed in section 3.5.2. A lookup table is therefore generated from the FEM parametric study results with reluctance values for each air gap as a function of rotor x-y position. The lookup table is incorporated into the RNM and used in the subsequent sections to generate results.

3.6 Reluctance network model

In the course of the refinement process the choice of leakage path was identified as a source of uncertainty. First a self-leakage path was used in the RNM which displayed discrepancies in both the flux levels and mutual inductances of the pole pairs adjacent to the excited pole pair. Next a mutual leakage path was investigated which resulted in much better correlation of the FEM and RNM results. The choice of reluctance path is influenced by the geometry of the specific experimental system and various configurations may be investigated to determine the optimal model.

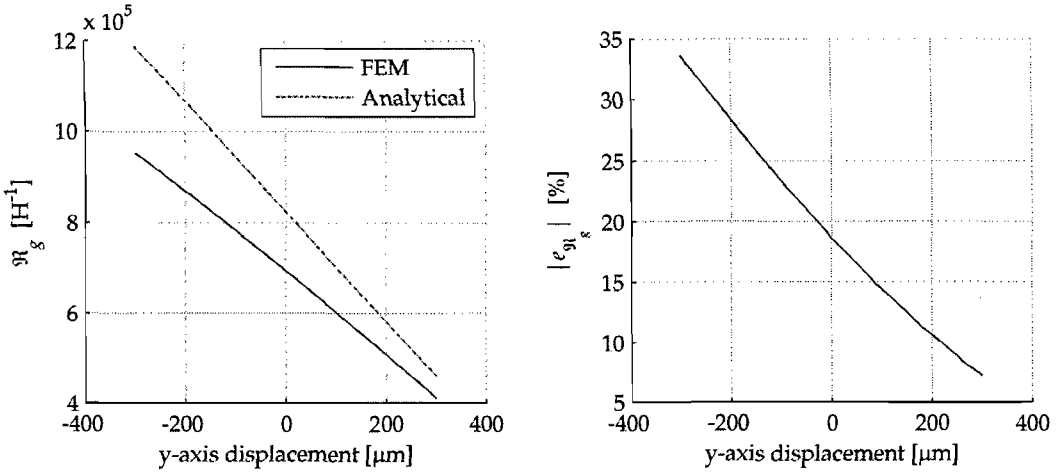

Figure 3.13: Parametric study results: FEM vs. Analytical

3.6.1 Self-leakage topology

Topology

Figure 3.14 displays the reluctance network for the self-leakage topology. The governing equations for this topology, based on work done by Meeker [11], are included in appendix B and are derived in a similar fashion as the model described in section 3.6.2. An advantage of this configuration is that the self-leakage is simply added to the self-inductance terms and does not form part of the reluctance network calculations.

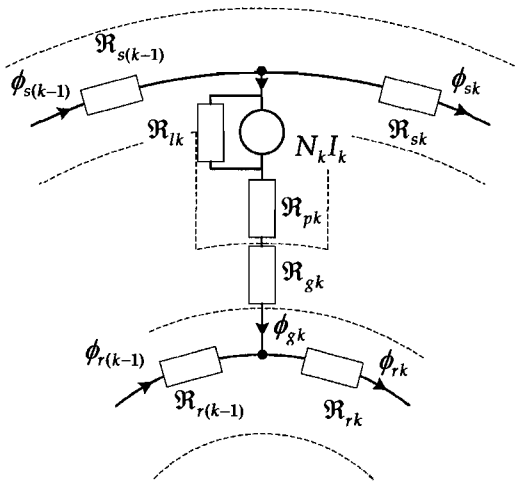

Figure 3.14: Self-leakage reluctance network

Results

The FEM and RNM results are compared in terms of the self- and mutual inductances of the excitation coil as well as the flux levels in the respective poles according to the referencing convention in figure 3.3.

Figures 3.15 and 3.16 display the FEM and self-leakage RNM results for the linear case with a 10 A excitation on PP_1. The self-leakage RNM displays remarkable correlation to the FEM results

in terms of self-inductance (L_{11}) and flux levels in the excited legs of the model (ϕ_1 and ϕ_2) as shown in figure 3.15. The maximum absolute percentage error in L_{11} is less than 0.6 % and in ϕ_1 and ϕ_2 less than 0.8 % for the entire excursion of y-axis positions. Good correlation is also observed between the FEM and RNM results for the mutual inductance L_{13} and fluxes ϕ_5 and ϕ_6 with maximum absolute percentage errors of less than 5.1 % and 4.5 % respectively.

The maximum absolute percentage error in mutual inductances L_{12} and L_{14} as well as in the flux levels in poles P_3 and P_8 (ϕ_3 and ϕ_8) display offsets which could not be corrected by adjusting model variables. L_{12} and L_{14} display error offsets of more than 40 % compared to the 0.6 % and 5.1 % of L_{11} and L_{13} respectively. The flux levels in the poles adjacent to the exciting pole pair, ϕ_3 and ϕ_8 display maximum absolute percentage errors of 14 % compared to the 3 % error in the fluxes ϕ_4 and ϕ_7. The results imply that there is an unmodelled flux path between P_1 and P_8 as well as between P_2 and P_3. The maximum percentage errors for all the inductances and fluxes are summarised in table 3.2.

Table 3.2: Modelling errors - Linear self-leakage RNM FEM verification

Parameter	L_{11}	ϕ_1	ϕ_2	L_{12}	ϕ_3	ϕ_4	L_{13}	ϕ_5	ϕ_6	L_{14}	ϕ_7	ϕ_8
Max abs error [%]	0.6	0.8	0.8	44	14	3	5.1	4.5	4.5	44	3	14

From the results shown in figures 3.15 and 3.16 it appears that the self-leakage RNM is incomplete. An additional flux path must be introduced in the form of a mutual leakage path between the pole tips in order to rectify the offsets in the flux levels in poles P_3 and P_8. This will also add a constant to the mutual inductances L_{12} and L_{14} which may eliminate the offsets. In the following section the mutual leakage RNM is discussed in more detail.

3.6.2 Mutual leakage topology

Topology

The reluctance network which incorporates the mutual leakage path is shown in figure 3.17. The leakage reluctance path connects the adjacent pole tips and as the following sections will show, improves correlation between the FEM and RNM results.

Governing equations

One drawback of this model is that there are now $5P$ linear independent equations linking the $5P$ fluxes in the active magnetic bearing (AMB) compared to the $3P$ equations of the self leakage reluctance model (P referring to the number of poles). The mutual leakage reluctance model is therefore computationally more expensive. The governing magnetic equations are derived in the same fashion as described in [8]. The sign convention as shown in figure 3.17 is assumed to write the set of $5P$ independent linear equations. The $5P$ independent linear equations are:

- $P-1$ loop equations in the stator (down the pole, clockwise in the leakage path, up the next pole and back anticlockwise through the stator):

$$\Re_{pk}\phi_{pk} + \Re_{lk}\phi_{lk} - \Re_{p(k+1)}\phi_{p(k+1)} - \Re_{sk}\phi_{sk} = N_k I_k - N_{(k+1)} I_{(k+1)} \tag{3.31}$$

- $P-1$ loop equations around the air gaps (from pole to rotor, clockwise in the rotor, from rotor to next pole and back anticlockwise through the leakage path):

$$\Re_{gk}\phi_{gk} + \Re_{rk}\phi_{rk} - \Re_{g(k+1)}\phi_{g(k+1)} - \Re_{lk}\phi_{lk} = 0 \tag{3.32}$$

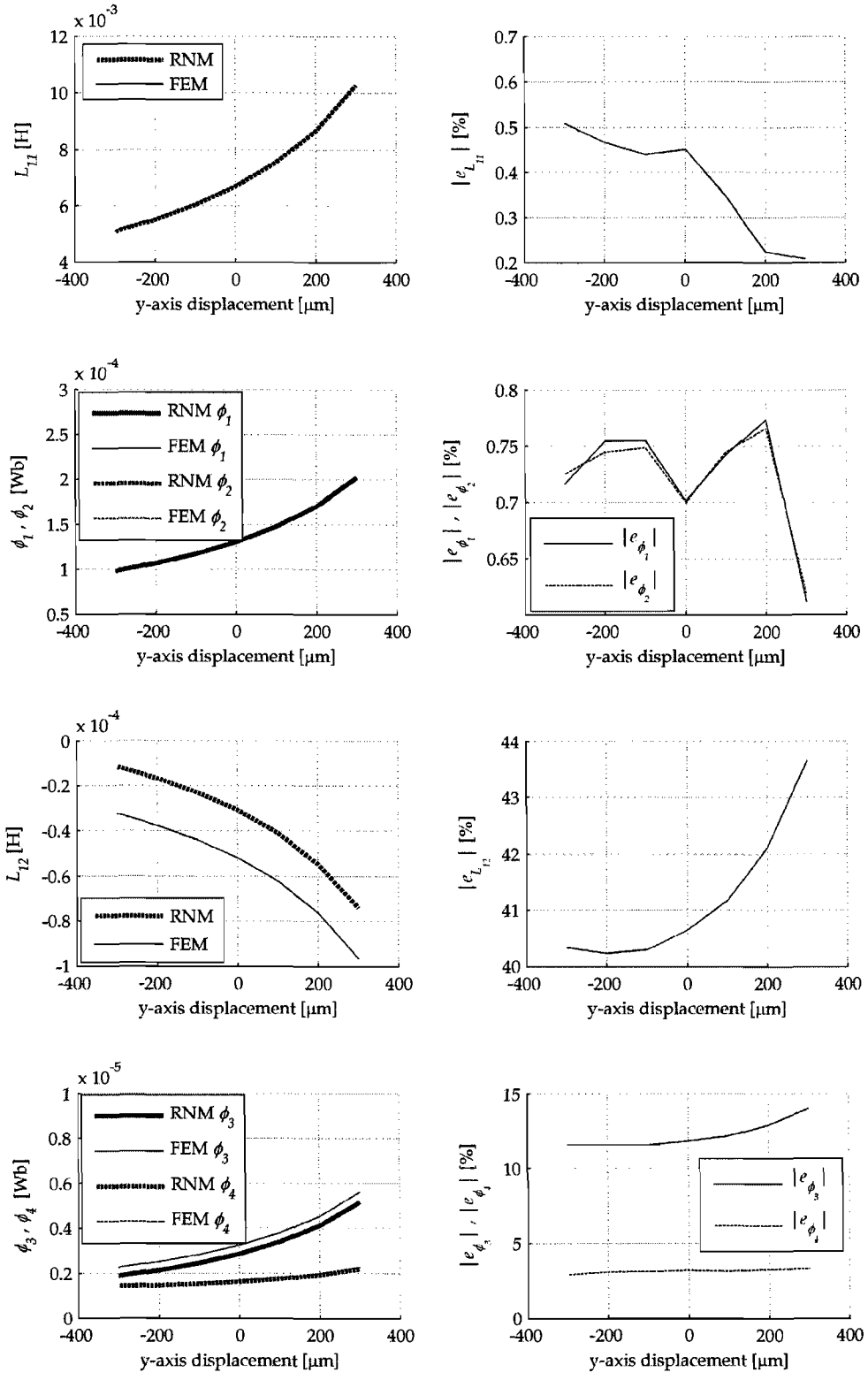

Figure 3.15: Linear self-leakage RNM FEM verification (L_{11}, L_{12}, ϕ_1 to ϕ_4)

- $P-1$ conservation equations for nodes connecting the poles to the stator back iron:

$$\phi_{p(k+1)} - \phi_{sk} + \phi_{s(k+1)} = 0 \tag{3.33}$$

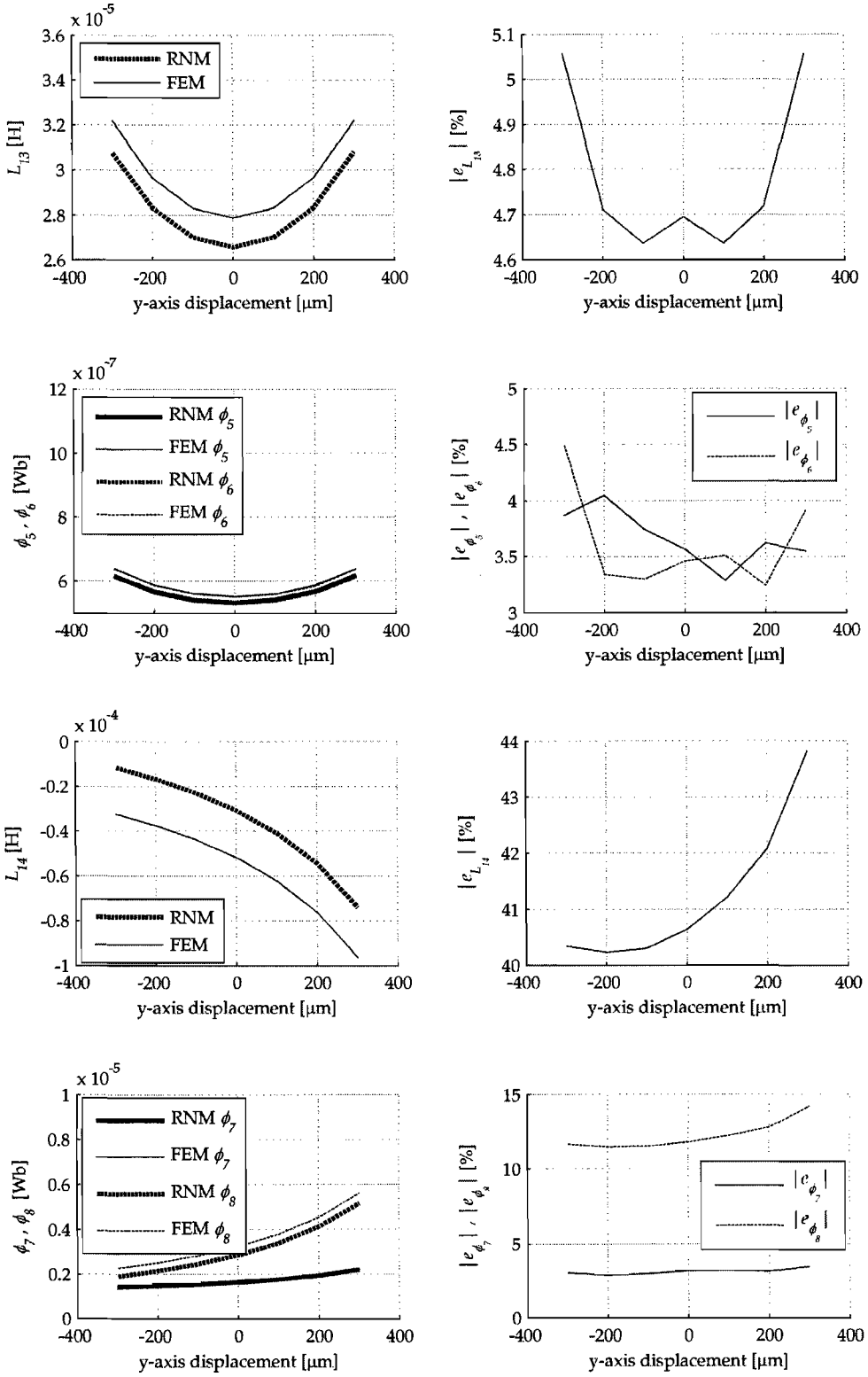

Figure 3.16: Linear self-leakage RNM FEM verification (L_{13}, L_{14}, ϕ_5 to ϕ_8)

- $P-1$ conservation equations for nodes connecting the poles to the air gaps and leakage

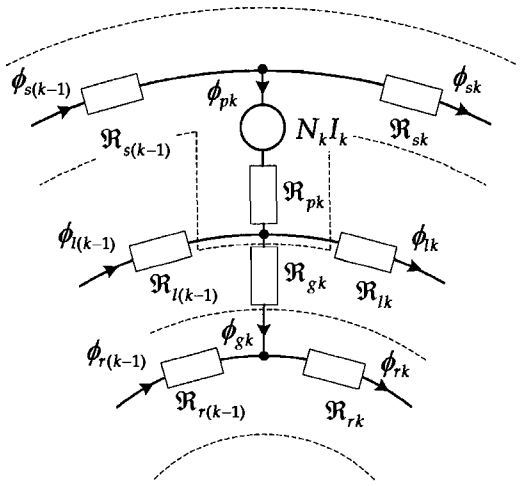

Figure 3.17: Mutual leakage reluctance network

paths:

$$-\phi_{p(k+1)} + \phi_{g(k+1)} - \phi_{lk} + \phi_{l(k+1)} = 0 \tag{3.34}$$

- $P-1$ conservation equations for nodes connecting the air gaps to the rotor:

$$\phi_{g(k+1)} + \phi_{rk} - \phi_{r(k+1)} = 0 \tag{3.35}$$

- One conservation equation of all fluxes flowing into the rotor:

$$\sum_{k=1}^{P} \phi_{gk} = 0 \tag{3.36}$$

- One conservation equation of all fluxes flowing from the stator back iron:

$$\sum_{k=1}^{P} \phi_{pk} = 0 \tag{3.37}$$

- One loop equation around the rotor:

$$\sum_{k=1}^{P} \Re_{rk}\phi_{rk} = 0 \tag{3.38}$$

- One loop equation around the stator:

$$\sum_{k=1}^{P} \Re_{sk}\phi_{sk} = 0 \tag{3.39}$$

- One loop equation around the leakage paths:

$$\sum_{k=1}^{P} \Re_{lk}\phi_{lk} = 0 \tag{3.40}$$

Reluctances

The variables $\Re_p$, $\Re_r$ and $\Re_s$ correspond to the magnetic iron reluctance of the pole, rotor and stator respectively. These reluctances can be determined using (3.41).

$$\Re = \frac{l}{\mu_0 \mu_r a} \tag{3.41}$$

The effective reluctance path length l is approximated for the pole, rotor and stator by (3.42), (3.43) and (3.44) respectively.

$$l_p = \frac{r_c + r_s}{2} - r_p \tag{3.42}$$

$$l_r = \theta \frac{r_r + r_j}{2} \tag{3.43}$$

$$l_s = \theta \frac{r_c + r_s}{2} - r_p \tag{3.44}$$

The pole pitch θ (angle between the poles) is determined by the number of poles P in the AMB and is given by (3.45). For the case at hand $P = 8$.

$$\theta = \frac{2\pi}{P} \tag{3.45}$$

The air gap reluctances are determined from a lookup table generated by the FEM analysis described in section 3.5.3.

Equations in matrix form

Equations (3.31)-(3.40) can be expressed in matrix form as:

$$\mathbf{\Re \Phi} = \mathbf{NI} \tag{3.46}$$

The flux in each leg of the RNM can now be determined by inverting the reluctance matrix $\mathbf{\Re}$ as shown in (3.47).

$$\mathbf{\Phi} = \mathbf{\Re}^{-1}\mathbf{NI} \tag{3.47}$$

The inductance can now be determined from the fluxes utilising:

$$\mathbf{L} = \mathbf{T}'\mathbf{\Re}^{-1}\mathbf{N} \tag{3.48}$$

where $\mathbf{T}$ is defined as a matrix with $5P$ rows and m (the number of coils) columns. The (k, l) entry of $\mathbf{T}$ represents the number of turns of the l^{th} coil about the k^{th} flux and should also include the sign according to the chosen convention [11]. In (3.48) the diagonal entries represent the self-inductances of the coils and the off-diagonal entries the mutual inductances.

Genetic algorithm optimisation of leakage reluctance

The mutual leakage RNM discussed in the previous section contains two variables that are unknown. The first is the mutual leakage path reluctance $\Re_{lm}$ and the second is the self-leakage reluctance $\Re_{ls}$ which is necessary to determine the air gap reluctances from the lookup table generated by the FEM analysis. It is not an easy task to obtain values for these variables. Analytical models are often used and it is a tedious task to obtain accurate values for the leakage reluctances. For this reason the MATLAB® Genetic Algorithm Optimisation Toolbox was used to obtain values for $\Re_{lm}$ and $\Re_{ls}$.

The fitness function compares the linear FEM analysis and the RNM for the rotor centered in the x-axis and for a varying y-axis rotor position within the backup bearing limits. The FEM and RNM results are compared in terms of:

- self-inductance,
- mutual inductances and
- flux levels in the AMB poles.

The absolute percentage error between the FEM model and RNM for each of the mentioned parameters is obtained in each y-axis position. The mean absolute percentage error for each parameter is then obtained and used in the fitness function. Mathematically the fitness function for an eight pole heteropolar magnetic bearing with four coils (adjacent poles paired) can be expressed as:

$$fitness = \frac{\sum_{k=1}^{4} e_k}{4} \tag{3.49}$$

with

$$e_k = \frac{(2\bar{e}_{L_{(1,k)}} + \bar{e}_{\phi_{(2k-1)}} + \bar{e}_{\phi_{(2k)}})}{4} \quad \text{for} \quad k = 1 \ldots 4 \tag{3.50}$$

where for example the mean of the absolute percentage error in inductance for m y-axis positions is given by:

$$\bar{e}_{L_{(1,k)}} = \frac{\sum_{j=1}^{m} e_{L_{(1,k)}(y(j))}}{m} \tag{3.51}$$

where $y(j)$ represents a y-axis rotor position within the backup bearing range. The absolute percentage error between the RNM and FEM for each of these y-axis positions can be obtained by:

$$e_{L_{(1,k)}(y(j))} = \left| \frac{L_{RNM(1,k)}(y(j)) - L_{FEM(1,k)}(y(j))}{L_{FEM(1,k)}(y(j))} \right| 100. \tag{3.52}$$

The output of the genetic algorithm optimisation is $\Re_{lm} = 1.1344 \times 10^8$ H^{-1} and $\Re_{ls} = 3.5119 \times 10^8$ H^{-1}. These leakage reluctance values are assumed constant and will be used in the subsequent sections to generate results.

Linear results

The results for the linear case mutual leakage RNM are displayed in figures 3.18 and 3.19. Again excellent correlation between the FEM and RNM results are observed for L_{11}, ϕ_1 and ϕ_2 with maximum absolute percentage errors of less than 0.95 % and 0.85 % for the inductance and flux respectively. The maximum absolute percentage errors of above 40 % in mutual inductances L_{12} and L_{14} are reduced to less than 3.5 %. The mutual inductance L_{13} also displays better correlation and the error is reduced from 5.1 % to less than 1.4 %. The flux levels ϕ_3 and ϕ_8 also show improvement with the maximum absolute percentage error reduced from 14 % to below 11 %. The flux levels ϕ_4 and ϕ_7 however display inferior correlation compared to the self-leakage RNM results and the maximum error increased from 3 % to just below 8 %. The flux levels ϕ_5 and ϕ_6 display an increase in error from 4.5 % to 60 %. It is interesting to note that the results for L_{12}, ϕ_3, ϕ_4 and L_{14}, ϕ_8, ϕ_7 are the same portraying symmetry between PP_2 and PP_4. The maximum percentage errors for all the inductances and fluxes are summarised in table 3.3.

Table 3.3: Modelling errors - Linear mutual leakage RNM FEM verification

Parameter	L_{11}	ϕ_1	ϕ_2	L_{12}	ϕ_3	ϕ_4	L_{13}	ϕ_5	ϕ_6	L_{14}	ϕ_7	ϕ_8
Max abs error [%]	0.95	0.85	0.85	3.5	11	8	1.4	60	60	3.5	8	11

The discrepancies in flux levels may be attributed to the method by which the flux is determined in the FEM model. The flux density B is integrated over an area situated half way between

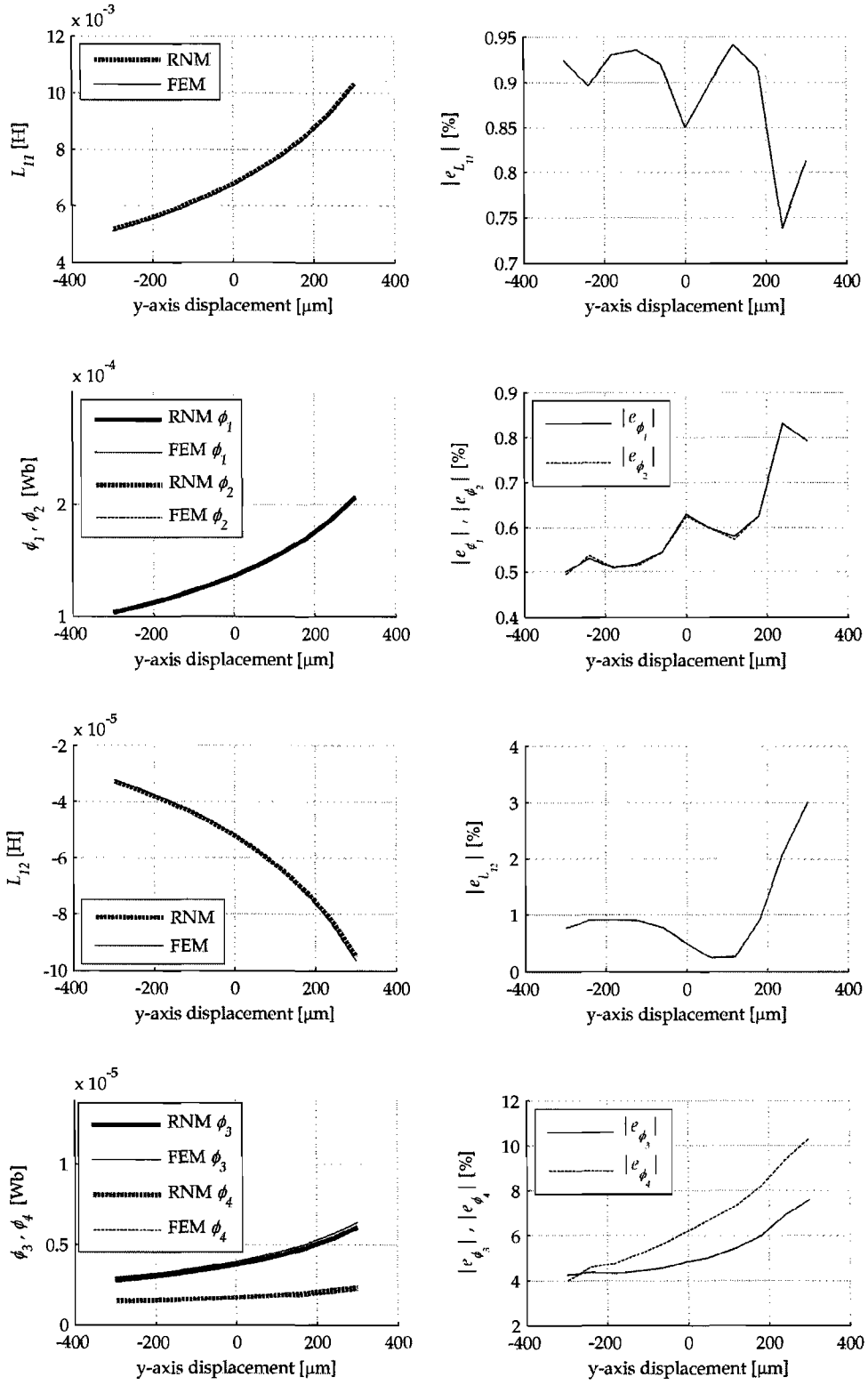

Figure 3.18: Linear mutual leakage RNM FEM verification (L_{11}, L_{12}, ϕ_1 to ϕ_4)

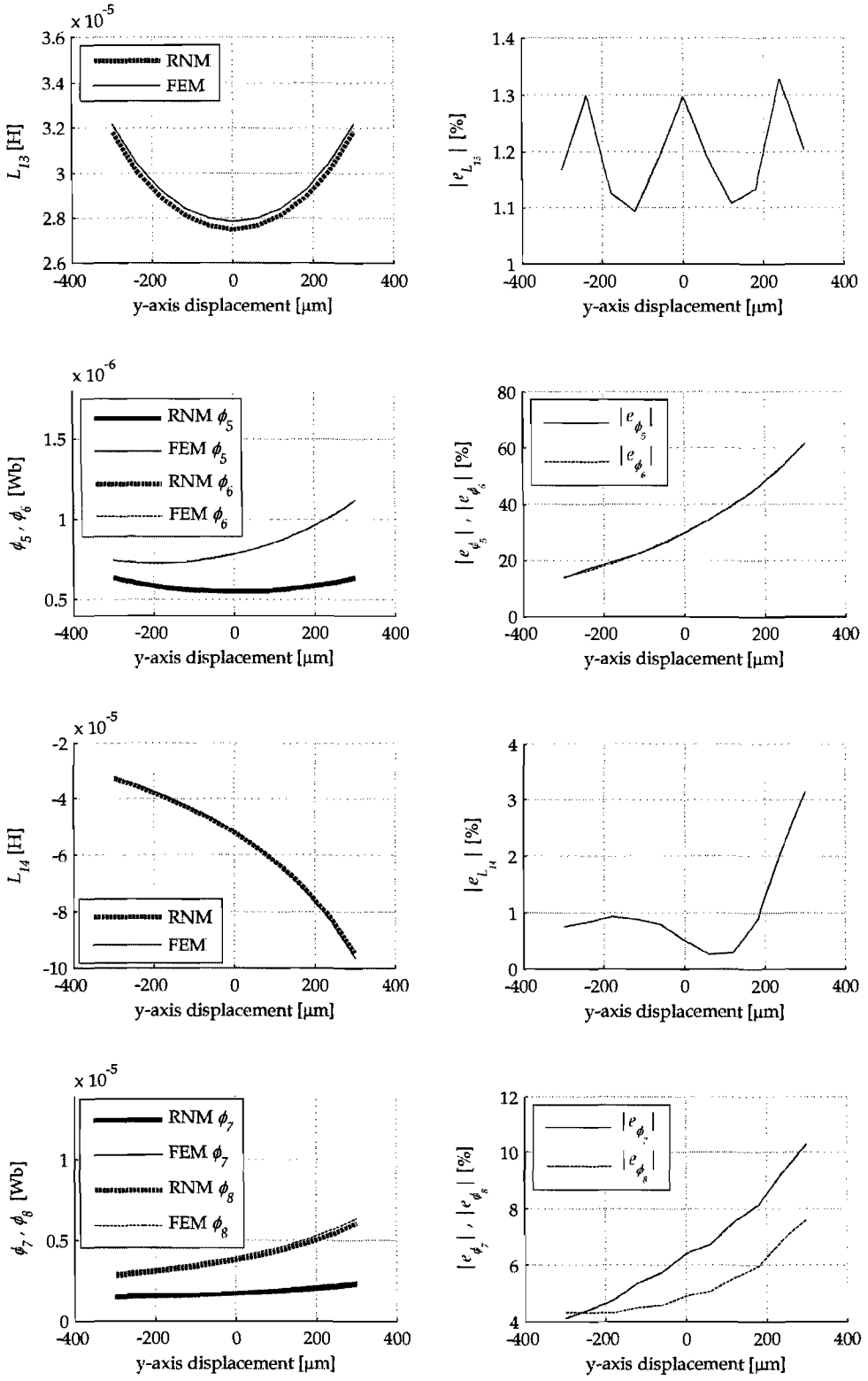

Figure 3.19: Linear mutual leakage RNM FEM verification (L_{13}, L_{14}, ϕ_5 to ϕ_8)

the pole tip and stator inner radius to obtain the total flux flowing in the pole. This area is defined by the line half way between the pole tip and stator inner radius shown in figure 3.7 and the axial length of the bearing. The flux obtained by integration is assumed to include the flux that crosses the air gap as well as the mutual leakage flux. This value is then compared to the flux flowing in the pole of the mutual leakage RNM which does include both the flux crossing the air gap and the mutual leakage flux. The mutual leakage flux path between the pole tips is however only an approximation and in reality it is distributed over the entire pole length. The mutual leakage flux path assumption as well as the method of determining the flux in the FEM model may cause the resulting flux levels to differ. The inductance on the other hand, as obtained from the magnetic vector potential A, is therefore a more accurate measure of determining the level of correlation.

3.6.3 Magnetic material nonlinearity

Nonlinear material behaviour

The nonlinear behaviour of the magnetic material is incorporated into the model by utilising a flux density dependent relative permeability $\mu_r(B)$. The governing equations in matrix form are given by (3.53).

$$\mathfrak{R}(\mathbf{\Phi})\mathbf{\Phi} = \mathbf{NI} \tag{3.53}$$

The nonlinear relative permeability curve is obtained from the peak magnetisation curve data supplied by the manufacturers of the silicon steel sheets (Cogent^{tm} M400-50A). Figure 3.20 displays the relative permeability as a function of flux density. This information is incorporated into the RNM by using a lookup table.

The nonlinear system described in (3.53) is solved through iteration. The Newton-Raphson method is investigated due to its simplicity and speed. It is one of the most useful and best known algorithms that rely on the continuity of the function and its first and second derivatives. This additional information allows the technique to converge faster than either the bisection or false position methods [69], [66].

Unfortunately, for the problem at hand, the Newton-Raphson method does not converge under all conditions. The simple iteration method is also investigated and modified by reducing the step size. The step size reduction is accomplished by using an average of the current and previous three solutions of the fluxes as a new estimate of the final solution. Although this method does not converge as fast as the Newton-Raphson method, it converges under all conditions. The modified iteration method is used to obtain solutions for the nonlinear mutual leakage RNM in the following section.

Nonlinear results

The nonlinear magnetic material properties are now incorporated into the model by utilising the relative material permeability as shown in figure 3.20. The reluctance of each leg of the magnetic material is now a function of the flux level and a solution is obtained by means of iteration. As with the linear results only PP_1 (I_1) is excited and the currents in PP_2, PP_3 and PP_4 are set to zero ($I_2 = I_3 = I_4 = 0$ A). Three different levels of excitation are presented, i.e. $I_1 = 2$ A, $I_1 = 6$ A and $I_1 = 10$ A. The rotor is again centered in the x-axis and both models are evaluated for a range of y-axis rotor positions.

Figures 3.21 and 3.22 display the results for an excitation current of $I_1 = 2$ A. The self-inductance L_{11} and fluxes ϕ_1 and ϕ_2 of the FEM and RNM correlate to within 1.6 %, 0.8 % and 0.4 % respectively. It is interesting to note that the nonlinear results do not portray symmetry between PP_2 and PP_4 as was the case with the linear results. The mutual inductances L_{12}, L_{13} and L_{14} display maximum absolute errors of 4.8 %, 2 % and 3 % respectively. The fluxes ϕ_3 and ϕ_8 display

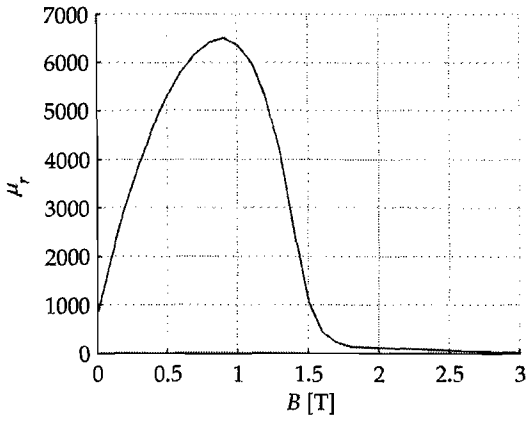

Figure 3.20: Magnetic material relative permeability curve

maximum errors of 3.5 % and 13 % respectively and ϕ_4 and ϕ_7 display maximum errors of 5 % and 18 % respectively. The flux in PP_3, ϕ_5 and ϕ_6, display maximum errors of 10 % and 55 % respectively. The discrepancies in flux levels may be attributed to the method used to compare the two models as explained in section 3.6.2. The maximum percentage errors for all the inductances and fluxes are summarised in table 3.4.

Table 3.4: Modelling errors - Nonlinear mutual leakage RNM FEM verification (2 A)

Parameter	L_{11}	ϕ_1	ϕ_2	L_{12}	ϕ_3	ϕ_4	L_{13}	ϕ_5	ϕ_6	L_{14}	ϕ_7	ϕ_8
Max abs error [%]	1.6	0.8	0.4	4.8	3.5	5	2	10	55	3	18	13

Figures 3.23 and 3.24 display the results for $I_1 = 6$ A and $I_2 = I_3 = I_4 = 0$ A. The maximum percentage errors for all the inductances and fluxes are summarised in table 3.5.

Table 3.5: Modelling errors - Nonlinear mutual leakage RNM FEM verification (6 A)

Parameter	L_{11}	ϕ_1	ϕ_2	L_{12}	ϕ_3	ϕ_4	L_{13}	ϕ_5	ϕ_6	L_{14}	ϕ_7	ϕ_8
Max abs error [%]	1.8	0.3	0.2	3.8	8.8	7.2	13.5	25	90	4.6	35	20

Figures 3.25 and 3.26 display the results for $I_1 = 10$ A and $I_2 = I_3 = I_4 = 0$ A. The maximum percentage errors for all the inductances and fluxes are summarised in table 3.6.

Table 3.7 contains a summary of the maximum absolute percentage errors between the RNM and FEM results for both the linear and nonlinear cases. The linear results of the FEM and RNM correlate closely except for fluxes ϕ_5 and ϕ_6 which may be attributed to the method employed to determine the flux levels in the FEM model (refer to section 3.6.2). Discrepancies between the FEM and RNM results for fluxes ϕ_5 and ϕ_6 are also noticed in the nonlinear analysis for all levels of excitation. The fact that the mutual inductance L_{13} shows good correlation between the FEM and RNM results for the linear case and low levels of excitation in the nonlinear case further corroborates the claim that the discrepancies in ϕ_5 and ϕ_6 are due to a measurement error and not due to a modelling error.

The parameters L_{11}, ϕ_1 and ϕ_2 display excellent correlation in both the linear and nonlinear cases for all levels of excitation current. This is a significant result since these parameters are much more dominant in the self-sensing scheme due to their large values, than those of the mutual inductances and corresponding fluxes. Unfortunately the mutual inductances as well as flux levels in non-excited poles display large discrepancies under highly saturated conditions (high excitation currents and small air gaps).

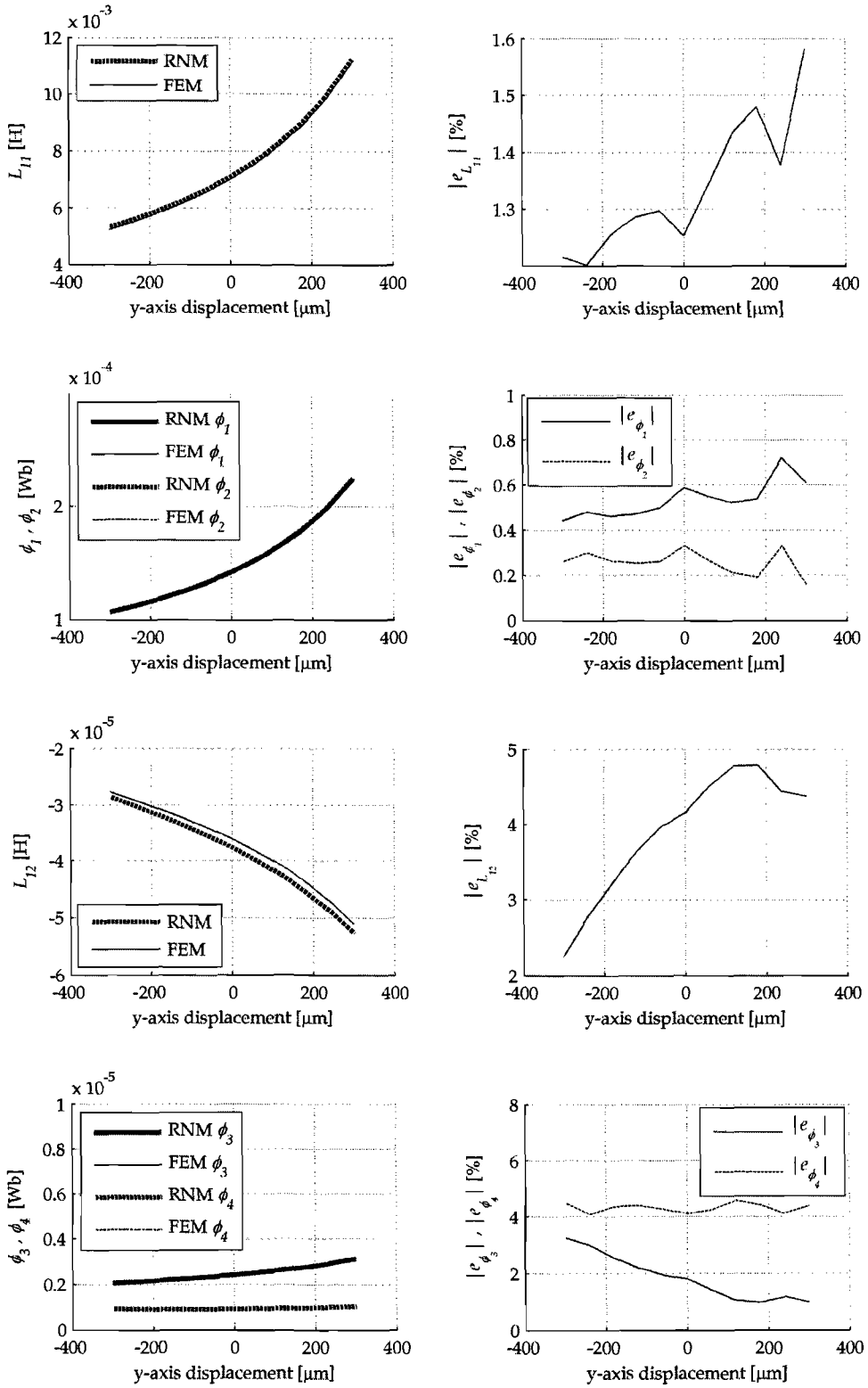

Figure 3.21: Nonlinear mutual leakage RNM FEM verification (L_{11}, L_{12}, ϕ_1 to ϕ_4 for $I_1 = 2$ A)

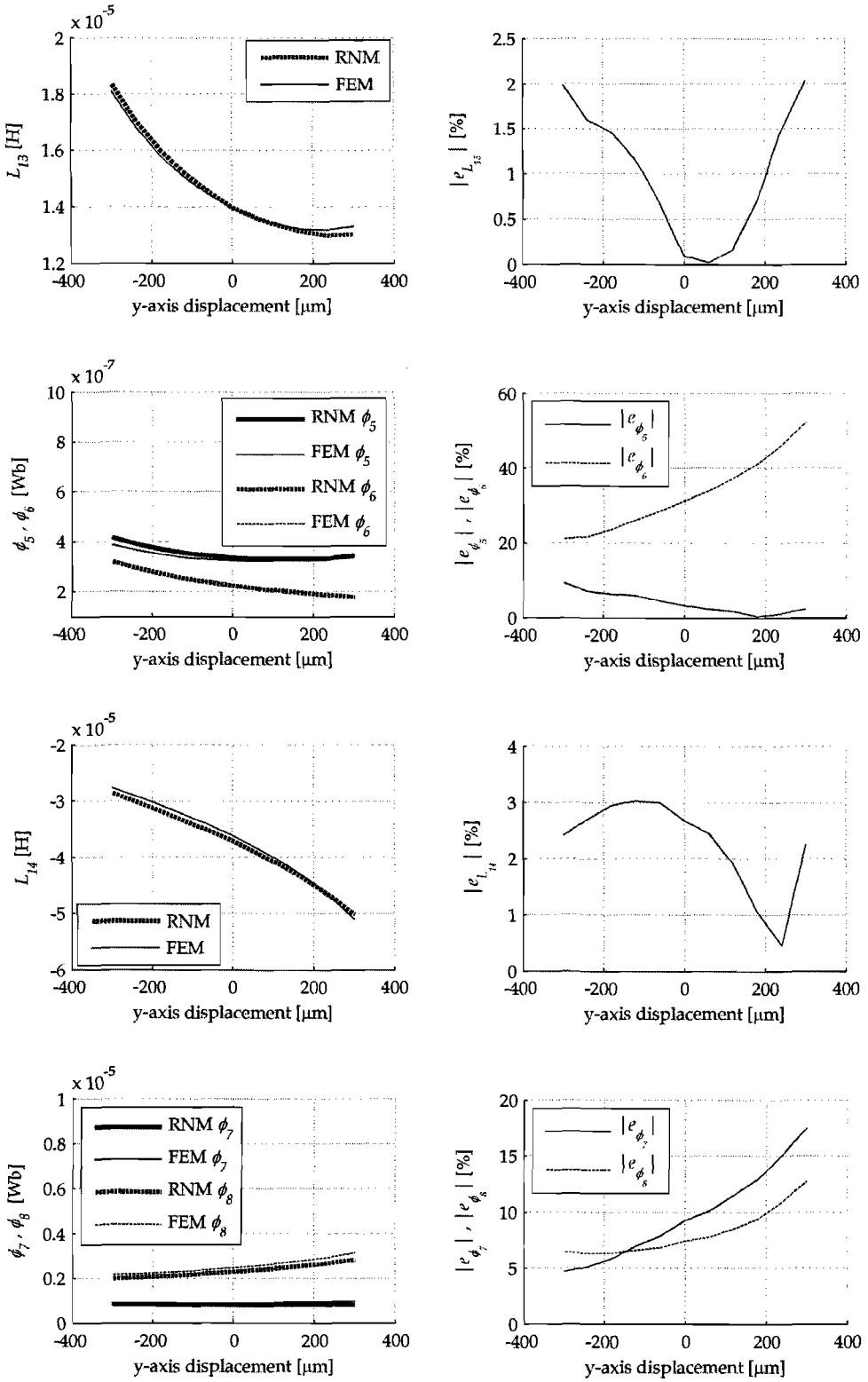

Figure 3.22: Nonlinear mutual leakage RNM FEM verification (L_{13}, L_{14}, ϕ_5 to ϕ_8 for $I_1 = 2$ A)

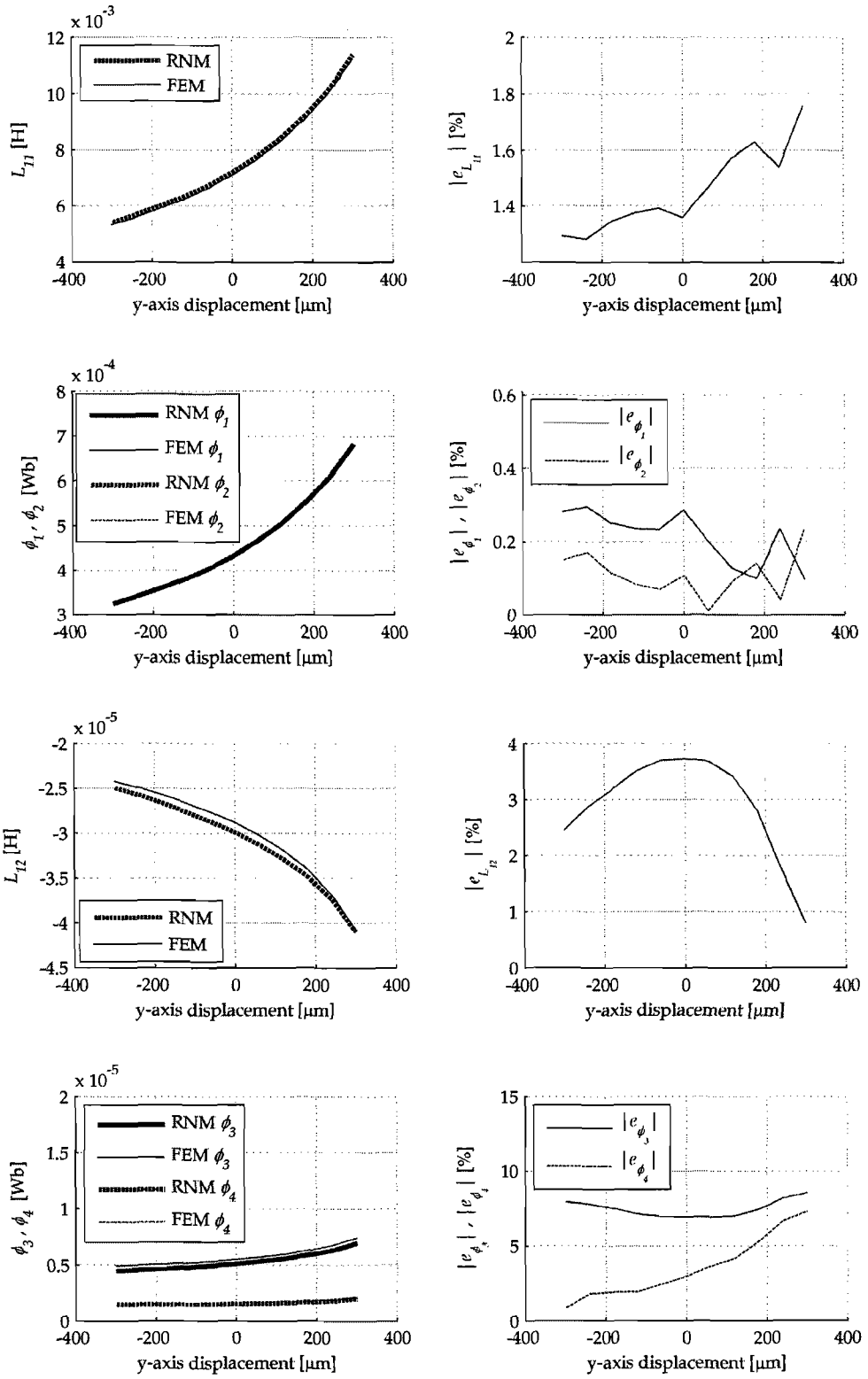

Figure 3.23: Nonlinear mutual leakage RNM FEM verification (L_{11}, L_{12}, ϕ_1 to ϕ_4 for $I_1 = 6$ A)

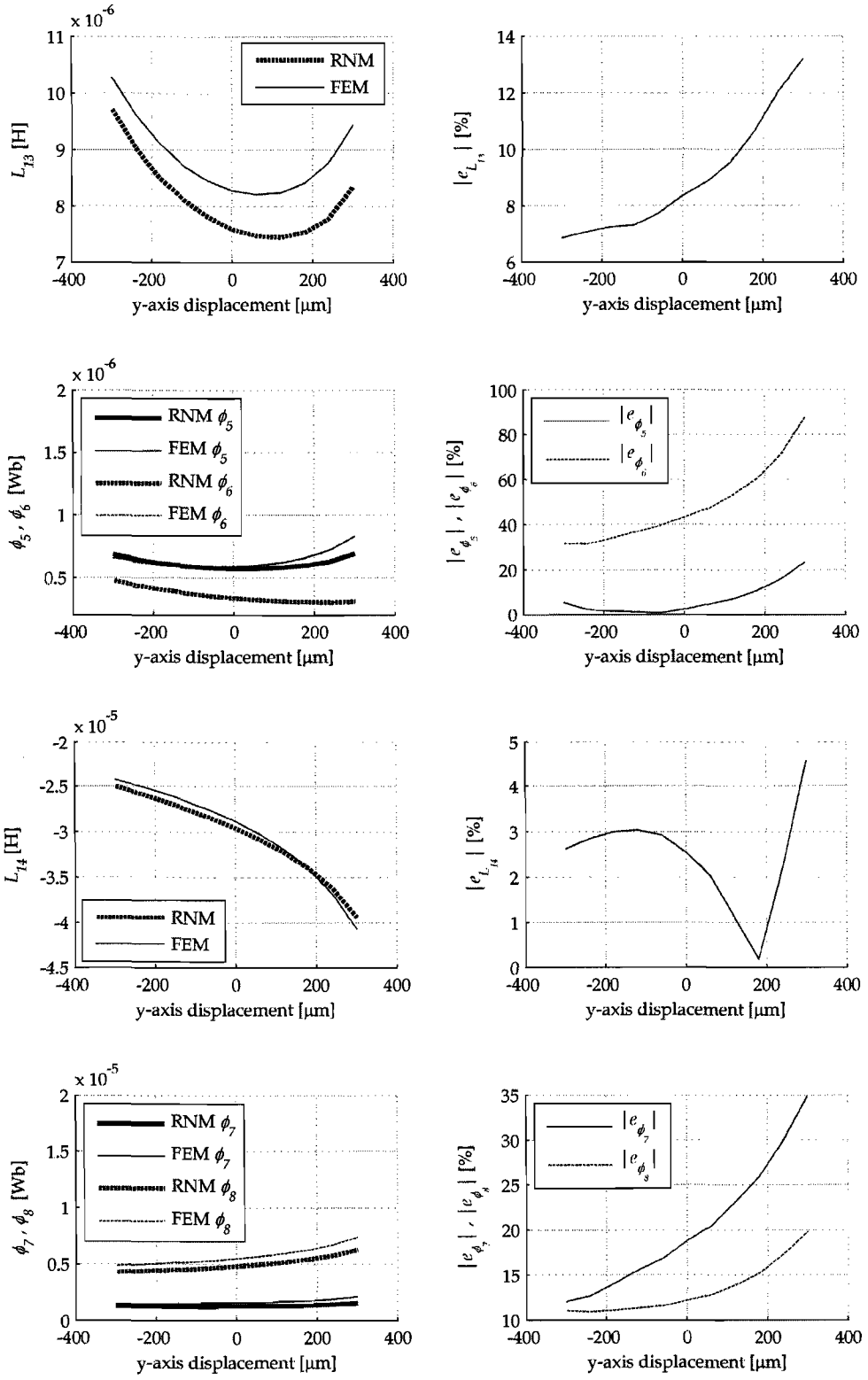

Figure 3.24: Nonlinear mutual leakage RNM FEM verification (L_{13}, L_{14}, ϕ_5 to ϕ_8 for $I_1 = 6$ A)

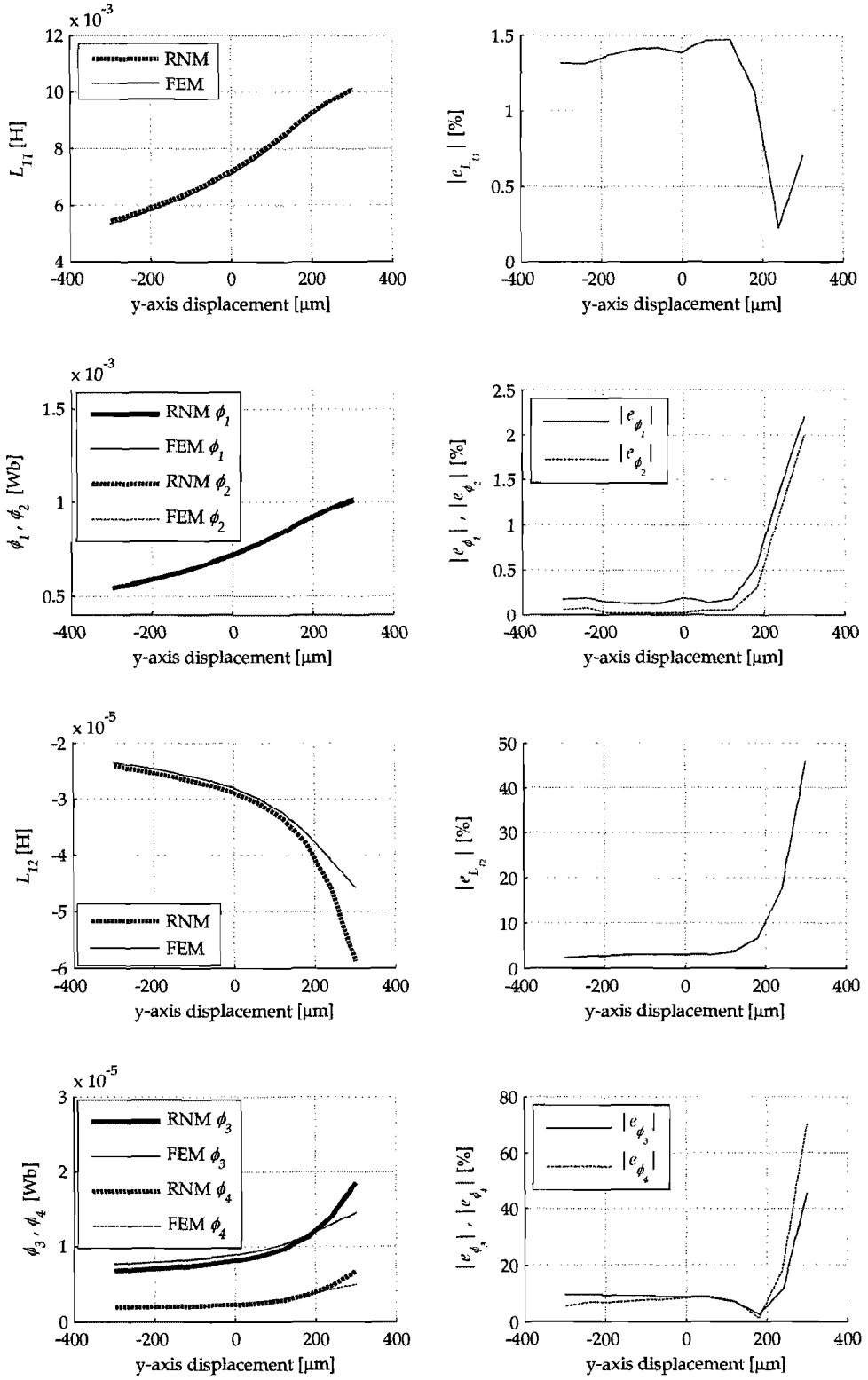

Figure 3.25: Nonlinear mutual leakage RNM FEM verification (L_{11}, L_{12}, ϕ_1 to ϕ_4 for $I_1 = 10$ A)

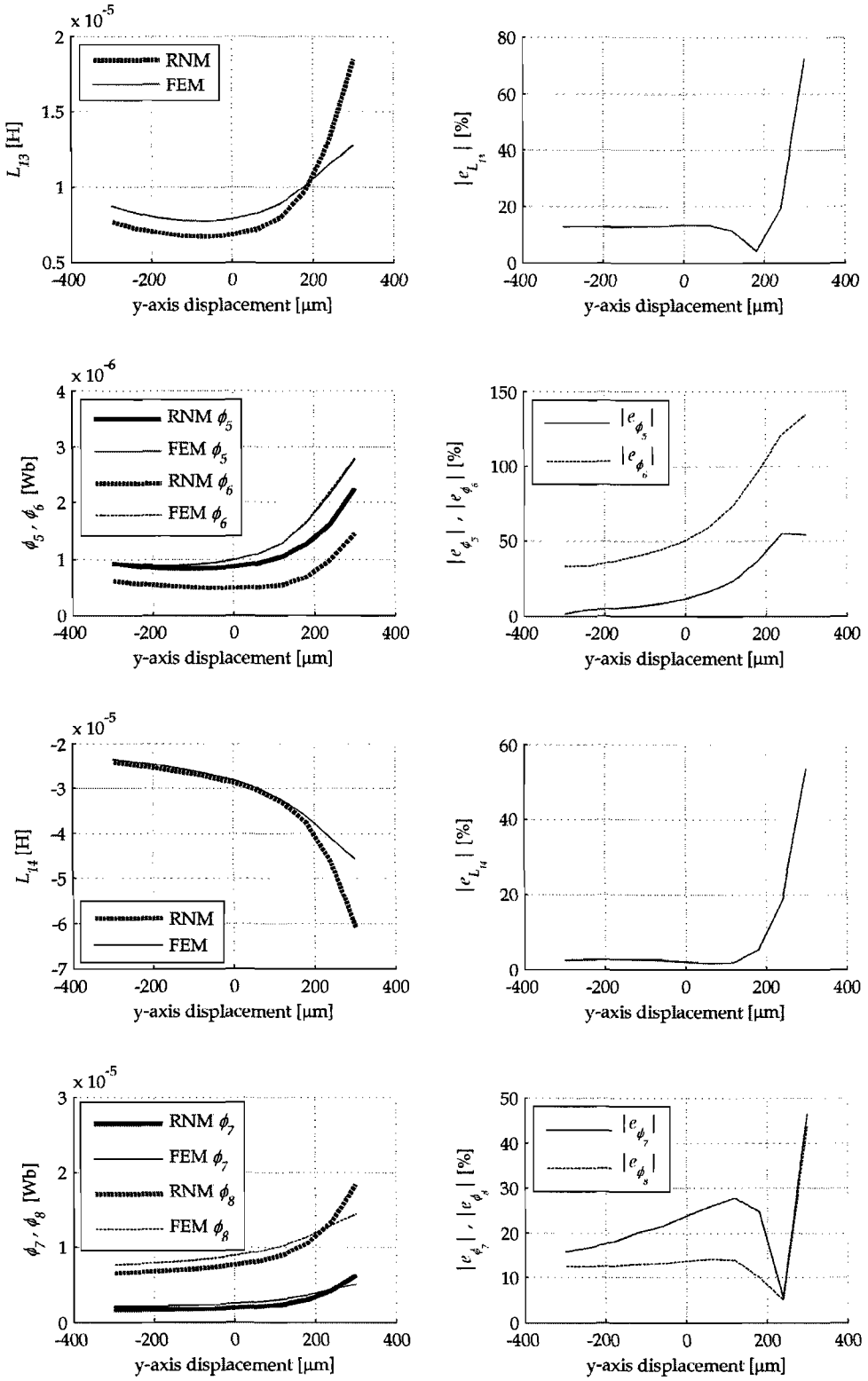

Figure 3.26: Nonlinear mutual leakage RNM FEM verification (L_{13}, L_{14}, ϕ_5 to ϕ_8 for $I_1 = 10$ A)

Table 3.6: Modelling errors - Nonlinear mutual leakage RNM FEM verification (10 A)

Parameter	L_{11}	ϕ_1	ϕ_2	L_{12}	ϕ_3	ϕ_4	L_{13}	ϕ_5	ϕ_6	L_{14}	ϕ_7	ϕ_8
Max abs error [%]	1.5	2.3	2	47	48	70	73	55	135	55	47	44

Table 3.7: Summary of the modelling errors between the FEM and RNM results

Parameter	**Maximum absolute error [%]**			
	Linear	$I_1 = 2$ A	$I_1 = 6$ A	$I_1 = 10$ A
L_{11}	0.95	1.6	1.8	1.5
ϕ_1	0.85	0.8	0.3	2.3
ϕ_2	0.85	0.4	0.2	2
L_{12}	3.5	4.8	3.8	47
ϕ_3	11	3.5	8.8	48
ϕ_4	8	5	7.2	70
L_{13}	1.4	2	13.5	73
ϕ_5	60	10	25	55
ϕ_6	60	55	90	135
L_{14}	3.5	3	4.6	55
ϕ_7	8	18	35	47
ϕ_8	11	13	20	44

In an attempt to explain the large discrepancies between the FEM and RNM at high flux levels the apparent inductance used to compare the two models are analysed. Figure 3.27 displays two possible flux levels for a certain excitation current. The figure shows that even under high levels of saturation, the level of error in L is closely related to the error in ϕ and the apparent inductance is still a good measure to compare the two models. Reluctance paths that are not modelled, which become dominant under highly saturated conditions, might be one explanation for the large discrepancies. At this stage however the source of the discrepancies are not certain.

When an AMB is operated in the so-called differential mode[2] it is highly unlikely that both of the actuators will be in saturation at the same time. Furthermore all four coils will be used simultaneously to estimate the rotor position in the parameter estimation scheme which may then compensate for model shortcomings. For this reason further investigations into the mechanisms responsible for these discrepancies are not undertaken until their influence on the self-sensing scheme is established.

At this stage the mutual leakage RNM is optimised and satisfactory correlation is observed between FEM and RNM results. The choice of flux path in the mutual leakage RNM is therefore

[2]Two geometrically opposing actuators are driven symmetrically about some bias point

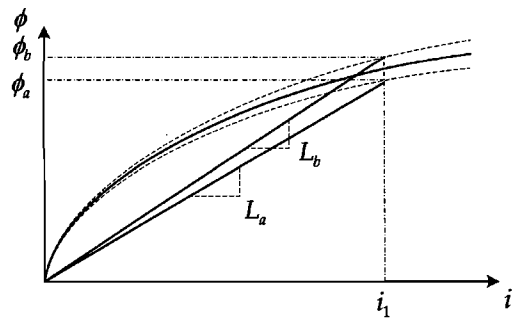

Figure 3.27: Nonlinear mutual leakage RNM FEM apparent inductance discrepancies

verified. The accuracy of the 40 node model as compared to the 80,000 nodes of the FEM is also illustrated.

3.7 Experimental verification (dc)

The next step in the refinement process is to verify the RNM results with experimental results. More specifically the dc response of the RNM is verified with measurements obtained with an RLC-meter. The rotor of the AMB system is clamped at various positions and the coil terminal impedance is measured. The lowest excitation frequency available on the RLC-meter (50 Hz) is used and measurements verified that the eddy current effects at this frequency may be neglected. The material relative permeability, for use in the RNM, was experimentally determined as $\mu_r = 1223$ for the low levels of excitation present in the measurements.

Figures 3.28, 3.29 and 3.30 display the RLC-meter measurements, the RNM results and the error between the results respectively. From figure 3.30 it can be seen that the maximum absolute percentage error of $\pm$ 5 % is observed with $x = 0$. Figure 3.31 therefore displays the absolute percentage error between the RLC-meter and RNM results for various y-axis positions within the backup bearing range with $x = 0$. From this result a maximum absolute percentage error of just above 7 % is observed.

The RNM and FEM results correlated extremely well under linear conditions which may be compared to low excitation conditions as those experienced during RLC-meter measurements. The measured and FEM results therefore also do not correlate better than 7 % which suggests that there must be uncertainty surrounding model parameters. Model parameters with uncertainty include: the material permeability and bearing dimensions (e.g. lamination stacking factor). The exact mechanism responsible for the remaining error between the RLC-meter and RNM results is not identified at this stage. The influence of the error on the self-sensing scheme will first be established to determine whether further investigations are warranted.

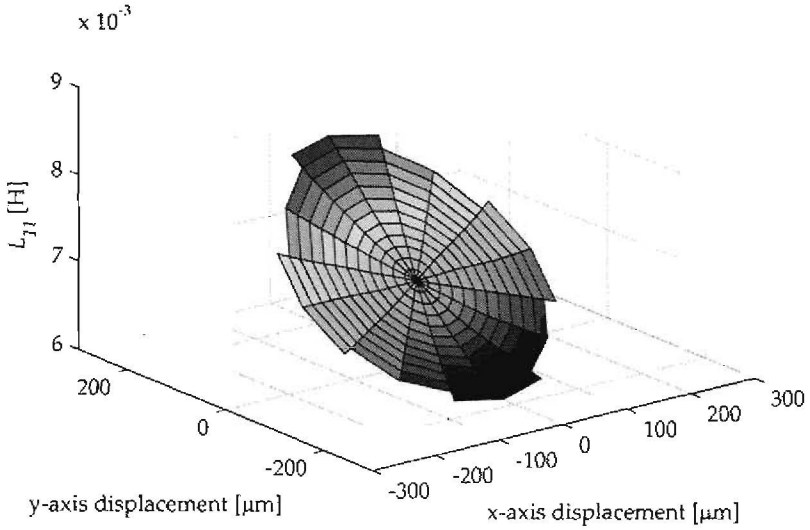

Figure 3.28: RLC-meter measurements of L_{11} at 50 Hz for various x and y-axis positions

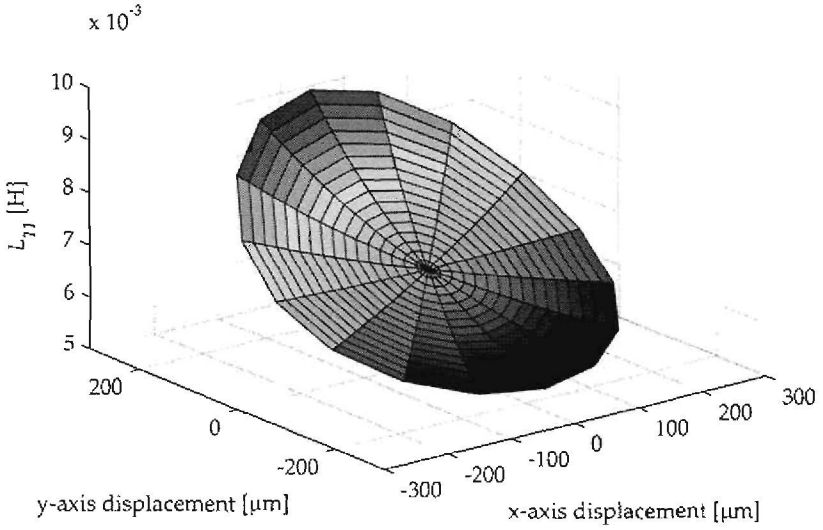

Figure 3.29: RNM results for L_{11} at various x and y-axis positions

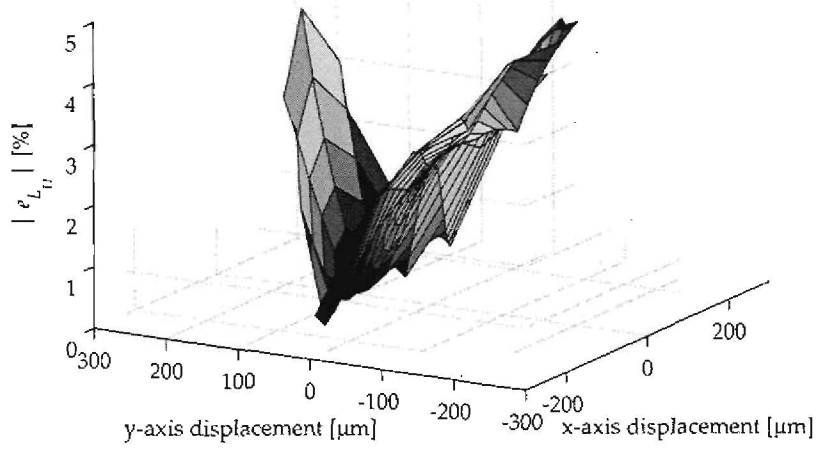

Figure 3.30: RLC-meter RNM L_{11} verification

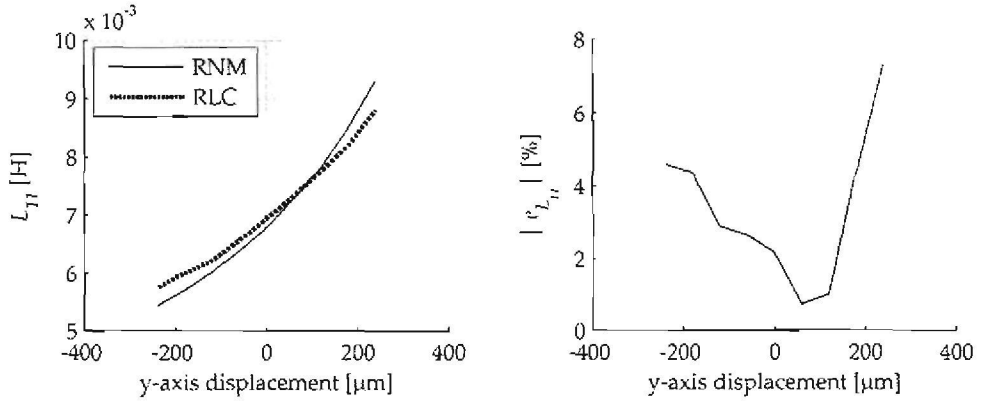

Figure 3.31: RLC-meter RNM L_{11} verification ($x = 0$)

3.8 Eddy current correction

All that remains now is to verify the RNM's ability to accurately predict the fundamental frequency impedance of the various coil terminals. The dominating mechanism responsible for the frequency dependency of the coil impedance is the eddy current effect. Eddy currents are induced in the lamination material due to varying magnetic flux which results in a reduction in inductance and an increase in the resistance observed at the terminals. As discussed in section 2.7 this effect can be modelled by either a rate dependent permeability term or a single turn secondary winding driving a chain of resistors and inductors. The present work utilises the rate dependent permeability term to obtain the bearing impedance at the switching frequency.

The complex material permeability can be obtained from (2.7) and is shown to be a function of the material dc permeability. The dc flux distribution must therefore first be established before the complex permeability term may be implemented. A flow diagram of the model is presented in figure 3.32 which includes the nonlinear saturation as well as eddy current correction.

As inputs the model receives the rotor position (x, y) and average coil currents (I_1 to I_4). It then uses the x and y coordinates to obtain accurate air gap reluctance values for each air gap from a lookup table. The air gap reluctances together with the average coil currents I_1 to I_4 are then used to obtain the fluxes in each leg of the RNM with initial material reluctance values. The new flux levels are then used to determine new relative material permeability ($\mu_0\mu_r$) values for each branch of the RNM and a process of iteration is followed until it converges to determine a working point. Once the problem has converged the flux levels are used to determine the incremental material permeability ($\mu_0\mu_{r\Delta}$) for each leg of the RNM from a lookup table. The incremental permeability terms are then used together with (2.7) to obtain complex permeability terms for each leg of the magnetic material. The complex inductance matrix is then determined from (3.48) making use of the complex permeability and can be used to determine the complex impedance with $\mathbf{Z} = j\omega\mathbf{L}$ where $\omega = 2\pi f_s$ and f_s is the switching frequency.

In the magnetic bearing it is very difficult to measure the flux in each leg of the bearing. The task of determining $\mu_0\mu_{r\Delta}$ is therefore not an easy one due to the complex hysteretic relationship between the magnetisation M and the magnetic field H. The relationship between M and H has been extensively studied in the past and many mathematical models have been developed to explain the hysteretic behaviour (e.g. [70], [71], [72], [73]). The goal of these studies was not only to predict losses but also to realise more accurate models of ferromagnetic materials which may be utilised in electromagnetic designs.

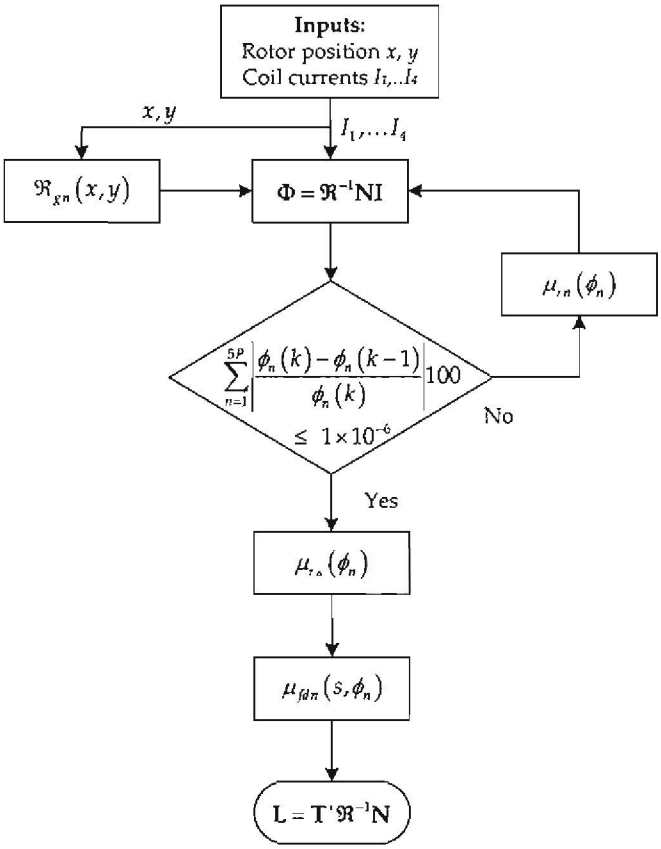

Figure 3.32: Nonlinear RNM flow diagram

The formation of the hysteresis loops can be attributed to different underlying physical mechanisms [74] which include: magnetisation rotation, domain wall motion and nucleation. In most materials these mechanisms are present at the same time in different proportions and are usually interdependent. This makes it extremely difficult to isolate the mechanisms and treat them one at a time [72].

Two popular models used to explain the dynamic behaviour of magnetisation are the Preisach and Jiles-Atherton models. The former is a mathematical description of the material behaviour [73] and the latter is based on modelling the frictional force which opposes the domain wall motion [70].

The Jiles-Atherton model presented in [70] does not model minor loops accurately, nor does it model frequency dependence and the model parameters are difficult to determine. Work was continued on this model to include minor loop behaviour and frequency dependence (e.g. [71]). In [75] an empirical model is presented which models the hysteresis by a nonlinear differential equation for the rate of change of M. This function depends directly on H and therefore the parameters can be determined directly from measured data. Research has also been conducted to realise models that reduce the computational burden [72] compared to the integral (e.g. Preisach) or differential (e.g. Jiles-Atherton) models.

The present work neglects hysteresis and makes use of the initial magnetisation curve which is obtained from the peak magnetisation data in the material data sheet. The initial magnetisation curve is used since the working point excursion closely correlates to that of the process used to obtain the experimental results. For practical application of the RNM in a self-sensing scheme it is however proposed to use the anhysteretic curve.

A modified Langevin equation can be used to describe the anhysteretic curve which is history independent and represents the skeleton of the hysteresis loop [70]. For isotropic material the anhysteretic curve may be expressed as:

$$M(H_e) = M_s \left(\coth \frac{H_e}{b} - \frac{b}{H_e} \right) \tag{3.54}$$

where M_s is the saturation magnetisation and b is a parameter with dimensions of magnetic field which characterises the shape of the anhysteretic magnetisation. H_e is the effective field which may be obtained from:

$$H_e = H + \beta M \tag{3.55}$$

where β is the mean field parameter representing the inter-domain coupling which must be obtained experimentally. H is the actual internal magnetic field experienced by the domain within the solid. The incremental relative permeability $\mu_{r\Delta}(H_e)$ can now be obtained by differentiating (3.54) with respect to the magnetic field H:

$$\frac{dM}{dH} = \frac{M_s[b^2 \sinh^2(H_e/b) - H_e^2]}{b(H_e^2 - \beta M_s b)\sinh^2(H_e/b) + \beta M_s H_e^2}. \tag{3.56}$$

The result of (3.56) can now be used to determine the incremental relative permeability as shown in (3.57) by remembering that $B = \mu_0(M + H)$.

$$\mu_{r\Delta} \approx \frac{1}{\mu_0}\frac{\partial B}{\partial H} = \frac{\partial M}{\partial H} + 1 \tag{3.57}$$

The magnetic flux density can be expressed as a function of the effective field H_e by substituting the magnetic field H of (3.55) and the magnetisation M of (3.54) into $B = \mu_0(M + H)$:

$$B = \mu_0 \left[H_e + M_s(1 - \beta) \left(\coth \frac{H_e}{b} - \frac{b}{H_e} \right) \right]. \tag{3.58}$$

The solution of (3.58) can now be obtained through iteration with either H_c or B as input. In order to obtain the anhysteretic curve for the material used in the experimental system, experimental measurements are taken. The measurement configuration shown in figure 3.33 is used to investigate the material behaviour and determine values for both the apparent and incremental material permeability terms. Figure 3.34 displays the resulting hysteresis curve for an excitation frequency of 50 Hz. The dashed line in the centre of the B-H envelope represents the anhysteretic curve as presented in [70]. Figure 3.35 displays the relative permeability μ_r and the incremental relative permeability $\mu_{r\Delta}$ as obtained from the data sheet and experimental measurements.

3.9 Experimental verification (ac)

Experimental results for the magnetic bearing coil impedance at the switching frequency are obtained by exciting the coil of pole pair 1 (PP_1) with a two-state switching power amplifier (PA). The resulting coil current and voltage waveforms are captured using a digital oscilloscope. The impedance is determined by performing a fast Fourier transform (FFT) analysis on the data and dividing the resulting fundamental voltage component with the corresponding current component.

The relative permeability μ_r obtained from the material data sheet and shown by the solid line in figure 3.35 is used in the RNM to realise the nonlinear material behaviour. The flux in each leg of the RNM is calculated and used to determine new reluctances in an iterative process. Once the RNM has converged to a solution the incremental relative permeability $\mu_{r\Delta}$ obtained from the data sheet and shown by the solid line in figure 3.35 is used together with the eddy current correction term (2.7) to obtain the rate dependent permeability and model the magnetic bearing coil impedance at the switching frequency.

Figure 3.36 displays the FFT analysis results together with the RNM results for pole pair 1 (PP_1) with an excitation current of $I_1 = 0$ A. The magnitude of the impedance is given by $|Z_{11}|$, the equivalent series resistance due to eddy currents by R_{e11} and the inductance of the coil by L_{11}. The maximum absolute percentage errors for these parameters are 20 %, 42 % and 33 % respectively. In figure 3.37 the excitation current is increased to $I_1 = 9$ A. The maximum absolute percentage errors for parameters Z_{11}, R_{e11} and L_{11} increases to 60 %, 58 % and 70 % respectively.

In previous sections the RNM is verified with a FEM model and dc measurements and good correlation is obtained between modelled and measured results. The large discrepancies between the measured and modelled results can therefore be attributed to the eddy current correction term in the RNM which is strongly dependent on the B-H curve working point that contains large uncertainty. In the following section the eddy current model is refined to obtain better correlation between modelled and measured results.

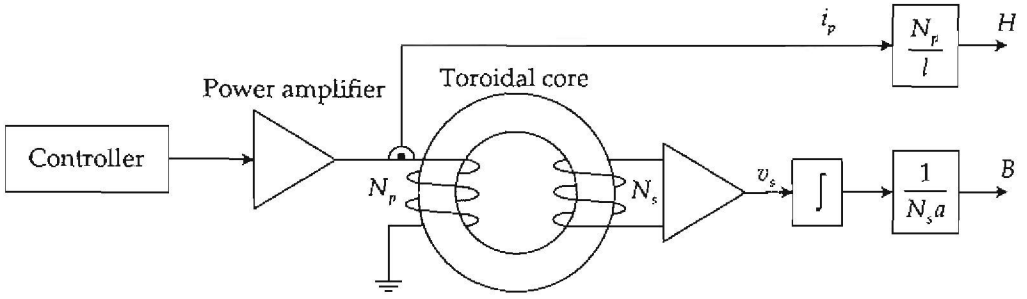

Figure 3.33: Material $B - H$ curve measurement configuration

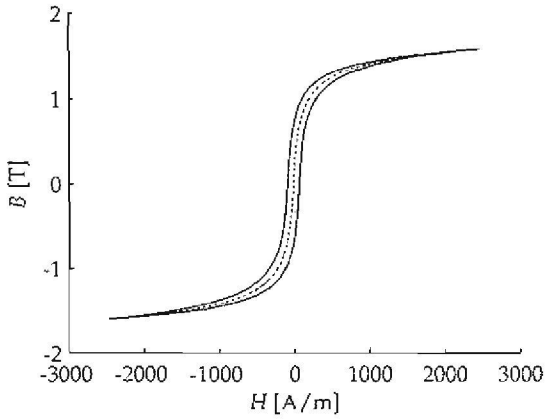

Figure 3.34: Magnetisation curve with hysteresis

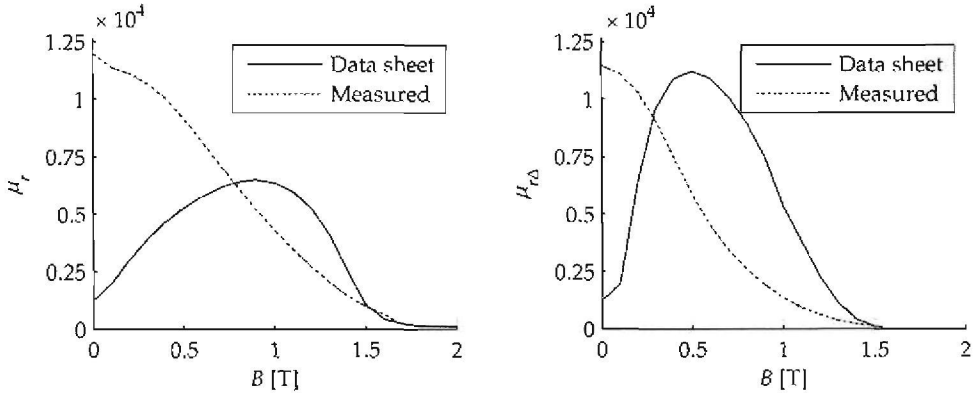

Figure 3.35: Incremental relative permeability

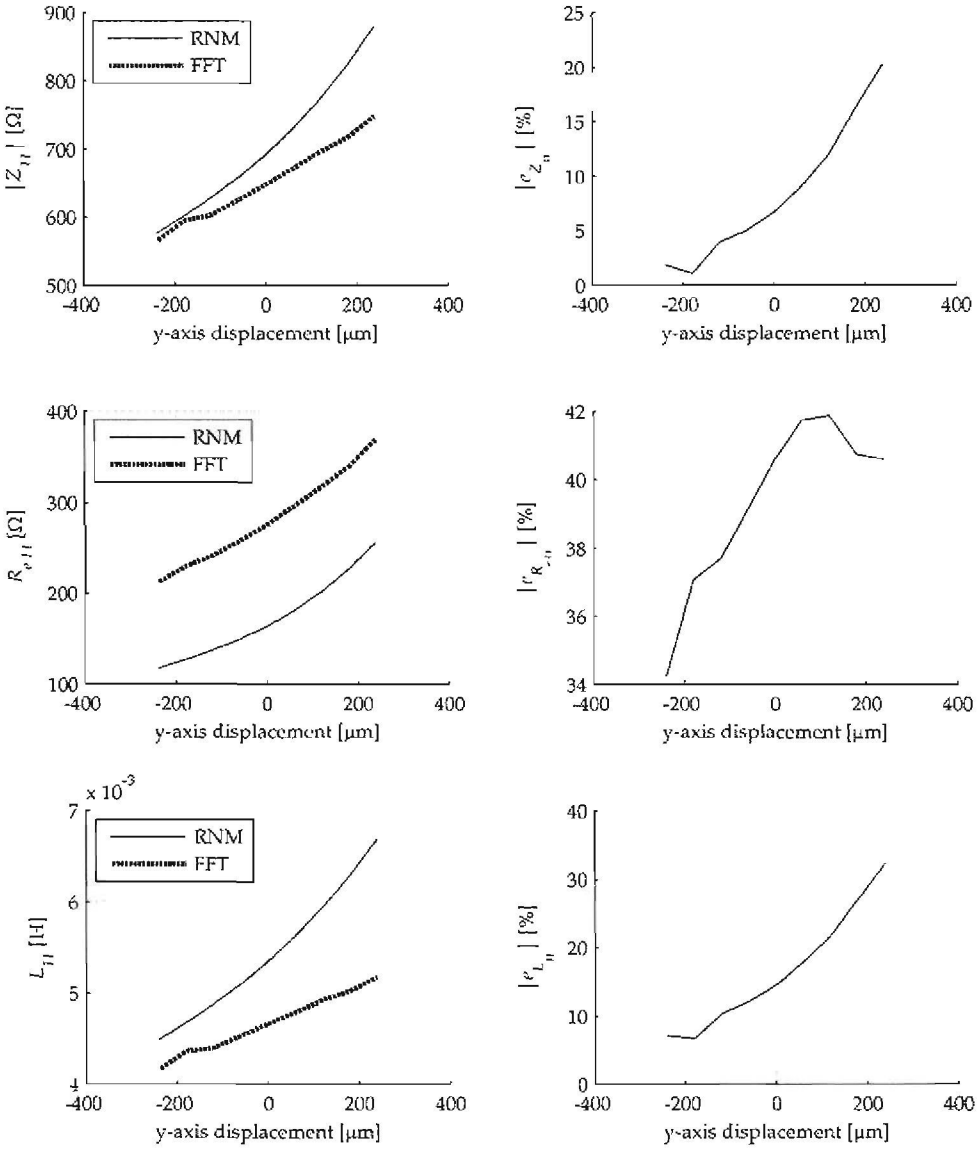

Figure 3.36: RNM FFT analysis verification (Z_{11}, R_{e11} and L_{11} for $I_1 = 0$ A)

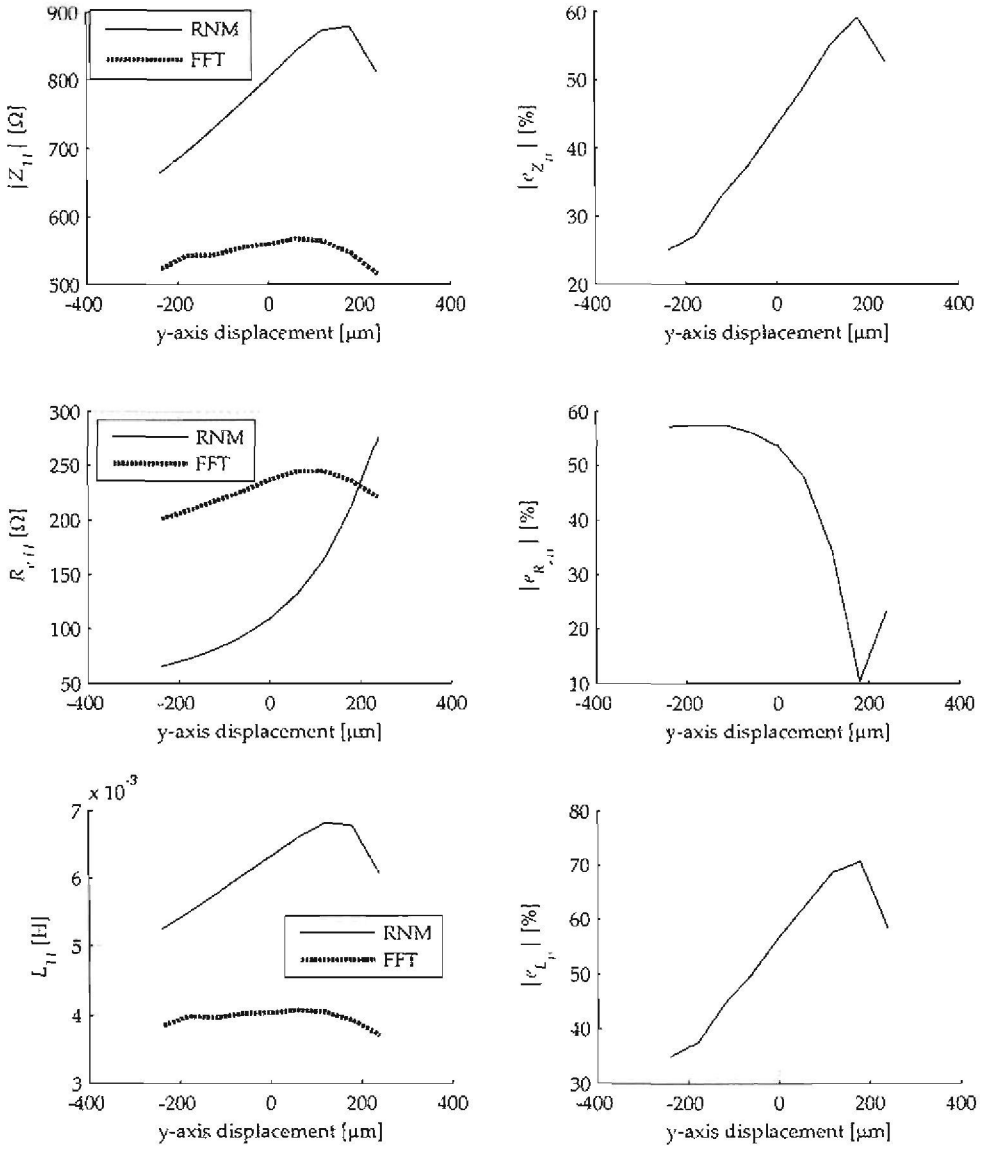

Figure 3.37: RNM FFT analysis verification (Z_{11}, R_{e11} and L_{11} for $I_1 = 9$ A)

3.10 Complex incremental permeability correction

The rate dependent permeability utilises the incremental permeability and an analytical expression to obtain a complex material permeability. The correlation between the switching frequency impedance of the RNM and the experimental measurements are poor and insufficient for self-sensing implementation. In order to improve the correlation considerable effort was taken to accurately characterise the BH-curve of the silicon iron laminations. This however did not improve the correlation. The discrepancies are caused by uncertainties regarding the incremental relative permeability $\mu_{r\Delta}$, the material resistivity ρ as well as the rate dependent permeability term.

An alternative approach to the modelling of the eddy currents is suggested in the present work where the complex permeability of the silicon iron laminations is experimentally determined. The complex material permeability which is a function of the flux levels in the model may then be incorporated into the RNM using a simple lookup table. A number of toroidal discs of the silicon lamination material are stacked and excited with a switching PA through a primary coil. Care is taken to ensure that the flux density excursion caused by the switching amplifier is the same as the excursion in the AMB system. This is accomplished by making use of the same switching frequency and ensuring that the $dB/dt = v/Na$ is the same for both configurations.

Figure 3.38 displays the experimentally determined magnitude and phase of the complex material permeability as a function of flux density. The magnitude and phase of the analytical complex material permeability is also included to illustrate the differences between the results. Large discrepancies between the modelled and measured results are observed in both the magnitude and phase for flux densities below 1.3 T.

Figure 3.39 displays the improved results when the experimentally determined complex permeability term is implemented in the RNM. The improved maximum absolute percentage errors for parameters Z_{11}, R_{e11} and L_{11} and an excitation current of $I_1 = 0$ A is 13 %, 17 % and 17 % respectively. When an excitation current of $I_1 = 9$ A is investigated the maximum absolute percentage errors for parameters Z_{11}, R_{e11} and L_{11} slightly increases to 22 %, 23 % and 22 % respectively. Table 3.8 contains a summary of the absolute percentage errors between the modelled and measured results and clearly highlights the improvement due to the experimentally determined complex permeability.

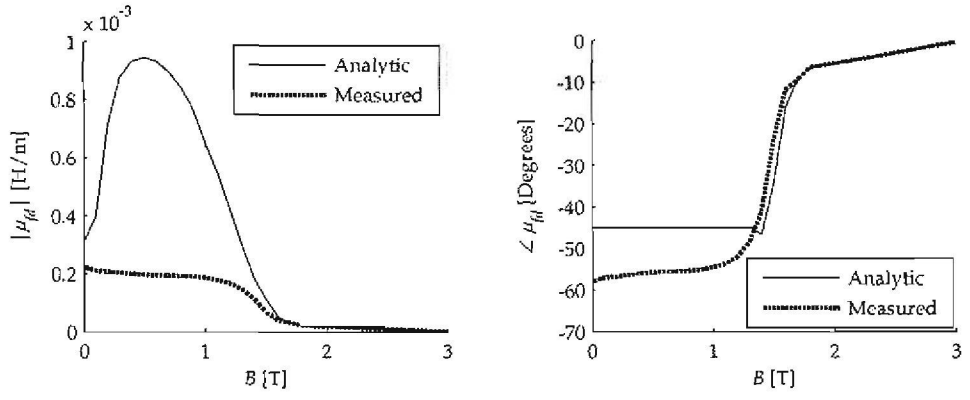

Figure 3.38: Measured and analytical results for complex material permeability μ_{fd}

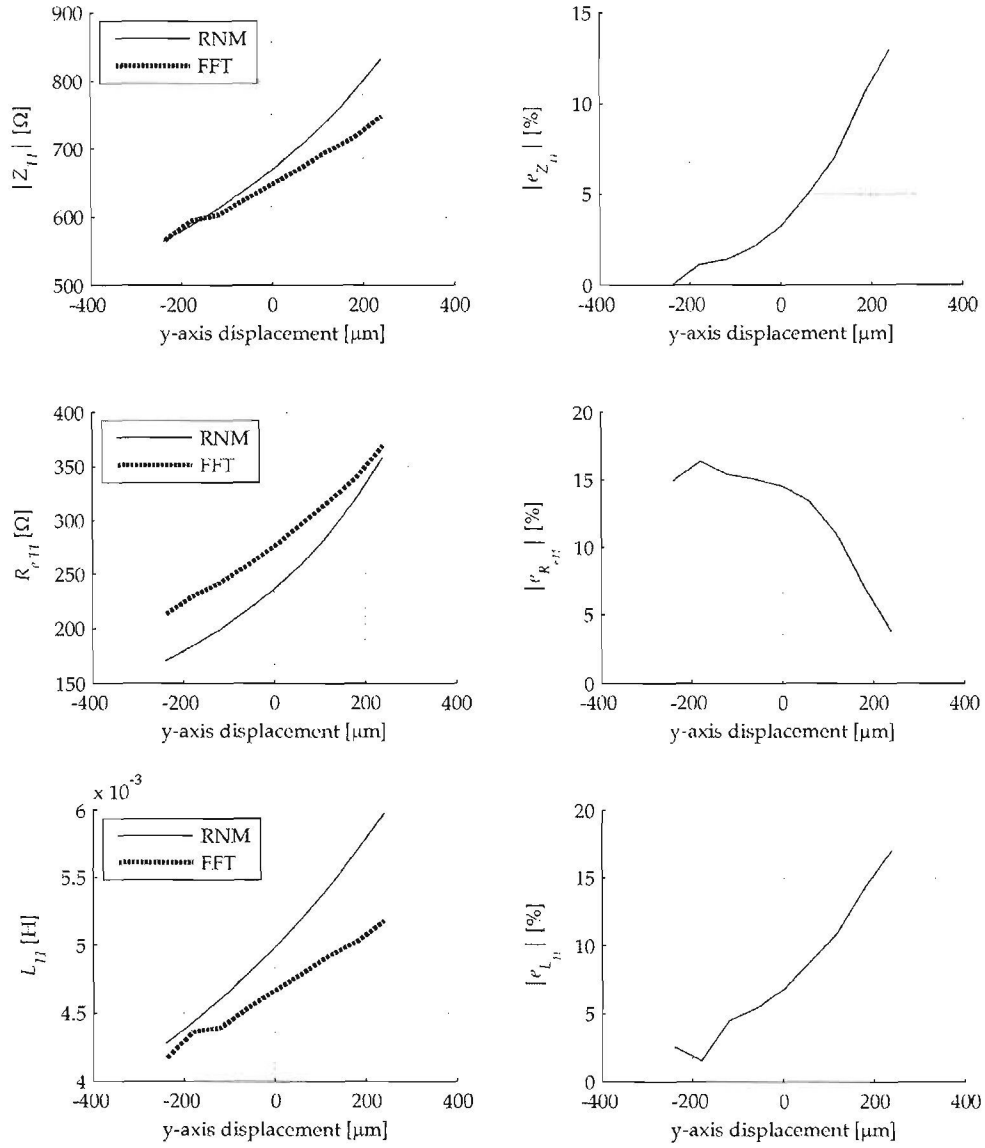

Figure 3.39: RNM FFT analysis verification (Z_{11}, R_{e11} and L_{11} for $I_1 = 0$ A)

Table 3.8: Summary of the modelling errors between the FFT and RNM results

I_1	$\lvert Z_{11} \rvert$	R_{e11}	L_{11}
Data sheet μ_r and $\mu_{r\Delta}$			
0 A	20 %	42 %	33 %
9 A	60 %	58 %	70 %
Data sheet μ_r and experimental μ_{fd}			
0 A	13 %	17 %	17 %
9 A	22 %	23 %	22 %

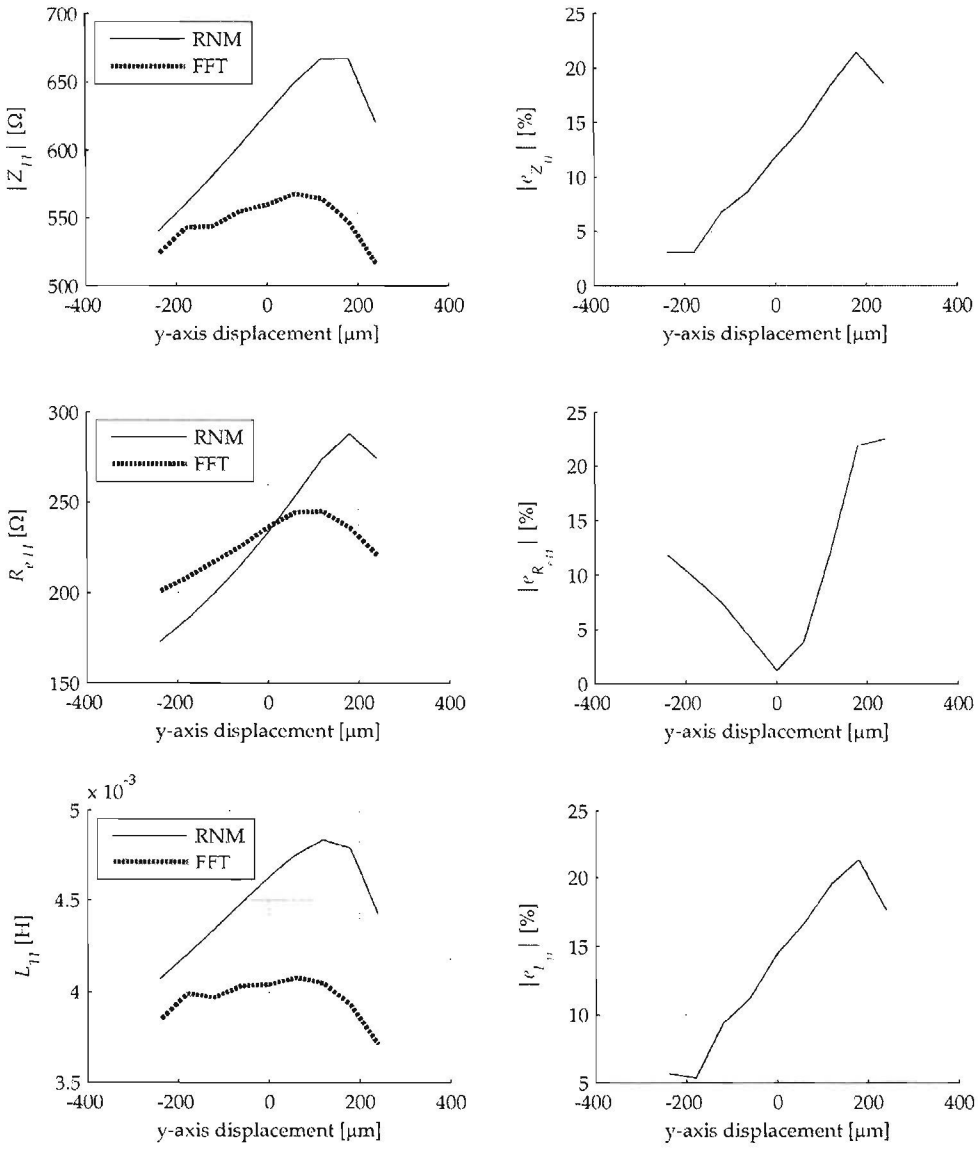

Figure 3.40: RNM FFT analysis verification (Z_{11}, R_{e11} and L_{11} for $I_1 = 9$ A)

The quest of chapter 3 is the development of a high fidelity active magnetic bearing model that is suitable for self-sensing implementation. The main focus of this chapter is the model refinement process which is used to identify and correct mechanisms that contribute to modelling uncertainty and error. A RNM is developed and it is established that a 40 node RNM can achieve high levels of accuracy when compared to an 80,000 node FEM analysis. The RNM is also verified with RLC-meter measurements and switching frequency impedance measurements. The novel approach to experimentally determine the complex material permeability as presented in this chapter is verified and shows improved correlation between modelled and measured results. The level of error due to each mechanism is also quantified and may be used in subsequent chapters to determine the effects of these errors on the self-sensing performance.

CHAPTER 4

Position estimation

Chapter 4 starts off with a discussion of the position estimation scheme which utilises a nonlinear observer based on the reluctance network model developed in the previous chapter. Next the parameter estimator is discussed in more detail. Issues such as amplitude and phase extraction as well as the effect of duty cycle variation on the output of the demodulation process are covered. The parameter estimator discussion is concluded with a stability analysis of the nonlinear observer. The simulation platform used to evaluate the position estimation performance is also presented. The chapter is concluded with position estimation results to demonstrate the basic functionality of the self-sensing scheme.

4.1 Position estimation scheme

In the present work the position of the levitated body is estimated from the first harmonic component of the current waveform. This is possible since the ripple amplitude is dependent on the bearing inductance which in turn is a function of rotor position. Unfortunately the ripple amplitude is not only dependent on the rotor position but is also influenced by power amplifier duty cycle variation and low frequency current components. To overcome these problems an inductor model of the magnetic bearing is utilised.

The switching frequency in the present work is chosen as low as possible since the sensitivity of the demodulated current to position variation decreases as the frequency of the switching waveform increases [4]. This phenomenon is mainly due to the increase in eddy currents as the frequency increases which in turn increases the magnetic material reluctance. The configuration therefore becomes less sensitive to a variation in the air gap reluctance. A frequency dependent model of the magnetic bearing was developed to investigate these effects and the model is presented in appendix A. The switching frequency for the present work is chosen just above the audible range: $f_s = 20$ kHz.

Before the position estimation discussion continues a few concepts are clarified. The first is the frequency translation of the inductor model. The reluctance network model (RNM) developed in the previous chapter only models the impedance at the switching frequency. When the 20 kHz impedance is extracted from the demodulated voltage and current waveforms the impedance varies with the rotor position which is much slower than the switching frequency. The model can now be solved at lower frequencies compared to a complete inductor model which must be solved at the switching frequency or higher. To clarify this concept figure 4.1 shows two equivalent systems. System (a) contains a complete inductor model which models both low and high frequencies. The output of the model is a current waveform which contains both control and sensing components. The current signal is then demodulated to extract the amplitude and phase

information at the first harmonic (switching frequency). System (b) contains a model for the low frequency response of the system only. The voltage signal is first demodulated to extract the amplitude and phase information at the switching frequency which serve as input to the model. The output of the model is a demodulated current signal which is equivalent to that of system (a).

Two possible configurations may be employed to accomplish position estimation by means of the inductor model. The first approach shown in figure 4.2 is known as the model inversion approach which was adopted in [4]. The inductor model is inverted and the demodulated voltage ($\underline{V}$) and current ($\underline{I}$) signals as well as an average current signal (i_{avg}) serve as inputs to the model which generates a position estimate ($\hat{x}$). Figure 4.3 shows the second approach; a nonlinear estimator based on the model as adopted in [32], [52]. In this approach the model receives as input the demodulated voltage ($\underline{V}$), average current (i_{avg}) and a position estimate ($\hat{x}$). The output is a demodulated current estimate ($\underline{\hat{I}}$) which is compared to the demodulated current ($\underline{I}$) to produce an error signal (e). The error signal is fed to a proportional-integral (PI) controller which generates a position estimate. The coupled RNM developed in the previous chapter is unfortunately not invertible and the parameter estimator approach is adopted. The estimator proposed in [32], [52] utilises a complete inductor model which models low and high frequencies. The complete inductor model must however be solved at higher frequencies than the switching frequency. This places constraints on the required processing bandwidth. In the present work a frequency shifted model is utilised which may be solved at much lower frequencies.

Figure 4.4 displays a schematic of the position estimation scheme as implemented in simulation. The amplitude and phase information of the first harmonic components of the magnetic bearing current and voltage waveforms are extracted. The average coil currents are used to determine the flux distribution in the RNM which models the nonlinear behaviour of the magnetic material. The inductance matrix is then used to determine the switching frequency impedance. The complex voltages are used together with the complex impedance to obtain estimates of the complex coil currents. The errors between the measured and modelled currents are then fed to PI controllers which yield estimates of the x, y rotor positions. For the self-sensing scheme proposed by the present work the x and y estimations are decoupled. When referring to figure 3.3 this implies that i_1 and i_3 are used to estimate y and i_2 and i_4 are used to estimate x. The self-sensing scheme is analysed and evaluated in simulation to demonstrate feasibility. The work that follows discusses each component of the position estimation scheme shown in figure 4.4.

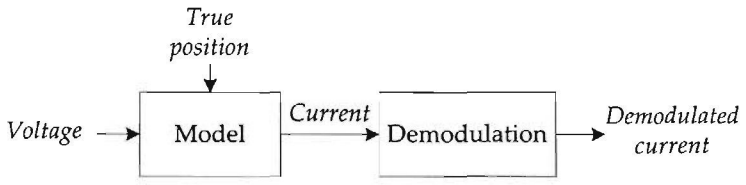

(a) Complete model

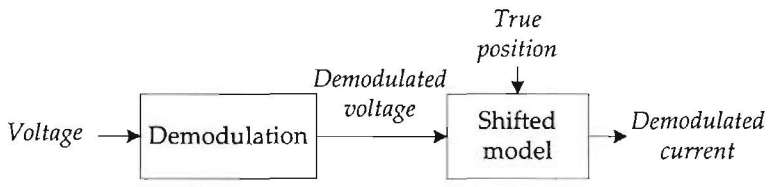

(b) Low frequency model

Figure 4.1: Model shifted in frequency [4]

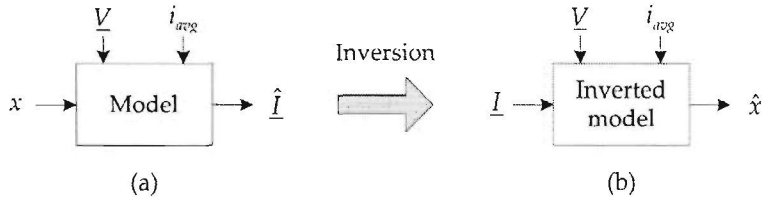

Figure 4.2: Model inversion [4]

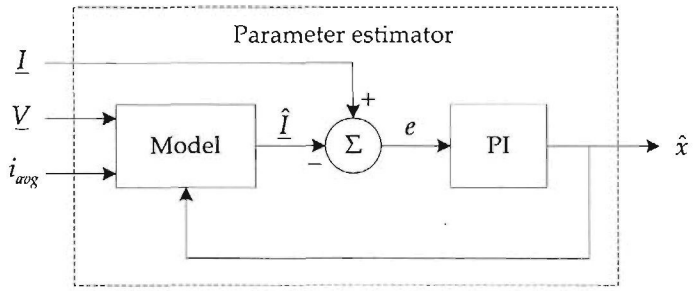

Figure 4.3: Parameter estimation [4]

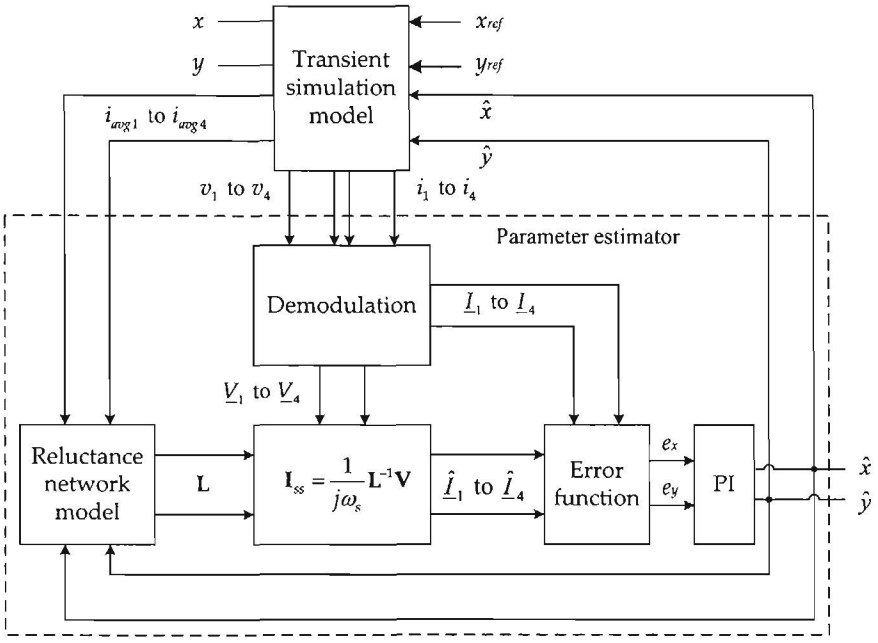

Figure 4.4: Position estimation scheme

4.2 Parameter estimator

The multiple input multiple output (MIMO) parameter estimator scheme displayed in figure 4.4 is developed in the subsequent sections. The process entails the choice of error function, choice of demodulation process as well as establishing boundaries for the PI controller parameters.

In a thorough analysis a state space model of the AMB system can be developed, which includes all nonlinear phenomena. The model will then facilitate the analysis of the proposed MIMO self-sensing scheme with established methodologies e.g. μ-synthesis to optimise estimator performance. The development of a state space model for the system is however a fundamental challenge due to the nonlinear nature of the system.

In the present work a much simpler approach is adopted. The complex coupled system is simplified by assuming that each pole pair may be analysed on its own without being influenced by the other pole pairs. Also, as a first approach, the estimation of the x and y positions are decoupled and only the amplitude information of the coil current and voltage waveforms is used.

The first step then is to establish a linear relationship between the coil voltage and current waveforms which describes the simplified actuator. Next, a demodulation process is chosen and a transfer function is derived for use in the stability analysis. The effect of duty cycle variation must also be investigated and described in a suitable manner for use in the stability analysis.

The final step in the parameter estimator development process is the establishment of boundaries for the PI controller parameters with a suitable stability analysis technique. The technique will utilise the linear model of the simplified actuator together with the transfer function of the demodulation process and the description of the duty cycle effect.

4.2.1 General approach

In order to simplify the analysis of the parameter estimator the coupled network is ignored for now and each pole pair is treated as an isolated actuator. The simplified actuator can then be represented by figure 2.2. The relationship between the voltage, current and position is given by (2.3). In the present work the rotor position can be assumed constant at the switching frequency and the $\frac{dx}{dt}$ term in (2.3) may be ignored. Substituting s with $(g_0 \pm x)$ and applying the Laplace transform yields:

$$V(\mathrm{s}) = \mu_0 N^2 a \frac{1}{2(g_0 \pm x) + \frac{l}{\mu_r}} \mathrm{s}I(\mathrm{s}) + I(\mathrm{s})R \tag{4.1}$$

By applying the principle of superposition (4.1) can be expressed in phasor form at the switching frequency ω_s as follows:

$$\underline{V} = \mu_0 N^2 a \frac{1}{2(g_0 \pm x) + \frac{l}{\mu_r}} (\mathrm{j}\omega_s)\underline{I} + \underline{I}R \tag{4.2}$$

Since the coil resistance is small compared to the coil reactance at the switching frequency it may be ignored. Assuming that the amplitude and phase extraction is ideal and neglecting core reluctance, an estimate of the demodulated current is given by:

$$\hat{\underline{I}} = \frac{1}{\mathrm{j}\omega_s} \frac{2(g_0 \pm \hat{x})}{\mu_0 N^2 a} \underline{V} \tag{4.3}$$

As a first approach only the amplitude of the demodulated current estimate is compared to the actual demodulated current amplitude and the error used to update the position estimate $\hat{x}$. Mathematically this is represented by:

$$x^* = \arg\min_{\hat{x}} \left(|\underline{I}| - |\hat{\underline{I}}(\hat{x})| \right) \quad \text{with} \quad \hat{x} \in [x_{min}, x_{max}] \tag{4.4}$$

where x_{min} and x_{max} are determined by the backup bearing clearance. The position estimation updates the air gap length which is a parameter of the system, hence the name; *parameter estimation*. More specifically this approach may be called a primitive adaptive system [32], [76]. Self-optimising (adaptive) control can be divided into two parts. Firstly it provides the system with a means of continuously monitoring its own performance as compared to an index of performance (IP) or optimum condition. Secondly the system is provided with a means of adjusting its own parameters in closed-loop to drive the actual performance towards the desired performance [76].

The simplified structure of the estimator for a single degree of freedom is shown in figure 4.5. In the present work coils are configured in differential mode and the top and bottom air gaps are given by $(g_0 - x)$ and $(g_0 + x)$ respectively. Since both air gaps are influenced by the same change in rotor position x, it is possible to improve linearity and signal to noise ratios of the estimated position signal by using information from both coil current waveforms. This configuration may also alleviate the problem of magnetic saturation.

The demodulated current amplitudes $|\underline{I}_2|$ and $|\underline{I}_4|$ from the two opposing actuators are subtracted from each other which eliminates the nominal air gap g_0 and is already a signal that may be used as position error. Unfortunately the signal is not only a function of rotor position but also duty cycle, magnetic saturation, etc. Therefore the voltage signals are demodulated and fed to a frequency shifted model which yields demodulated current amplitude estimates $|\hat{\underline{I}}_2|$ and $|\hat{\underline{I}}_4|$. Again the two demodulated current amplitude estimates are subtracted from each other. The estimated displacement signal $\hat{u}$ is then subtracted from the true displacement signal u to produce an error e. The error serves as input to the PI controller which in turn generates the position estimate $\hat{x}$ that is used in the frequency shifted model. The position estimate is adjusted until the difference in true and estimated demodulated coil currents are identical. The accuracy of the position estimate is therefore a function of the accuracy of the model. The working point dependency of the model is included by feeding the average currents i_{avg2} and i_{avg4} to the respective models.

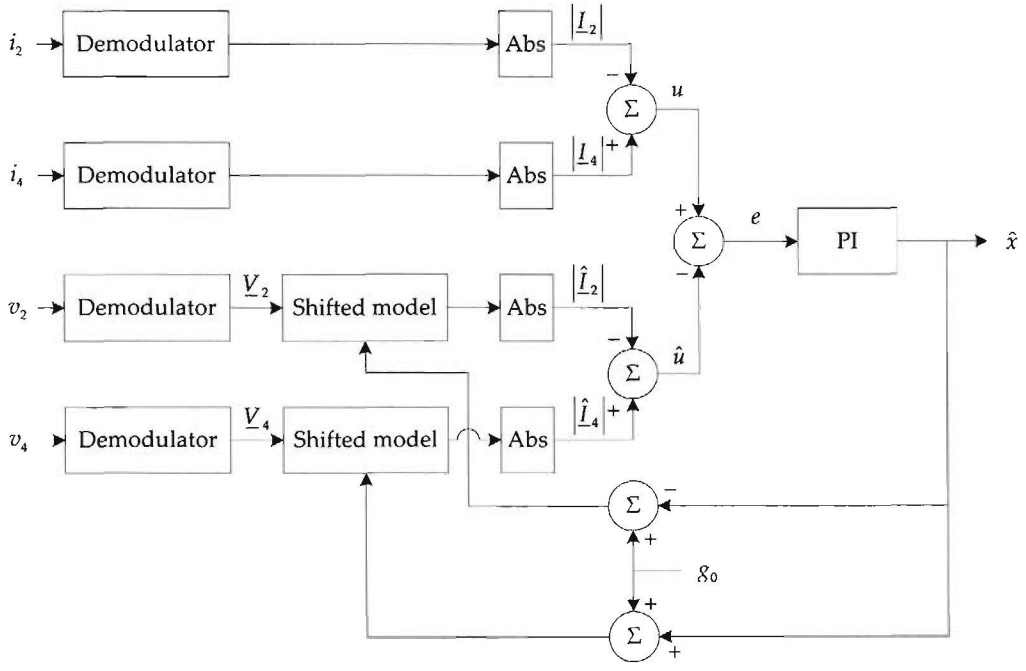

Figure 4.5: Estimator schematic for a single degree of freedom (x-axis)

4.2.2 Demodulation

The amplitude and phase information of the current and voltage waveforms is extracted by means of a fast Fourier transform (FFT). The amplitude and phase spectra provide a complementary method of representing a time varying waveform which provides more useful information about the frequency content of the waveform. As discussed earlier a frequency shifted model will be used and therefore only the amplitude and phase information of the first harmonic is of importance. Figure 4.6 shows the schematic of the demodulation process incorporating an FFT. The sampled data is first windowed and detrended where after the FFT is computed. Only the first harmonic (switching frequency) information is extracted and passed on.

In order to motivate the window size and rate at which the FFT is performed, a few pitfalls regarding the FFT process is discussed. Four pitfalls are identified in [77] and they are:

- **Sampling rate and aliasing** - Aliasing refers to the spurious low frequency components caused by inadequate anti-aliasing filtering and too low sampling rate. Before a signal is sampled it must be passed through an anti-aliasing filter to limit its highest frequency to half the sampling frequency. The anti-aliasing filter pass-band is therefore determined by the sampling rate and the stop-band attenuation is determined by the resolution of the analogue to digital converter.

- **Scalloping loss or picket-fence effect** - A discrete Fourier transform generates regularly spaced harmonic amplitude and phase components. The spacing between the components are influenced by the length of the sampled waveform. A signal that falls between two adjacent harmonic frequency components in the spectrum can therefore not be properly represented. The signal energy is shared by the two adjacent harmonics and the nearby spectral amplitude will be distorted. The problem can be solved by adding augmenting zeros to the data, thereby rearranging harmonic components to be more closely spaced and coincide with signal frequencies. Scalloping loss is defined as the maximum reduction in processing gain which occurs mid-way between the harmonically related frequencies.

- **Trend removal** - A trend in a time series can be defined as a slow or gradual change in some property of the series over the entire interval under consideration. Trend removal or detrending is therefore a statistical or mathematical process of removing the trend from the series. Detrending is conducted prior to spectrum computation to eliminate the trend from the data in order to avoid large errors in the estimated spectrum.

- **Spectral leakage and spectral smearing** - When an FFT is computed on a set of sampled data it is not the same as the true FFT of the continuous process. The reason for this is that the sampled data is truncated at the beginning and end, a phenomenon known as windowing. The computed spectrum is therefore the true spectrum convoluted with that of the window function. The spectrum of a rectangular pulse window is given by the sinc function and consists of a main lobe and an infinite number of side lobes. Each signal component is now convoluted with the sinc function, and so the amplitude spectrum of the signal will be distorted by the addition and subtraction of the large number of window side lobes and main lobes. This may introduce spurious peaks or conceal true peaks in the spectrum and the phenomenon is known as spectral leakage. The spectral leakage may be minimised by

Figure 4.6: Demodulator schematic

choosing the window function to minimise side lobe levels. Unfortunately this increases the main lobe width causing it to spread to adjacent side lobes. This aliases the side lobes and is repeated at each harmonic frequency. The overall effect is an aliasing of the signal spectrum which is known as smearing. A careful choice of windows and their parameters is therefore needed to strike the optimum balance between statistical accuracy and frequency resolution of the estimate.

The sampling rate in the present work is chosen as 1 MHz which corresponds to the maximum sampling rate which is practically realisable. No aliasing filters are required in the simulation environment since the sampling is synchronised with the power amplifier switching and no noise is present. The window size is chosen to ensure that the 20 kHz component exactly coincides with one of the regularly spaced harmonic amplitude and phase components of the FFT. Detrending is implemented in order to avoid large errors in the estimated spectrum. This is accomplished by computing the least-squares fit of a straight line to the data and subtracts the resulting function from the data.

In the present work there are low frequency components, typically below 1 kHz and high frequency components (switching frequency). Since only the switching frequency amplitude and phase information is of importance the window width must be chosen to ensure that the side lobes of the sinc function attenuates to a level where the two frequencies do not influence each other. Figure 4.7 displays the rectangular pulse (window) in the time domain and the corresponding Fourier transform. It is clear that the window has a limited bandwidth in the frequency domain which is determined by its width in the time domain. The frequency bandwidth of the signal is therefore inversely proportional to the time duration of the signal [78].

From figure 4.7 it is clear that a narrow window will deliver the best bandwidth results, whereas a wider window will result in a more accurate spectral estimate. A trade-off therefore exists between the accuracy of the spectral estimate and the bandwidth of the signal. In the present work the optimum window width was found to be four periods of the switching frequency. This results in adequate spectral accuracy and a -3 dB cutoff frequency of 2 kHz. A rectangular window is used to ensure that the spectral amplitude information is accurate and with the choice of window width there is also minimal spectral leakage.

A transfer function for the demodulation process must now be established. The windowing effect may be modelled by the sinc function or alternatively by a sampler and zero-order hold. The FFT is also computed at a fixed rate and this implies that a second sampler and zero-order hold must be included in the transfer function. Figure 4.8 shows the representation of the demodulator with two sampler and zero-order holds in cascade.

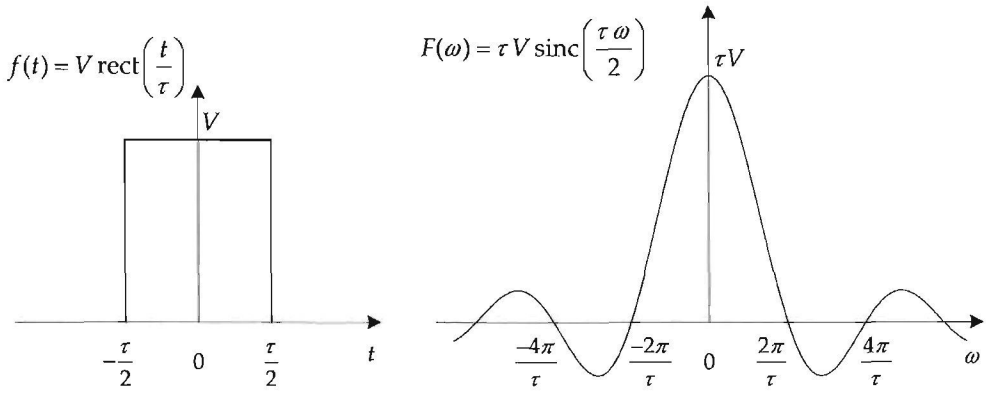

Figure 4.7: A rectangular pulse and its Fourier transform [78]

Figure 4.8: Representation of the demodulator

A sampler and zero-order hold can be represented by the following transfer function [78]:

$$G_{ho} = \frac{1}{T}\frac{1-e^{-Ts}}{s} \tag{4.5}$$

with T the sampling time. The demodulation process which models the effect of the process on the modulated signal is obtained from:

$$F(s) = \frac{1}{T_1}\left(\frac{1-e^{-T_1 s}}{s}\right)\frac{1}{T_2}\left(\frac{1-e^{-T_2 s}}{s}\right) \tag{4.6}$$

with T_1 the width of the window and T_2 the period at which the FFT is performed.

In order to verify the transfer function its frequency response is compared to the frequency response of a simulation of the demodulation process. For the analysis the position is assumed to vary sinusoidally which modulates the switching frequency component's amplitude. The input to the demodulator shown in figure 4.6 is therefore given by: $i_2 = A_1 \sin(\omega_x t) A_2 \sin(\omega_s t)$. A_1 and A_2 are the amplitudes of the modulating and carrier signals respectively. Next the frequency of the modulating signal ω_x is varied from very low frequencies up to the switching frequency. The output of the demodulator should ideally be $\underline{I_2} = A_1 \sin(\omega_x t)$. The windowing and fixed implementation frequency of the FFT process however introduces attenuation and phase shift at higher frequencies. An FFT is performed on the output of the demodulator to obtain the amplitude and phase information of the frequency component of interest. This information can now be compared to that of the input signal. The length of the input signal is chosen carefully to ensure that the input signal's frequency coincides with a harmonic component of the FFT and to ensure adequate accuracy of the spectral estimate.

The frequency response of the demodulator simulation with the modulated signal as input and the modulating signal as output, is shown in figure 4.9. The frequency response of the proposed model (4.6) is also included, revealing remarkable correlation with the simulated demodulator. The results are for a window width of 200 µs (5 kHz) and the FFT is performed at a frequency of 20 kHz which translates to an overlap of 75 %. The frequency at which the FFT is performed is chosen to ensure that the frequency response of the demodulation process is dominated by the windowing effects. When data is windowed with a window that is optimised to minimise the side lobes, the data is tapered to zero at the beginning and end of the window. If an event of short duration is situated in the tapered region the information may be lost. Overlap processing of 50 % to 75 % provides up to 90 % of the possible performance improvement for most weighting functions [77] which implies that most of the signal's frequency content stays intact. For the present work overlap processing is not a prerequisite since only the fundamental frequency is of interest but the FFT must be computed at a frequency high enough to ensure adequate bandwidth results.

4.2.3 PWM amplifier harmonic analysis

The amplitude and phase information of the first harmonic is a function of duty cycle. In order to investigate the relation between duty cycle and fundamental amplitude a harmonic analysis is conducted. Under the assumption that the duty cycle variation is much slower than the switching frequency ω_s the voltage V can be approximated by the trigonometric form of the Fourier series as:

$$V(t) = a_0 + \sum_{k=1}^{\infty}\left(a_k \cos(k\omega_s t) + b_k \sin(k\omega_s t)\right) \tag{4.7}$$

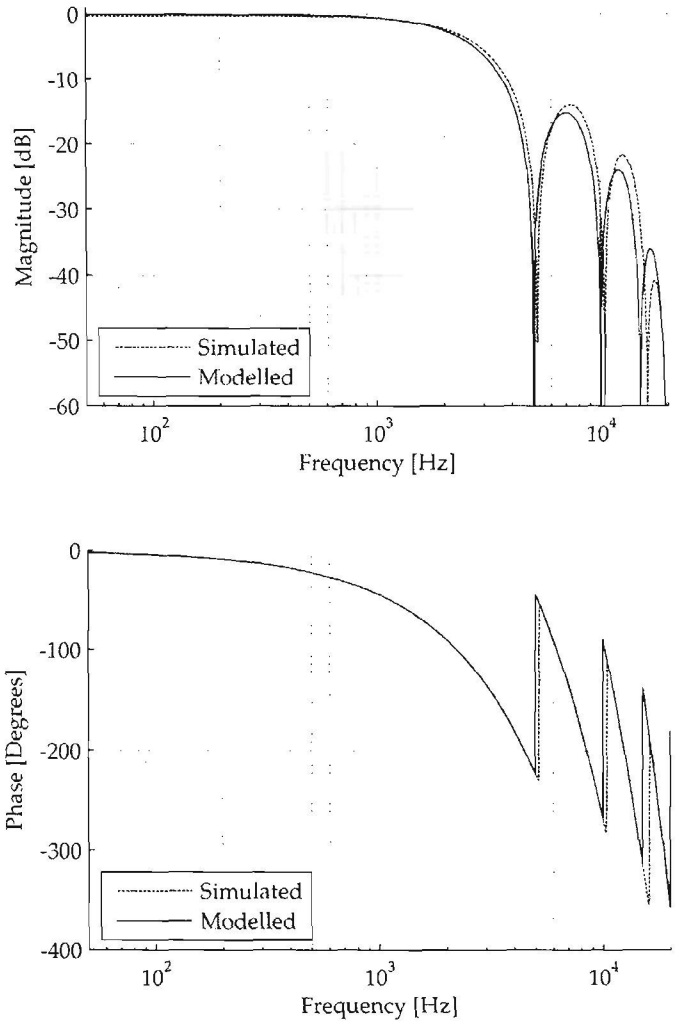

Figure 4.9: Simulated and modelled frequency response of the demodulation process

with

$$a_k = \frac{2}{T_s}\int_0^{T_s} V(t)\cos(k\omega_s t)dt \tag{4.8}$$

and

$$b_k = \frac{2}{T_s}\int_0^{T_s} V(t)\sin(k\omega_s t)dt. \tag{4.9}$$

In the present work only the first harmonic or fundamental frequency (switching frequency ω_s) is considered. The resulting coil voltage waveform for a single switching cycle is shown in figure 4.10 with α the duty cycle and $T_s = 2\pi/\omega_s$.

The low frequency term in (4.7) is obtained by determining the average over one switching cycle:

$$\begin{aligned} a_0 &= \frac{1}{T_s}\int_0^{\alpha T_s} V_p\, dt - \frac{1}{T_s}\int_{\alpha T_s}^{T_s} V_p\, dt \\ &= V_p(2\alpha - 1) \end{aligned} \tag{4.10}$$

Remembering that $\omega_s = 2\pi/T_s$, a_1 is now obtained from (4.8) by:

$$\begin{aligned} a_1 &= \frac{2}{T_s}\int_0^{\alpha T_s} V(t)\cos(\omega_s t)dt + \frac{2}{T_s}\int_{\alpha T_s}^{T_s} V(t)\cos(\omega_s t)dt \\ &= \frac{2V_p}{T_s\omega_s}\left[\sin\omega_s t|_0^{\alpha T_s} - \sin\omega_s t|_{\alpha T_s}^{T_s}\right] \\ &= \frac{2V_p}{\pi}\sin(2\pi\alpha) \end{aligned} \tag{4.11}$$

In the same fashion b_1 is obtained from (4.9) by:

$$\begin{aligned} b_1 &= \frac{2}{T_s}\int_0^{\alpha T_s} V(t)\sin(\omega_s t)dt + \frac{2}{T_s}\int_{\alpha T_s}^{T_s} V(t)\sin(\omega_s t)dt \\ &= \frac{2V_p}{T_s\omega_s}\left[-\cos\omega_s t|_0^{\alpha T_s} + \cos\omega_s t|_{\alpha T_s}^{T_s}\right] \\ &= \frac{2V_p}{\pi}\left[1 - \cos(2\pi\alpha)\right] \end{aligned} \tag{4.12}$$

The fundamental amplitude of the voltage waveform which is applied to the magnetic bearing coil is clearly a function of duty cycle. This relationship is obtained from:

$$\begin{aligned} |\underline{V}| &= \sqrt{a_1^2 + b_1^2} \\ &= \frac{2V_p}{\pi}\sqrt{\sin^2(2\pi\alpha) + (1 - \cos(2\pi\alpha))^2} \\ &= \frac{4V_p}{\pi}\sin(\pi\alpha) \end{aligned} \tag{4.13}$$

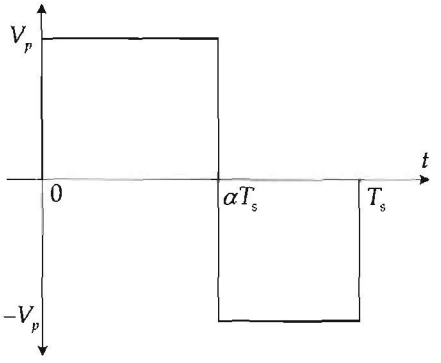

Figure 4.10: Coil voltage waveform for one switching cycle

Figure 4.11 shows the first harmonic component of the voltage waveform as a function of duty cycle. The duty cycle is restricted to $0.25 \leq \alpha \leq 0.75$ which will ensure that the fundamental amplitude does not decrease below $1/\sqrt{2}$ of the maximum amplitude.

4.2.4 Estimator stability

In order to establish a simplified block diagram of the estimator, the relationship between demodulated current and duty cycle must first be established. The relationship between the amplitude of the fundamental component voltage and the duty cycle is determined in the previous section in (4.13). A constant K which relates the output of the demodulator to the position x is now derived. Using (4.3) and (4.13) the output of the demodulator is obtained from:

$$\begin{aligned} |\hat{\underline{I}}| &= \frac{1}{\omega_s} \frac{2(g_0 \pm x)}{\mu_0 N^2 a} \frac{4V_p}{\pi} \sin(\pi\alpha) \\ &= K(g_0 \pm x) \end{aligned} \tag{4.14}$$

with

$$K = \frac{4V_p}{\pi^2 f_s \mu_0 N^2 a} \sin(\pi\alpha) \tag{4.15}$$

The duty cycle effect is treated as a nonlinear time-varying gain K that satisfies:

$$K_{min} \leq K \leq K_{max} \tag{4.16}$$

With $\alpha = 0.5$, $K = K_{max}$ can be obtained from:

$$K_{max} = \frac{4V_p}{\pi^2 f_s \mu_0 N^2 a} . \tag{4.17}$$

The minimum gain occurs when the duty cycle varies the most from 50 %, i.e. 25 % or 75 %. K_{min} can be obtained from:

$$K_{min} = \frac{4V_p}{\pi^2 f_s \mu_0 N^2 a} \frac{1}{\sqrt{2}} \tag{4.18}$$

By combining (4.6) and (4.14) the output of the demodulation process is obtained as:

$$|\hat{\underline{I}}| = KF(s)(g_0 \pm X) \tag{4.19}$$

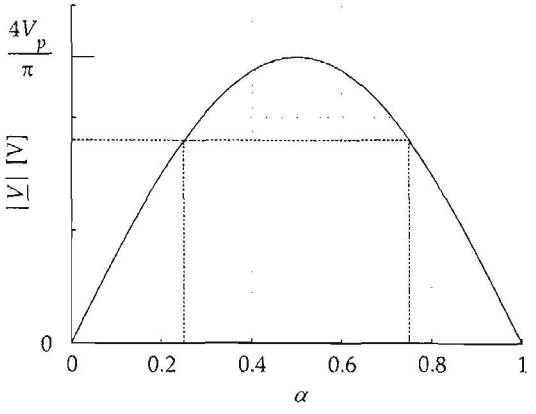

Figure 4.11: First harmonic amplitude as a function of duty cycle

to the switching frequency. The model is however not able to accurately predict the coil impedance beyond this point.

The equivalent series reactance displayed in figure A.5 also shows good correlation between the modelled and measured results for frequencies up to the switching frequency. Beyond this point however large discrepancies are observed between the predicted and experimental results. It is also important to note the absence of the resonant point in the modelled data which is visible in the experimental data in both figures A.4 and A.5.

From the absence of the resonant point in the predicted data it is clear that the capacitance must be included. Figure A.6 displays the predicted and experimental results for the equivalent series resistance with the parasitic capacitance included. The resonant point is now also visible in the modelled results and the correlation between modelled and measured results show marked improvement at high frequencies. This is also visible in the equivalent series reactance results shown in figure A.7. The resonant point is predicted within 27 % of the measured value which implies that either or both the core model and the parasitic capacitance model contain uncertainty.

A.5 Conclusions

A frequency dependent model for heteropolar magnetic bearings is presented which includes an analytical model for the parasitic winding capacitance. The parasitic capacitance is assumed constant and in parallel with an equivalent series resistance and reactance. The equivalent series resistance and reactance values are obtained from a coupled RNM which realises the frequency dependency with a rate dependent complex material permeability term. Results show marked improvement for high frequencies when the parasitic capacitance is included in the model.

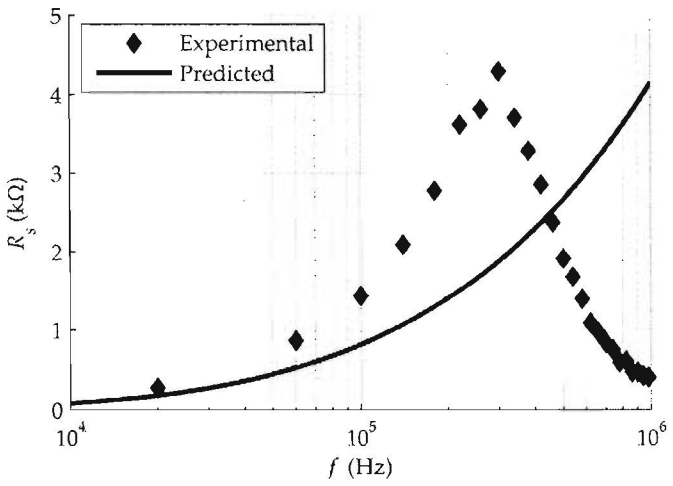

Figure A.4: Experimental and predicted series resistance (C excluded)

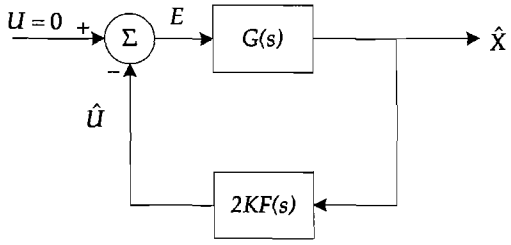

Figure 4.13: Block diagram for circle criterion

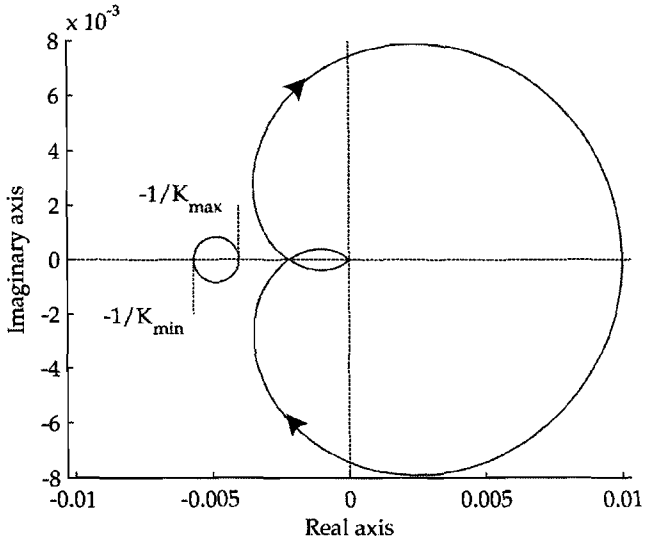

Figure 4.14: The $2G(j\omega)F(j\omega)$-locus and disk $D(K_{min}, K_{max})$

The circle criterion results in the worst case boundary as shown in [32]. The black dot in figure 4.15 represents the gains used in the simulations ($K_p = 3 \times 10^{-3}$ and $K_i = 30$).

4.3 Transient simulation model

A high fidelity model of the magnetic bearing has been realised in chapter 3. The model is incorporated into a nonlinear parameter estimator based self-sensing scheme as discussed in the previous sections. The next step is to establish a platform with which the self-sensing scheme may be evaluated and the stability of the position estimation scheme may be analysed. The present work will establish a high fidelity transient simulation model (TSM) of the physical system which will serve as verification platform. The TSM accurately models saturation effects, hysteresis and eddy current effects. A network based model is used to include cross-coupling effects.

A flow diagram of the TSM execution is shown in figure 4.16. The model receives as input position references for both the x and y-axis. These are compared to the true rotor position to generate the error signals for the PD position controllers. Each axis is controlled separately in the so-called differential mode. The position controllers generate four current reference signals which serve as input to the power amplifier stage. The power amplifiers are voltage mode current controlled amplifiers with a small signal bandwidth of 2.5 kHz. The amplifiers generate appropriate voltage signals that are applied to the magnetic model. The magnetic model determines the four bearing coil currents as well as the fluxes in each leg of the magnetic bearing. The current signals are fed back to the power amplifier stage for current control. The fluxes are used to determine the resulting force on the rotor in both the x and y direction. The two forces are applied to a point mass model of the rotor which models the movement of the rotor. A detailed discussion of the TSM is presented in appendix C as well as verification of the TSM with experimental measurements.

Figure 4.17 displays a voltage signal generated by the power amplifier stage and the resulting current waveform. The abrupt change in the current waveform, which seems strange for an inductive load, is introduced by the eddy current model. Eddy current effects can be modelled by including a single turn coil around each laminated, flux carrying leg of the magnetic material. Each coil then drives a chain of resistors and inductors as discussed in [11]. [81] used the same approach and truncated the network to the first resistor which is the approach used in the present work. The single turn coil then drives a single resistor and when a voltage is applied an in phase

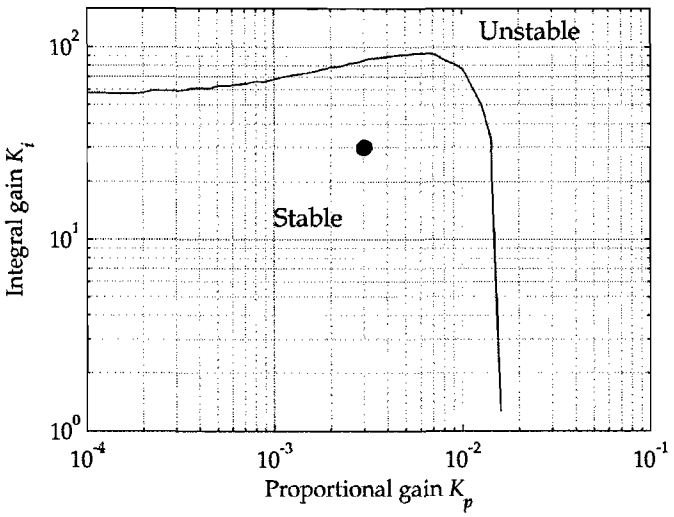

Figure 4.15: Parameter estimator stability according to circle criterion

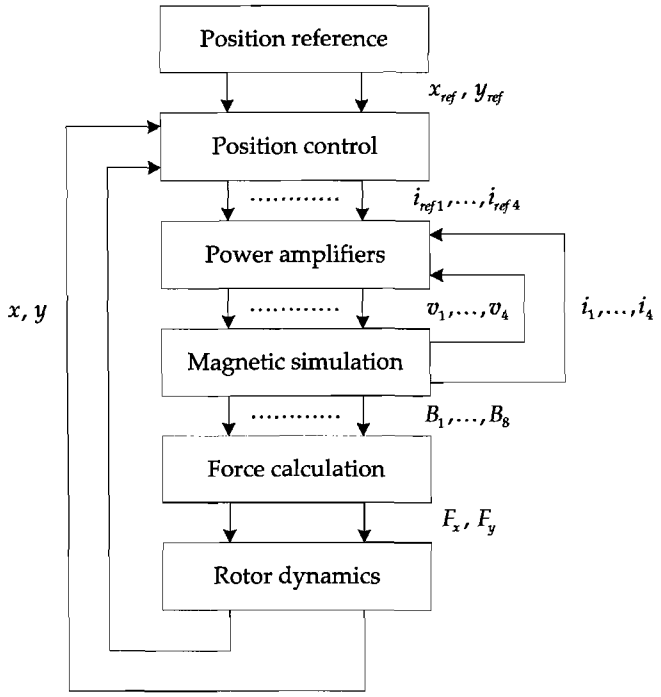

Figure 4.16: Transient simulation model flow diagram

current component immediately flows in the resistor accounting for the step in the current waveform. In order to produce a resulting current waveform which correlates much closer to that of a practical system an inductor can be added [82]. For the current work however, the inclusion of the inductance will increase the complexity of the simulation platform without adding any value and is therefore excluded. More details regarding the eddy current model is included in appendix C.

The TSM incorporates hysteresis and saturation by means of an analytical model that is presented in [81]. The parameters of the hysteresis model are determined in the present work using MATLAB®'s genetic algorithm optimisation toolbox. The model parameters for the M400-50A Cogent™ silicon steel as determined from the genetic algorithm optimisation process is summarised in table C.1. Figure 4.18 displays the modelled and measured hysteresis curve for the M400-50A Cogent™ silicon steel.

Next the parameters of the anhysteresis model presented by Jiles-Atherton in [70] are determined using MATLAB®'s genetic algorithm optimisation toolbox. The model parameters are summarised in table 4.1. Figure 4.19 displays the modelled and measured anhysteresis curve for the M400-50A Cogent™ silicon steel.

With the parameters of the magnetisation model and the anhysteretic model determined, these models may now be used to extract the complex μ_{fd} term. In the present work the hysteresis is not included in the self-sensing model, only the eddy current effects which is also a function of the *B-H* curve. The *B-H* curve is approximated by the Jiles-Atherton anhysteresis curve and values for the complex μ_{fd} must be obtained for various points on the anhysteresis curve.

The complex μ_{fd} term is extracted in the same fashion as described in section 3.10. A simple

Table 4.1: Jiles-Atherton anhysteresis model parameters

Parameter	Value	Unit
M_s	1.265e6	[A/m]
b	100	[A/m]
β	1.8e-3	

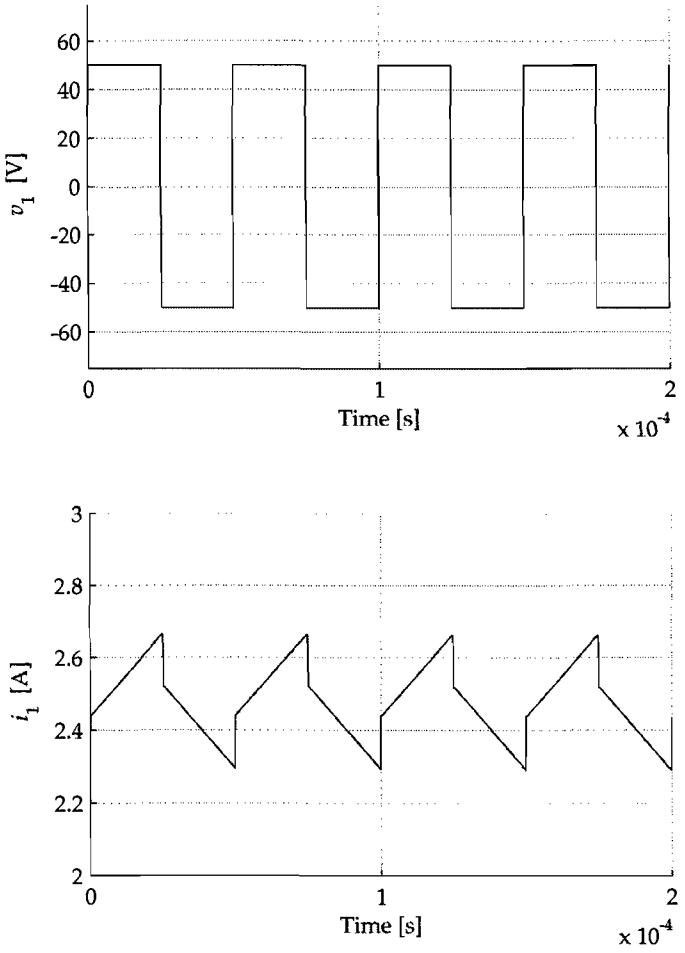

Figure 4.17: Transient simulation model voltage and current waveforms

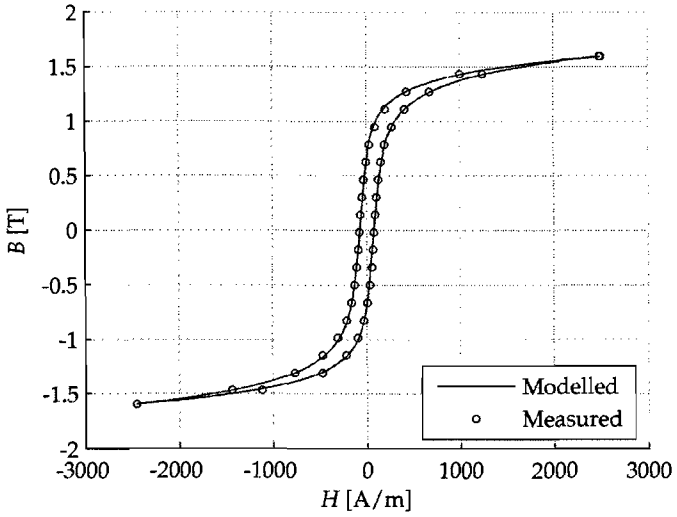

Figure 4.18: Magnetisation model for M400-50A silicon sheet steel

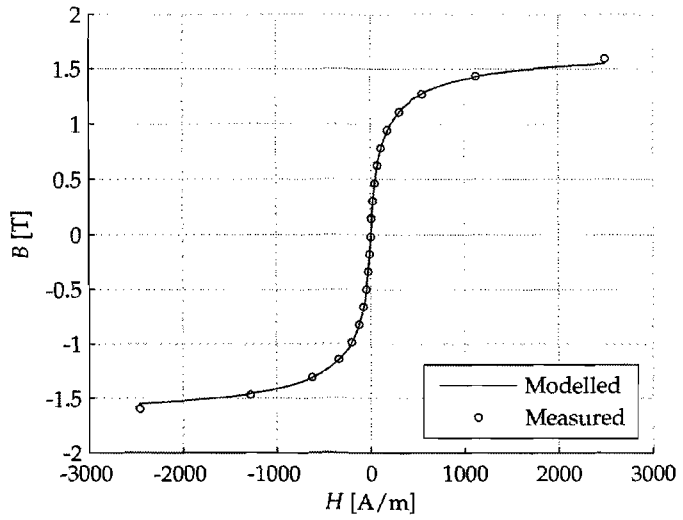

Figure 4.19: Anhysteresis model for M400-50A silicon sheet steel

transient simulation model is established for a toroidal core configuration. The configuration is excited with a switching amplifier and care is taken to ensure that the flux density excursion caused by the switching amplifier is the same as the excursion in the TSM of the AMB. This is accomplished by making use of the same switching frequency and ensuring that the $dB/dt = v/Na$ is the same for both configurations. The complex impedance of the toroidal configuration is obtained from the current and voltage waveforms. It is simple to obtain the complex μ_{fd} term from the complex impedance since all the physical parameters (e.g. number of turns, mean flux path length, etc.) of the measurement configuration is known. The dc current is increased in order to obtain impedances at different flux densities. A lookup table is generated with different flux densities and corresponding complex μ_{fd} terms.

4.4 Position estimation results

The purpose of this section is to demonstrate the basic functionality of the position estimation scheme in the simulation environment. This is accomplished by demonstrating the estimator's ability to track a varying rotor position. The linearity of the position estimator is also investigated. A detailed performance analysis will only be presented in chapter 5, comprising an in-depth investigation of issues such as bandwidth, cross-coupling and saturation to name but a few. Although the analysis of the parameter estimator has been done ignoring the coupled network, the actual estimator implementation uses the fully coupled RNM as developed in chapter 3.

4.4.1 Position control loop closed with true position

The first step in the process of demonstrating basic functionality of the position estimation scheme is to suspend the AMB with the true position and to compare the estimator output to the true position. The position of the shaft is varied to establish whether the estimated position tracks the true position. This is achieved by applying references: $y_{ref} = 0$ and $x_{ref} = 175 \times 10^{-6} \sin(2\pi 5t)$ and using the true x and y positions for position control. Figure 4.20 displays the results of this analysis for both the x- and y-axis over a period of 200 ms. From the y-axis result it is clear that there is a dc offset between the true and estimated positions. The ± 10 µm offset is due to discrepancies between the TSM and the RNM and will be investigated further in chapter 5. The

x-axis results for a varying position reference shows that the estimated output does track the true position.

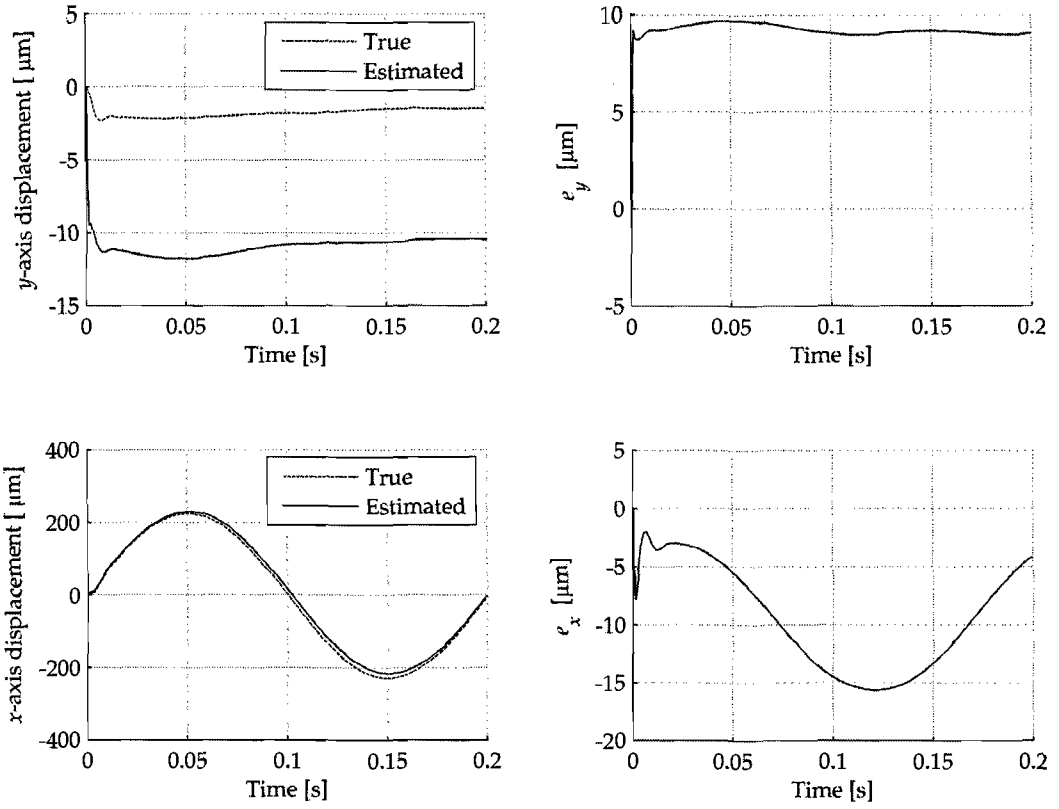

Figure 4.20: True and estimated y- and x-axis displacement ($y_{ref} = 0$, $x_{ref} = 175 \times 10^{-6} \sin(2\pi 5t)$). Position loops closed with true positions

Figure 4.21 displays the estimated x-axis displacement as a function of the true displacement as well as a linear approximation and the corresponding residuals. The response of the estimated position displays excellent linearity; 1.05 % over the 500 µm measuring range. Again a dc offset (12.6 µm) is observed which may be attributed to discrepancies between the two models.

4.4.2 Position control loop closed with estimated position

Now that the estimator's ability to track the true position is demonstrated it is time to close the position control loop with the estimated position. Unfortunately using the estimated position as feedback in the position control loop leads to destabilisation of the system. Upon further investigation it is shown that by filtering the estimated position signal before using it as feedback the position control loop can be stabilised. The noise introduced by the demodulation process must be attenuated to an acceptable level to ensure stability. For the case at hand a fourth order Bessel low pass filter (LPF) with a cutoff frequency of 1 kHz is chosen. The filter severely limits the bandwidth of the position estimation scheme but is absolutely necessary for stability.

The effect of the LPF is evident in the transient phenomenon during startup as seen in the y-axis position of figure 4.22. Stable suspension is realised but the dynamic performance of the system is influenced. The dc offset in the y position is again present and the estimated x position tracks the true x position.

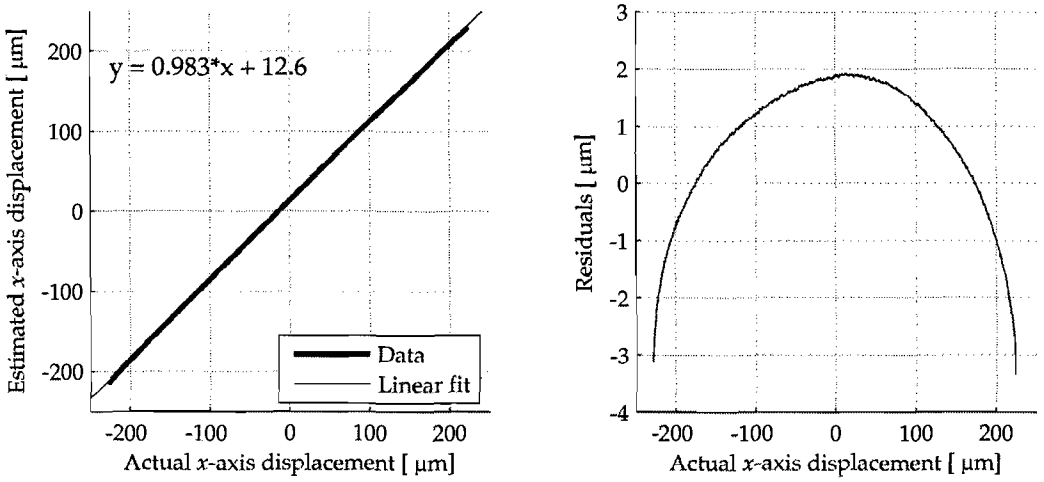

Figure 4.21: True and estimated x-axis displacement and linear approximation. Position loops closed with true positions

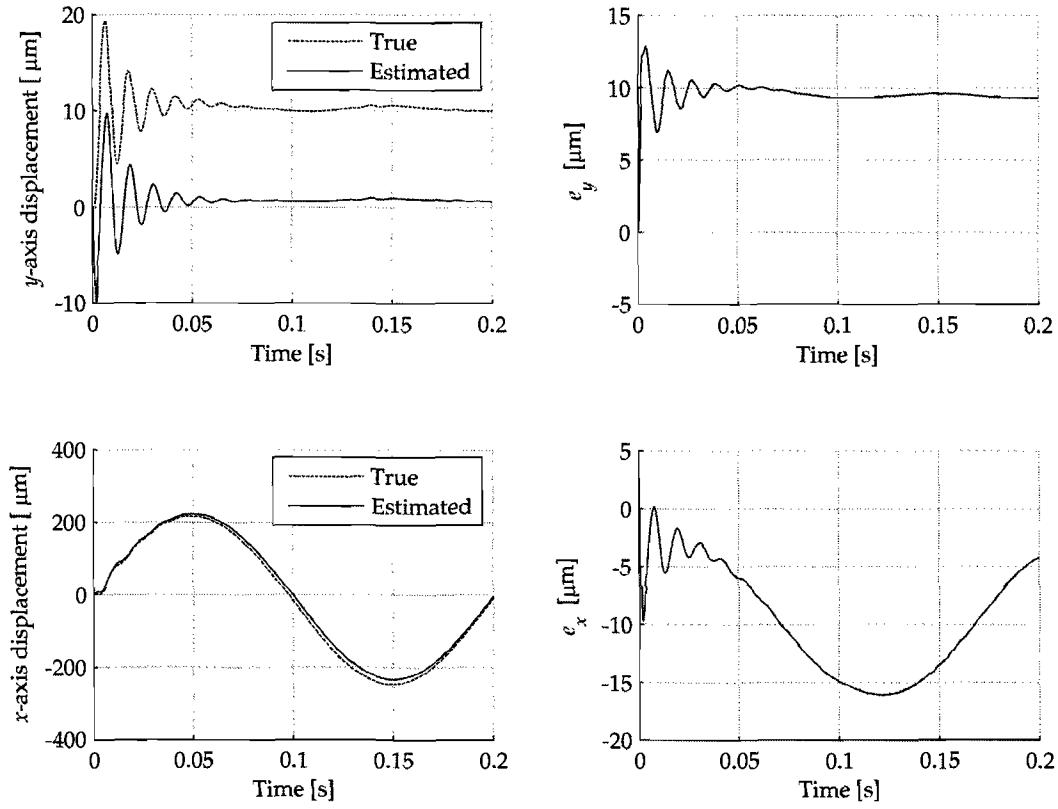

Figure 4.22: True and estimated y- and x-axis displacement ($y_{ref} = 0$, $x_{ref} = 175 \times 10^{-6} \sin(2\pi 5t)$). Position loops closed with estimated positions

The linearity of the self-sensing scheme is 1.05 % as obtained from figure 4.23. This result is the same as the previous which implies that the only inferiority of the self-sensing position compared

to the true position at this stage is the bandwidth limitation.

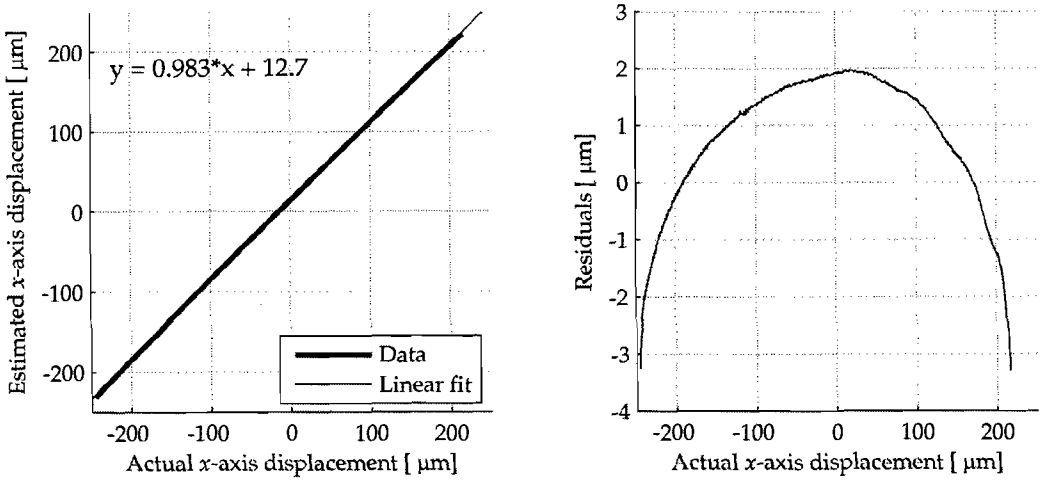

Figure 4.23: True and estimated x-axis displacement and linear approximation. Position loops closed with estimated positions

Chapter 4 starts off by introducing the reader to the general concept of the position estimation scheme as implemented in the present work. This is followed by an introduction to the the parameter estimator approach which stands central to the position estimation process. Issues regarding the demodulation process as well as the influence of duty cycle variation are addressed and the section is concluded with a stability analysis of the parameter estimator. The TSM is introduced next and the suitability of the model as evaluation platform is demonstrated. The chapter is concluded with simulated results which demonstrate the basic functionality of the self-sensing scheme. A detailed performance analysis of the position estimation scheme will be presented next in chapter 5.

CHAPTER 5

Performance evaluation

The purpose of chapter 5 is firstly to characterise the performance of the position estimator-based self-sensing scheme as proposed in chapter 4. Secondly, in view of the fact that the main theme of the thesis is focussed on the modelling of the heteropolar magnetic bearing, it is important to investigate the effect of modelling error on the position estimate.

A sensor's performance is characterised in terms of measuring range, linearity, sensitivity, resolution and frequency response. The measuring range in the present work is determined by the backup bearing range which is 1 mm. The sensitivity as well as the resolution of the self-sensing scheme in the simulation environment are much higher than would be possible to practically realise. This is due to the lack of analogue to digital converters and current and voltage measurement circuits in the simulation environment which will dominate the sensitivity and resolution of the self-sensing scheme. The performance evaluation therefore focusses on linearity and frequency response. Other criteria as highlighted in chapter 2 that are of importance for self-sensing are duty cycle effects, cross-coupling and saturation. The stability margin of the active magnetic bearing (AMB) system is also analysed according to ISO 14839-3.

The final sections of chapter 5 address issues regarding modelling uncertainty by analysing the effect of discrepancies between the experimental system and the reluctance network model (RNM) on the position estimate.

5.1 Sensor static performance

The performance evaluation is divided into two parts. The first is presented in this section and is concerned with the sensor's static performance. The second part is presented in section 5.2 and is concerned with the dynamic performance of the position estimation scheme. For the static performance evaluation the position control loop is not closed and the position of the shaft is forced (in the simulation environment) to the desired location. This is the equivalent to mechanically fixing the rotor position in the experimental system. The static evaluation takes a look at sensor linearity, the effect of duty cycle variation and cross-coupling on the position estimate and the effect of saturation on the position estimate.

5.1.1 Linearity

Linearity is normally specified as the percentage deviation from a linear correlation between the measured quantity and sensor output signal over the maximum measuring range [13]. Figure 5.1 is a graphic representation of the definition of linearity.

The self-sensing linearity is determined by obtaining the estimated position as a function of

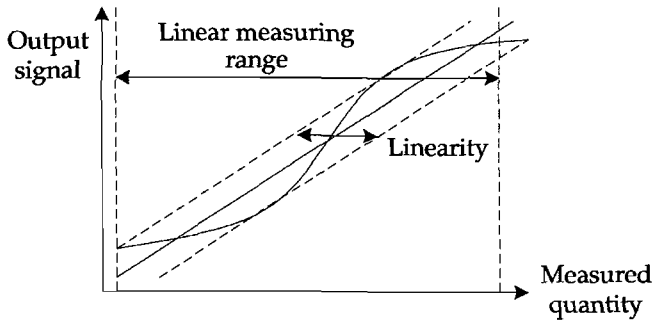

Figure 5.1: Linearity in sensors [13]

the true position for an excursion over the entire backup bearing range. A linear correlation between the true position and estimated position is established and the residuals are used to determine the linearity. The position of the rotor is forced in the simulation while the duty cycle is held constant at 50 % which implies that the average coil currents will be zero. The material nonlinearity is also excluded from the analysis to isolate all other effects on the estimated position.

Figure 5.2 displays the estimated x-axis position as a function of the true position for a full excursion of the backup bearing range. The self-sensing linearity is recorded as 0.34 % for the full excursion over the backup bearing range. The self-sensing scheme displays excellent linearity when the material nonlinearity and duty cycle effects are eliminated. In the following sections the duty cycle, cross-coupling and material nonlinearity effects will be investigated. These effects will not be quantified in terms of linearity but rather as a percentage error.

5.1.2 Duty cycle variation

In order to analyse the effect of duty cycle variation, the position of the shaft is held in the zero x, y position, the material nonlinearity is ignored and the duty cycle is varied. Since the amplitude of the fundamental component of the voltage signal attenuates with the same amount for a fixed increase or decrease in duty cycle, see figure 4.11, no error in the estimated position is expected when the duty cycles are varied in the differential mode. The duty cycle of only one of the two

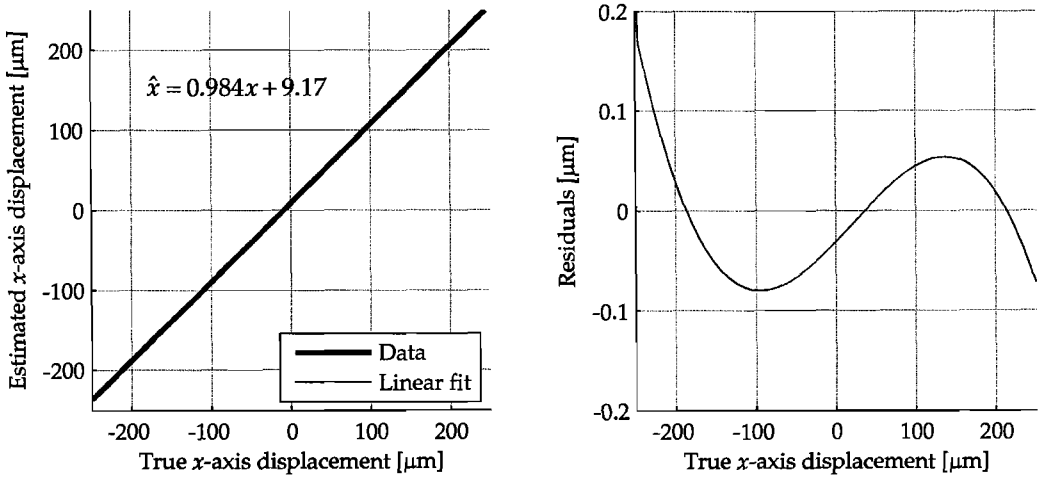

Figure 5.2: Self-sensing linearity

coils in the differential configuration must therefore be varied while the other is held constant. For this analysis the duty cycles of coils 1, 3 and 4 are held constant at 50 % and the duty cycle of coil 2 is defined by $\alpha_2 = 0.5 + 0.25\sin(2\pi 20t)$. The maximum or minimum duty cycle (75 % or 25 %) causes the amplitude of the fundamental component to decrease with a factor 0.707. The effect this has on the estimated position estimate is investigated.

Figure 5.3 displays the simulated results. Apart from the 10 μm dc offset an additional error is induced in the estimated position by the varying duty cycle. The peak-to-peak variation in the position estimation error, excluding the 10 μm dc offset, is 25 μm with a frequency twice that of the duty cycle variation. The frequency doubles due to the fact that an increase or decrease from the nominal 50 % duty cycle has the same effect on the fundamental amplitude. The maximum error of 25 μm translates to a 5 % error in the position estimate with respect to the backup bearing range.

The error in the y-axis position which is also shown in figure 5.3 is caused by cross-coupling. A maximum error of 1 μm peak-to-peak about the 10 μm dc offset is recorded for the maximum duty cycle variation. This result illustrates that the RNM approach effectively includes mutual coupling in the position estimation scheme. Cross-coupling will now be investigated in more detail.

5.1.3 Cross-coupling

During investigations it was noted that mutual coupling between two opposing pole pairs, that are driven in the differential mode, is substantial. To investigate this phenomenon and quantify

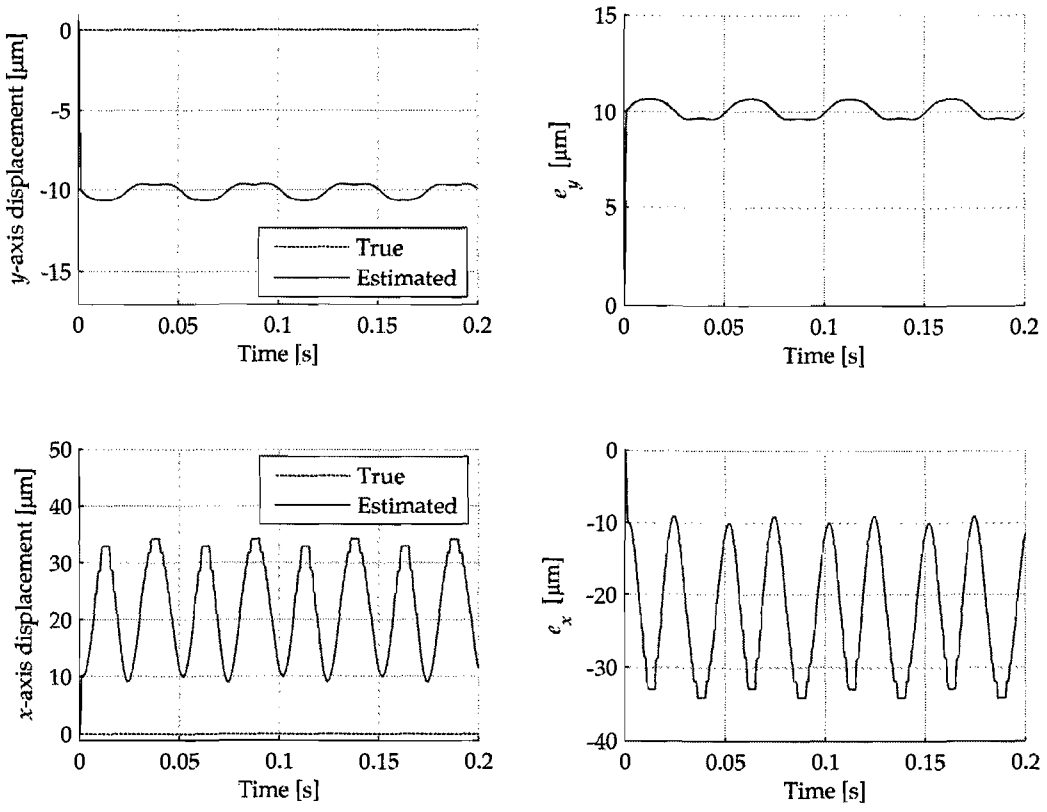

Figure 5.3: Effect of duty cycle variation on position estimation

the maximum possible error in the estimated position, the following analysis is conducted. The x- and y-axis positions are forced to zero and the duty cycles of coils 1 and 3 (y-axis) are held constant at 50 % while the duty cycles of coils 2 and 4 are defined by $\alpha_2 = 0.5 + 0.25\sin(2\pi 20t)$ and $\alpha_4 = 0.5 - 0.25\sin(2\pi 20t)$ respectively. This will eliminate the effect of duty cycle variation and is the worst case scenario for mutual coupling between PP_2 and PP_4. The material nonlinearity is discarded in the simulation to eliminate saturation effects. The mutual inductance terms of the RNM are initially ignored in the position estimation scheme in order to quantify the error. Figure 5.4 displays the results for the analysis with large discrepancies between the true and estimated x-axis positions.

Ignoring the 10 μm dc offset, the error is shown to be sinusoidal with an amplitude of more than 100 μm. This amounts to 40 % of the backup bearing range which is a substantial error. A peak-to-peak error of 2 μm is observed in the y-axis.

When the mutual inductance terms of the RNM are included in the position estimation scheme and the analysis is repeated, marked improvement is noted. Figure 5.5 displays the results which show that the amplitude of the error in the x-axis is reduced to 20 μm which corresponds to 8 % of the backup bearing range. The results of the y-axis stay more or less unchanged with a small increase in peak-to-peak error due to noise.

5.1.4 Saturation

Magnetic saturation is perhaps one of the most vexing problems faced by self-sensing researchers today [7]. In order to investigate and quantify the effect of saturation on the performance of the

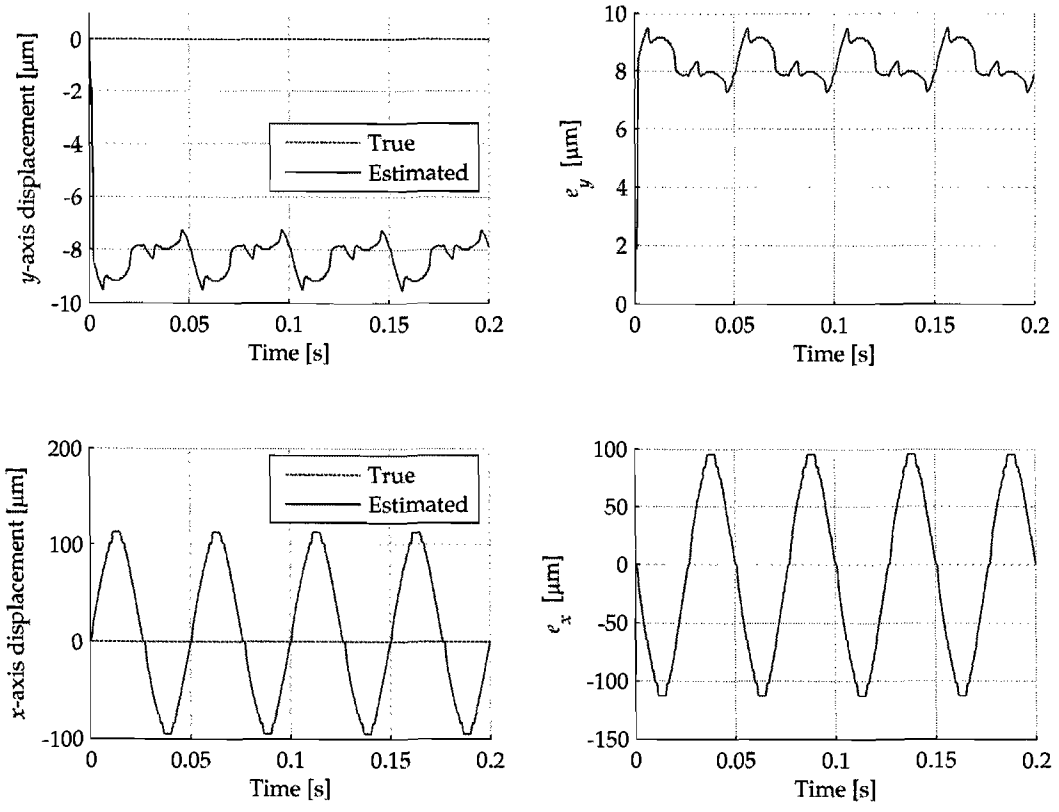

Figure 5.4: Static cross-coupling effects (Mutual inductances excluded from the estimator model)

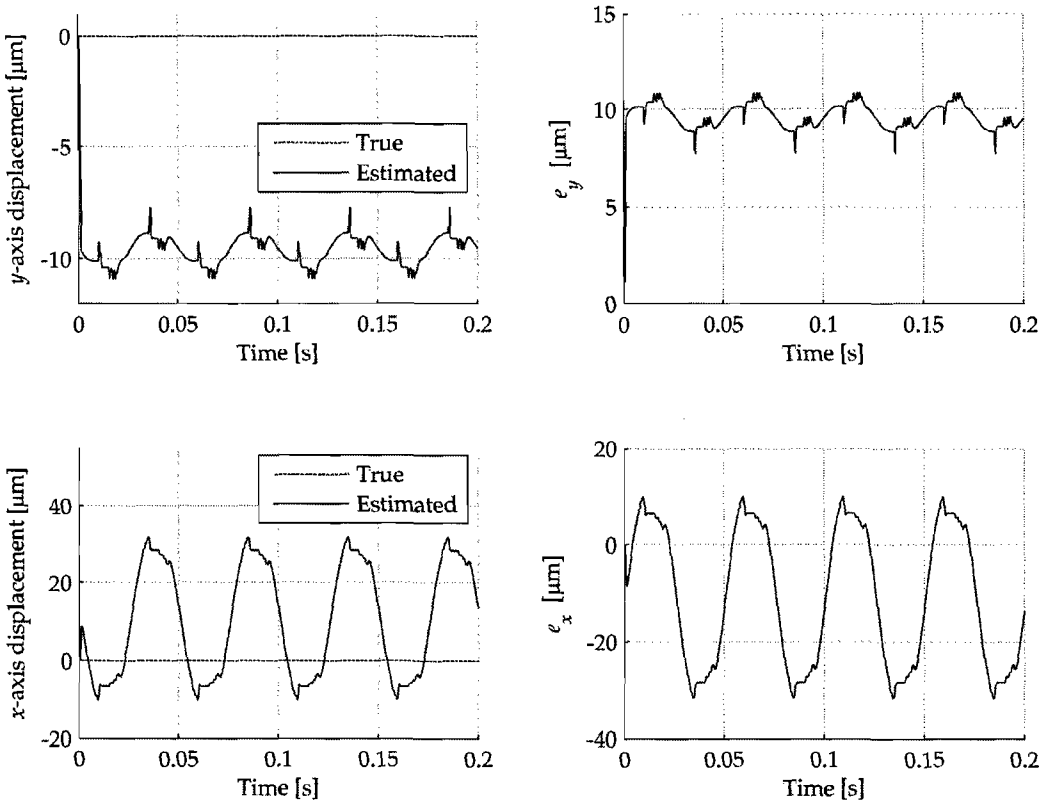

Figure 5.5: Static cross-coupling effects (Mutual inductances included in the estimator model)

proposed position estimation scheme, the magnetic bearing is intentionally driven into saturation and the estimated position is monitored. This is accomplished by again pinning the rotor in the zero x, y position, and using the following current references: $i_{1\,ref} = i_{3\,ref} = 7.5$ A, $i_{2\,ref} = 7.5 + 7.5\sin(2\pi 10t)$ and $i_{4\,ref} = 7.5 - 7.5\sin(2\pi 10t)$. This leads to magnetic flux densities of above 1.3 T.

Figure 5.6 displays results for the estimated position under saturation conditions. It is clear from the results that a sign reversal, which establishes positive feedback, is caused by the material saturation. This causes the estimated position to clamp at the backup bearing limit. The explanation for this phenomenon, which takes place at 20 ms, is that as the electromagnet saturates, its inductance decreases resulting in an increase in current ripple. This causes the demodulated current signal of the saturated electromagnet to be more dominant in the position estimation scheme. Considering only the saturated actuator's response, it is clear where the positive feedback originates from. As soon as the slope of the inductance as a function of position reverses due to saturation, a sign reversal takes place.

A solution to this problem is presented in the present work by introducing weights which scale both the transient simulation model (TSM) and RNM demodulated currents. The weights are adjusted to ensure that the actuator with the lowest flux density contributes the most to the position estimate. This approach is graphically presented in figure 5.7 where the saturation factor λ_x is defined as the difference between the average flux densities of the two opposing pole pairs (PP_2 and PP_4 in figure 3.3). The saturation factors λ_x and λ_y are determined from:

$$\lambda_y = ((B_1 - B_2) - (B_5 - B_6))/2 \quad \{\lambda_y \in \mathbb{R} | -1 \leq \lambda_y \leq 1\} \tag{5.1}$$

$$\lambda_x = ((B_4 - B_3) - (B_8 - B_7))/2 \quad \{\lambda_x \in \mathbb{R} | -1 \leq \lambda_x \leq 1\}. \tag{5.2}$$

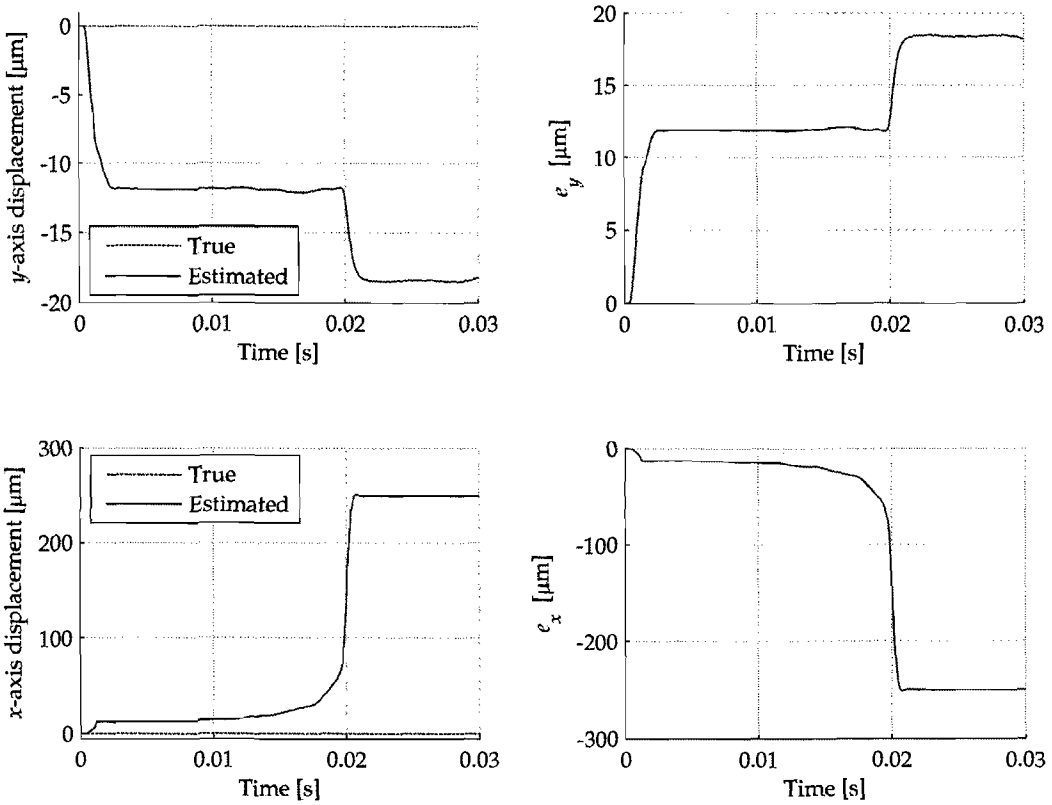

Figure 5.6: Effect of magnetic saturation on position estimation

Parameters B_1 to B_8 are the respective flux densities for poles P_1 to P_8 and the signs in (5.1) and (5.2) correspond to the referencing convention used throughout the thesis as illustrated in figure 3.3.

The weighting concept is recommended as opposed to using only the demodulated coil current of the actuator with the lowest flux density. This approach is advantageous for two reasons; firstly to eliminate discontinuities in the estimated position which will occur when switching between the two demodulated currents, and secondly to exploit the advantages (increase in sensitivity and linearity) of the differential configuration under normal operation.

The proposed current weighting scheme is now evaluated under the exact same excitation conditions of the previous result i.e. $i_{1\,ref} = i_{3\,ref} = 7.5$ A, $i_{2\,ref} = 7.5 + 7.5\sin(2\pi 10t)$ and $i_{4\,ref} = 7.5 - 7.5\sin(2\pi 10t)$.

Figure 5.8 displays the position estimation results. As is evident from the x-axis results the estimated position deviates less than 5 μm from the dc offset of ±12 μm for flux densities peaking at over 1.3 T. This is a remarkable result indicating that the proposed self-sensing scheme may eliminate the problems posed by saturation when only one of the two opposing electromagnets is driven into saturation.

5.2 Sensor dynamic performance

The second part of the performance evaluation is concerned with the sensor's dynamic performance. For the dynamic analyses the rotor is suspended with either the true or estimated position. The system is then subjected to dynamic disturbances in the form of disturbance forces or reference positions. The dynamic performance evaluation comprises cross-coupling investigations, bandwidth measurements and stability margin evaluation.

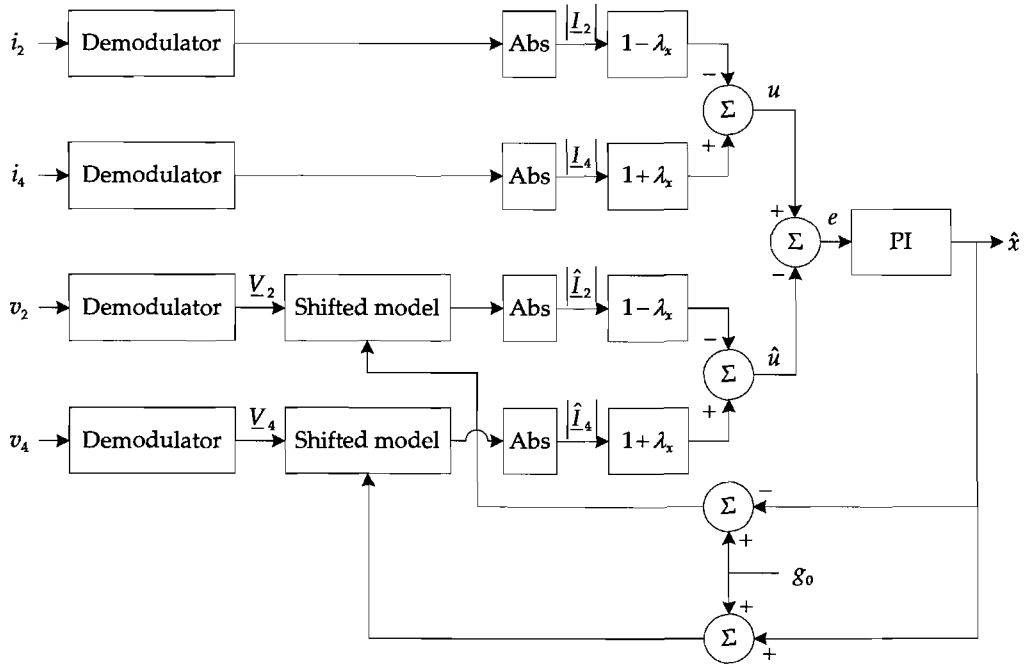

Figure 5.7: Estimator schematic with current weighting included

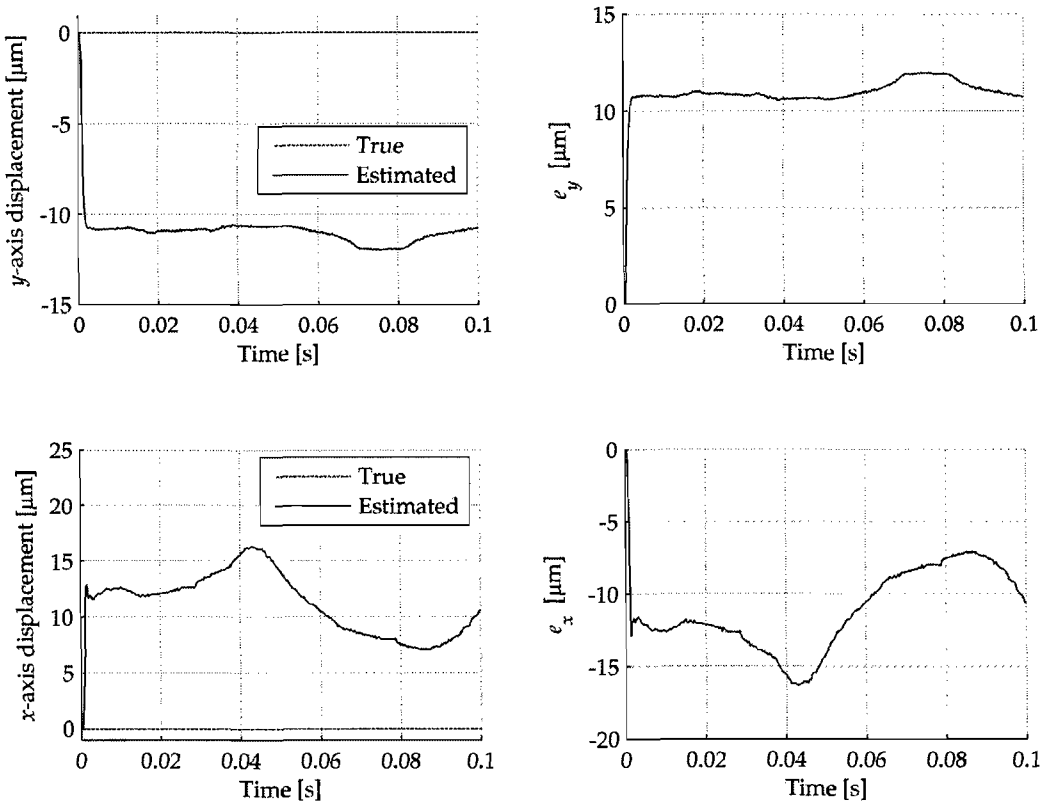

Figure 5.8: Effect of magnetic saturation on position estimation (current weighting included)

5.2.1 Cross-coupling

The effect of coupling between the x- and y-axis is investigated by suspending the rotor with the estimated positions and applying a disturbance force in the x-axis. The system is suspended for 50 ms before the sinusoidal disturbance force with an amplitude of 50 N and a frequency of 20 Hz is applied. The mutual inductance terms which interconnect the different pole pairs are initially neglected in the RNM and the results are displayed in figure 5.9. From the results it is clear that the system becomes unstable as soon as the disturbance force is applied and the rotor delevitates in the x-axis at 78 ms. Also important to note is the error in the estimated y-axis position which is a direct result of excluding mutual inductance terms from the position estimation model. An 8 μm error is induced between the estimated and true positions, when ignoring the 10 μm dc offset.

Figure 5.10 displays the results for the case where the mutual inductance terms are included in the analysis. The inclusion of the mutual inductance terms allows the self-sensing system to stably suspend the rotor in the x-axis and marked improvement is noted in the y-axis results. The maximum deviation in the y-axis error is almost negligible demonstrating the effectiveness of the coupled network model. Ignoring the 10 μm offset in the x-axis position, the error amplitude is roughly 15 μm The magnitude of the error is similar to that of figure 5.5 and may also be caused by cross-coupling effects due to duty cycle variation.

Work done in [8] showed that cross-coupling may not be neglected for certain systems. In the present work it was also shown that cross-coupling may introduce large errors in the estimated position when excluded from the self-sensing model and may even destabilise the position estimation scheme under certain conditions. In [4] the effects of cross-coupling are eliminated by

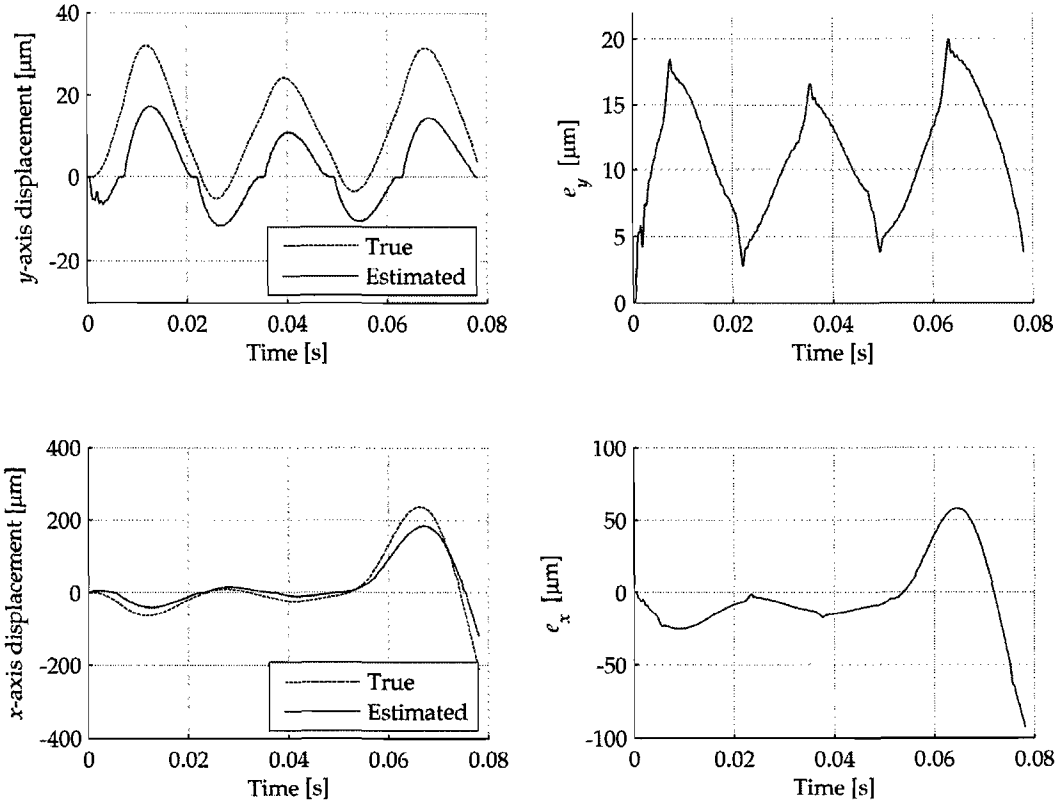

Figure 5.9: Dynamic cross-coupling effects (Disturbance force of 50 N on x-axis from 50 ms, mutual inductances excluded)

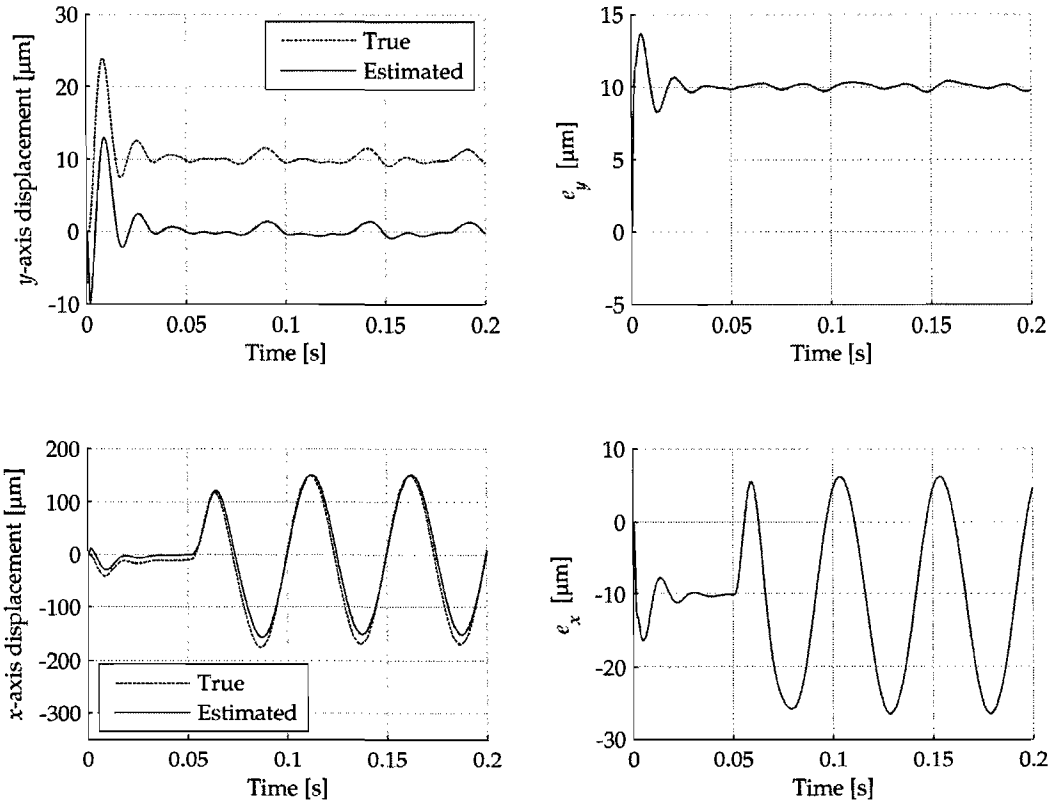

Figure 5.10: Dynamic cross-coupling effects (Disturbance force of 50 N on x-axis from 50 ms, mutual inductances included)

mechanically separating the individual actuators. This approach however has the disadvantage of increasing the manufacturing cost of the magnetic bearing. The present work demonstrates that a coupled RNM may be used in a parameter estimator approach to successfully counteract cross-coupling effects. If it is possible to practically realise the present self-sensing scheme the problem of cross-coupling may be eliminated without mechanical separation of the individual actuators.

5.2.2 Bandwidth

The frequency response of the estimated position compared to the true position is analysed by adding a constant amplitude sinusoidal signal to the position reference signal. Small position and current variations are used so that the system may be assumed linear in the working point. The frequency of the reference signal is increased from 10 Hz up to 2 kHz which is well above the expected self-sensing bandwidth.

Bandwidth describes the maximum rate of change in the true position that the estimator will be able to track. Bandwidth can be decided on either the magnitude or phase relationship between the estimated and true position. The magnitude should ideally be close to 0 dB and the phase lag should be as small as possible. Phase lag may destabilise the system and the exact amount can be determined by a stability analysis of the controller and estimator combined.

Figure 5.11 displays the frequency response of the estimated position compared to the true position as determined from simulation. The point where the estimated and true positions deviate more than 3 dB is reached at 270 Hz. The self-sensing bandwidth may however be lower than 270 Hz since the phase lag at this point is already 40 degrees. The bandwidth of the position estimation scheme is very low which has an undesirable effect as will be demonstrated in the following section.

5.2.3 Stability margin evaluation

The negative stiffness property of magnetic bearings, resulting from static magnetic force, renders them inherently unstable. Feedback control is therefore needed to produce positive stiffness and damping in order to stably suspend a rotor in the centre position. Figure 5.12 displays a block diagram of the AMB control system. The rotor plant receives as input the resulting force produced by the AMB and disturbance force and generates as output the rotor displacement. The rotor displacement is converted by the position sensors and fed to the controller which in turn generates appropriate current reference signals. The power amplifiers convert these signals into power signals which energise the electromagnetic actuators producing a force acting to stably suspend the rotor in the desired position.

To ensure safe reliable operation of an AMB rotor system, it is important to evaluate the system's stability and the system's margin of stability. The margin is of particular importance since it calls for a minimum level of robustness with respect to system variations and disturbance forces. System variations refer to, for example, gain variations caused by sensor sensitivity to temperature variations, and disturbance forces refer to, for example, unbalance forces and higher harmonic forces [29]. The process of evaluating the stability margin of such a system from an AMB control point of view is presented in [29].

Several analysis tools are available to evaluate the system's stability, including gain-phase margin, Q-factors, Nyquist plot criteria and the sensitivity function. In order to utilise these tools, the open and closed loop transfer functions for the system are derived next. By injecting a harmonic or random excitation signal X_e and measuring E and X_s, the open and closed loop transfer functions can be obtained. The open loop transfer function is given by:

$$G_o(s) = \frac{X_s(s)}{E(s)} \tag{5.3}$$

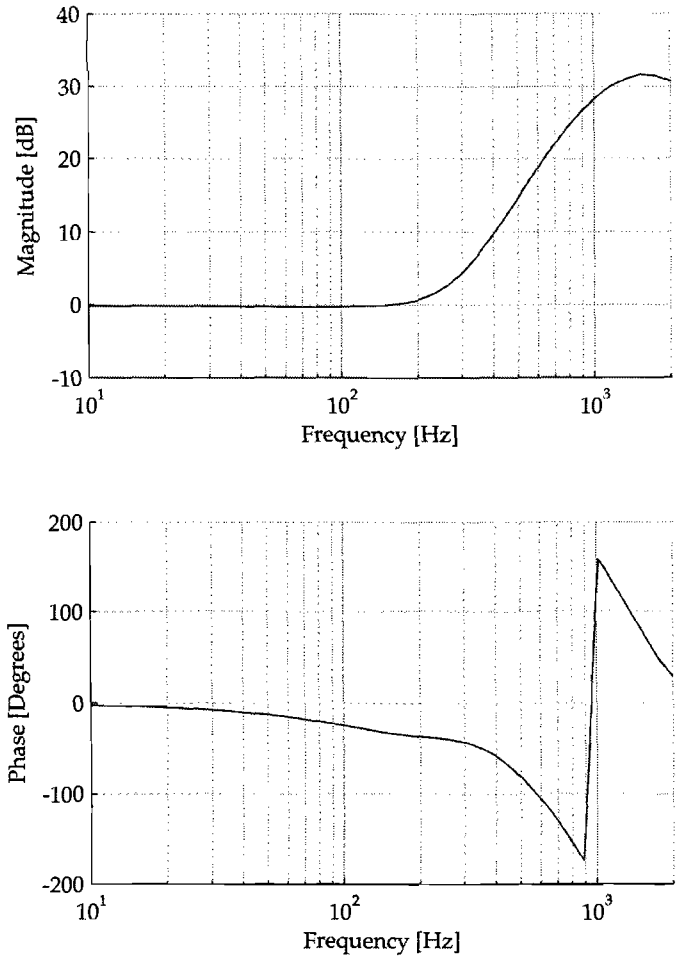

Figure 5.11: Frequency response of estimated position with respect to true position

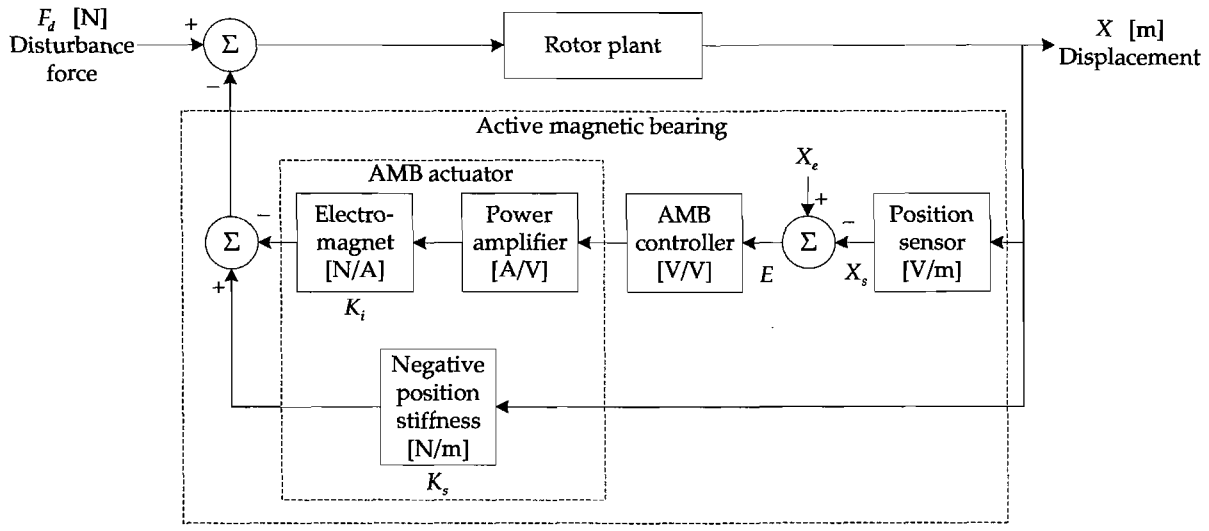

Figure 5.12: AMB control system block diagram [29]

and the closed loop transfer function can be obtained from:

$$G_c(s) = \frac{X_s(s)}{X_e(s)} \tag{5.4}$$

with the two transfer functions related by:

$$G_c(s) = \frac{G_o(s)}{1 + G_o(s)} \quad \text{and} \quad G_o(s) = \frac{G_c(s)}{1 - G_c(s)}. \tag{5.5}$$

From the Bode plot of the closed loop transfer function the different harmonic peaks may be analysed. The sharpness or Q-factor of the peaks which fall within the operating range are regulated by ISO 10814. ISO 14839-3 on the other hand evaluates the stability margin of all the resulting peaks.

The Nyquist criterion may also be used to evaluate system stability. The stability margin is determined by obtaining the minimum distance between the critical point (-1,0) and the Nyquist plot of $G_o(j\omega)$. The minimum distance is obtained when $1 + G_o(j\omega)$ reaches a minimum but can also be obtained by determining the maximum of the inverse $1/[1 + G_o(j\omega)]$. The latter expression defines the sensitivity function:

$$G_s(s) = \frac{1}{1 + G_o(s)}. \tag{5.6}$$

Using (5.5) in conjunction with (5.3) and (5.4), G_s can be expressed as:

$$G_s(s) = \frac{E(s)}{X_e(s)} \tag{5.7}$$

with $s = j\omega$. The sensitivity function may be used to determine the system's stability margin. When measuring the sensitivity, the excitation signal's frequency must be increased from low frequencies to a maximum frequency f_{max} which is set at the larger of:

a) three times the rated speed, or

b) a maximum frequency of 2 kHz.

If a digital controller is utilised in the AMB system, the maximum frequency must be restricted to half the sampling frequency (Shannon frequency). The sensitivity of all of the axes in the AMB-rotor system must be evaluated at standstill and at the maximum continuous rated speed.

The zone limits for the evaluation of the stability margin, as obtained from [29], is shown in table 5.1. The definition of each stability zone is determined by adapting the guidelines of ISO 7919-1 and is quoted from ISO 14839-3:

> **Zone A:** The sensitivity functions of newly commissioned machines would normally fall within this zone.
>
> **Zone B:** Machines with the sensitivity functions within this zone are normally considered acceptable for unrestricted long-term operation.
>
> **Zone C:** Machines with the sensitivity functions within this zone are normally considered unsatisfactory for long-term continuous operation. Generally, the machine may be operated for a limited period in this condition until a suitable opportunity arises for remedial action.
>
> **Zone D:** The sensitivity functions within this zone are normally considered to be sufficiently severe to cause damage to the machine.

Table 5.1: Peak sensitivity at zone limits [29]

Zone	Peak sensitivity	
	Level	Factor
A/B	8 [dB]	2.5
B/C	12 [dB]	4
C/D	14 [dB]	5

The sensitivity of the AMB system is evaluated firstly by suspending the system with the true position and applying an excitation signal with an amplitude of 10 μm and varying frequency. Figure 5.13 displays the system sensitivity as a function of frequency for a range from 10 Hz to 2 kHz. The sensitivity peaks at 71 Hz with a value of just above 6 dB which falls within zone A as can be seen in table 5.1.

A single peak is present due to the point mass model used for the rotor which has a single critical frequency at:

$$f_c = \frac{1}{2\pi}\sqrt{\frac{k_{eq}}{m}} \tag{5.8}$$

with k_{eq} the equivalent stiffness of the AMB system and m the equivalent mass of the rotor at the bearing location. For the present work the bearing is designed for a equivalent stiffness of 0.5 kN/m but from the TSM results it is clear that the equivalent stiffness is closer to 1 kN/m. The increase in equivalent stiffness is a result of the pole which is added in the differential path of the PD controller to decrease the controller's sensitivity to high frequency noise. The pole is placed at $\omega = 1000$ rad/s which falls well within the bandwidth of the controller and consequently influences the equivalent stiffness of the AMB system.

Figure 5.14 displays the system sensitivity when the position control loop is closed with the estimated position. A large increase in peak sensitivity is noted from 6 dB to 14 dB which places the system on the edge of the C/D zone. The sensitivity function of the machine is therefore considered unsatisfactory for long term operation and borders on sufficiently severe to cause damage to the machine.

This is a disappointing result and a brief investigation showed that the sensitivity may be lowered by decreasing the bias current (i_b) level from 5 A to 3 A. The PD position controller's K_P and K_D gains must then be adjusted to obtain the same stiffness and damping parameters as

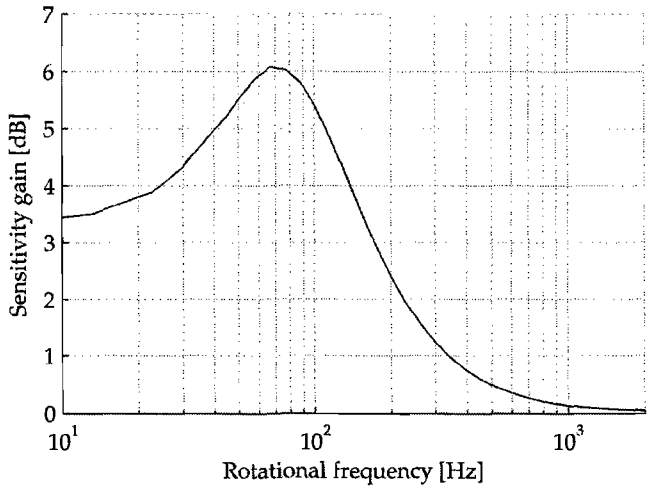

Figure 5.13: Bode plot of the sensitivity function G_s (Suspension with true position)

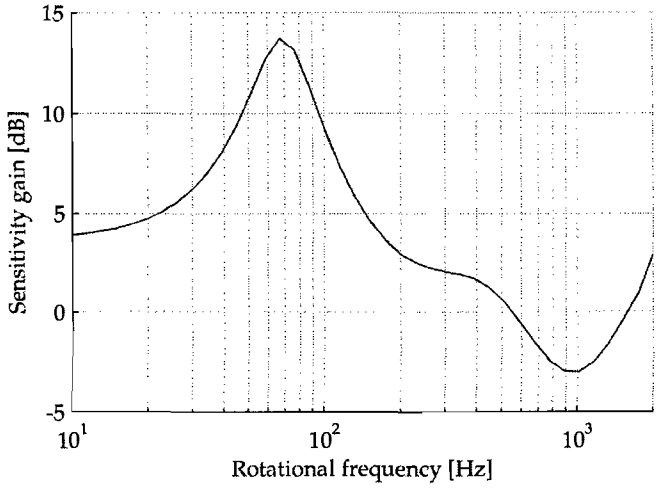

Figure 5.14: Bode plot of the sensitivity function G_s (Suspension with estimated position)

before. An integral gain is also added which will significantly reduce the system's sensitivity for low frequency disturbances. Figure 5.15 displays the new system sensitivity curve for position control with the true position. The peak sensitivity of 6 dB as recorded in figure 5.13 is now reduced to 4 dB without altering the bearing's stiffness or damping parameters. The maximum linear force region of the bearing is however reduced by 40 %.

Figure 5.16 displays the sensitivity curve with position control implemented with the estimated position. The peak sensitivity of 14 dB as recorded in figure 5.14 is lowered to just above 8 dB which is a significant improvement. This implies that the performance is improved from sufficiently severe to cause serious damage to satisfactory for unrestricted long-term operation.

The focus of the present work was however not to implement an optimum parameter estimator scheme which utilises the RNM to accomplish self-sensing, but to merely demonstrate the feasibility. Further work is therefore needed to optimise the position estimation scheme in order to achieve better system robustness. Issues that may be looked at include the demodulation process

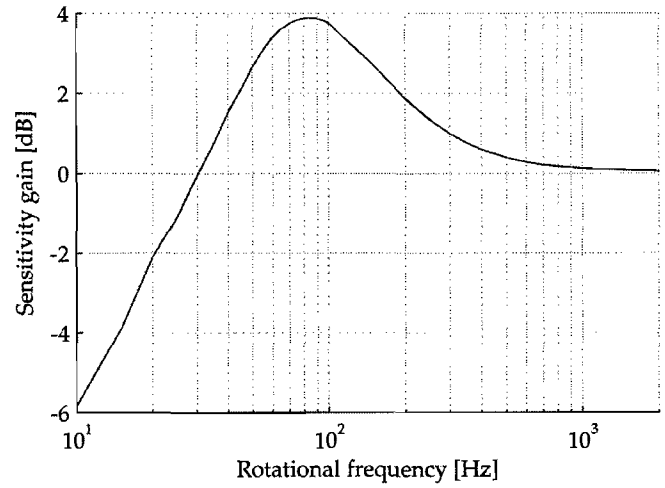

Figure 5.15: Bode plot of the sensitivity function G_s (Suspension with true position, $i_b = 3$ A)

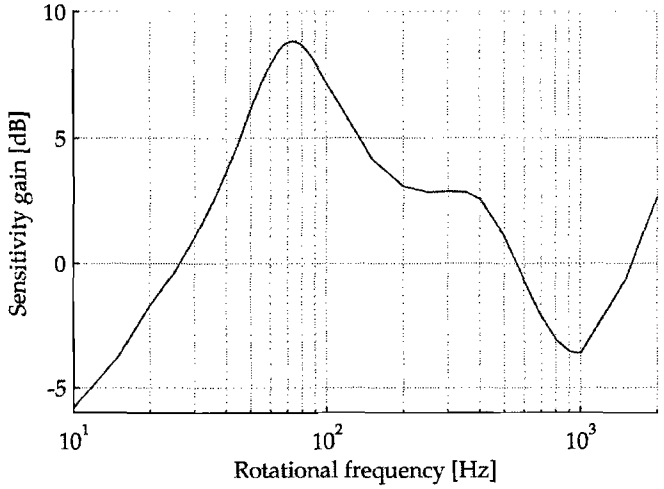

Figure 5.16: Bode plot of the sensitivity function G_s (Suspension with estimated position, $i_b = 3$ A)

that was used and the use of both the amplitude and phase values of the demodulated currents as input to the parameter estimator. A more elaborate parameter estimation scheme may also be investigated where the x- and y-axis are not decoupled.

5.3 Modelling uncertainty

It is important to investigate and, if possible, quantify the effects of modelling uncertainty on the position estimation process. In chapter 3 the main contributors to modelling uncertainty were identified, and the levels of error quantified in the model refinement process.

Bearing dimensions was identified as a possible source of modelling uncertainty and it was shown that precise measurement is needed to accurately determine the dimensions. The air gap reluctance was also identified as a source of potentially large modelling discrepancies. This problem was however solved by using a lookup table with accurate values of the air gap reluctances as determined from the FEM parametric study. The choice of leakage path in the RNM must also be evaluated to ensure that it is correct for the bearing geometry in question.

The final and most important source of modelling uncertainty that was identified is the material complex permeability. The complex material permeability represents the modelling parameter with the largest amount of uncertainty. This is due to the almost impossible task of accurately predicting the exact location on the *B-H* curve. Unlike the other contributors of modelling uncertainty, the exact location on the *B-H* curve and the corresponding complex material permeability are not addressed in the present work. The *B-H* curve excursion is approximated with an anhysteretic curve which results in a source of modelling uncertainty.

The discrepancy between the experimentally determined inductance and that of the RNM will be reproduced between the TSM and the RNM by manipulating the $B - \mu$ relationship of the RNM. This will be done in such a way that the inductance is both over- and underestimated with the same maximum amount as recorded between the experimental system and the RNM. The error between the experimental system and the RNM is documented in table 3.8 and a maximum error of 22 % is recorded when the rotor is clamped in the $y = 100$ μm position while keeping $x = 0$ and the coil currents are specified as: $I_1 = 9$ A and $I_2 = I_3 = I_4 = 0$ A.

The magnetic material of PP1 moves closer to saturation as the air gap reluctance decreases with an increase in y. This causes the material reluctance to have a larger influence on the total

reluctance. Discrepancies between the modelled and experimental material reluctances are therefore emphasised when the air gap reluctance decreases. These discrepancies in turn will result in large discrepancies between the modelled and measured magnetic bearing impedances.

A static analysis is first conducted where it can be assumed that the error between the true location on the *B-H* curve and the location on the anhysteretic curve is small. In order to reproduce the error in self-inductance, a gain is introduced in both the relative and complex material permeability terms. The exact value of the gain is experimentally determined by clamping the rotor in the position which resulted in the largest error and varying the gain until the absolute value of the TSM's impedance is over- and underestimated by 22 %.

In the TSM and RNM environment the rotor position is forced to $y = 0$ and various x-axis positions are investigated. The coils in the TSM are supplied with the following current references: $I_1 = I_3 = I_4 = 0$ A and $I_2 = 9$ A. The self-inductance is then both over- and underestimated to investigate errors in both directions. Figure 5.17 displays the true and estimated x-axis results with the optimal RNM. These results may serve as benchmark for comparison to the results of the over- and underestimation of the inductance.

Figure 5.18 displays the error between the estimated and true positions for the case where the inductances are overestimated by 22 %. The change in inductance influences the gain between the true and estimated positions which is evident when the linearity of the result is investigated as displayed in figure 5.19. The gain between the estimated and true positions is 0.8 where it should be close to 1. The linearity for the overestimated inductance case is however still extremely good: 2.72 %.

Figures 5.20 and 5.21 respectively display the error in estimated position and linearity for the case where the inductance is underestimated by 22 %. Large errors are present near the backup bearing limits where the self-sensing saturates into the limits. At the negative x-axis backup bearing, this is caused by the clamping of the estimated position. The estimated position should in fact be less than -250 µm and the integrator keeps on integrating in the negative direction to correct the error. Once the error reverses the integrator takes a short period of time to integrate in the opposite direction and correct the error. The error at the positive x-axis backup bearing location is caused by magnetic saturation. Ignoring the regions where the position estimate moves into its limits the linearity is obtained as 4.36 %.

The effect of a relatively slow flux excursion is also investigated by suspending the rotor in the zero x, y position with an integral gain included in the position control and applying a disturbance force with a ramp function in the x-axis. The disturbance force starts at 50 ms with a value of 0 N and is linearly increased to 300 N at 300 ms. The results are first obtained without a gain error in

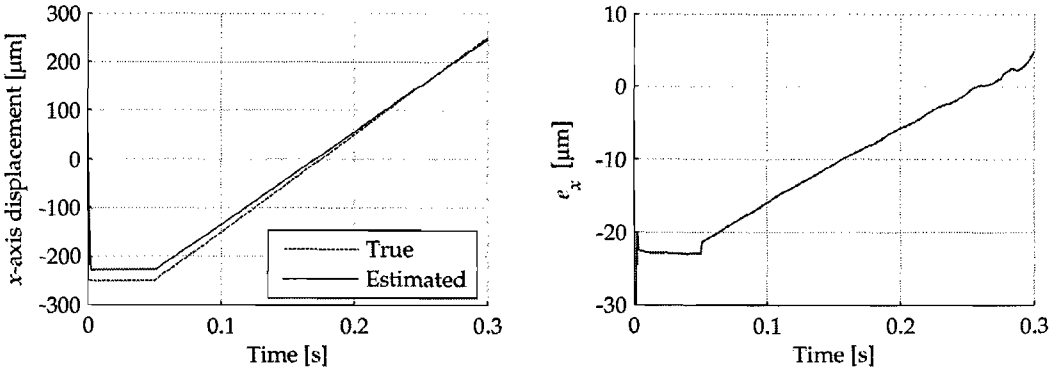

Figure 5.17: Self-sensing results with optimal RNM ($I_2 = 9$ A and $I_1 = I_3 = I_4 = 0$ A)

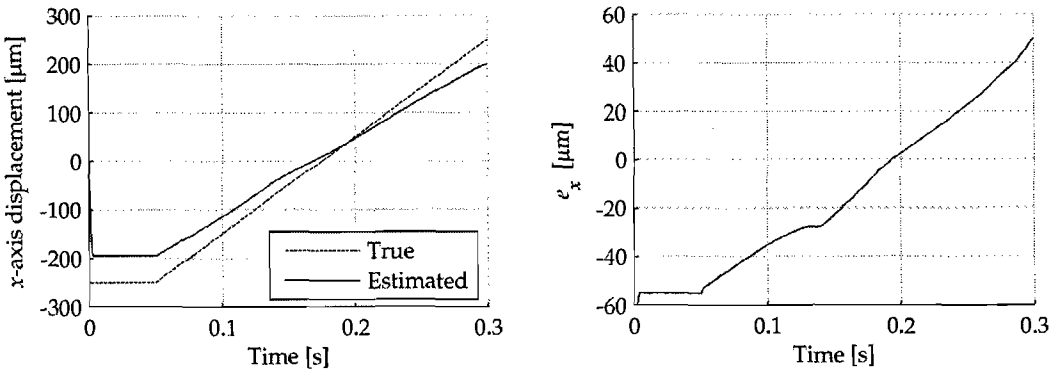

Figure 5.18: Self-sensing results with 22 % overestimation of inductances ($I_2 = 9$ A and $I_1 = I_3 = I_4 = 0$ A)

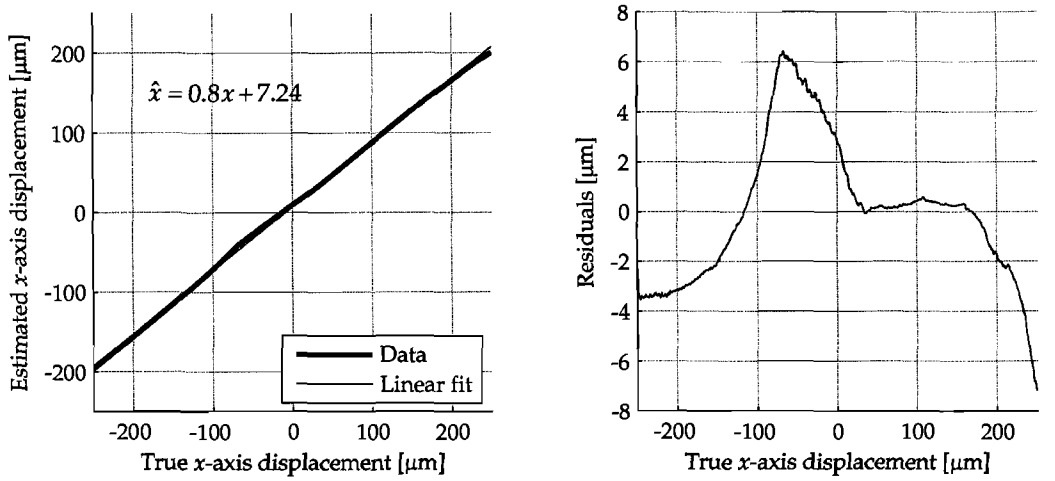

Figure 5.19: Self-sensing x-axis linearity (22 % overestimation of inductances)

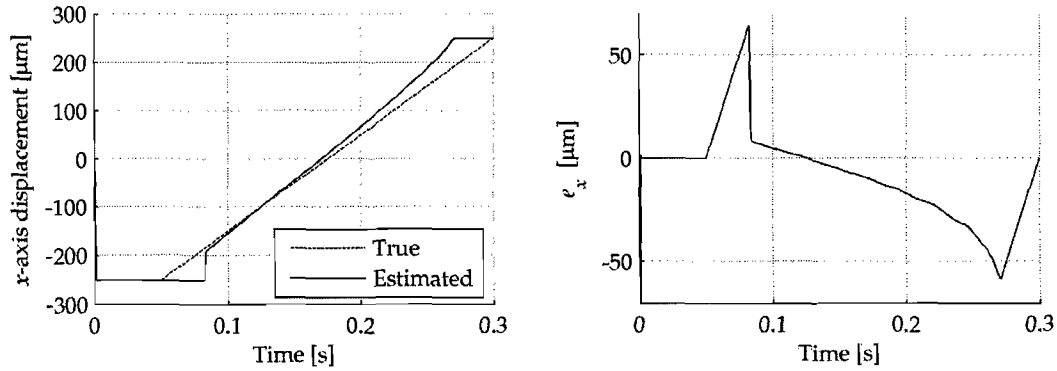

Figure 5.20: Self-sensing results with 22 % underestimation of inductances ($I_2 = 9$ A and $I_1 = I_3 = I_4 = 0$ A)

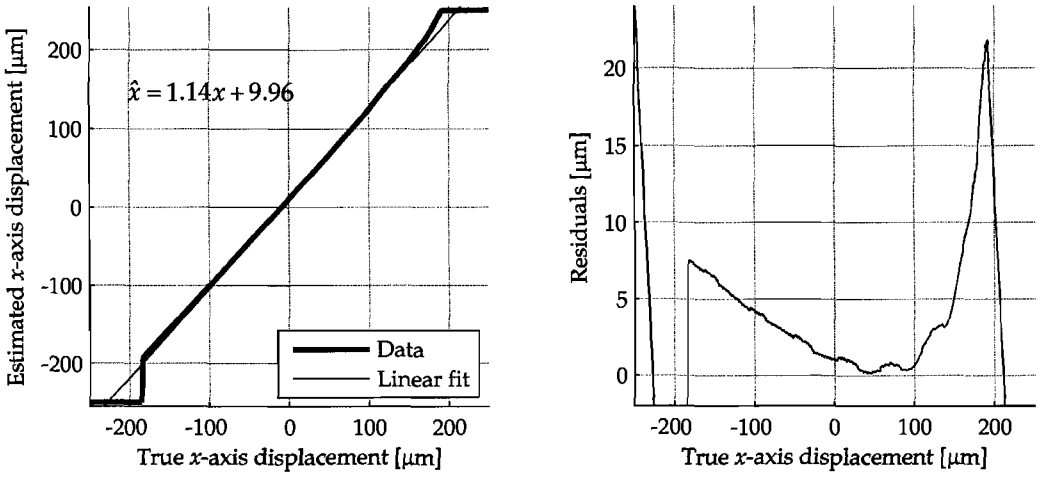

Figure 5.21: Self-sensing x-axis linearity (22 % underestimation of inductances)

the material permeability to use as benchmark. Figure 5.22 displays the true and estimated x-axis results for the ramped disturbance force in the positive x-axis direction. It can be seen that as soon as the disturbance force is applied the estimated position moves to 30 μm and the integral term is too small to bring it back to zero. Unfortunately the integral term cannot be increased since that will destabilise the system and the simulation time cannot be increased due to computer memory constraints. Fortunately the displacement in the x-axis does not increase beyond the 30 μm offset and the results can be used for the present investigation.

Figure 5.23 displays the flux densities in poles P_4 and P_8. As the force increases in the positive x-axis direction the flux density decreases and increases in poles P_4 and P_8 respectively. Figure 5.24 displays the demodulated coil currents $|I_2|$, $|\hat{I}_2|$ and $|I_4|$, $|\hat{I}_4|$ which correlate closely.

Figure 5.25 displays the estimated and true positions for the same force ramp with 22 % underestimation of the inductances. As can be seen there is an almost 50 % increase in the offset between the estimated and true position. The flux density results are not shown since they closely correlate with that of figure 5.23. Figure 5.26 displays the demodulated coil currents $|I_2|$, $|\hat{I}_2|$ and $|I_4|$, $|\hat{I}_4|$ for the case where the inductance is underestimated with 22 %. From the figure it is clear that the TSM and RNM demodulated coil currents also display a 22 % offset with respect to each

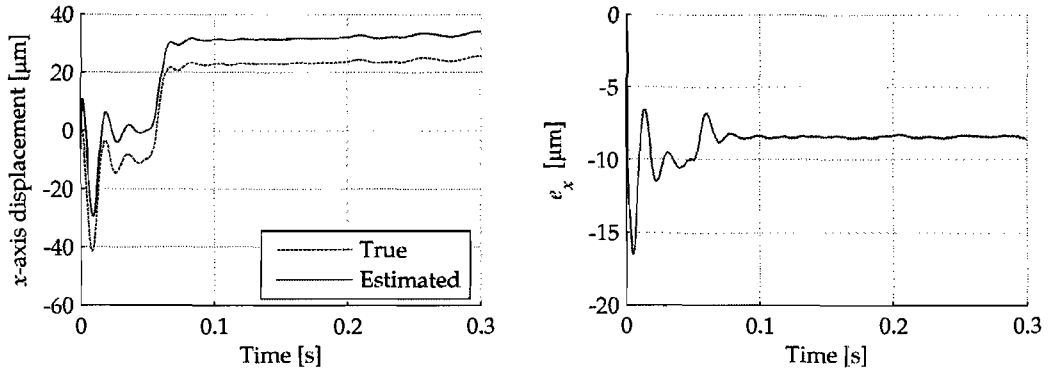

Figure 5.22: Ramped disturbance force position results (0 to 300 N at 50 to 300 ms)

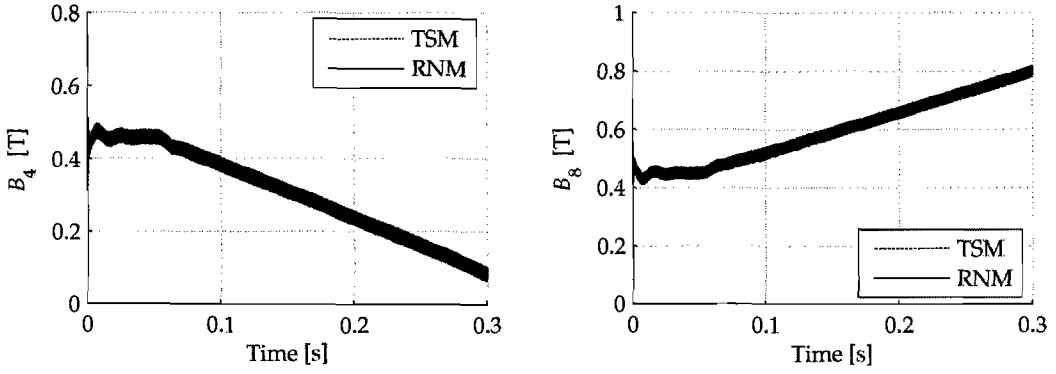

Figure 5.23: Ramped disturbance force flux density results (0 to 300 N at 50 to 300 ms)

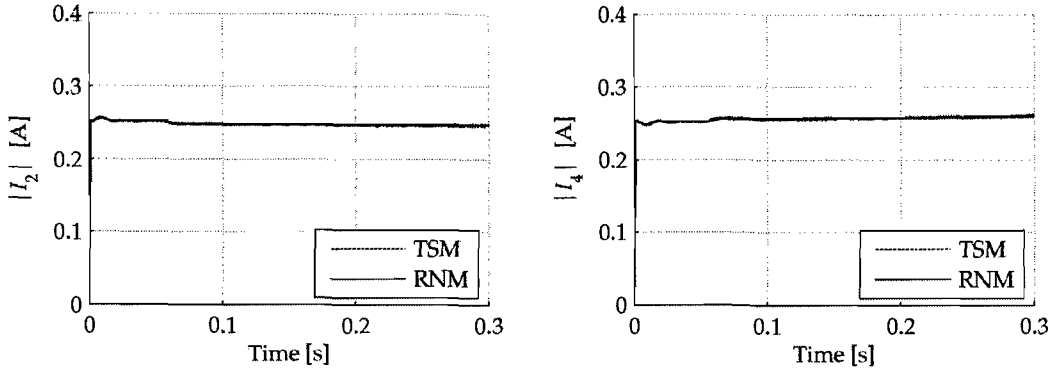

Figure 5.24: Ramped disturbance force demodulated current results (0 to 300 N at 50 to 300 ms)

other.

Finally the effect of the gain error between the RNM and TSM's material permeability is investigated by applying a sinusoidal disturbance force. The results shown in figure 5.10 will be reproduced with the error included in order to investigate the effect. The results displayed in figure 5.27 closely correlate with the results in figure 5.10. This suggests that the error in material permeability does not have a big impact on the system performance under these test conditions.

To further investigate the effect, the nonlinear material behaviour is removed from the RNM and the test is repeated. Figure 5.28 displays the result when a linear RNM is used in the position estimation scheme while the TSM remains nonlinear. The results seem almost unchanged suggesting that the excursion on the *B-H* curve is negligible for the case of the 50 N disturbance force.

The reason why the results of both figures 5.27 and 5.28 correlate closely with that of figure 5.10 is that only a small flux excursion is present in these analyses. The magnetic circuit reluctance comprises the air gap reluctance which is a function of rotor position and the magnetic material reluctance which is a function of flux density. For the case at hand the flux density excursion is negligible and the material reluctance can be assumed constant. The large offsets in the demodulated currents between the various analyses are eliminated by the differential configuration. The change in demodulated coil current amplitude is now only a function of the rotor position (air gap reluctance) and there is no additional error in the estimated position. In figures 5.18 and 5.20 an error in the estimated position is present since a large excursion in flux density is experienced.

5.4 Summary of performance evaluation

The self-sensing scheme presented in the thesis displays excellent linearity when the material nonlinearity and duty cycle variation are eliminated. This demonstrates that it will be possible to obtain excellent linearity results if the model utilised in the self-sensing scheme accurately models the effects of duty cycle variation and material nonlinearity.

From the results it was shown that it is very difficult to investigate duty cycle effects since a change in duty cycle also induces cross-coupling effects. A static cross coupling analysis showed that the exclusion of mutual coupling terms results in large errors in the estimated position.

Saturation was also investigated and results showed that saturation is capable of system destabilisation. The problem is addressed by implementing a novel demodulated current weighting scheme which is able to estimate the position even with one of the two actuators in deep

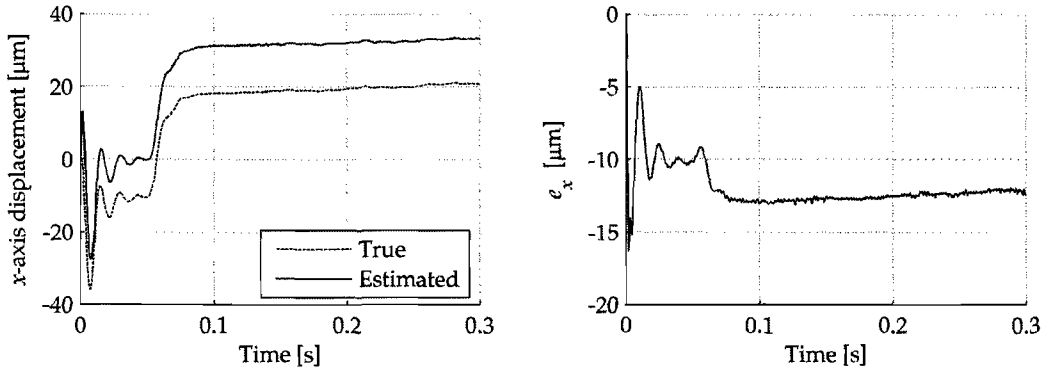

Figure 5.25: Ramped disturbance force position results with 22 % underestimation of inductances (0 to 300 N at 50 to 300 ms)

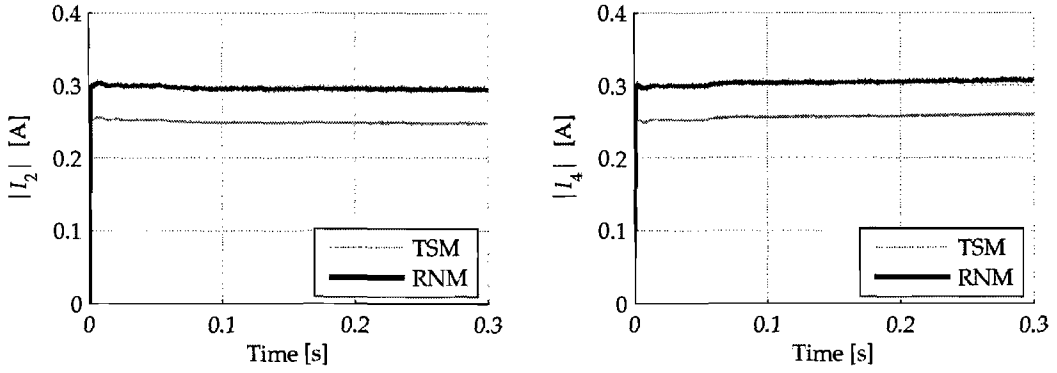

Figure 5.26: Ramped disturbance force demodulated current results with 22 % underestimation of inductances (0 to 300 N at 50 to 300 ms)

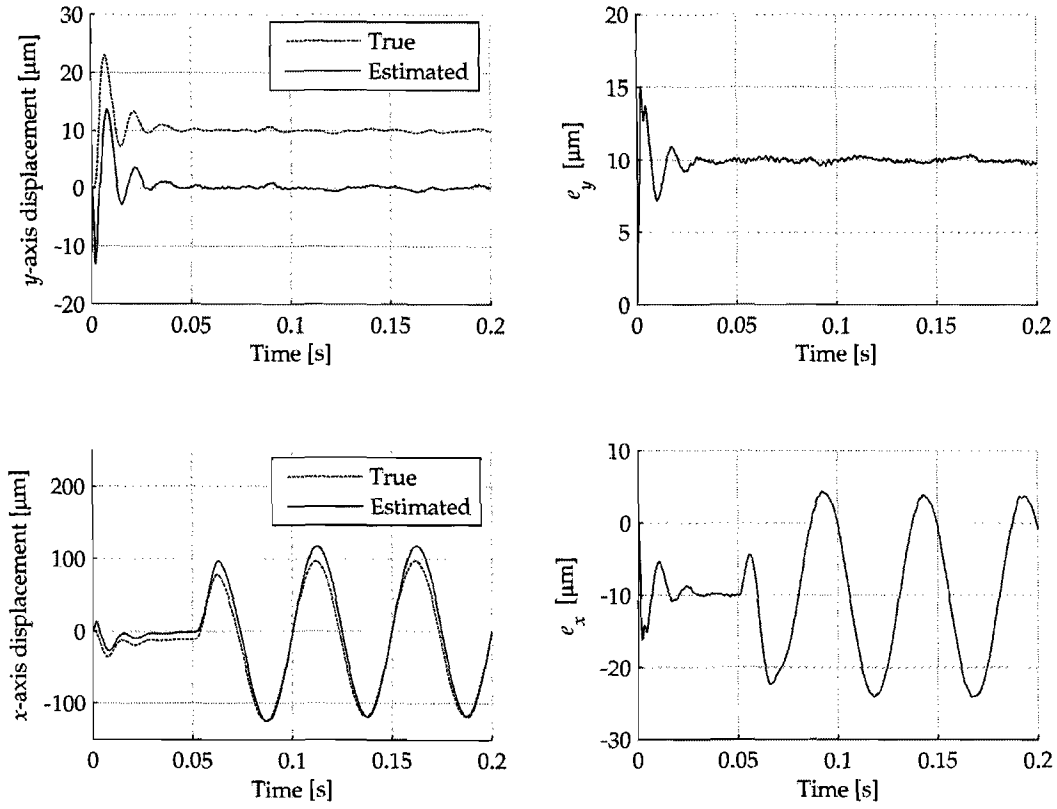

Figure 5.27: Modelling uncertainty (Disturbance force of 50 N on x-axis from 50 ms, 22 % underestimation)

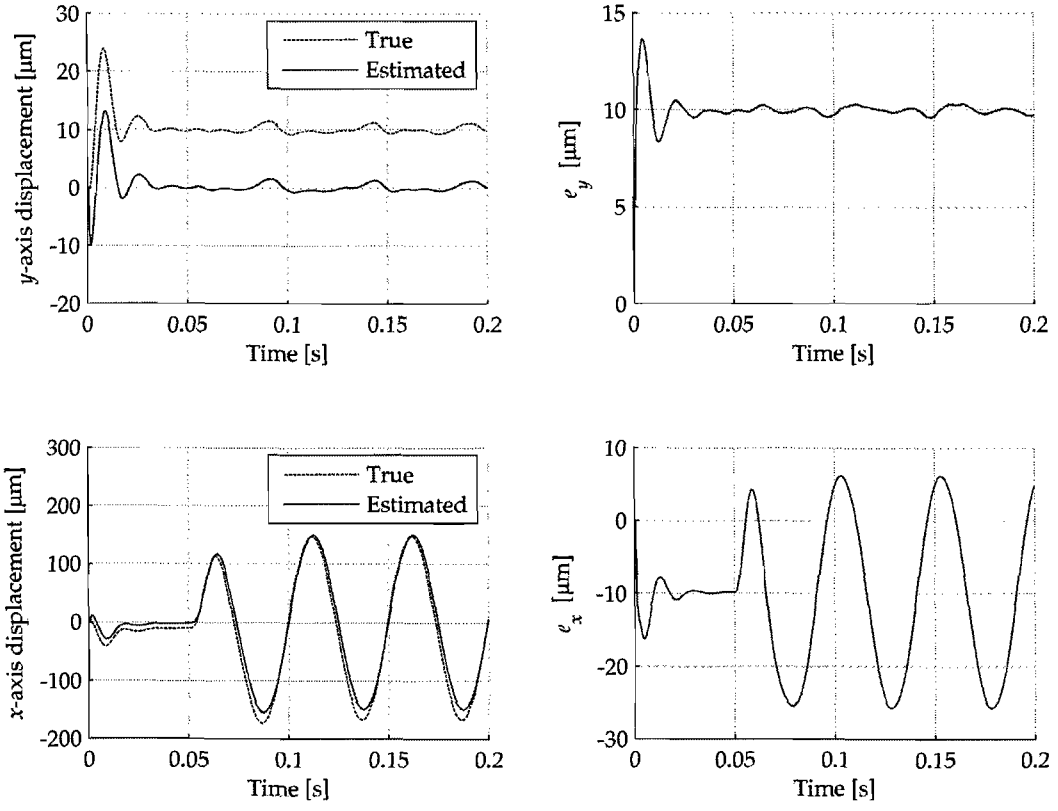

Figure 5.28: Modelling uncertainty (Disturbance force of 50 N on x-axis from 50 ms, linear RNM)

saturation.

A dynamic cross-coupling investigation showed that the elimination of mutual inductance terms from the model employed in the self-sensing scheme may destabilise the system. When the mutual inductance terms are included, the self-sensing scheme is able to stably suspend the rotor with reduced levels of error.

The bandwidth of the self-sensing scheme is shown to be extremely low (270 Hz). This is undesirable for an AMB system and future work is needed to improve the bandwidth.

The self-sensing system's sensitivity was shown to be inadequate for commercial application with the experimental system parameters as they were. By lowering the bias current level and including an integral gain in the position controller, the sensitivity was lowered to an acceptable level for practical application. Future work is needed to further optimise the self-sensing scheme for better sensitivity results.

In the modelling uncertainty section it was demonstrated that the presence of uncertainty in the material permeability is a problem when a large flux density excursion is present. It is therefore important to ensure that the modelled and experimental material characteristic correlate closely. This is however a very difficult task.

Chapter 5 is concerned with the performance evaluation of the novel MIMO parameter estimation scheme. It is demonstrated that the self-sensing scheme is able to suspend the rotor with excellent linearity and relatively good precision. The chapter highlights the importance of including the mutual coupling terms in the model if they are present in the experimental system. The problem of saturation is addressed using a novel approach of current weighting. The current weighting scheme proves successful in alleviating the problems associated with saturation. The dynamic analysis established that the self-sensing bandwidth is poor. The system parameters also needed to be adjusted to obtain adequate sensitivity results. Future work is therefore needed to optimise the self-sensing schemes' performance in terms of bandwidth and sensitivity. The largest source of modelling uncertainty is identified as the nonlinear nature of the magnetic material. It is concluded that if high accuracy is required, it is crucial to accurately match the nonlinear material behaviour of the self-sensing model to that of the experimental system.

CHAPTER 6

Conclusions and recommendations

6.1 Introduction

Although there are a number of successful industrial applications of active magnetic bearings (AMBs), the technology has not yet reached its full potential. In the ongoing drive for even wider acceptance and application of AMB technology in industry, AMB vendors and researchers are striving to make AMBs more reliable and economical. Many efforts in this regard are under way including system optimisation as a whole and component integration.

Position sensors and the associated cabling represent a large portion of the capital layout for small and medium size AMB systems. In the drive for cost reduction, researchers and AMB vendors have investigated and developed low cost position sensors such as the ones proposed in [17], [18], [19]. These sensors however still have the drawbacks of additional wiring to and from the AMB system as well as non-collocation of the sensor and actuator; two problems that may be eliminated by implementing a suitable self-sensing scheme.

The self-sensing approach adopted by the present work is based on the amplitude modulation approach utilising the switching amplifier ripple as high frequency source. The switching amplifier ripple as high frequency source is used since it is readily available in the AMB system and requires the least amount of additional components. The decision of the amplitude modulation approach is based on the findings of recent experiments [4], [52], which achieved sensitivity levels below the best achievable levels predicted by [27]. Recent work [53] attributes this phenomenon to an over simplification of the model used in [27]. The work in [28], [53], [55] establishes that the use of switching ripple for self-sensing leads to increased robustness.

Limitations and shortcomings of previously implemented self-sensing systems based on the amplitude modulation approach, utilising the switching amplifier ripple as high frequency source, include:

Cross-coupling - Cross-coupling in the self-sensing context refers to the phenomenon where a change in position or force in one axis induces an error in the estimated position of the perpendicular axis. In [8] it was demonstrated that ignoring cross-coupling may lead to failure of the self-sensing scheme under certain conditions. In the past the problem was dealt with by mechanically separating the individual pole pairs. This however has the effect of increasing the manufacturing cost of the magnetic bearing.

Ripple amplitude - In [53] and [55] it was demonstrated that, regardless of the signal processing approach, the robustness of the self-sensing AMB is determined by the ripple amplitude. The performance of self-sensing approaches will therefore tend to improve with the presence

of high levels of high frequency current ripple. According to Maslen [7] this limitation seems fundamental and implies that robust self-sensing systems will be less efficient in terms of electrical power consumption.

Eddy currents - Eddy currents reduce the magnetic material permeability which in turn reduces the overall sensitivity of the magnetic actuator as a sensor. The main parameters influencing the eddy currents are the excitation frequency and the thickness of the lamination material that is used.

Saturation - Saturation is probably the most vexing problem faced by self-sensing researchers [7]. Studies ([32], [46], [52] amongst others) have shown that the sensitivity of the switching ripple to air gap may actually reverse due to saturation leading to ambiguous position estimates.

The purpose of the thesis was to address some of the aforementioned shortcomings of current self-sensing techniques by implementing an improved model for the heteropolar magnetic bearing. To alleviate the problem of cross-coupling a coupled reluctance network model (RNM) was incorporated into a nonlinear parameter estimation scheme to realise a self-sensing system. The RNM is supplied with x and y position estimates as well as the demodulated coil voltages and average coil currents. The RNM produces estimates of the demodulated coil currents that are compared to the actual demodulated coil currents to produce error signals. The error signals are in turn fed to PI controllers which produce position estimates for x and y. The coupled RNM successfully incorporated cross-coupling effects into the self-sensing scheme as demonstrated in chapter 5.

With regards to the ripple amplitude, the focus of the present work was to realise a robust self-sensing system and the duty cycle was therefore limited (25 % to 75 %) to ensure adequate high frequency ripple. The limitation in duty cycle limits the realisable coil voltages to $+0.5V_p$ and $-0.5V_p$. The voltage on the power amplifier dc bus (V_p) was therefore doubled to ensure that the power bandwidth of the AMB stays unchanged. The ripple amplitude therefore never reduces to zero and is larger than under normal conditions which implies higher losses as well as better robustness.

The eddy current effect was addressed by choosing the switching frequency as low as possible (20 kHz; just above the audible range) and by including eddy currents in the model utilised in the self-sensing scheme.

Magnetic saturation was addressed by including magnetic material nonlinearity in the RNM. This was accomplished by determining the flux distribution through a process of iteration. Results obtained from the 40 node RNM were shown to closely correlate with results generated by a finite element method (FEM) model with 80,000 nodes. The fact that RNMs are much faster to solve than their FEM counterparts and their ability to precisely map the magnetic behaviour of magnetic bearings, render them the preferred option for online implementation in a self-sensing scheme.

The proposed self-sensing scheme was evaluated in a simulation environment which utilises a transient simulation model (TSM). The TSM incorporates all of the important aspects that influence self-sensing performance including eddy currents, cross-coupling and the magnetic material hysteretic behaviour. Results showed that a practically useful self-sensing system may be feasible. The self-sensing performance is however inferior to that of a dedicated position sensor in terms of system sensitivity and bandwidth.

6.2 Unique contribution

Five original contributions are made during the course of the thesis which are focused on the current shortcomings of the models used in self-sensing schemes. The contributions are listed in

order of increasing importance:

Frequency shifted model: Previous work on nonlinear estimators made use of analogue inductor models [32], [52]. The RNM used in the parameter estimator of the present work, models the switching frequency impedance alone and is therefore a frequency shifted model. The use of this frequency shifted model in the parameter estimation approach implies that the model no longer needs to be analogue and can be solved at a fixed frequency. For the present work the PI loop of the estimator is solved at 100 kHz and acceptable levels of performance were also obtained when the loop was implemented at 50 kHz. This is an important contribution towards the practical implementation of a coupled model which incorporates cross-coupling effects.

Air gap fringing: One contribution of the present work is the identification of the air gap reluctance and more specifically air gap fringing as a parameter which may introduce large modelling errors. The modelling of the air gap reluctance is generally done by neglecting fringing effects [4], [32], [52]. In [8] the air gap reluctance was determined through integration to incorporate pole face curvature effects which also neglects fringing effects. Meeker [11] incorporated fringing by determining a more accurate air gap reluctance with a FEM analysis. For this study the rotor was however only positioned in the centre position.

In the present work (chapter 3) the air gap reluctance is also determined using a magnetostatic FEM analysis for a range of possible x and y rotor positions and the information is stored in a lookup table. Neglecting the air gap fringing in the case at hand, results in a 34 % error in the air gap reluctance which directly translates to a 34 % error in estimated position.

Complex material permeability: Another unique contribution lies in the modelling of the eddy currents with a complex permeability which is experimentally determined. The experimental measurement is conducted using a number of toroidal discs of the silicon lamination material and exciting the stack with a switching PA through a primary coil. The experimentally determined complex permeability is then incorporated into a lookup table with flux density as indexing parameter. The introduction of the experimentally determined μ_{fd} term, reduced the worst case error in the $|Z_{11}|$ parameter from 60 % to 22 % which is a marked improvement. The experimentally determined μ_{fd} term improves the modelling accuracy and therefore also the accuracy of the self-sensing scheme.

Saturation Saturation is a vexing problem [7] and in chapter 5 it is demonstrated that the proposed self-sensing scheme destabilises when one of the actuators moves into deep saturation. This is caused by reversal of the sensitivity of the switching ripple to air gap [7], [46], [52]. A number of solutions to the problem have been suggested. In [8] it is suggested that the problem may be solved by using both geometrically opposing pole pairs to estimate position. When ambiguous position estimates occur as a result of saturation, two possible positions will result of which only the correct one will be present in both estimates. In [9] a multiple input multiple output (MIMO) parameter estimation scheme is proposed and since then self-sensing literature has generally stayed away from the problem. In a recent article [7] this area was identified as relatively ripe for contribution.

In the present work the problem is solved by the novel approach presented in chapter 5 where a simple current weighting function is implemented. Two geometrically opposing pole pairs are driven in the so-called differential mode to form a single actuator for one degree of freedom. Weights are then assigned to the demodulated currents of each coil to ensure that the coil of the pole pair with the lowest flux density, contributes the most to the position estimation process. The weighting scheme proves effective and is able to accurately

estimate the position when no more than one of the two pole pairs is in saturation at any given time.

MIMO parameter estimation scheme: A previous study [9] suggested the use of a MIMO parameter estimation scheme to overcome problems associated with saturation. In [8] it is suggested that a coupled RNM may be used to solve problems caused by cross-coupling. The present work therefore focuses on developing a novel MIMO parameter estimator scheme. The demonstration of feasibility and basic functionality of such a scheme is one of the most important contributions of the thesis. At the heart of the parameter estimator scheme lies a coupled RNM of the heteropolar magnetic bearing. As a first approach the estimation of the x and y positions are separated and done individually. The coupled RNM is then simplified to a linear system without coupling between the different pole pairs, to perform a parameter estimator stability analysis. The analysis proved adequate to predict possible PI controller parameters for stable operation of the parameter estimator.

6.3 Future work

As stated in chapter 1, the fundamental goal of this thesis was to develop an improved model for self-sensing heteropolar magnetic bearings. The improved model had to address issues such as cross-coupling and saturation which degrade self-sensing system performance. Although the study significantly contributed towards alleviating some of the modelling challenges, the study reveals some definite outstanding problems that warrant further investigation:

MIMO parameter estimation scheme: In the present work the estimation of the x and y rotor positions is accomplished with two separate parameter estimators and one coupled RNM. Further work is needed to realise a coupled MIMO parameter estimation scheme which estimates both x and y rotor positions using information of all four pole pairs simultaneously. A μ-synthesis approach for stability analysis is recommended. This method is however based on a state space model for the system; a fundamental challenge due to the nonlinear nature of the system.

Modelling uncertainty: In chapter 5 it was shown that when uncertainty is introduced in the material permeability, the parameter estimator reduces the error between the differences of geometrically opposing pole pairs' demodulated coil currents to zero but the true and estimated coil currents display offsets.

The uncertainty may possibly be addressed by introducing a second parameter estimator which estimates the material complex permeability, or estimate a correction factor for the permeability, in order to minimise the errors between the measured and modelled demodulated coil currents of both the opposing electromagnets. The possibility of implementing a second estimator and its impact on the stability of the system must be investigated. The effect of modelling uncertainty could be more thoroughly investigated through an elaborate Monte Carlo analysis.

Improved robustness: Self-sensing system robustness proves to be inferior to that of dedicated position sensor systems. Further work is therefore needed to optimise the position estimation scheme in order to achieve better system robustness. Issues that may be looked at include the demodulation process that was used and the use of both the amplitude and phase values of the demodulated currents as input to the parameter estimator.

Bandwidth: The bandwidth of the self-sensing system is very low and may pose problems for certain AMB applications. The simple PI controller in the estimator may be replaced with a more complex controller which may improve the bandwidth of the estimator.

Practical implementation: Once the self-sensing approach is proven fundamentally sound, the practical implementation of the MIMO parameter estimation scheme most certainly warrants future work. In order to realise a practical implementation, much work is needed to optimise the RNM for high speed implementation. In this regard the numerical iteration process, which is used to determine the flux distribution in the RNM, needs to be revised to optimise its speed of convergence. The cycle time of the parameter estimator PI control loop (rate at which the RNM must be evaluated) must be optimised with a detailed analysis.

Results from chapter 5 suggest that the change in the magnetic material reluctance as a result of flux excursions in the linear portion of the *B-H* curve, may be neglected with small error in estimated position. With this in mind the reluctance of the paths which link the different pole pairs may be assumed constant. A further simplification may be to reduce the flux paths to four independent paths, one for each pole pair. The flux in each pole pair can then be determined individually and the saturation effect included. The mutual inductance terms must however be retained and will become constants that may be determined prior to implementation. This will include the dominating cross-coupling effects, greatly reduce the computational intensity and possibly facilitate practical implementation.

The development of a state space model of the AMB system which includes all nonlinear phenomena will facilitate the analysis of the proposed MIMO self-sensing scheme. Such a model will allow established methodologies e.g. μ-synthesis to optimise modelling accuracy as well as estimator performance to achieve acceptable levels of system robustness.

6.4 Closure

The purpose of the thesis was to establish an improved model for the eight-pole heteropolar self-sensing magnetic bearing. The improved model had to facilitate position estimation with higher levels of accuracy through reduced sensitivity to phenomena such as cross-coupling and saturation.

In order to accomplish lower levels of sensitivity to phenomena such as cross-coupling and saturation a MIMO parameter estimator approach was adopted as suggested by [9]. At the heart of the estimator lies a coupled RNM as proposed by [8]. The RNM which is based on work done by Meeker [11] was further optimised though a process of model refinement as discussed in chapter 3. The refinement process facilitated the choice of leakage flux path as well as the further refinement of the air gap reluctance and complex material permeability by implementing lookup tables. The MIMO parameter estimation scheme together with the refined RNM yielded a self-sensing scheme with lower levels of sensitivity to cross-coupling and saturation. It was demonstrated in chapter 5 that it is possible to realise a self-sensing AMB with sensitivity levels that are considered acceptable for unrestricted long-term operation, using the improved model.

One of the most important contributions of the present work is that it demonstrates the possibility of constructing a MIMO parameter estimation self-sensing scheme, with a coupled RNM at the heart, that alleviates problems such as saturation and cross-coupling. This was however only a first approach to demonstrate the suitability of the improved RNM for such a scheme and future work is needed to analyse and optimise the MIMO parameter estimation scheme.

Continued work is needed on a theoretical basis which may explain the phenomenon where recent experiments, [4] and [52], achieved sensitivity levels below the best achievable levels predicted by [27]. The theoretical basis may then serve as a platform from which new and more robust self-sensing schemes may be developed.

The self-sensing scheme proposed in the thesis was difficult to stabilise and displayed inferior levels of sensitivity and bandwidth compared to dedicated position sensors. A linear (state space) model of the system is required to facilitate an optimisation process.

There are two commercial applications of the self-sensing technology to date and both place moderate requirements on the position estimation. Much work is still needed to realise a self-sensing scheme that will meet more stringent requirements. Self-sensing therefore remains a tough challenge with several unaddressed issues.

BIBLIOGRAPHY

[1] M. Kasarda, "An overview of active magnetic bearing technology and applications," *The Shock and Vibration Digest*, vol. 32, no. 2, pp. 91–99, March 2000.

[2] Y. Suyuan, Y. Guojun, S. Lei, and X. Yang, "Application and research of the active magnetic bearing in the nuclear power plant of high temperature reactor," in *Proceedings of the 10th International Symposium on Magnetic Bearings*, Martigny, Switzerland, Aug. 2006, pp. 1–7.

[3] A. Katoh and T. Masuzawa, "Optimized design for a hybrid magnetic bearing for the artificial heart," in *Proceedings of the 10th International Symposium on Magnetic Bearings*, Martigny, Switzerland, Aug. 2006, pp. 1–7.

[4] A. Schammass, "A self-sensing active magnetic bearing: Modulation approach," PhD thesis, Swiss Federal Institute of Technology Lausanne - EPFL, Lausanne, Switzerland, July 2003.

[5] E. H. Maslen, "State-of-the-art and future directions for AMB control and applications," in *Proceedings of the Sixth International Symposium on Magnetic Suspension Technology*, Torino, Italy, Oct. 2001.

[6] M. Brunet and B. Wagner, "Innovation: Self-sensing technology, simplified mechanical design," S2M News, number 5, Dec. 2005.

[7] E. H. Maslen, "Self-sensing for active magnetic bearings: overview and status," in *Proceedings of the 10th International Symposium on Magnetic Bearings*, Martigny, Switzerland, Aug. 2006, pp. 13–19.

[8] N. Skricka and R. Markert, "Influence of cross-axis sensitivity and coordinate coupling on self-sensing," in *Proceedings of the Sixth International Symposium on Magnetic Suspension Technology*, Turin, Italy, Oct. 2001, pp. 179–184.

[9] M. D. Noh and E. H. Maslen, "Self-sensing magnetic bearings (Part II)," in *Proceedings of the Fifth International Symposium on Magnetic Bearings*, Kanazawa, Japan, Aug. 1996, pp. 113–118.

[10] A. Schammass, R. Herzog, P. Bühler, and H. Bleuler, "New results for self-sensing active magnetic bearings using modulation approach," *IEEE Transactions on Control Systems Technology*, vol. 13, no. 4, pp. 509–516, Jul. 2005.

[11] D. C. Meeker, E. H. Maslen, and M. D. Noh, "An augmented circuit model for magnetic bearings including eddy currents, fringing, and leakage," *IEEE Transactions on Magnetics*, vol. 32, no. 4, pp. 3219–3227, July 1996.

[12] P. Alves and B. Alavi, "Magnetic bearing improvement program at NOVA," in *Proceedings of the International Gas Turbine & Aeroengine Congress and Exhibition*, Birmingham, United Kingdom, 1996.

[13] G. Schweitzer, H. Bleuler, and A. Traxler, *Active Magnetic Bearings: Basics, Properties and Applications of Active Magnetic Bearings*, authors reprint ed. Zurich, Switzerland: Authors working group, 2003.

[14] H. Bleuler, "A survey of magnetic levitation and magnetic levitation types," *JSME International Journal, Series III*, vol. 35, no. 3, pp. 335–342, Sep. 1992.

[15] J. Boehms, R. Gerber, and N. Kiley, "Sensors for magnetic bearings," *IEEE Transactions on Magnetics*, vol. 29, no. 6(2), pp. 2962–2964, Nov. 1993.

[16] D. Shin and J. Kim, "Design and implementation of PCB-type capacitance displacement sensor collocated with magnetic bearings," *Sensors and Actuators A: Physical*, vol. 71, pp. 223–229, 1998.

[17] R. Larsonneur and P. Bühler, "New radial sensor for active magnetic bearings," in *Proceedings of the 9th International Symposium on Magnetic Bearings*, University of Kentucky, Lexington KY, USA, Aug. 2004.

[18] P. Bühler, "Device for contact-less measurement of distances in multiple directions," European Patent No. EP 1 422 492, Jun. 2004.

[19] L. Burdet, T. Maeder, R. Siegwart, P. Buehler, and B. Aeschlimann, "Thick-film radial position sensor for high temperature active magnetic bearings," in *Proceedings of the 10th International Symposium on Magnetic Bearings*, Martigny, Switzerland, Aug. 2006, pp. 204–205.

[20] B. Hanson and M. Levesley, "Self-sensing applications for electromagnetic actuators," *Sensors and Actuators A: Physical*, vol. 116, no. 2, pp. 345–351, Jun. 2004.

[21] G. Genta and S. Carabelli, "Noncollocation effects on the rigid body rotordynamics of rotors on AMB," in *Proceedings of the Seventh International Symposium on Magnetic Bearings*, ETH Zurich, Switzerland, Aug. 2000, pp. 63–68.

[22] D. Vischer and H. Bleuler, "A new approach to sensorless and voltage controlled AMBs based on network theory concepts," in *Proceedings of the Second International Symposium on Magnetic Bearings*, Tokyo, Japan, Jul. 1990, pp. 301–306.

[23] ——, "Self-sensing active magnetic levitation," *IEEE Tansactions on Magnetics*, vol. 29, no. 2, pp. 1276–1281, Mar. 1993.

[24] L. Kucera, "Robustness of self-sensing magnetic bearing," in *Magnetic Bearing Industrial Conference*, Alexandria, USA, 1997.

[25] Y.-K. Tzeng and T. C. Wang, "A novel compensating approach for self-sensing maglev systems with controlled-PM electromagnets," *IEEE Transactions on Magnetics*, vol. 31, no. 6, pp. 4208–4210, Nov. 1995.

[26] T. Mizuno, K. Araki, and H. Bleuler, "Stability analysis of self-sensing magnetic bearing controllers," *IEEE Transactions on Control Systems Technology*, vol. 4, no. 5, pp. 572–579, Sep. 1996.

[27] N. Morse, R. Smith, B. Paden, and J. Antaki, "Position sensed and self-sensing magnetic bearing configurations and associated robustness limitations," in *Proceedings of the 37th IEEE Conference on Decision and Control*, vol. 3, Tampa, Frorida USA, Dec. 1998, pp. 2599–2604.

[28] E. H. Maslen, "Formal parameter estimation for self-sensing," in *Proceedings of the 10th International Symposium on Magnetic Bearings*, Martigny, Switzerland, Aug. 2006.

[29] I. TC108/SC2/WG7, "Mechanical vibration: Vibration of rotating machinery equipped with active magnetic bearings, part 3: Evaluation of stability margin," ISO Standard, ISO 14839-3, 2004.

[30] N. M. Thibeault and R. S. Smith, "Magnetic bearing measurement and associated robustness and performance limitations," *ASME Journal of Dynamic Systems, Measurement, and Control*, vol. 124, pp. 589–598, Dec. 2002.

[31] T. Mizuno and H. Bleuler, "Self-sensing magnetic bearing control system design using the geometric approach," *Control Engineering Practice*, vol. 3, no. 7, pp. 925–932, Jan. 1995.

[32] M. D. Noh, "Self-sensing magnetic bearing driven by a switching power amplifier," PhD Thesis, University of Virginia, Virginia, USA, Jan. 1996.

[33] R. Mueller, F. Bedenig, H. Bleuler, T. Mizuno, H. Tanaka, H. Ueyama, and A. Kubo, "Position sensorless AMB in four degrees of freedom," in *Proceedings of the Fifth International Symposium on Magnetic Bearings*, Kanazawa, Japan, Aug. 1996, pp. 101–106.

[34] M. Mirishita and H. Ito, "The self-gap-detecting electromagnetic suspension system with robust stability against variation of levitation mass," in *Proceedings of the International Symposium on Power Electronics, Electrical Drives, Automation and Motion*, Taorima, Italy, May 2006.

[35] Y. Okada, K. Matsuda, and B. Nagai, "Sensorless magnetic levitation control by measuring the PWM carrier frequency component," in *Proceedings of the Third International Symposium on Magnetic Bearings*, Alexandria, VA, USA, Jul. 1992, pp. 176–183.

[36] K. K. Sivadasan, "Analysis of self-sensing active magnetic bearings working on inductance measurement principle," *IEEE Transactions on Magnetics*, vol. 32, no. 2, pp. 329–334, Mar. 1996.

[37] M. D. Noha and E. H. Maslen, "Self-sensing magnetic bearings using parameter estimation," *IEEE Transactions on Instrumentation and Measurement*, vol. 46, no. 1, pp. 45–50, Feb. 1997.

[38] P. Tsao, S. R. Sanders, and G. Risk, "Self-sensing homopolar magnetic bearing: Analysis and experimental results," in *Proceedings of the 1999 IEEE Industry Applications Conference - 34th IAS Annual Meeting*, 1999, pp. 2560–2565.

[39] D. T. Montie and E. H. Maslen, "Self-sensing in fault tolerant magnetic bearings," *ASME Journal of Engineering for Gas Turbines and Power*, vol. 123, p. 864870, Oct. 2001.

[40] T. Kurosu, K. Matsuda, and Y. Okada, "Self-sensing control technique of self-bearing motor," in *Proceedings of the Eighth International Symposium on Magnetic Bearings*, Mito, Japan, Aug. 2002, pp. 293–298.

[41] M. Komori and C. Shiraishi, "Superconducting bearings assisted by self-sensing AMBs in liquid nitrogen," *JMSE International Journal, Series C*, vol. 46, no. 2, pp. 397–402, 2003.

[42] L. Li, T. Shinshi, and A. Shimokohbe, "State feedback control for active magnetic bearings based on current change rate alone," *IEEE Transactions on Magnetics*, vol. 40, no. 6, pp. 3512–3516, Nov. 2004.

[43] R. L. Maresca, "A general method for designing low-temperature drift, high-bandwidth, variable-reluctance position sensors," *IEEE Transactions on Magnetics*, vol. 22, no. 1, pp. 118–123, Mar. 1986.

[44] R. H. Frazier, P. J. Gilinson, and G. A. Oberbeck, *Magnetic and Electric Suspensions.* Cambridge, MA, USA: MIT Press, 1974.

[45] J. Yim, J. Kim, S. Sul, H. Ahn, and D. Han, "Sensorless position control of active magnetic bearings based on high frequency signal injection method," in *Proceedings of the Applied Power Electronics Conference and Exposition: APEC*, vol. 1, Feb. 2003, pp. 83–88.

[46] N. Skricka and R. Markert, "Compensation of disturbances on self-sensing magnetic bearings caused by saturation and coordinate coupling," in *Proceedings of the Seventh International Symposium on Magnetic Suspension Technology*, ETH Zurich, Switzerland, Aug. 2000, pp. 165–169.

[47] D. T. Montie and E. H. Maslen, "Experimental self-sensing results for a magnetic bearing," in *Proceedings of the ASME International Gas Turbine Institute Turbo Expo*, June 2001.

[48] C. Choi and K. Park, "Self-sensing magnetic levitation using a LC resonant circuit," *Sensors and Actuators A: Physical*, vol. 72, p. 169177, 1999.

[49] M. D. Noh and E. H. Maslen, "Self-sensing magnetic bearings (Part I)," in *Proceedings of the Fifth International Symposium on Magnetic Bearings*, Kanazawa, Japan, Aug. 1996, pp. 95–100.

[50] D. T. Montie and E. H. Maslen, "Experimental self-sensing results for a magnetic bearing," in *Proceedings of the Seventh International Symposium on Magnetic Bearings*, ETH Zurich, Switzerland, Aug. 2000, pp. 171–176.

[51] T. Mizuno, T. Ishii, and K. Araki, "Self-sensing magnetic suspensoin using hysteresis amplifiers," *Control Engineering Practice*, vol. 6, pp. 1133–1140, Jul. 1998.

[52] D. T. Montie, "Performance limitations and self-sensing magnetic bearings," PhD Thesis, University of Virginia, Virginia, USA, Jan. 2003.

[53] E. H. Maslen, D. T. Montie, and T. Iwasaki, "Robustness limitations in self-sensing magnetic bearings," *ASME Journal of Dynamic Systems, Measurement and Control*, vol. 128, pp. 197–203, Jun. 2006.

[54] A. Schammass and H. Bleuler, "Experimental results on self-sensing AMB using a three-state PWM amplifier," in *Proceedings of the Eighth International Symposium on Magnetic Bearings*, Mito, Japan, Aug. 2002, pp. 289–292.

[55] K. S. Peterson, R. H. Middleton, and J. S. Freudenberg, "Fundamental limitations in active magnetic bearings when modeled as linear periodic systems," in *Proceedings of the American Controls Conference*, Jun. 2006, p. 6.

[56] M. Antila, "Electromechanical properties of radial active magnetic bearings," PhD thesis, Helsinki University of Technology, P.O. Box 3000, FIN-02015, HUT, Finland, November 1998.

[57] B. Polajzer, G. Strumberger, J. Ritonja, O. Tezak, D. Dolinar, and K. Hameyer, "Impact of magnetic nonlinearities and cross-coupling effects on properties of radial active magnetic bearings," *IEEE Transactions on Magnetics*, vol. 40, no. 2, pp. 798–801, Mar. 2004.

[58] Y. Tremaudant, M. Brunet, and U. Schroeder, "Active magnetic bearing with automatic detection of the position thereof," International Patent, Application No: PCT/FR2005/000626, Disignee: Societe de Mecanique Magnetique, March 2005.

[59] N. Skricka and R. Markert, "Improvements of the integration of active magnetic bearings," *Mechatronics*, vol. 12, pp. 1059–1068, 2002.

[60] D. J. Griffiths, *Introduction to electrodynamics*, 3rd ed. Upper Saddle River, New Jersey, USA: Prentice Hall, 1999.

[61] J. J. Cathey, *Electric Machines: Analysis and Design Applying MATLAB®*. New York, USA: McGraw Hill, 2001.

[62] R. L. Stoll, *The analysis of eddy currents*. London: Oxford University Press, 1974.

[63] *AC/DC Module User's Guide*, Comsol 3.3 ed., COMSOL AB, Technoparkstrasse,CH-8005 Zürich, Switzerland, August 2006.

[64] D. Meeker, *Finite element method magnetics*, version 3.3 ed., March 2003.

[65] D. Hanselman, *Brushless permanent magnet motor design*. Cranston, Rhode Island: The Writer's Collective, 2003.

[66] E. Kreyszig, *Advanced Engineering Mathematics*, 9th ed. Hoboken, NJ, USA: John Wiley and Sons, 2006.

[67] K. Binns and P. Lawrenson, *Analysis and computation of electric and magnetic field problems*, 2nd ed. Pergamon Press, Oxford, 1973, ch. 6, pp. 117–128.

[68] Z. Zhu and D. Howe, "Instantaneous magnetic field distribution in brushless permanent magnet dc motors, part iii: Effect of stator slotting," *IEEE Transaction on Magnetics*, vol. 29, no. 1, pp. 143–151, Jan. 1993.

[69] J. H. Mathews, *Numerical Methods for Mathematics, Science, and Engineering*, 2nd ed. Englewood Cliffs, NJ, USA: Prentice Hall, 1992.

[70] D. C. Jiles and D. L. Atherton, "Theory of ferromagnetic hysteresis," *Journal of Magnetism and Magnetic Materials*, vol. 61, no. 1, pp. 48–60, Sep. 1986.

[71] D. C. Jiles, "Modelling the effects of eddy current losses on frequency dependent hysteresis in electrically conducting media," *IEEE Transactions on Magnetics*, vol. 30, no. 6, pp. 4326–4328, Nov. 1994.

[72] L. de Almeida, G. Deep, A. Lima, and H. Neff, "Limiting loop proximity hysteresis model," *IEEE Transactions on Magnetics*, vol. 39, no. 1, pp. 523–528, Jan. 2003.

[73] A. Benabou, S. Clénet, and F. Piriou, "Comparison of the Preisach and Jiles-Atherton models to take hysteresis phenomenon into account in finite element analysis," *COMPEL*, vol. 23, no. 3, pp. 825–834, 2004.

[74] G. Bertotti, *Hysteresis in Magnetism: For Physicists, Material Scientists, and Engineers*. San Diego, California, USA: Academic Press, 1998.

[75] H. Brachtendorf and R. Laur, "Modeling of hysteresis in magnetic cores with frequency-dependent losses," *Journal of Magnetism and Magnetic Materials*, vol. 183, pp. 305–312, 1998.

[76] J. E. Gibson, *Nonlinear automatic control*. McGraw-Hill, 1963, ch. 11, pp. 491–547.

[77] E. Ifeachor and B. Jervis, *Digital signal processing: A practical approach*, 2nd ed. Harlow, England: Prearson Education, 2002, ch. 11, pp. 681–725.

[78] C. Phillips and H. Nagle, *Digital control system analysis and design*, 3rd ed. Upper Saddle River, New Jersey: Prentice Hall, 1995, ch. 3, pp. 89–130.

[79] R. Dorf and R. Bishop, *Modern control systems*, 9th ed. Upper Saddle River, New Jersey: Prentice Hall, 2001.

[80] S. Shinners, *Modern control system theory and application*, 2nd ed. Reading, Massachusetts: Addison-Wesley Publishing company, 1979.

[81] M. D. Noh, D. T. Montie, and E. H. Maslen, "A simulation model for the analysis of transient magnetic bearing performance," in *Proceedings of the 7th International Symposium on Magnetic Bearings*, ETH Zurich, Switzerland, Aug. 2000, pp. 177–181.

[82] E. Maslen, T. Iwasaki, and R. Mahmoodian, "Self-sensing magnetic bearings: development of a virtual probe," in *Proceedings of NSF Design, Service, and Manufacturing Grantees and Research Conference*, St. Louis, Missourie, 2006.

[83] A. Massarini and M. Kazimierczuk, "Self-inductance of inductors," *IEEE Transactions on Power Electronics*, vol. 12, no. 4, pp. 671–676, Jul. 1997.

[84] G. Grandi, M. Kazimierczuk, and A. M. *et al*, "Model of laminated iron-core inductors for high frequencies," *IEEE Transactions on Magnetics*, vol. 40, no. 4, pp. 1839–1845, Jul. 2004.

[85] M. Kazimierczuk, G. Grandi, and A. Massarini, "High-frequency small-signal model of ferrite core inductors," *IEEE Transactions on Magnetics*, vol. 35, no. 5, pp. 4185–4191, Sep. 1999.

[86] M. Hodgdon, "Application of a theory of ferromagnetic hysteresis," *IEEE Transactions on Magnetics*, vol. 24, no. 1, pp. 218–221, Jan 1988.

APPENDIX A

Frequency dependent impedance model for heteropolar magnetic bearings

Accurate models of magnetic bearings are essential during bearing design to optimise bearing performance. Furthermore the drive for robust/reliable self-sensing and possible alternative self-sensing strategies also motivate the frequency response analysis of magnetic bearings. A frequency dependent lumped parameter model is developed based on the work done by Meeker [11]. The model also incorporates a frequency independent capacitance which greatly improves the frequency response at high frequencies. The frequency dependent parameters are obtained from a reluctance network core model as presented in chapter 3. The core model includes eddy-current as well as fringing and leakage correction. Good correlation is obtained between modelled and experimental results up to 1 MHz.

A.1 Introduction

The motivation for this work is to accurately model the frequency response of an active magnetic bearing (AMB). Better understanding of the processes contributing to a reduction in inductance and an increase in equivalent series resistance with an increase in frequency may be of particular use for self-sensing implementation. During the design phase of a high bandwidth AMB it is also important to estimate the losses in the magnetic material due to eddy-currents induced by the switching ripple.

Figure A.1 (a) displays a frequency dependent lumped parameter model proposed by Meeker [11] to represent the frequency response of a laminated heteropolar AMB. The equivalent series resistance and inductance are obtained from a reluctance model that makes use of a complex material permeability term. The complex material permeability term was presented by Stoll and models the eddy current effect in the lamination material. The core losses are mainly due to eddy currents induced in the laminated iron core. These eddy currents have two effects [62]:

1. Eddy currents produce ohmic losses which must be drawn from the supply. For an outside observer this looks like an apparent increase in resistance.

2. Eddy currents reduce the flux-carrying capacity of the core and thus reduce the inductance of the winding.

The inductance determined from the reluctance model is complex and when the reactance is calculated, the real term presents the series equivalent core resistance and the imaginary term the reactance due to inductance. Fringing and leakage effects are compensated for by adding a constant leakage reluctance path and determining accurate values for the air gap- and leakage-reluctances through finite element methods (FEM).

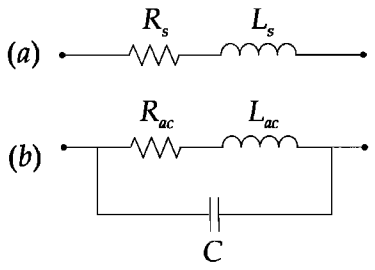

Figure A.1: Equivalent lumped parameter circuit of an inductor (a) series model, (b) RLC model [83]

This model displays good correlation with experimental results for frequencies up to a few kHz. At higher frequencies the results do not correlate well which may be due to unmodelled parasitic capacitances. The aim of this work is to present a model with frequency dependent lumped parameters which displays good correlation with the frequency behaviour of a laminated heteropolar magnetic bearing. Figure A.1 (b) displays a model which is frequently used [83], [84] to represent the behaviour of laminated iron core inductors.

The equivalent series resistance R_{ac} and inductance L_{ac}, shown in figure A.1 (b), are frequency-dependent components due to eddy currents in the core material but can also include skin and proximity effects in the windings [85]. For the present work the skin and proximity effects of the windings are ignored. The total ac resistance R_{ac} is therefore only a function of the equivalent series core resistance. The total inductance L_{ac} can be written as $L_{ac} = L_{m(ac)} + L_{l(ac)}$, where $L_{m(ac)}$ is the main inductance of the coil and $L_{l(ac)}$ is the winding leakage inductance.

The *RLC* lumped parameter model shown in figure A.1 (b) is used in this work to model the magnetic bearing's frequency response. The self capacitance of the winding is derived from an analytical model based on the physical structure of the winding. The leakage inductance $L_{l(ac)}$ may be obtained from a FEM model by assuming a constant leakage inductance as proposed in [11]. The main inductance and the series core resistance are obtained from the reluctance model proposed by Meeker [11] and refined in chapter 5. Results show that the inclusion of the parallel parasitic capacitance greatly improves the lumped parameter model's high frequency response.

A.2 Self-capacitance

For accurate prediction of the high frequency response of inductors and in this case an AMB the effects of stray capacitance may not be neglected. The capacitance may be determined experimentally but in most cases it is advantageous to predict the value with a model. An analytical model is presented in [83] for predicting the stray capacitance of inductors. It is based on the physical structure of the windings i.e. geometry parameters and the number of winding layers.

The distributed parasitic capacitance is then modelled by a single lumped parameter connected between the winding terminals as shown in figure A.1 (b). The parasitic capacitance of the inductor is frequency independent [84] and according to [83] consists of the following components:

1. turn-to-turn capacitance - same layer,
2. turn-to-turn capacitance - adjacent layers,
3. turn-to-core and turn-to-shield capacitances.

In [83] it is shown that the turn-to-turn capacitance of adjacent turns on the same layer and the turn-to-turn capacitance of adjacent turns of different layers are the same with good approximation. This capacitance must be determined over three regions; the capacitance of both the

insulating coatings and the capacitance of the air gap. Taking advantage of the fact that uniformly wound single wire multilayer windings can be represented by basic cells, as shown in figure A.2, an expression for the stray capacitance can be obtained.

The overall turn-to-turn capacitance is given by (A.1) as shown in [83]

$$C_{tt} = \varepsilon_0 l_t \left[\frac{\varepsilon_r \theta^*}{\ln(D_o/D_c)} + \cot\left(\frac{\theta^*}{2}\right) - \left(\frac{\pi}{12}\right) \right] \tag{A.1}$$

with

$$\theta^* = \arccos\left(1 - \frac{\ln(D_o/D_c)}{\varepsilon_r}\right) \tag{A.2}$$

where ε_0 is the permittivity of free space, ε_r is the dielectric constant of insulation material, D_o the wire diameter including insulation and D_c the wire diameter excluding insulation. In [83] it is also shown that the turn-to-core and turn-to-shield capacitance can be taken as twice the turn-to-turn capacitance ($C_{tc} = 2C_{tt}$). With the turn-to-core and turn-to-turn capacitances known it is possible to construct the capacitance network, nèglecting the winding inductances and resistances. The resulting capacitance is then given as:

$$C = kC_{tt} \tag{A.3}$$

where k is a coil configuration factor that can be determined through analysis of the equivalent capacitance network.

A.3 Magnetic bearing model

The magnetic bearing core is modelled using a reluctance network model (RNM). Two possible configurations are presented in the thesis; the self-inductance model and the mutual inductance model. For the present work the mutual inductance RNM is used as documented in chapter 3. The rate dependent complex material permeability term as presented in [11], [62] is used to establish the frequency dependence and is given by (A.4)

$$\mu_{fd}(s) = \mu \left[\frac{\tanh\left(\sqrt{s\sigma\mu}\frac{d}{2}\right)}{\sqrt{s\sigma\mu}\frac{d}{2}} \right] \tag{A.4}$$

with s the complex frequency, d the lamination thickness, μ the magnetic permeability ($\mu_0\mu_r$) and σ the electrical conductivity of the material.

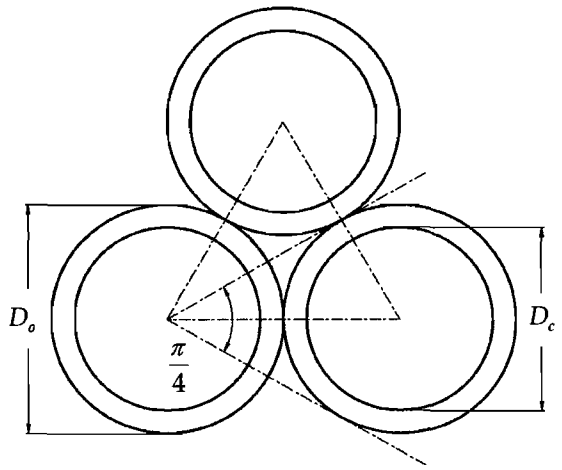

Figure A.2: Basic cell representing the turn-to-turn capacitance [83]

The mutual inductance RNM already incorporates the leakage inductance into the inductance calculated for each pole pair. The total ac series resistance is therefore given by $R_{ac} = \mathbb{R}[L_{11}]$ and inductance by $L_{ac} = \mathbb{I}[L_{11}]$. The complex frequency s may now be substituted with $j\omega$ and the impedance evaluated at different frequencies.

A.4 Results

A.4.1 Method

The frequency response of the bearing can now be predicted with the RLC-lumped parameter frequency dependent model. The different methods of determining the lumped parameters are verified by comparing experimental results to the predicted results. Figure A.3 depicts the series equivalent circuit as will be measured for the radial magnetic bearing with R_s and X_s given by (A.5) and (A.6) respectively.

$$R_s = \frac{R_{ac}}{(1-\omega^2 L_{ac}C)^2 + (\omega C R_{ac})^2} \tag{A.5}$$

$$X_s = \frac{\omega L_{ac}\left(1-\omega^2 L_{ac}C - \frac{CR_{ac}}{L_{ac}}\right)}{(1-\omega^2 L_{ac}C)^2 + (\omega C R_{ac})^2} \tag{A.6}$$

(A.5) and (A.6) can now be used to predict the frequency response of the magnetic bearing. Firstly the frequency independent capacitance is determined using (A.1)-(A.3). The equivalent series resistance R_{ac} and inductance L_{ac} are determined as discussed in section A.3. Experimental results are obtained using a switching power amplifier switching at 20 kHz and 50 % duty cycle. The complex impedance of the magnetic bearing is determined by applying the Fast Fourier Transform (FFT) to the current and voltage waveforms generated by the power amplifier. The frequency dependent impedance is then determined at each harmonic frequency by dividing the voltage FFT results with the current FFT results. The resulting complex impedance is represented by the series equivalent circuit shown in figure A.3.

A.4.2 Model parameters

The magnetic bearing coil consists of two neighbouring coils connected in series. The parasitic capacitance is determined by analysing the complex capacitance network in ORCAD. From the analysis the coil configuration factor k as used in (A.3) is determined to be $k = 3.279$. Using (A.1) and (A.2) the turn-to-turn capacitance (C_{tt}) is estimated as 33.567 pF. Using the coil configuration factor the total parasitic capacitance for one pole pair of the radial magnetic bearing is estimated at 110 pF. The wire capacitance (in parallel with the coil capacitance) is measured as 95 pF resulting in a total capacitance value of 205 pF. For the present work the mutual inductance model is used and the remainder of the model parameters are documented in chapter 3.

A.4.3 Results

The frequency response of the circuit in figure A.1 (a) is presented first where the parasitic capacitance is neglected. Figure A.4 displays the experimental and predicted results for the equivalent series resistance. The modelled and measured results display good correlation for frequencies up

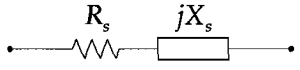

Figure A.3: Series equivalent lumped parameter circuit for AMB

to the switching frequency. The model is however not able to accurately predict the coil impedance beyond this point.

The equivalent series reactance displayed in figure A.5 also shows good correlation between the modelled and measured results for frequencies up to the switching frequency. Beyond this point however large discrepancies are observed between the predicted and experimental results. It is also important to note the absence of the resonant point in the modelled data which is visible in the experimental data in both figures A.4 and A.5.

From the absence of the resonant point in the predicted data it is clear that the capacitance must be included. Figure A.6 displays the predicted and experimental results for the equivalent series resistance with the parasitic capacitance included. The resonant point is now also visible in the modelled results and the correlation between modelled and measured results show marked improvement at high frequencies. This is also visible in the equivalent series reactance results shown in figure A.7. The resonant point is predicted within 27 % of the measured value which implies that either or both the core model and the parasitic capacitance model contain uncertainty.

A.5 Conclusions

A frequency dependent model for heteropolar magnetic bearings is presented which includes an analytical model for the parasitic winding capacitance. The parasitic capacitance is assumed constant and in parallel with an equivalent series resistance and reactance. The equivalent series resistance and reactance values are obtained from a coupled RNM which realises the frequency dependency with a rate dependent complex material permeability term. Results show marked improvement for high frequencies when the parasitic capacitance is included in the model.

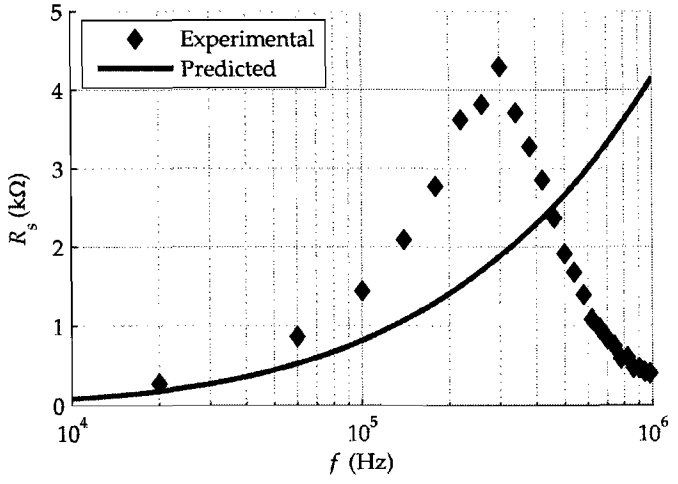

Figure A.4: Experimental and predicted series resistance (C excluded)

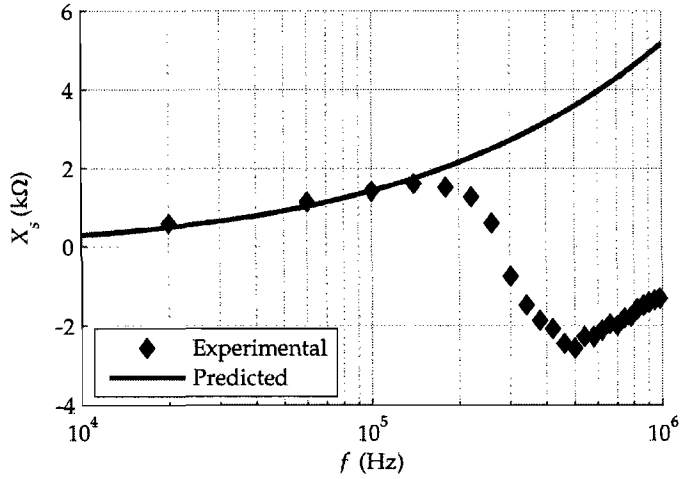

Figure A.5: Experimental and predicted series reactance (*C* excluded)

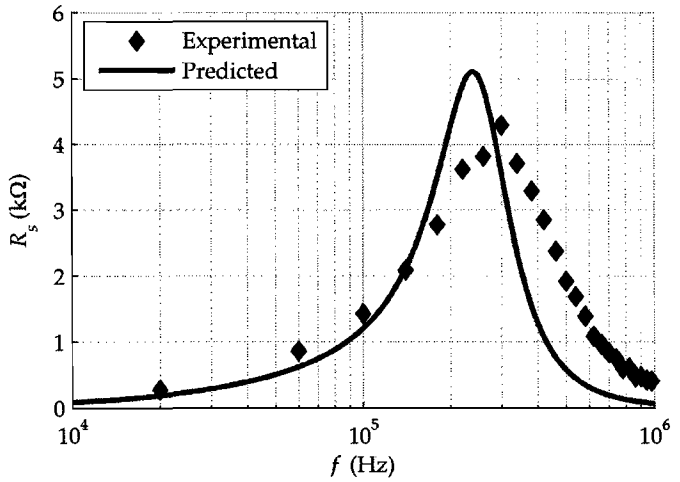

Figure A.6: Experimental and predicted series resistance (*C* included)

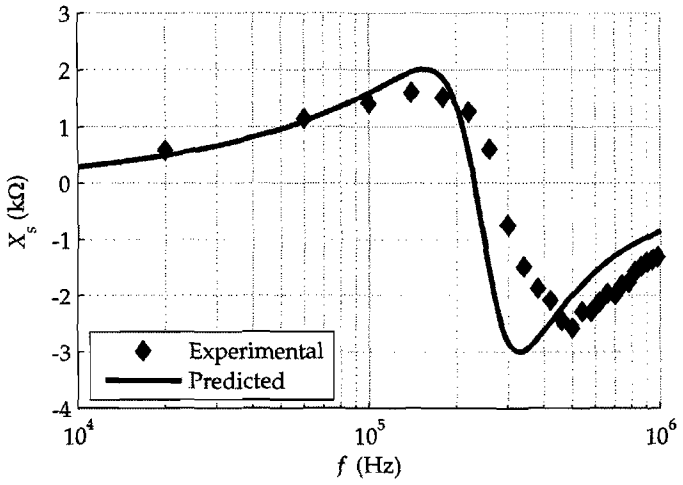

Figure A.7: Experimental and predicted series reactance (*C* included)

APPENDIX B

Self-inductance reluctance network model

B.1 Governing equations

A self-leakage reluctance network model (RNM) for an eight-pole heteropolar magnetic bearing is presented. The model was developed by Meeker [11] and includes leakage and fringing as well as eddy-current effects. Meeker [11] included eddy current correction which was developed from a 1-dimensional eddy current model proposed by Stoll [62]. An additional self-leakage path is also defined which is easily incorporated into the model since the only effect it has, is to increase the self-inductance. Fringing effects are compensated for by determining accurate air gap reluctance values. Both the air gap reluctance and leakage reluctance are determined by means of a magnetostatic FEM model. A single pole of the reluctance model is shown in figure B.1.

For this P pole radial magnetic bearing there are P fluxes in the stator, P fluxes in the poles and P fluxes in the rotor that must be determined; $3P$ fluxes in total. Following the method proposed in [11], a set of $3P$ independent linear equations can be written:

- P - 1 loop equations (down the pole, clockwise in the rotor, up the next pole and returning counter-clockwise through the stator)

$$\begin{aligned}(\Re_{pk}+\Re_{gk})\phi_{gk}+\Re_{rk}\phi_{rk}-(\Re_{p(k+1)}+\Re_{g(k+1)})\phi_{g(k+1)}-\Re_{sk}\phi_{sk}\\ =N_kI_k-N_{(k+1)}I_{(k+1)}\quad k=1,\ldots,P-1\end{aligned} \tag{B.1}$$

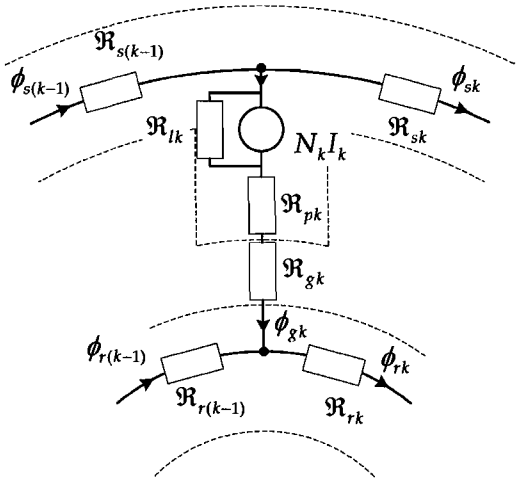

Figure B.1: Equivalent reluctance model for symmetrical radial magnetic bearing

- P - 1 conservation equations for intersections on the rotor

$$\phi_{p(k+1)} + \phi_{rk} - \phi_{r(k+1)} \quad k = 1, \ldots, P-1 \tag{B.2}$$

- P - 1 conservation equations for intersections on the stator

$$\phi_{p(k+1)} - \phi_{sk} + \phi_{s(k+1)} \quad k = 1, \ldots, P-1 \tag{B.3}$$

- conservation of all fluxes going into the rotor

$$\sum_{k=1}^{P} \phi_{gk} = 0 \tag{B.4}$$

- one loop equation around the rotor

$$\sum_{k=1}^{P} \Re_{rk}\phi_{rk} = 0 \tag{B.5}$$

- one loop equation around the stator.

$$\sum_{k=1}^{P} \Re_{sk}\phi_{sk} = 0 \tag{B.6}$$

These $3P$ equations (B.1)-(B.6) for the fluxes can be rearranged in matrix form as:

$$\mathbf{\Re\Phi} = \mathbf{NI} \tag{B.7}$$

The fluxes in each path of the radial magnetic bearing can now be determined by inverting the reluctance matrix as shown in (B.8).

$$\mathbf{\Phi} = \mathbf{\Re}^{-1}\mathbf{NI} \tag{B.8}$$

As proposed in [11] the inductance can now be determined using:

$$\mathbf{L} = \mathbf{T}_s'\mathbf{\Re}^{-1}\mathbf{N} + \mathbf{I}_I\frac{N^2}{\Re_L} \tag{B.9}$$

where $\mathbf{T}_s$ is a matrix with $3P$ rows and m columns. m is the number of windings in the bearing and the (j, k) entry of $\mathbf{T}_s$ represents the number of turns of the j^{th} winding about the k^{th} flux. The self-inductance of each winding is represented by the diagonal terms while the off-diagonal terms represent the mutual inductances. The leakage inductance is merely added to the self inductance using the identity matrix $\mathbf{I}_I$ to obtain the total inductance of each coil.

The reluctances of the iron paths ($\Re_r$, $\Re_s$ and $\Re_p$) are determined from the effective core length l and the cross sectional area a.

$$\Re = \frac{l}{\mu_{fd}(s)a} \tag{B.10}$$

$\mu_{fd}(s)$ is the frequency dependent core permeability derived from the one dimensional formulation for eddy-currents in laminated magnetic material developed in [11], [62] and is given by (B.11).

$$\mu_{fd}(s) = \mu\left[\frac{\tanh\left(\sqrt{s\sigma\mu}\frac{d}{2}\right)}{\sqrt{s\sigma\mu}\frac{d}{2}}\right] \tag{B.11}$$

s is the complex frequency, d the lamination thickness, μ the magnetic permeability ($\mu_0\mu_r$) and σ the electrical conductivity of the material.

B.2 Leakage and fringing correction

The air gap and leakage reluctances are determined by firstly defining a leakage reluctance path as shown in figure B.1. Next the bearing inductances are determined by FEM for the case where the material is assumed to be infinitely permeable. At this point the reluctances $\Re_g$ and $\Re_l$ can be chosen to minimise the differences between corresponding entries of the circuit theory inductance matrix L (assuming infinite permeability) and the field theory inductance matrix $\hat{\mathbf{L}}$. Values for the air gap reluctances $\Re_g$ and the leakage reluctances $\Re_l$ are then obtained through a least squares fit.

A two-dimensional model is used to determine the leakage and fringing effects. The magnetic vector potential is then related to the flux by

$$\mathbf{B} = \frac{dA}{dy}\hat{x} - \frac{dA}{dx}\hat{y} \tag{B.12}$$

with x, y, $\hat{x}$ and $\hat{y}$ as shown in figure B.2. The magnetostatic field satisfies the differential equation

$$\nabla^2\mathbf{A} = -\mu_0\mathbf{J} \tag{B.13}$$

where $\mathbf{J}$ is the coil current density flowing in the $\hat{z}$ direction [60]. The infinitely permeable material is modelled by implementing the boundary condition

$$\nabla A \cdot \mathbf{n} = 0 \tag{B.14}$$

at the air-iron interface. In (B.14) $\mathbf{n}$ is a vector normal to the interface. The assumption of infinite permeable material limits the solution area for the radial bearing to the air between the rotor and the stator as shown in figure B.2 which depicts the solution area of an 8-pole bearing.

When considering a symmetrical bearing with the rotor centred, it is sufficient to find the solutions for a single active coil. Using superposition all other solutions can then be determined. The mutual- and self-inductances are determined by integration from the solution of the magnetic vector potential with one active coil:

$$\hat{L}_{jk} = l_{ax}\frac{\iint A_j J_k \, dx \, dy}{I_j I_k} \tag{B.15}$$

where l_{ax} is the axial length of the bearing. A_j is the contribution to A due to current in the j^{th} coil, J_k the current density contribution due to the k^{th} coil and I_j and I_k the currents in the j^{th} and

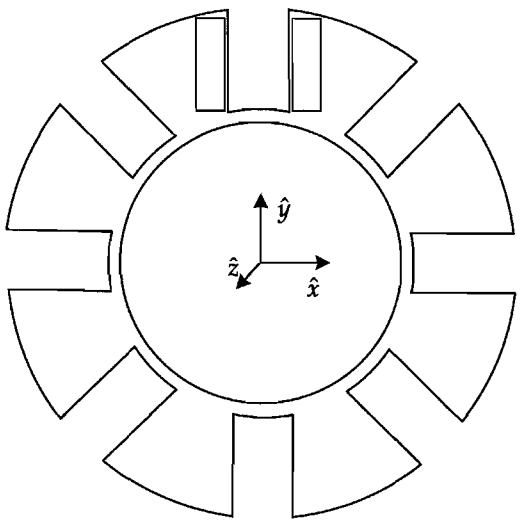

Figure B.2: Solution area for magnetic vector potential

k^{th} coils respectively. The integration is taken over the entire solution area with the only nonzero contribution in the area of the k^{th} coil.

Using circuit theory and assuming infinite permeable material, the self inductance of each coil of a symmetrical bearing is given by (B.16).

$$L_{jj} = \frac{P-1}{P}\left(\frac{N^2}{\Re_g}\right) + \frac{N^2}{\Re_l} \tag{B.16}$$

The first term on the right in (B.16) accounts for the self inductance and the second accounts for the leakage inductance. The off-diagonal terms (mutual inductance) are given by (B.17).

$$L_{jk} = \frac{-1}{P}\left(\frac{N^2}{\Re_g}\right) \quad j \neq k \tag{B.17}$$

$\mathbf{L}$ and $\hat{\mathbf{L}}$ can now be equated which results in an over determined set of linear equations that can be solved for $\Re_g^{-1}$ and $\Re_l^{-1}$. For the symmetrical case at hand it is sufficient to consider only the first row of $\mathbf{L}$ and $\hat{\mathbf{L}}$ denoted by $\mathbf{L}_1$ and $\hat{\mathbf{L}}_1$. By decomposing $\mathbf{L}_1$ as shown in (B.18)

$$\mathbf{L}_1' \equiv \mathbf{M}\begin{bmatrix} \Re_g^{-1} \\ \Re_l^{-1} \end{bmatrix} \quad \text{where} \quad \mathbf{M} = \begin{bmatrix} N^2\frac{P-1}{P} & N^2 \\ \frac{-N^2}{P} & 0 \\ \vdots & \vdots \\ \frac{-N^2}{P} & 0 \end{bmatrix} \tag{B.18}$$

the least squares solution for the air gap and leakage reluctances is given by (B.19).

$$\begin{bmatrix} \Re_g^{-1} \\ \Re_l^{-1} \end{bmatrix} = [\mathbf{M}'\mathbf{M}]^{-1}\mathbf{M}'\hat{\mathbf{L}}_1' \tag{B.19}$$

The reluctance network model is complete now that accurate values for the air gap and leakage reluctances are determined. The model may now be used to predict equivalent series core resistance and inductance values at different frequencies using (B.9).

B.2.1 Results

The air gap and leakage reluctances are obtained using the resulting $\hat{\mathbf{L}}$ as obtained by FEM.

$$\hat{\mathbf{L}}_1' = \begin{bmatrix} 3.1693 \\ -0.4715 \\ -0.4413 \\ -0.4235 \\ -0.4176 \\ -0.4235 \\ -0.4413 \\ -0.4714 \end{bmatrix} \times 10^{-3} \quad \text{H} \tag{B.20}$$

Using (B.19) $\Re_g$ and $\Re_l$ are determined as:

$$\begin{aligned} \Re_g &= 6.807 \times 10^5 \quad \text{H}^{-1} \\ \Re_l &= 3.161 \times 10^7 \quad \text{H}^{-1} \end{aligned}$$

Using normal circuit theory, the nominal air gap reluctance is determined by (B.21).

$$\Re_{g\,\text{nominal}} = \frac{g_0}{\mu_0 a_g} = 7.975 \times 10^5 \quad \text{H}^{-1} \tag{B.21}$$

From this result it can be seen that fringing effects reduce the air gap reluctance by 15 %.

APPENDIX C

Transient simulation model

In the process of self-sensing implementation an accurate model of the system may facilitate algorithm development and serve as a platform for self-sensing evaluation. This appendix describes the development of a simulation model for an 8-pole radial heteropolar magnetic bearing which includes saturation, hysteresis and eddy current effects. The coupled network is based on work presented in [81] and incorporates cross-coupling effects. The mentioned effects are the most important to consider when implementing self-sensing and makes this model suitable for self-sensing investigations.

C.1 Hysteresis and saturation modelling

One of the most vexing problems in self-sensing is the nonlinear nature of the magnetisation process of the magnetic material. There are numerous models available capable of describing complicated magnetisation processes such as those presented by Hodgdon [86] and Jiles and Atherton [70]. These models normally describe the magnetisation process in terms of differential or integral equations. The complexity of these models however makes it difficult to employ them in simulation models for the purpose of self-sensing evaluation. A less complex approach is proposed in [81] where an analytical model describing the nonlinear behaviour of the magnetic material is implemented. In this model the B-H curve is confined by two envelopes given by:

$$H_1(B) = \frac{B}{\mu_0\mu_{r0}} + \frac{\sigma}{\mu_0}\left(1 - \frac{1}{\mu_{r0}}\right)\log(1 + \eta\, e^{(B-B_s)/\sigma}) + H_r \tag{C.1}$$

$$H_2(B) = \frac{B}{\mu_0\mu_{r0}} - \frac{\sigma}{\mu_0}\left(1 - \frac{1}{\mu_{r0}}\right)\log(1 + \eta\, e^{(-B-B_s)/\sigma}) - H_r \tag{C.2}$$

where (C.1) and (C.2) each represents two asymptotes. The first is where the material is not yet in saturation with the slope represented by $\mu_0\mu_{r0}$ and the second where the material is in saturation and the slope converges to the permeability of free space μ_0. The sharpness of the transition between the two asymptotes is controlled by the parameter σ. η is determined from the interception of the asymptote for large flux densities on the B axis. The separation between the two envelopes, given by H_r, controls the excursion depth of the hysteresis loop in the H direction.

The model presents the magnetisation as a function of flux density as shown in (C.3).

$$H(B) = \begin{cases} H_1(B) - [H_1(B_0) - H(B_0)]\, e^{\beta_a|B-B_0|} & \text{if } \dot{B} \geq 0 \\ H_2(B) - [H_2(B_0) - H(B_0)]\, e^{\beta_a|B-B_0|} & \text{if } \dot{B} < 0 \end{cases} \tag{C.3}$$

In (C.3) B_0 is the flux density at the instant that the derivative of the flux density $\dot{B}$ changes its sign. The parameter β_a controls the shape of the actual B-H curve. The model parameters are

identified by curve fitting the experimental data. The model parameters for the M400-50A Cogent silicon steel is summarised in table C.1.

C.2 Eddy current modelling

Eddy currents are induced in the magnetic material due to the switching of the power amplifiers used to drive the magnetic bearing's coils. The eddy currents induced in the laminated iron core have two effects [62]:

1. Eddy currents produce ohmic losses which must be drawn from the supply. For an outside observer this looks like an apparent increase in resistance if a series resistor inductor model is assumed for the coil.

2. Eddy currents reduce the flux-carrying capacity of the core and thus reduce the inductance of the winding.

These effects may be modelled by either using a rate dependent material permeability or by introducing a fictitious single turn secondary coil driving a chain of resistors and inductors [11].

The model presented here makes use of the fictitious single turn secondary coil driving a single resistor. The accuracy of this model is heavily dependent on the amount of flux linking this eddy current loop [81]. Firstly it is recognised that the eddy currents stay within a given lamination. This results in a reduction in the total flux linked by the fictitious coil of a factor determined by the thickness of the lamination and the thickness of the lamination stack. This approach however over estimates the flux linking the coils since it assumes the eddy currents are flowing only on the surface of the lamination. Assuming a homogeneous distribution of the eddy currents in the characteristic skin depth δ, the driving flux can be obtained from (C.4)

$$\phi_{ec} = \left(\frac{d-\delta}{l_{ax}}\right)\phi \tag{C.4}$$

with d the lamination thickness and l_{ax} the lamination stack thickness. The resistance seen by the eddy currents can be approximated by the stator resistivity ρ, times the mean current path length divided by the area. For a magnetic circuit with a lamination width w (perpendicular to flux and lamination direction), and a mean flux path length l (parallel to flux), the resistance is given by (C.5).

$$r_{ec} = \frac{2\rho w}{l\delta} \tag{C.5}$$

This resistance value connected to the fictitious single turn coil, models the magneto motive force (MMF) drop across each section of lamination material due to eddy currents. This reduces the flux and as a result the inductance. The eddy currents flowing through the eddy current resistor in the secondary coil is drawn from the supply which, for an outside observer, looks like an apparent increase in resistance between the coil terminals.

Table C.1: Hysteresis and saturation model parameters

Parameter	Value	Unit
μ_{r0}	8594	
η	0.0143	
σ	0.21312	T
B_s	1.6120	T
β_a	5.7662	T^{-1}
H_r	74.308	At/m

C.3 Governing equations

The referencing convention used throughout the appendix is illustrated in figure C.1. Adjacent poles are paired by connecting their respective coils in complementing polarity. Pole 1 (P_1) and pole 2 (P_2) constitute pole pair 1 (PP_1) with electrical terminal descriptors v_1 and i_1. The remaining 3 pole pairs are paired in a like manner. The 8-pole magnetic bearing utilises the classical NSSNNSSN pole configuration.

With the most important issues addressed it is now possible to develop a simulation model. Figure C.2 shows the numbering of the flux paths for an 8-pole heteropolar magnetic bearing. It also depicts the flux sign convention. As can be seen the flux flow is positive in the clockwise direction for both the rotor and the stator and positive in the poles flowing in the direction of the rotor.

The simulation model makes use of Faraday's law to determine the flux rate of change in the poles of the bearing as proposed by Noh [81]. A set of 24 linear independent equations is then compiled as proposed by Meeker [11] to determine the rate of change of the fluxes in all 24 paths. For an 8 pole magnetic bearing with two adjacent coils wound in series and neighbouring pole pair configured so that the poles are ordered (NSSNNSSN) as shown in figure C.1, Faraday's law gives:

$$N\frac{d\phi_{2k-1}}{dt} - N\frac{d\phi_{2k}}{dt} = v_k - ri_k \quad k = 1,3 \tag{C.6}$$

$$-N\frac{d\phi_{2k-1}}{dt} + N\frac{d\phi_{2k}}{dt} = v_k - ri_k \quad k = 2,4 \tag{C.7}$$

From (C.6) it is clear that ϕ_1 is flowing in the 1st pole which is also the first leg of the first pole pair as shown in figure C.1. A positive voltage applied to the coil of the first pole pair will result in a positive rate of change in the flux flowing in pole 1 and a negative rate of change for the flux in pole 2. In order to establish a (NSSNNSSN) convention Faraday's law applied to the second pole

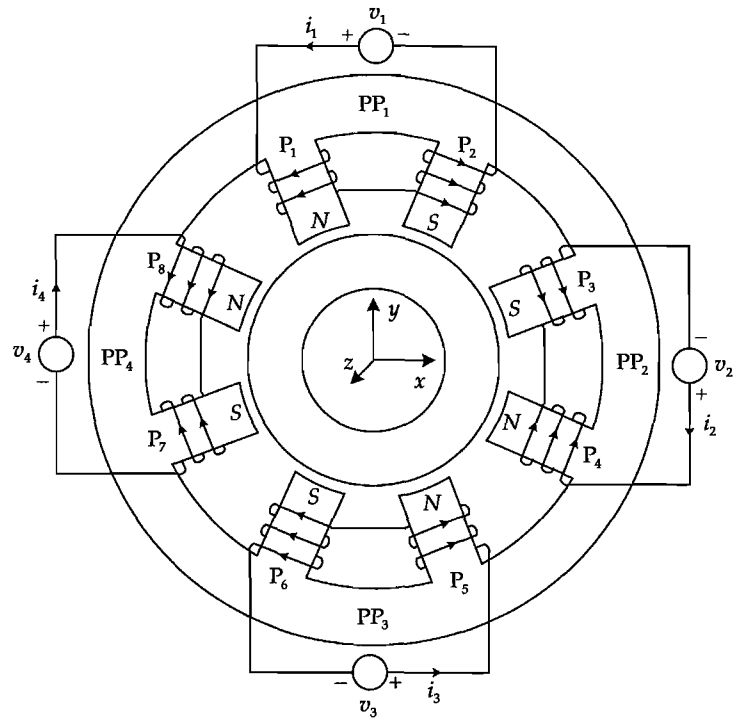

Figure C.1: Referencing convention illustration

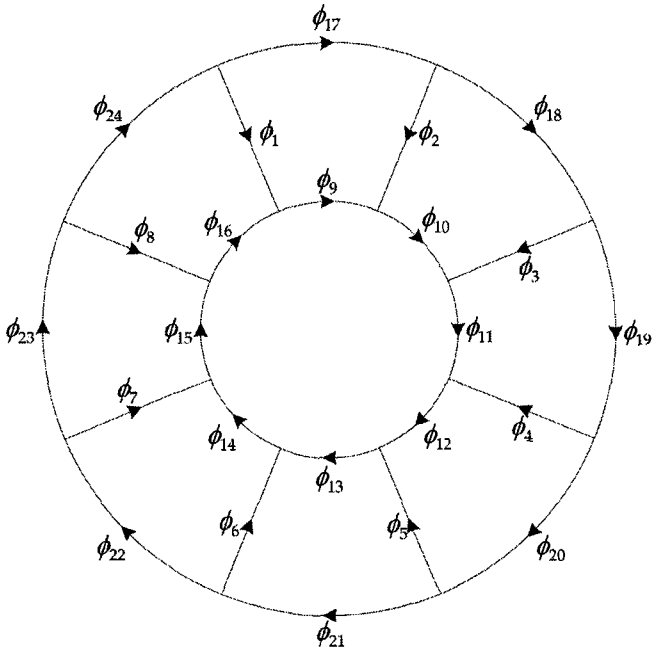

Figure C.2: Flux path numbering

pair results in (C.7). Here a negative rate of change in the flux flowing in the 3rd pole will result from a positive voltage across the second pole pair coil and a positive rate of change for the flux in the 4th pole.

The effects of the eddy currents are included by modelling a fictitious single turn secondary coil as discussed. Applying Faraday's law results in

$$\gamma \frac{d\phi_k}{dt} = -r_{ec_k} i_{ec_k} \quad k = 1, \ldots, 24 \tag{C.8}$$

where

$$\gamma = \frac{d - \delta}{l_{ax}} \tag{C.9}$$

For this 8-pole radial magnetic bearing there are 8 fluxes in the stator, 8 fluxes in the poles and 8 fluxes in the rotor that must be determined; 24 fluxes in total. Following the method proposed in [11] a set of 24 independent linear equations can be written:

- 7 loop equations (towards the center through a pole, clockwise in the rotor, up the next pole and returning counter-clockwise through the stator)

$$\begin{aligned} l_k H_k + g_k H_{g_k} + l_{k+8} H_{k+8} - g_{k+1} H_{g_{k+1}} - l_{k+1} H_{k+1} - l_{k+16} H_{k+16} \\ = N i_k + i_{ec_k} + i_{ec_{k+8}} - N i_{k+1} - i_{ec_{k+1}} - i_{ec_{k+16}} \quad k = 1, \ldots, 7 \end{aligned} \tag{C.10}$$

- One loop equation around the rotor

$$\sum_{k=9}^{16} l_k H_k = \sum_{k=9}^{16} i_{ec_k} \tag{C.11}$$

- One loop equation around the stator

$$\sum_{k=17}^{24} l_k H_k = \sum_{k=17}^{24} i_{ec_k} \tag{C.12}$$

- 7 conservation equations for intersections on the rotor

$$\phi_{k+1} + \phi_{k+8} - \phi_{k+9} = 0 \quad k = 1,\ldots,7 \tag{C.13}$$

- 7 conservation equations for intersections on the stator

$$\phi_{k+1} - \phi_{k+16} + \phi_{k+17} = 0 \quad k = 1,\ldots,7 \tag{C.14}$$

- Conservation of all the fluxes entering the rotor

$$\sum_{k=1}^{8} \phi_k = 0 \tag{C.15}$$

The magnetic field H in the preceding discussion is obtained from C.1, C.2 and C.3 which incorporates the hysteretic behaviour of the magnetic material into the model. Assuming that the rate of change of the flux also adheres to the conservation equations, (C.13), (C.14) and (C.15), the following can be written:

$$\dot{\phi}_{k+1} + \dot{\phi}_{k+8} - \dot{\phi}_{k+9} = 0 \quad k = 1,\ldots,7 \tag{C.16}$$

$$\dot{\phi}_{k+1} - \dot{\phi}_{k+16} + \dot{\phi}_{k+17} = 0 \quad k = 1,\ldots,7 \tag{C.17}$$

$$\sum_{k=1}^{8} \dot{\phi}_k = 0 \tag{C.18}$$

Rewriting (C.6), (C.7) and (C.8) in terms of current and substituting into (C.10), (C.11) and (C.12), together with (C.16), (C.17) and (C.18) result in 24 equations for the rate of change of the fluxes that can be rearranged in matrix form as

$$\mathbf{C}\dot{\mathbf{\Phi}} = \mathbf{LH} + \mathbf{GH_g} + \mathbf{NV} \tag{C.19}$$

with:

$\mathbf{C}$ - A 24×24 matrix containing all the coefficients of the rate of flux.

$\mathbf{N}$ - A 24×4 matrix describing the relationship between coil voltage and rate of flux change. (hierdie is nie heeltemal reg nie is dit? wat van $\mathbf{C}^{-1}$)??

$\mathbf{V}$ - A 4×1 matrix containing the voltages applied to each pole pair.

For more details regarding the matrixes refer to section C.6. The rate of change of the fluxes in each path of the radial magnetic bearing can now be determined by inverting the matrix $\mathbf{C}$ as shown in (C.20).

$$\dot{\mathbf{\Phi}} = \mathbf{C}^{-1}\mathbf{LH} + \mathbf{C}^{-1}\mathbf{GH_g} + \mathbf{C}^{-1}\mathbf{NV} \tag{C.20}$$

The fluxes in each path of the radial bearing can now be determined through numerical integration of (C.20). Due to the fact that the simulation model is based on the rate of change of the fluxes alone, the numerical integration may cause drift which will imply that (C.13), (C.14) and (C.15) will not hold. This phenomenon must be investigated in order to establish the fidelity of the model.

The coil currents may now be determined by using (C.6) and (C.7). The coil currents are then expressed in matrix form as:

$$\mathbf{I} = \mathbf{I_V V} + \mathbf{I_\Phi}\dot{\mathbf{\Phi}} \tag{C.21}$$

with

$\mathbf{I}$ - A 4×1 matrix containing the coil currents of each pole pair.

$\mathbf{I_V}$ - A 4×4 matrix describing the relationship between coil voltage and coil current.

$\mathbf{I_\Phi}$ - A 4×24 matrix describing the relationship between the coil current and flux rate of change.

The model described thus represents the magnetic dynamic behaviour of the 8-pole heteropolar magnetic bearing with coil voltages v_1 to v_4 as inputs and coil currents i_1 to i_4 as well as the flux in each leg of the coupled network as outputs. The next paragraph discusses the incorporation of this model into a complete model of the AMB system, i.e. the electromagnetic actuators, suspended body and position control.

C.4 Dynamic model

A flow diagram of the dynamic simulation model is shown in figure C.3. The model is given a position reference for both the x and y directions after which two proportional-derivative (PD) position controllers, one for the x-axis and one for the y-axis, determine two control currents. Each control current is added to and subtracted from a bias current level to generate current references for the positive and negative directions respectively. These four current references are fed to the power amplifiers (PAs) which in turn generate voltages that are fed to the magnetic simulation model. The resulting coil currents are fed back to the PAs where they are used together with their references and proportional-integral (PI) controllers to establish the PAs duty cycles.

The magnetic simulation determines the 8 flux densities in the poles of the magnetic bearing. These flux densities are then used to determine the forces exerted on the rotor using (C.22).

$$F_k = \frac{1}{2}\frac{B_k^2\, a_k}{\mu_0} \quad [\mathrm{N}] \tag{C.22}$$

where a_k is the pole face area and B_k the flux density in the air gap. In order to obtain the resulting forces in the x and y directions, the angle of the poles must be taken into account. Taking the

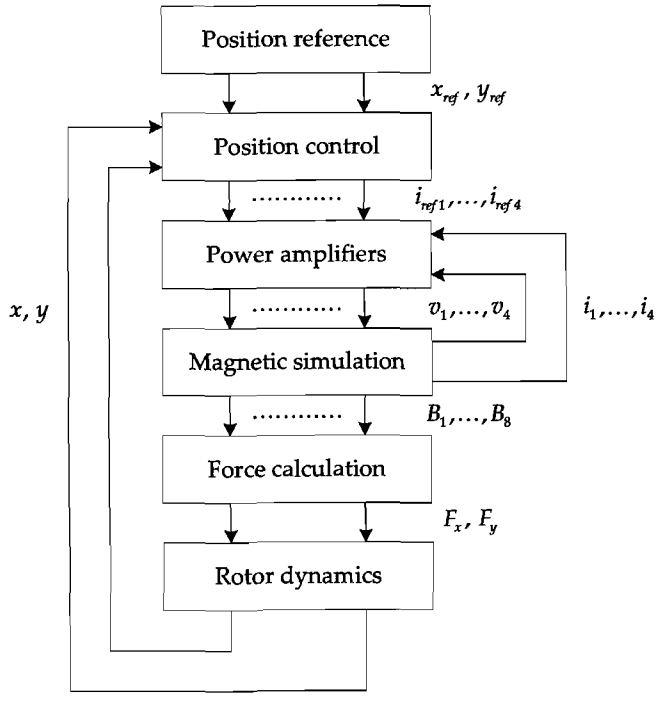

Figure C.3: Dynamic simulation model flow diagram

positive x-axis as 0 degrees, the angle of each pole can be expressed as:

$$\varphi_k = 112.5 - 45(k-1) \quad \text{[Degrees]} \quad k = 1, \ldots, 8. \tag{C.23}$$

The resultant magnetic force in the x and y directions can now be determined using (C.24)

$$\mathbf{F} = \frac{a_k}{2\mu_0} \begin{bmatrix} \cos(\varphi_1) & \cos(\varphi_2) & \cdots & \cos(\varphi_8) \\ \sin(\varphi_1) & \sin(\varphi_2) & \cdots & \sin(\varphi_8) \end{bmatrix} \mathbf{B_k} \tag{C.24}$$

with

$$\mathbf{B_k} = \begin{bmatrix} B_1^2 & B_2^2 & \ldots & B_8^2 \end{bmatrix}^T \tag{C.25}$$

(C.24) results in a (2x1) matrix $\mathbf{F}$ with the first row the resulting force in the x-direction and the second the resulting force in the y-direction. The acceleration of the mass can now be determined using the resulting forces. The position is then determined by twice integrating the accelerations.

C.5 Simulation results

C.5.1 Conservation of fluxes

The accuracy of the simulation is first determined by verifying that the model satisfies (C.13), (C.14) and (C.15) even though they are not explicitly included in the model. Figure C.4 displays the resulting errors for (C.13), (C.14) with $k = 1$ and (C.15) respectively. The maximum errors are approximately 2×10^{-16} Wb, 4×10^{-16} Wb and 7×10^{-16} Wb. The maximum flux level in pole 2 is 3×10^{-4} Wb which is in the vicinity of 12 orders larger than the errors. These results validate the assumption that the derivative of the flux adheres to the same conservation equations as the flux themselves. The small error is presumably due to the numerical integration and the finite word length of the variables in the simulation.

C.5.2 Current and voltage waveforms

A further step of verification is to compare simulated voltage and current waveforms with measured data. Figure C.5 displays modelled and measured data for both the voltage and current waveforms. The discontinuity in the current switching waveform is caused by eddy current effects.

The sharp transitions in the modelled current waveform is a result of the over simplification of the impedance connected to the single turn secondary coil with which the eddy current effect is modelled. In the present work the impedance consists of a single resistor r_{ec}. An inductor may be included which will introduce the RL transient at the switching instances. Discrepancies exist between the simulated and measured amplitude of the eddy current jump. The problem may be addressed by either refining the eddy current resistance r_{ec} or by refining γ (flux linkage constant).

C.5.3 System simulation

To verify the RNM a step response is measured on the experimental system and the results are compared to that of the RNM. Figure C.6 displays a 50 μm step response for both the experimental system and the TSM. Good correlation is observed with respect to rise times and percentage overshoot. The dc offset in the settling values and the discrepancy observed at the top of the rising edge may respectively be attributed to a gain that is not modelled accurately and some unmodelled dynamics. For the purpose of self-sensing investigation these discrepancies may be ignored and the model is now verified and may serve as a platform for self-sensing investigations.

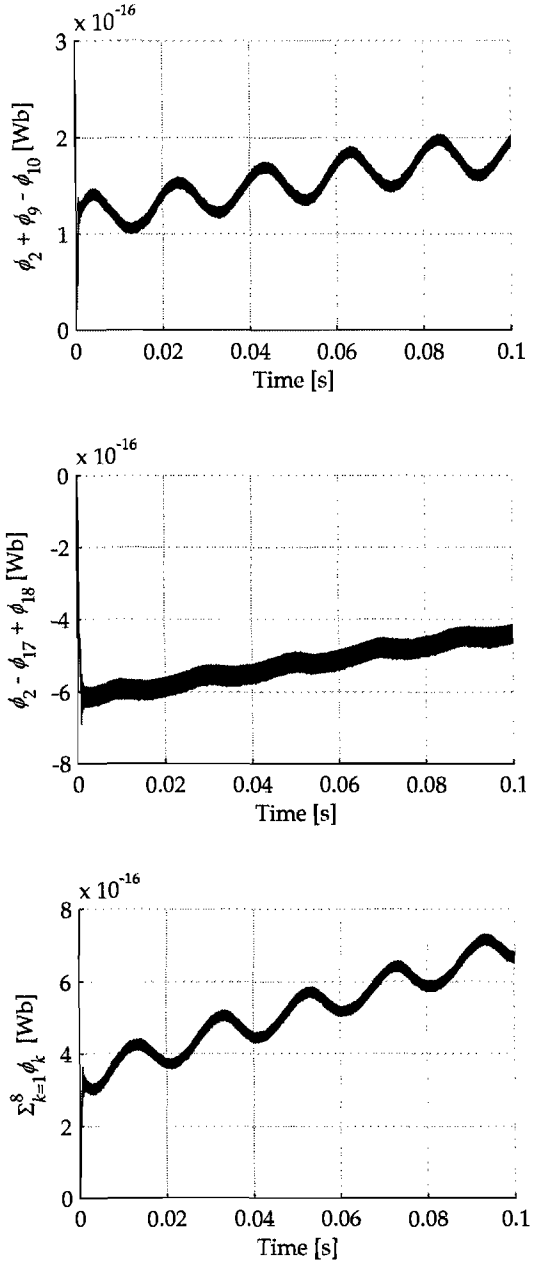

Figure C.4: Conservation of fluxes

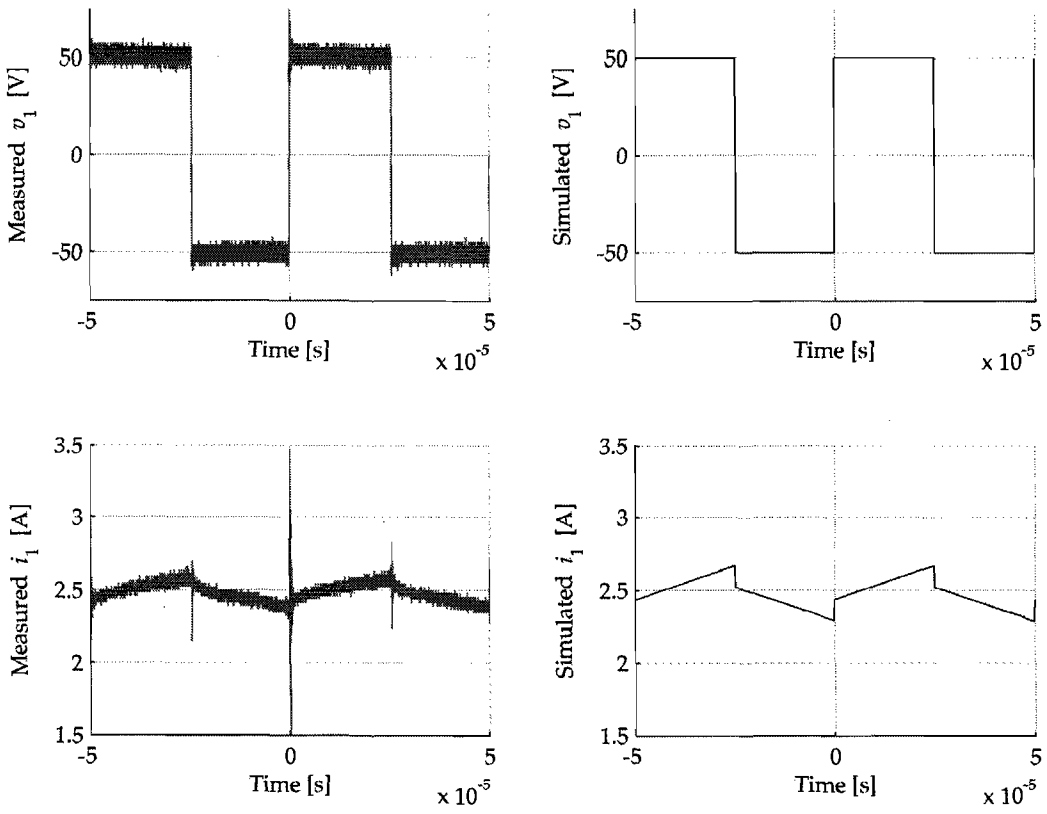

Figure C.5: Measured and simulated current and voltage waveforms

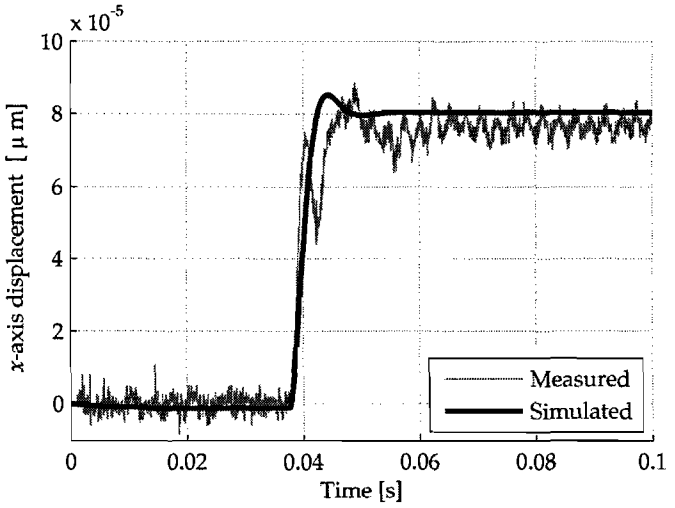

Figure C.6: Measured and simulated 50 µm step response

C.6 Matrixes

Derivative of flux vector:

$$\dot{\mathbf{\Phi}}_{24\times1} = \begin{bmatrix} \dot{\phi}_1 & \dot{\phi}_2 & \dots & \dot{\phi}_{24} \end{bmatrix}^T \tag{C.26}$$

Interconnection and flux conservation matrix

$$\mathbf{C}_{24\times24} = \begin{bmatrix} \mathbf{C_{L1}} \\ \mathbf{C_{L2}} \\ \mathbf{C_N} \end{bmatrix} \tag{C.27}$$

7 loop equations (Ampère's loop input):

$$\mathbf{C_{L1}}_{7\times24} = \begin{bmatrix} -\frac{2N^2}{r_1}-\frac{\gamma}{rec_1} & \frac{2N^2}{r_1}+\frac{\gamma}{rec_2} & 0 & 0 & 0 & 0 & 0 & 0 \\ \frac{N^2}{r_1} & -\frac{N^2}{r_1}-\frac{\gamma}{rec_2} & \frac{N^2}{r_2}+\frac{\gamma}{rec_3} & -\frac{N^2}{r_2} & 0 & 0 & 0 & 0 \\ 0 & 0 & -\frac{2N^2}{r_2}-\frac{\gamma}{rec_3} & \frac{2N^2}{r_2}+\frac{\gamma}{rec_4} & 0 & 0 & 0 & 0 \\ 0 & 0 & \frac{N^2}{r_2} & -\frac{N^2}{r_2}-\frac{\gamma}{rec_4} & \frac{N^2}{r_3}+\frac{\gamma}{rec_5} & -\frac{N^2}{r_3} & 0 & 0 \\ 0 & 0 & 0 & 0 & -\frac{2N^2}{r_3}-\frac{\gamma}{rec_5} & \frac{2N^2}{r_3}+\frac{\gamma}{rec_6} & 0 & 0 \\ 0 & 0 & 0 & 0 & \frac{N^2}{r_3} & -\frac{N^2}{r_3}-\frac{\gamma}{rec_6} & \frac{N^2}{r_4}+\frac{\gamma}{rec_7} & -\frac{N^2}{r_4} \\ 0 & 0 & 0 & 0 & 0 & 0 & -\frac{2N^2}{r_4}-\frac{\gamma}{rec_7} & \frac{2N^2}{r_4}+\frac{\gamma}{rec_8} \end{bmatrix}$$

$$\begin{bmatrix} -\frac{\gamma}{rec_9} & 0 & 0 & 0 & 0 & 0 & 0 & 0 & \frac{\gamma}{rec_{17}} & 0 & 0 & 0 & 0 & 0 & 0 & 0 \\ 0 & -\frac{\gamma}{rec_{10}} & 0 & 0 & 0 & 0 & 0 & 0 & 0 & -\frac{\gamma}{rec_{18}} & 0 & 0 & 0 & 0 & 0 & 0 \\ 0 & 0 & -\frac{\gamma}{rec_{11}} & 0 & 0 & 0 & 0 & 0 & 0 & 0 & -\frac{\gamma}{rec_{19}} & 0 & 0 & 0 & 0 & 0 \\ 0 & 0 & 0 & -\frac{\gamma}{rec_{12}} & 0 & 0 & 0 & 0 & 0 & 0 & 0 & -\frac{\gamma}{rec_{20}} & 0 & 0 & 0 & 0 \\ 0 & 0 & 0 & 0 & -\frac{\gamma}{rec_{13}} & 0 & 0 & 0 & 0 & 0 & 0 & 0 & -\frac{\gamma}{rec_{21}} & 0 & 0 & 0 \\ 0 & 0 & 0 & 0 & 0 & -\frac{\gamma}{rec_{14}} & 0 & 0 & 0 & 0 & 0 & 0 & 0 & -\frac{\gamma}{rec_{22}} & 0 & 0 \\ 0 & 0 & 0 & 0 & 0 & 0 & -\frac{\gamma}{rec_{15}} & 0 & 0 & 0 & 0 & 0 & 0 & 0 & -\frac{\gamma}{rec_{23}} & 0 \end{bmatrix} \tag{C.28}$$

Loops around the rotor and stator:

$$\mathbf{C_{L2}}_{2\times24} = \begin{bmatrix} 0 & 0 & 0 & 0 & 0 & 0 & 0 & 0 & -\frac{\gamma}{rec_9} & -\frac{\gamma}{rec_{10}} & -\frac{\gamma}{rec_{11}} & -\frac{\gamma}{rec_{12}} & -\frac{\gamma}{rec_{13}} & -\frac{\gamma}{rec_{14}} & -\frac{\gamma}{rec_{15}} & -\frac{\gamma}{rec_{16}} \\ 0 & 0 & 0 & 0 & 0 & 0 & 0 & 0 & 0 & 0 & 0 & 0 & 0 & 0 & 0 & 0 \end{bmatrix}$$

$$\begin{bmatrix} 0 & 0 & 0 & 0 & 0 & 0 & 0 & 0 \\ -\frac{\gamma}{rec_{17}} & -\frac{\gamma}{rec_{18}} & -\frac{\gamma}{rec_{19}} & -\frac{\gamma}{rec_{20}} & -\frac{\gamma}{rec_{21}} & -\frac{\gamma}{rec_{22}} & -\frac{\gamma}{rec_{23}} & -\frac{\gamma}{rec_{24}} \end{bmatrix} \tag{C.29}$$

Conservation of the derivatives of the fluxes:

$$\mathbf{C_N}_{15\times24} = \begin{bmatrix} 0&1&0&0&0&0&0&0&1&-1&0&0&0&0&0&0&0&0&0&0&0&0&0&0 \\ 0&0&1&0&0&0&0&0&0&1&-1&0&0&0&0&0&0&0&0&0&0&0&0&0 \\ 0&0&0&1&0&0&0&0&0&0&1&-1&0&0&0&0&0&0&0&0&0&0&0&0 \\ 0&0&0&0&1&0&0&0&0&0&0&1&-1&0&0&0&0&0&0&0&0&0&0&0 \\ 0&0&0&0&0&1&0&0&0&0&0&0&1&-1&0&0&0&0&0&0&0&0&0&0 \\ 0&0&0&0&0&0&1&0&0&0&0&0&0&1&-1&0&0&0&0&0&0&0&0&0 \\ 0&0&0&0&0&0&0&1&0&0&0&0&0&0&1&-1&0&0&0&0&0&0&0&0 \\ 0&1&0&0&0&0&0&0&0&0&0&0&0&0&0&0&-1&1&0&0&0&0&0&0 \\ 0&0&1&0&0&0&0&0&0&0&0&0&0&0&0&0&0&-1&1&0&0&0&0&0 \\ 0&0&0&1&0&0&0&0&0&0&0&0&0&0&0&0&0&0&-1&1&0&0&0&0 \\ 0&0&0&0&1&0&0&0&0&0&0&0&0&0&0&0&0&0&0&-1&1&0&0&0 \\ 0&0&0&0&0&1&0&0&0&0&0&0&0&0&0&0&0&0&0&0&-1&1&0&0 \\ 0&0&0&0&0&0&1&0&0&0&0&0&0&0&0&0&0&0&0&0&0&-1&1&0 \\ 0&0&0&0&0&0&0&1&0&0&0&0&0&0&0&0&0&0&0&0&0&0&-1&1 \\ 1&1&1&1&1&1&1&1&0&0&0&0&0&0&0&0&0&0&0&0&0&0&0&0 \end{bmatrix} \tag{C.30}$$

Magnetic material length matrix:

$$\mathbf{L}_{24\times24} = \begin{bmatrix}
l_1 & -l_2 & 0 & 0 & 0 & 0 & 0 & 0 & l_9 & 0 & 0 & 0 & 0 & 0 & 0 & 0 & -l_{17} & 0 & 0 & 0 & 0 & 0 & 0 & 0 \\
0 & l_2 & -l_3 & 0 & 0 & 0 & 0 & 0 & 0 & l_{10} & 0 & 0 & 0 & 0 & 0 & 0 & 0 & -l_{18} & 0 & 0 & 0 & 0 & 0 & 0 \\
0 & 0 & l_3 & -l_4 & 0 & 0 & 0 & 0 & 0 & 0 & l_{11} & 0 & 0 & 0 & 0 & 0 & 0 & 0 & -l_{19} & 0 & 0 & 0 & 0 & 0 \\
0 & 0 & 0 & l_4 & -l_5 & 0 & 0 & 0 & 0 & 0 & 0 & l_{12} & 0 & 0 & 0 & 0 & 0 & 0 & 0 & -l_{20} & 0 & 0 & 0 & 0 \\
0 & 0 & 0 & 0 & l_5 & -l_6 & 0 & 0 & 0 & 0 & 0 & 0 & l_{13} & 0 & 0 & 0 & 0 & 0 & 0 & 0 & -l_{21} & 0 & 0 & 0 \\
0 & 0 & 0 & 0 & 0 & l_6 & -l_7 & 0 & 0 & 0 & 0 & 0 & 0 & l_{14} & 0 & 0 & 0 & 0 & 0 & 0 & 0 & -l_{22} & 0 & 0 \\
0 & 0 & 0 & 0 & 0 & 0 & l_7 & -l_8 & 0 & 0 & 0 & 0 & 0 & 0 & l_{15} & 0 & 0 & 0 & 0 & 0 & 0 & 0 & -l_{23} & 0 \\
0 & 0 & 0 & 0 & 0 & 0 & 0 & 0 & l_9 & l_{10} & l_{11} & l_{12} & l_{13} & l_{14} & l_{15} & l_{16} & 0 & 0 & 0 & 0 & 0 & 0 & 0 & 0 \\
0 & 0 & 0 & 0 & 0 & 0 & 0 & 0 & 0 & 0 & 0 & 0 & 0 & 0 & 0 & 0 & l_{17} & l_{18} & l_{19} & l_{20} & l_{21} & l_{22} & l_{23} & l_{24} \\
0 & 0 & 0 & 0 & 0 & 0 & 0 & 0 & 0 & 0 & 0 & 0 & 0 & 0 & 0 & 0 & 0 & 0 & 0 & 0 & 0 & 0 & 0 & 0 \\
\vdots & \vdots & \vdots & \vdots & \vdots & \vdots & \vdots & \vdots & \vdots & \vdots & \vdots & \vdots & \vdots & \vdots & \vdots & \vdots & \vdots & \vdots & \vdots & \vdots & \vdots & \vdots & \vdots & \vdots \\
0 & 0 & 0 & 0 & 0 & 0 & 0 & 0 & 0 & 0 & 0 & 0 & 0 & 0 & 0 & 0 & 0 & 0 & 0 & 0 & 0 & 0 & 0 & 0
\end{bmatrix} \tag{C.31}$$

Material magnetic field intensity vector:

$$\mathbf{H}_{24\times1} = \begin{bmatrix} H_1 & H_2 & \dots & H_{24} \end{bmatrix}^T \tag{C.32}$$

Air gap length matrix:

$$\mathbf{G}_{24\times8} = \begin{bmatrix}
g_1 & -g_2 & 0 & 0 & 0 & 0 & 0 & 0 \\
0 & g_2 & -g_3 & 0 & 0 & 0 & 0 & 0 \\
0 & 0 & g_3 & -g_4 & 0 & 0 & 0 & 0 \\
0 & 0 & 0 & g_4 & -g_5 & 0 & 0 & 0 \\
0 & 0 & 0 & 0 & g_5 & -g_6 & 0 & 0 \\
0 & 0 & 0 & 0 & 0 & g_6 & -g_7 & 0 \\
0 & 0 & 0 & 0 & 0 & 0 & g_7 & -g_8 \\
0 & 0 & 0 & 0 & 0 & 0 & 0 & 0 \\
\vdots & \vdots & \vdots & \vdots & \vdots & \vdots & \vdots & \vdots \\
0 & 0 & 0 & 0 & 0 & 0 & 0 & 0
\end{bmatrix} \tag{C.33}$$

Air gap magnetic field intensity vector:

$$\mathbf{H_g}_{8\times1} = \begin{bmatrix} H_{g1} & H_{g2} & H_{g3} & H_{g4} & H_{g5} & H_{g6} & H_{g7} & H_{g8} \end{bmatrix}^T \tag{C.34}$$

Input/interconnection matrix:

$$\mathbf{N}_{24\times4} = \begin{bmatrix}
-\frac{2N}{r_1} & 0 & 0 & 0 \\
\frac{N}{r_1} & -\frac{N}{r_2} & 0 & 0 \\
0 & \frac{2N}{r_2} & 0 & 0 \\
0 & -\frac{N}{r_2} & \frac{N}{r_3} & 0 \\
0 & 0 & -\frac{2N}{r_3} & 0 \\
0 & 0 & \frac{N}{r_3} & -\frac{N}{r_4} \\
0 & 0 & 0 & \frac{2N}{r_4} \\
0 & 0 & 0 & 0 \\
\vdots & \vdots & \vdots & \vdots \\
0 & 0 & 0 & 0
\end{bmatrix} \tag{C.35}$$

Voltage input vector:

$$\mathbf{V}_{4\times1} = \begin{bmatrix} v_1 & v_2 & v_3 & v_4 \end{bmatrix}^T \tag{C.36}$$

Current output vector:

$$\mathbf{I}_{4\times1} = \begin{bmatrix} i_1 & i_2 & i_3 & i_4 \end{bmatrix}^T \tag{C.37}$$

Current-voltage interconnection matrix:

$$\mathbf{I_{V\,4\times4}} = \begin{bmatrix} \frac{1}{r_1} & 0 & 0 & 0 \\ 0 & \frac{1}{r_2} & 0 & 0 \\ 0 & 0 & \frac{1}{r_3} & 0 \\ 0 & 0 & 0 & \frac{1}{r_4} \end{bmatrix} \tag{C.38}$$

Current-flux derivative matrix:

$$\mathbf{I_{\Phi\,4\times24}} = \begin{bmatrix} -\frac{N}{r_1} & \frac{N}{r_1} & 0 & 0 & 0 & 0 & 0 & 0 & 0 & \cdots & 0 \\ 0 & 0 & \frac{N}{r_2} & -\frac{N}{r_2} & 0 & 0 & 0 & 0 & 0 & \cdots & 0 \\ 0 & 0 & 0 & 0 & -\frac{N}{r_3} & \frac{N}{r_3} & 0 & 0 & 0 & \cdots & 0 \\ 0 & 0 & 0 & 0 & 0 & 0 & \frac{N}{r_4} & -\frac{N}{r_4} & 0 & \cdots & 0 \end{bmatrix} \tag{C.39}$$

A simulation model for an 8-pole heteropolar magnetic bearing, with neighbouring coils wound in series and configured as NSSNNSSN, is presented. The model includes nonlinear magnetisation effects (saturation and hysteresis) and also models eddy currents. The developed model allows for the implementation of a switching power amplifier and the resulting current waveforms correlate closely to experimental waveforms.

The model includes the most important effects which degrades self-sensing performance and is therefore suitable for self-sensing investigations. The model may serve as a platform to evaluate different self-sensing techniques and facilitate self-sensing algorithm development.